Aptamer-functionalized nanopore for the detection of closely-related proteins

Lucile Reynaud

THÈSE

Pour obtenir le grade de

DOCTEUR DE L'UNIVERSITE GRENOBLE ALPES

Spécialité : **Physique pour les Sciences du Vivant**

Arrêté ministériel : 25 mai 2016

Présentée par

Lucile REYNAUD

Thèse dirigée par
Arnaud BUHOT, Ingénieur de Recherche, CEA Grenoble,
et codirigée par
Aurélie BOUCHET-SPINELLI, Maître de Conférences, UGA, &
Camille RAILLON, Ingénieure de Recherche, CEA Grenoble.

Préparée au sein du **CEA Grenoble**

Institut de Recherche Interdisciplinaire de Grenoble (IRIG)

Département des Interfaces pour l'Energie, la Santé et l'Environnement (DIESE)

Service : Systèmes Moléculaires et nanoMatériaux pour l'Energie et la Santé (SyMMES)

Groupe : Chimie pour la Reconnaissance et l'Etude des Assemblages Biologiques (CREAB)

Dans **l'École Doctorale de Physique**

Aptamer-Functionalized Nanopore for the Detection of Closely-Related Proteins

Thèse soutenue publiquement le **24 Novembre 2020**,
devant le jury composé de :

Mr. Bertrand FOURCADE
Professeur à l'Université Grenoble Alpes, Président
Mr. Sébastien BALME
Maître de Conférences à l'Université de Montpellier, Rapporteur
Mr. Rabah BOUKHERROUB
Professeur à l'Université de Lille, Rapporteur
Mme. Corinne RAVELET
Maître de Conférences à l'Université Grenoble Alpes, Examinatrice
Mr. Hubert GIRAULT
Professeur à l'Ecole Polytechnique Fédérale de Lausanne, Examinateur
Mme. Pascale PHAM
Ingénieure de Recherche au CEA Grenoble, Examinatrice

Remerciements

Je souhaite remercier toutes les personnes ayant rendu ces trois ans de travail possible. Tout d'abord je remercie Mr Chandezon Frédérique à la tête du SYMMES pour avoir accepté ma venue dans le laboratoire au sein de l'équipe CREAB. Je remercie ensuite tout naturellement Mr Buhot Arnaud, mon directeur de thèse et chef d'équipe, pour le temps accordé à mon projet, les nombreuses discussions scientifiques très enrichissantes, pour avoir laissé sa porte de bureau ouverte en tout temps et avoir montré un optimisme sans faille même lorsque les moments étaient durs. Cet état d'esprit m'a beaucoup inspiré et je t'en remercie. Je remercie ensuite mes encadrantes Mme Raillon Camille, pour son expertise sur les nanopores et le temps accordé à mon projet, et Mme Bouchet-Spinelli, pour avoir été présente et avoir répondu avec patience et bienveillance à toutes mes questions novices en chimie de surface et dans bien d'autres domaines encore.

Je remercie Mme Mauduit Sarah, qui a montré une efficacité redoutable sur tous les aspects administratifs techniques rencontrés lors de ces trois ans. Du côté laboratoire, je remercie grandement Mr Mathey Raphaël, qui m'a montré les astuces d'un grand expérimentateur, et grâce à qui la fonctionnalisation de surface dans mon projet a pu avancer sereinement. Je remercie également Mr Jouneau Pierre-Henri de la PFNC pour le temps et la patience accordés sur le fameux Osiris, TEM capricieux, sans qui je n'aurais pas pu faire toutes ces expériences sur nanopores. Pour ma première année, j'ai passé beaucoup de temps en salle blanche. Je remercie donc chaleureusement Mr Thomassin Jean-Luc pour son aide précieuse sur les procédés de fabrication, ainsi que Mme Gri Martine, Mme Gomez Christelle, Mme Belloir Tiphaine et Mr Gaude Victor pour leurs aides respectives. Je tiens à remercier Mr Moreau Christophe de l'IBS pour m'avoir laissé prendre la main sur un banc expérimental nanopores dans son laboratoire. Je remercie également Mr Yates James de Nanopores Solutions pour ses échanges passionnés autour de ses produits. Je remercie Mr Mantegazza Frédérique (ILL) et Mr Ruty Nicolas (Grenoble-INP) pour leurs éclairages sur le langage Python et la programmation.

J'ai eu la chance de faire ma thèse dans un laboratoire plein de bonne humeur et d'énergie, alors merci à ceux qui en sont la cause. Je remercie tous les thésards, stagiaires, post-docs, permanents et autres qui ont croisé ma route au CREAB. Je remercie mes voisines de bureau préférées Cloé Desmet et Marielle El-Kazzy, qui me donnaient ma dose de bonne humeur journalière. Je remercie également Annette Délices pour ta présence chaleureuse et ta sagesse qui m'auront guidée pendant la majorité de ma thèse. Je remercie Abdul Ismaïl, grand chef, pour sa sympathie et la bonne ambiance des repas en sa compagnie. Je remercie chaleureusement tous les thésards qui auront accompagné mon quotidien au labo et en dehors. Les sages anciens : Ricardo Alvarado, Sophie Brenet, Eric Pardoux, Marine Boulade. Ceux qui auront affronté la thèse en même temps que moi : Charlotte Hurot, bravo pour ton parcours de warrior, Maud Savonnet, merci pour tous les moments où on a rigolé ensemble, Jon Weerakkody, à qui je souhaite bon courage pour la fin, et Daniel Marquez. Je remercie aussi la nouvelle génération de thésards qui reprennent le flambeau et continuent de faire vivre le CREAB, Marie et Elise, je vous souhaite à toutes les deux le meilleur pour votre dernière année et dans la vie en général. Une pensée également pour les super stagiaires Christelle Schneuwly et Lucie Descamps. Enfin, le CREAB ne serait pas le même sans ses membres permanents, je remercie donc pour leur bonne humeur au quotidien Élodie, Yanxia, Christine, PH, Didier, Martial, Yoann et José.

Je termine ces remerciements par mes ressources d'énergie et de convivialité extérieures. Je remercie mes amies de la barre qui ont été fidèles jusqu'à la soutenance ! Je remercie tous mes fantastiques élèves de Saint Marcellin à Pole And Move et mes superbes élèves de Pole Dance Grenoble. Merci enfin à ma famille. Et surtout, merci à Baptiste, pour être là avec moi tout simplement.

Table of Contents

List of Figures

List of Tables

1

State of the Art

Synopsis

Single molecule nanopore sensing is a promising technique that has been developed over the past two decades. In this chapter, we will review different aspects of this technology in order to introduce the main principles and the relevant literature that constitute the foundations of this thesis work. From biological to synthetic solid-state nanopores, we will also consider the different ways to operate surface chemistry for their functionalization. We will also assess the possible applications ranging from the advanced DNA sensing technology to the more recent uses in protein detection. A specific part will be dedicated to the use of aptamer technology combined with nanopore sensing. Finally, we will describe the aim of this thesis work which is the discrimination of closely related proteins with an aptamer functionalized nanopore.

The state of the art presented in this chapter has been the object of a review in the Journal Sensors:

Reynaud, L.; Bouchet-Spinelli, A.; Raillon, C.; Buhot, A. **Sensing with Nanopores and Aptamers: A Way Forward.** Sensors **20**, 4495 (2020)."

Table of contents

1.1 Biophysics, Biosensors and Single-Molecule Studies

1.1.1 Biophysics

Scale is important in the study of living organisms (Figure 1.1). Sizes can range from 25 meters (blue whales) to nanometers (biomolecules) and timescales range from billions of years (evolution) to femtoseconds (biochemical reactions). Biophysics is a science that studies life from various and multidisciplinary viewing angles and goes through those various scales[1]. The combination of life science and recent technological developments allows the biophysicist to bring quantitative information to understand complex biological systems and their interactions. The applications of biophysics are numerous, such as imaging systems, neurosciences or environmental ecosystem studies to cite a few. Biomedicine is one of those applications. Each human being has a unique genome and phenotype, and billions of different people are living a variety of lifestyles. That triggers an inherent complexity into finding a suitable medical treatment for each person. Over the past two decades, there has been an increasing interest toward P4 medicine[2,3], a discipline that follows four principles: Predictive, Personalized, Preventive, Participatory. It consists in an adapted medical therapy which holds the promise to find an optimal treatment for each patient, improve risk prevention and even lower medical costs. However, even at the individual level, the cellular heterogeneity adds complexity into understanding biological mechanisms. This discrepancy arises from the complex expression of genes, proteins and all metabolites. Up until now, a majority of analyses and tests are performed on a cell ensemble, providing an average bulk result that does not reflect the profile of each particular cell. That is where emerging technologies such as micro or nano fluidics and microfabricated devices meet biophysics in order to assess this problem and offer single-cell and single-molecule analyses[4–7]. With single-molecule analyses, the spatiotemporal accuracy of the measurement greatly improves the answers that research can offer to this complexity.

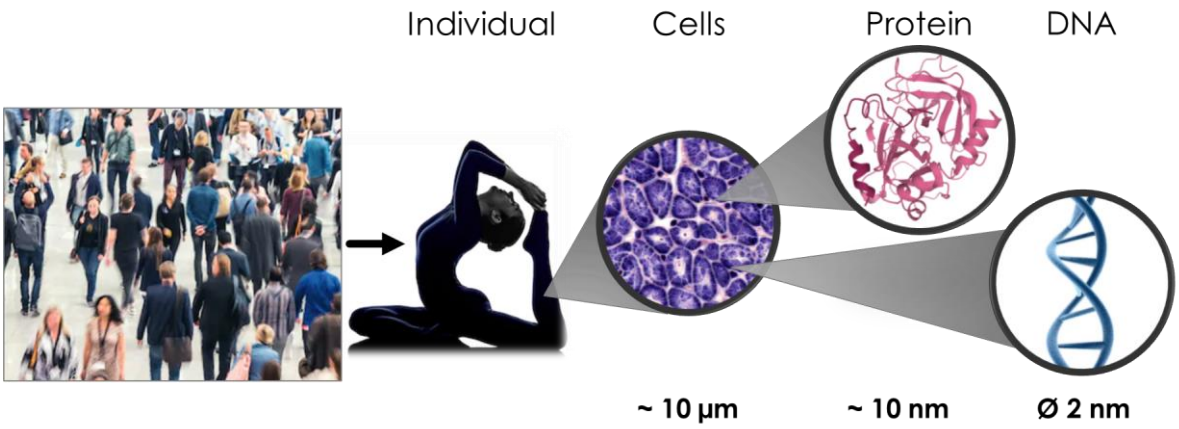

Figure 1.1: Illustration of typical size scales for cells, proteins and DNA that are the building blocks of all known living organisms. (Free images from Shutterstock.fr)

1.1.2 Protein Structure

Each cell of the human body carries a nucleus enclosing polynucleotide chains called DNA (deoxyribonucleic acid). Two DNA chains form a double helix as demonstrated first in the 50s by Watson and Cricks[8]. DNA contains the genetic code of a living being, which is all the information needed to form, grow, live and reproduce. DNA is transcripted into RNA (ribonucleic acid) which is in turn translated into proteins that perform a vast array of functions in the cell (structure, messaging, transport, enzymatic activity etc.). Understanding the genome and the proteome is key to develop new treatments and fundamentally understand complex biological systems.

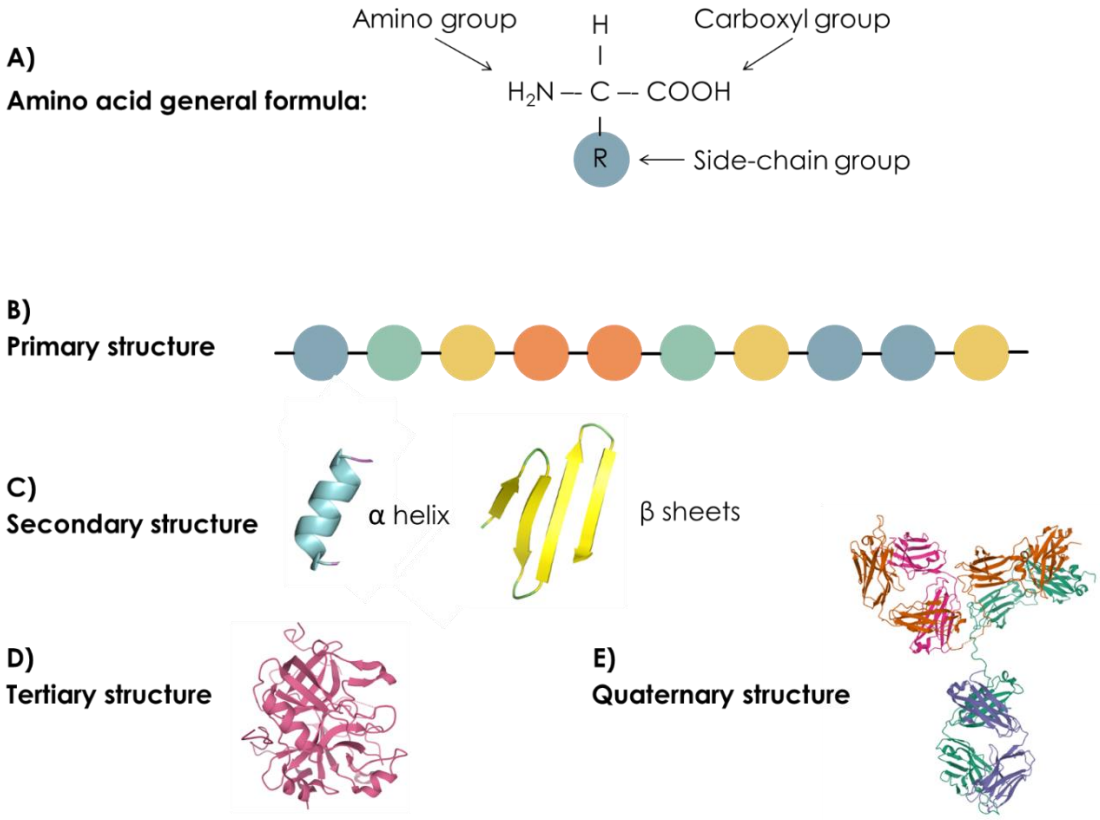

Figure 1.2: The different levels of protein structures. A) Amino acid general formula. B) Protein primary structure, an amino acid chain. C) Protein secondary structure, α helices and β sheets. D) Protein tertiary structure, full 3D conformation. Example with human α-thrombin (PDB: 1D3T) E) Protein quaternary structure, assembly of different protein chains. Example with human immunoglobulin G (PDB: 1HZH).

Proteins are structurally complex and functionally sophisticated molecules[9]. They offer a wide variety of functions with precise ligand binding affinities and enzymatic activities[10]. Amino-acids are the building blocks of proteins. They contain an amino group, a carboxyl group and a side-chain (Figure 1.2). The nature of the side-chain gives the properties of the amino acid, there are 20 different natural

side chains. Each type of protein is a unique sequence of amino acids linked through covalent peptide bonds. The linear sequence of amino acid, or polypeptide chain, is the primary structure of the protein. It is the first level of protein organization (up until four). The secondary structure consists in the reorganization of the polypeptide chain into α helices and β sheets arising from local interactions between neighboring amino acids (hydrogen bonds). A protein usually contains several α helices and β sheets that fold together to create the full three-dimensional organization, the tertiary structure of a protein. Finally, we talk about a quaternary structure when a protein is composed of several polypeptide chains formed as a complex[9].

1.1.3 Biosensors toward Single-Molecule Sensing

Advances in the study of DNA and proteins have been enabled by the extensive use of biochips over the past decades and the rise of single-molecule studies. Biochips are a microarray of biosensors that can monitor simultaneously biochemical reactions[11]. The first referenced biosensor in 1962 was an electrode measuring sugar and oxygen levels in blood samples[12]. Nowadays, thanks to the integration of microfabrication technologies and microfluidics, some devices are designed as lab-on-a-chip systems (LOC)[13]. Protein biochips are used in many areas of biological research, such as drug screening, study of protein interactions, biochemical activities, or immune responses[14]. The possibility to perform various experiments on a minimal quantity of sample holds great promises for personalized medicine[14,15].

A biosensor is generally composed of two elements, an immobilized biological probe (antibodies[16], DNA[17,18], proteins[19–21], etc.) and a transducer that converts the monitored biochemical reaction into a measurable physical signal (electrical, thermic, optical etc.). The immobilization techniques of the biological probe over the sensing surface are numerous[22]. Among the variety of biomolecular probes, aptamers have raised interest as an easily synthesizable, cheap, highly selective and stable probe for the specific recognition of various targets[23–26] such as proteins, vesicles or toxins. Aptamers are small single-stranded RNA or DNA oligonucleotides (15 to 60 bases). Their three-dimensional conformation provides affinity toward the target against which it has been selected (Figure 1.3). They are able to specifically bind proteins, small molecules, cells, bacteria... The aptamer selection is achieved with a Darwinian-like *in vitro* selection process called SELEX[27,28] (Systematic Evolution of Ligands by EXponential Enrichment). During this cyclic and repetitive approach, a library of different sequences and structures is incubated with the desired target. The bound sequences are then selected and amplified by PCR (polymerase chain reaction). This process is repeated until the remaining population represents only the aptamers with the most affinity toward the target.

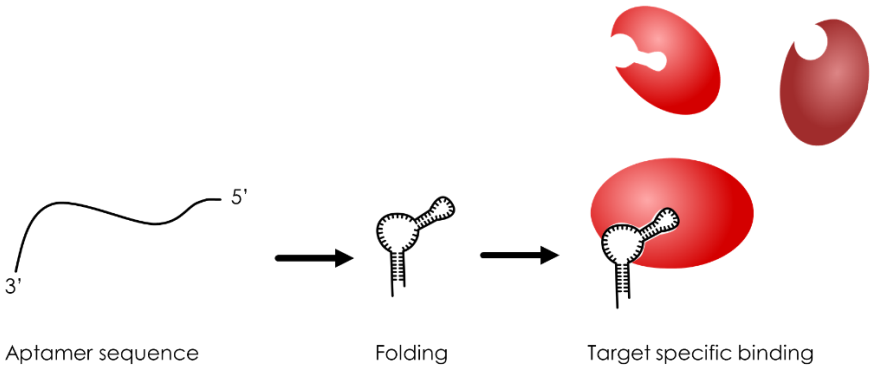

Figure 1.3: Illustration of aptamer binding principle adapted from reference[29].

To go further in the understanding of proteins and DNA, interest toward single-molecule studies techniques has grown over the past decade[5,7,30,31]. The field for detection and manipulation of single-molecules is expanding, we can mention several techniques such as single-molecule ELISA assays[32], optical trapping[33] and optical tweezers[34], single-molecule electrochemical assays[35] (SM-EC), surface-enhanced Raman spectroscopy[36] (SERS), nanoplasmonic sensing with localized surface plasmon resonance[37] (LSPR). Another promising technique for single-molecule study is nanopore sensing[5,38] and will be the main subject of the present thesis work. This label-free technology can be performed without the need of optical instruments and is based on the Coulter counter principle[39]. Nanopores are going to be described in the next part (Section 1.2).

1.2 Nanopore Sensing

1.2.1 Principle

Nanopore sensing is based on the Coulter counter[40] principle proposed in 1953, a resistive sensing device able to count and size objects going through an aperture. Nanopore technology comes from the merging of the Coulter counter and single-channel electrophysiology[41], which is the study of transmembrane current through lipid bilayers. In the 90s, studies about single-molecule translocation through a single biological nanopore in a planar lipid bilayer emerged[42]. In the beginning of the 2000s, the first solid-state nanopores for studies of single-molecule translocation were fabricated[43]. Recently, a new sub-group of solid-state nanopores called nanopipette is emerging[44]. Illustration of a biological, a solid-state nanopore and a nanopipette can be found in Figure 1.4.

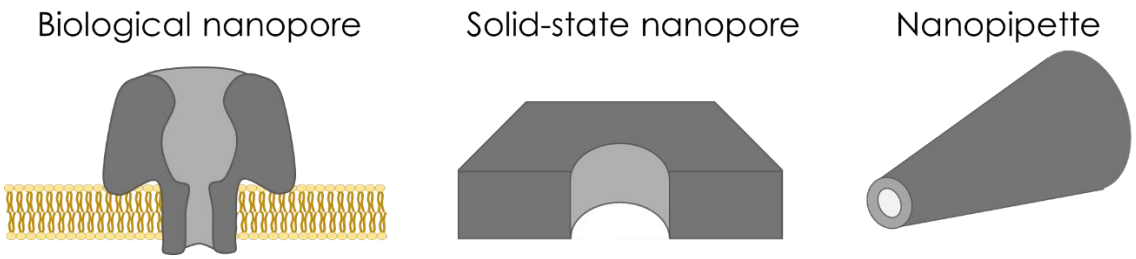

Figure 1.4: Illustration of a biological nanopore in a lipid bilayer (left) a solid-state nanopore fabricated in an insulating membrane (middle) and a nanopipette (right).

A typical nanopore device consists in a nanometric aperture in a dielectric membrane between two reservoirs of a conductive electrolyte solution. In this work, we consider nanopores ranging between 1 and 100 nm. An illustration of a solid-state nanopore and its principle is given on Figure 1.5. The nanopore is the only contact between the two reservoirs. Electrodes are immersed on each side of the membrane, and an electric current flowing through the nanopore is established when a voltage is applied across those electrodes[45]. This steady-state current is called open-pore current. Typically, current is monitored for different applied voltages and a linear current-voltage (I-V) curve is obtained. The nanopore conductance and size can be calculated from this curve[45]. More insights about the physical phenomena behind this principle will be discussed in the Chapter 3 of this work.

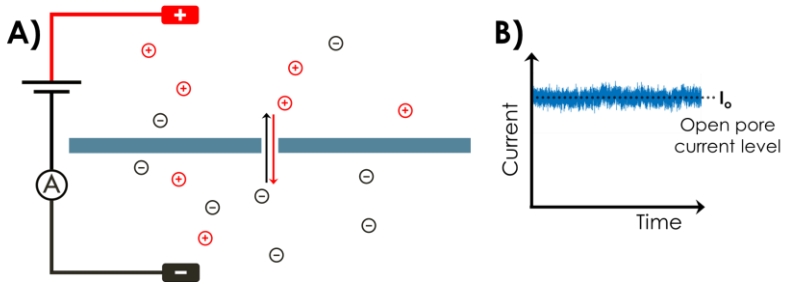

Figure 1.5: Illustration of solid-state nanopore principle. A) A dielectric membrane separates two electrolytes reservoirs that are connected solely through the nanopore. Electrodes are placed at each side of the membrane and a voltage is applied. B) Measured ionic current results from the electrolyte charges moving through the nanopore. I_o is the open-pore current level.

The principle of single-molecular detection is depicted on Figure 1.6. A voltage is applied between the two electrodes. When a biomolecule, such as DNA or protein, is added into one of the electrolyte reservoirs, it is electrophoretically driven through the nanopore (translocation) and a disruption in the current signal is observed. Consecutive disruptions correspond to successive biomolecule translocations in the nanopore. The current blockage amplitude ΔI is the difference between the open pore current and the current level when the biomolecule is inside the nanopore. The dwell-time δt corresponds to the duration of the translocation event. A statistical analysis of the current blockade amplitudes (ΔI) and dwell-times (δt) can provide information on the biomolecule such as its volume, charge or conformation inside the nanopore[45–47].

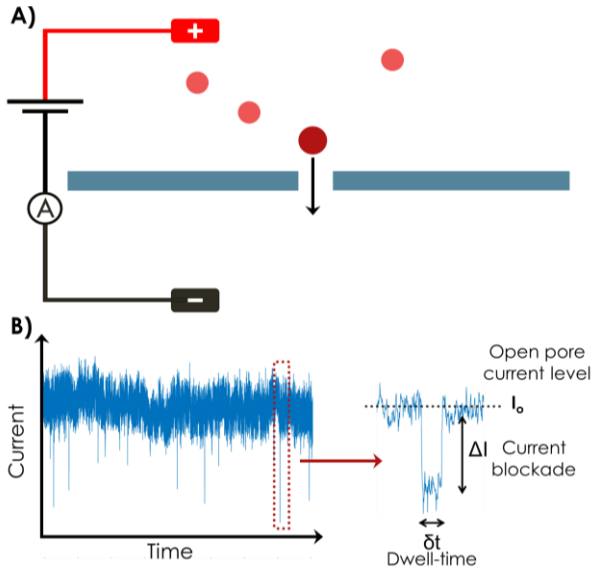

Figure 1.6: Illustration of single-molecule detection with a nanopore. A) A constant voltage is applied and the biomolecule is driven through the nanopore. B) Measured signal of current over time. The biomolecules cause current blockades ΔI for a duration or dwell-time δt when going through the nanopore.

1.2.2 Biological Nanopores

Biological pores are found in Nature as proteins acting as transport channels through the membrane of cells. They take various forms and purposes[48], such as ion channels proteins (for ionic transport), porins and aquaporins (for water-soluble components and water), nuclear pore complexes[49] (transport of oligonucleotides and proteins), pore-forming toxin peptides (that can trigger the lysis of the cell) or viral pores (for the transport of viral DNA into the infected cell). Those proteins or protein assemblies are inserted in a lipid bilayer. One of the most popular biological nanopores among single-molecule researchers is α-hemolysin. It was the biological nanopore used in 1996 by Kasianowicz *et al.* for the first demonstration of RNA and DNA single-molecule detection with a nanopore[42]. α-Hemolysin is a bacterial pore composed of assembled proteins and secreted by *Staphylococcus aureus* with a well-known crystal structure[50]. The pore measures 10 x 10 nm² and the lumen has a diameter ranging from 4.6 nm to 1.4 nm in its narrowest region. This pore enables highly reproducible DNA translocation experiments. Some other biological nanopores[51] commonly used for translocation of nucleic acids, small peptides or unfolded proteins are Outer membrane protein G OmpG[52] (with an internal diameter of 1.3 nm), *Mycobacterium smegmatis* porin A MspA[53] (1.2 nm) and Aerolysin AeL[54,55] (1.0 nm). However, for sensing larger molecules such as proteins, different biological nanopores with a wider diameter are also used, such as Cytolysin A ClyA[56,57] (diameter 3.3 nm) and phi29 motor pores[58,59] (3.6 nm). Examples of biological nanopores with their dimension are illustrated on Figure 1.7.

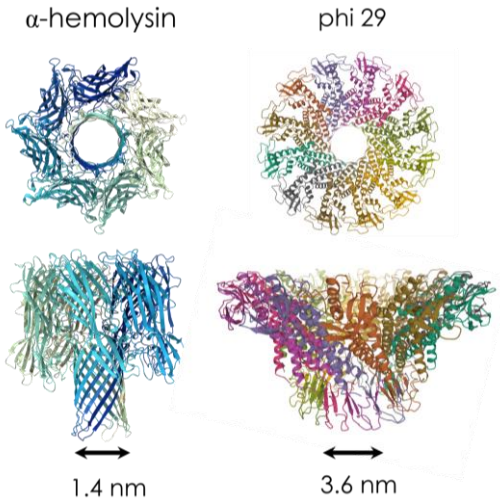

Figure 1.7: α-hemolysin nanopore structure (PDB: 7AHL) and Phi29 motor nanopore structure (PDB: 1JNB).

Biological nanopores have the advantages to offer highly reproducible translocation results thanks to a well-defined pore structure. The lipid bilayer in which they are embedded offers low electrical noise[60]. Their chemical structure can be tuned with the addition of functional groups thanks to genetic or molecular engineering[61] and the variety of available biological pores increases over time[62]. However,

they present a low mechanical and chemical stability over time[63], and the range of pore size is restricted which limits the possible applications.

1.2.3 Solid-State Nanopores

Synthetic nanopores, or solid-state nanopores, are fabricated pores drilled in a dielectric inorganic solid membrane. The first materials used were silicon nitride (Si_3N_4 or SiN_x) and silicon dioxide (SiO_2) because of the pre-existing expertise in the microfabrication of transistors[64]. It offers the possibility of a high-throughput fabrication of nanopores with a good control over size. In 2001, Li *et al*. reported the first nanopore with a diameter of 1.8 nm fabricated in SiN_x thanks to Focused Ion Beam (FIB)[43]. The nanopore was then used to detect single-events of DNA going through the nanopore. Another important advance was made when Storm *et al.* proposed to use a transmission electron microscope (TEM) to drill the membrane[65]. The advantage of TEM drilling is the immediate visual feedback over fabrication. Other techniques of fabrication include scanning transmission electron microscope[66] (STEM), electrochemical removing of atoms in molybdenum disulfide MoS_2[67] or dielectric breakdown[68]. It will be further discussed in Chapter 2. The material used for the dielectric membrane are various, apart from SiN_x and SiO_2, nanopores have been fabricated in thin materials for a higher sensitivity[60] such as graphene[69,70] or hafnium oxide[71]. There is a recent subclass of solid-state nanopores called glass nanocapillaries or nanopipettes[44,72–78], but we will not describe this specific category in this work.

Working on fabricated solid-state nanopores has some advantages over their biological counterparts[79]. They present tunable geometrical designs, a better mechanical stability over a wide range of experimental conditions such as pH and ionic strengths, and a possible control over surface chemistry (that we will tackle in subsection 1.2.5). The fabrication process is generally long and fastidious but some new techniques such as dielectric breakdown can overcome this problem[68]. Another drawback is the possible non-specific adsorption of analyte onto the surface, leading to pore clogging[80]. Those problems can be overcome thanks to surface functionalization or original combinations of biological nanopores with solid-state nanopores. We will discuss about these alternatives in the next sections.

1.2.4 Hybrid Nanopores

As mentioned earlier, biological nanopores such as α-hemolysin possess a precise structure and the potential for site-specific chemical modifications. However, the lipid bilayer in which it is embedded can be unstable. On the other hand, solid-state nanopores present a good robustness overtime but the reproducibility between each nanopore is more uncertain. The concept of hybrid nanopores combines the advantages of both types. A hybrid nanopore was first reported in 2010 by Hall *et al*.[81] with the insertion of an α-hemolysin biological pore in a solid-state nanopore using a DNA guiding tail (Figure 1.8 A). The integration of α-hemolysin into solid-state nanopores is since then performed in several other studies[82,83]. After that, other researches have shown different strategies for hybrid nanopores, such as the grafting of FG-nucleoporins into solid-state membranes to mimic nuclear pore complexes[84,85]. Another example is the insertion of a viral protein portal into a solid-state nanopore[86] (Figure 1.8 C). Challenges regarding such hybrid nanopores remain in the control of the protein insertion into the membrane, and the control of possible peripheral leakages around the biological pore. Another interesting approach toward hybrid nanopores is the increasingly popular use of DNA origami (Figure 1.8 B). They offer a good control over shape, size and other functional options[87,88]. DNA origami shaped as a nanopore docked onto solid-state nanopore has already been demonstrated in several studies[89–92] and single translocations of molecules such as proteins and DNA have been performed. Surface functionalized nanopores can also sometimes be categorized as hybrid nanopores. Due to the importance of surface functionalization in this work, we will tackle this category in the following section 1.2.5.

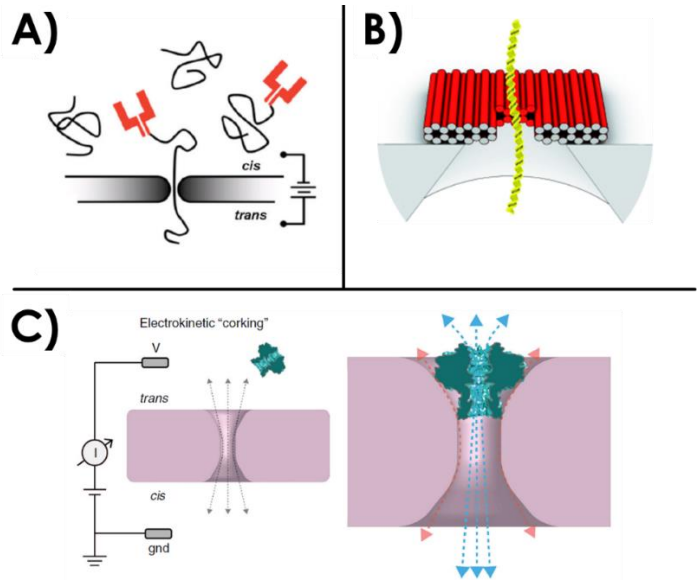

Figure 1.8: Examples of hybrid nanopores. A) First hybrid nanopore reported consisting in a α-hemolysin biological pore inserted in a solid-state nanopore[81]. B) A DNA origami nanopore from reference[90]. C) Virus portal protein inserted in a solid-state nanopore from reference[86].

1.2.5 Functionalized Solid-State Nanopores

After the fabrication of solid-state nanopores in the beginning of the 2000s, interest has grown over their inner surface functionalization[93]. Challenges and objectives met for the functionalization of nanopores can be the same encountered for the functionalization of biochips[22], and many functionalization techniques are inspired from the biosensor's field. The objectives for nanopore functionalization range from antifouling and anti-clogging properties[80,94–97] (reduction of non-specific interactions at the pore surface), to the addition of original functionality or offering biomimetic properties[98]. Some recent reviews describe all the different techniques and purposes of surface functionalization in nanopores[98–100].

A first technique consists in the controlled deposition of a coating material with a gas phase. It is inspired from microfabrication technologies: atomic layer deposition[101] (ALD) and chemical vapor deposition[102] (CVD). Such techniques are employed to monitor size and shape of the nanopore[103–105], or modify surface properties such as charge or hydrophobicity[103,104]. A good advantage of such a coating is that it can increase the stability of the membrane over time by preventing a slow etching by the electrolyte[106]. In particular, some studies have shown that the gas phase deposition of hafnium oxide has inhibited SiN_x dissolution[107]. Another technique consists in the use of surfactants adsorption or physisorption of chemical reagents on the surface. Surfactant can be used on the surface to reduce non-specific interactions of the biomolecule with the pore walls[95,108]. Physisorption can be used as a straightforward technique to coat a nanopore surface. A popular coating using this method is Poly-L-Lysin (PLL), a positively charged synthetic amino acid chain[109,110]. It also provides the possibility to engineer specific interactions with various proteins[111,112]. Layer-by-layer (LBL) self-assembly is another approach to nanopore functionalization. It consists in the formation of multilayer structure alternating between polyanionic and polycationic layers. The control of the deposition allows a fine-tuning of pore diameter[113], modify the surface physical characteristics[114–116] or even combine it with PLL in order to detect specific proteins[116,117]. Another commonly used technique for surface functionalization of gold-covered nanopores is the use of self-assembled monolayers (SAMs). They are composed of molecules bearing a thiol group which reacts and provokes the grafting on a gold layer surface. They are used in nanopore sensing for various applications such as the detection of specific analytes[84,118–120] or the addition of a functionality such as pore gating[121–123] . Lipid coating of nanopores is an increasingly popular technique due to the biomimetic features it provides[80,124]. It can prevent from non-specific adsorption of analytes to the pore walls, but can also be used to decorate the membrane surface with lipid anchored ligands or receptors[99] that are specific to target proteins. Lipid coating allows a reduction of protein's translocation speed and thus enhance the sensitivity of the sensor[47,80,96]. In most surface functionalization, the whole surface of the nanopore membrane is covered, inducing a loss in

recognition specificity inside the pore for sensing applications. ContactLess ElectroFunctionalization (CLEF) is a technique developed by our group that allows functionalizing only the inner part of micro and 200 nm pores[125–128]. Although this beholds great promises for the specific sensing of proteins[129], this technique has not been yet adapted to ~ 10 nm diameter nanopores and was not the object of this study.

The final surface functionalization technique that we will tackle in this manuscript is silanization. It involves the reaction of covalent binding between organo-silanes molecules with the hydroxyl groups on a surface[130,131], which are created after plasma treatment of SiO_2 or the thin oxidation layer on SiN_x in a solid-state nanopore. A reactive functional group (amine, carboxylic group, epoxide etc.) in the silane molecule allows the reaction with specific probes. In the nanopore field, silanization has been used to functionalize the surface of nanopores with various biomolecules[99] such as DNA[132–135], nucleoporins[85], cystein amino acid[136], peptides[137,138], polymer brushes[139] and various chemical components[93,140–143].

The functionalization of the surface of a nanopore is a good strategy for enhancing the detection of protein with solid-state nanopore[129]. In the next section, we will discuss the applications of nanopore sensing for DNA sequencing and the detection of proteins.

1.3 Nanopore Applications

1.3.1 DNA Sequencing

Nanopore sensing has been broadly used for DNA sequencing[144–146]. The electric field is used to drive the negatively charged DNA in the pore, and the drops in the ionic current caused by the translocation are used to distinguish nucleotides. This method has the advantage to avoid DNA modification or amplification and require minimal sample preparation[144,146]. There are indeed some challenges to face regarding such a technique. One of the most troublesome is the rapid DNA translocation velocity[144,147], which limits the identification of a single base in the current trace.

From a historical point of view, single-stranded DNA and RNA sensing with a nanopore has been introduced by Kasianowicz *et al*. in 1996[42], offering the perspective to sequence nucleic acids. Afterward, it has been rapidly considered that nucleotides segments could be differentiated one from another[148,149]. The differentiation of nucleotides from an immobilized single-stranded DNA sequence has finally been performed in a α-hemolysin pore in 2009[150,151], showing that nanopores could provide a sufficient resolution for sequencing as a rapid platform. The immobilization of the sequence allowed overcoming the challenge of high-speed translocation. Sequencing of DNA has later been performed with a biological nanopore coupled with a polymerase enzyme which slowed down the DNA and offered the required time resolution[152]. A commercial apparatus called MinION from Oxford Nanopore Technologies (United Kingdom) has been since released, using a biological nanopore on a lipid bilayer and an enzyme for the control of DNA motion in the nanopore[153,154]. This miniaturized device has already been extensively used to sequence DNA[155] and RNA[156,157] in various application domains[147,158] such as *Escherichia coli* genome sequencing[159] or early mutations in Alzheimer disease[160]. A photography of this commercial device is shown on Figure 1.9.

Figure 1.9 : Oxford Nanopore Technologies MinION commercial DNA sequencer[161].

DNA sensing with nanopore technology is proving to be a powerful tool in an increasing number of fields. In the medical field, it has been used for genomics[162], the detection of diseases[163], and oncology[164]. It has also been used to detect bacteria directly in tissue biopsies[165] and has potential application in forensics[166]. On a recent topic, nanopore sensing has been used to detect the respiratory virus SARS-CoV-2[167]. From an environmental perspective, DNA sensing with nanopores has been used to detect wild viruses[156,168–170], animals[171], or to study an ecosystem with bumblebee pollen[172]. The technique has also been tested on Antarctic samples[173], proving its versatility in wild sample detection. Besides, there has been a growing interest toward the use of nanopores for DNA sensing for astrobiology and life detection in space[174–177], and even toward its use in DNA hard drive technology and data storage[178].

1.3.2 Protein Sequencing

Determining the amino-acid sequence of a protein plays an important role in proteomic studies[179]. Even though the field of DNA sequencing with nanopores has advanced and reached the market with a commercial device[153], the development of single-molecule sequencing of proteins is an emerging yet promising field[180–183]. Challenges inherent to the detection of proteins arise and make it harder to detect than DNA. First, DNA has a relatively simple spatial linear structure while proteins exhibit a natural folding, their tertiary structure. Therefore, the nanopore-based sequencing of proteins requires an unfolding process. Secondly, the surface of a protein is not uniformly charged, and its translocation through the nanopore cannot be driven simply by the electrophoretic force[184]. Finally, protein sequencing requires the distinction between 20 amino acids, while DNA sequencing requires the distinction between only four bases.

The first step for protein sequencing with a nanopore is then to unfold its structure. Several means are employed such as high temperature[185–187] or high voltage[186,188,189]. Another solution is to denature the protein with different agents such as sodium dodecyl sulfate[66,190] (SDS), guanidium chloride[191] or urea[186]. After SDS treatment, the linearized peptide chain is more negatively charged which has been shown to be an advantage for the control of translocation through the pore[190]. The distinction between amino acids and protein sequencing with nanopores has shown promising debuts[192,193]. The spatial resolution of nanopore sensing is a key parameter to assess. Only one amino acid must be sensed in the pore. Distinction between individual amino acids has been suggested in some works[66,70,194] with the use of ultra-thin nanopores which length is similar or below the space between each amino acid or the diameter as close as possible to the size of an amino acid. Another difficulty arises from the time scale of linearized protein going through the pore, which is less than 1 ms[192]. With the average

acquisition frequency of 100 kHz, there is a high probability of event loss[195]. A way to overcome this problem is to extend the dwell-time of the protein in the pore. A method proposed by Ouldali *et al.* is to trap an amino acid within the nanopore with a polycationic carrier[196] (Figure 1.10), they showed that the identification of all 20 amino acids could be performed. Another solution is the "nanopore tweezer technology"[197–199,193], the protein is engineered with positively and negatively charged tails at its C- and N- termini. Therefore, during translocation those tails act as a tug-of-war pulling the peptide chain in both directions and increasing the dwell-time. Inspired by DNA sequencing, protein sequencing with nanopores uses proteins linearized in their primary structure. However, there is a growing interest toward the sensing of naturally folded protein in their tertiary or quaternary structure.

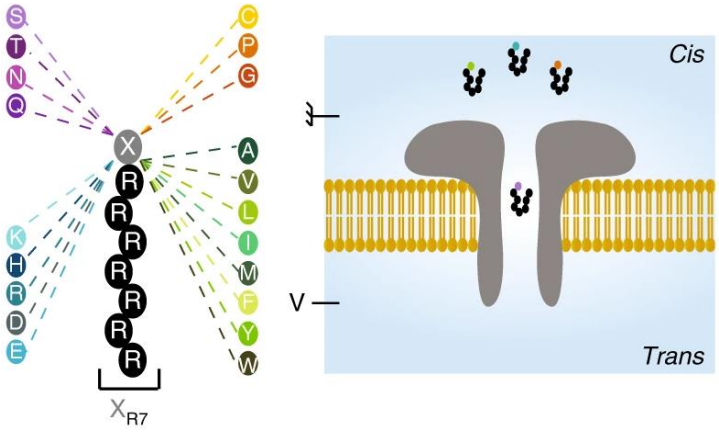

Figure 1.10: Discrimination of isolated amino acids trapped in a biological nanopore in the perspective of protein sequencing, from reference[196].

1.3.3 Protein Detection and Characterization

Protein detection and characterization in their native folded state is a key element in this thesis work. Single proteins going through the nanopore generates current drops. Those drops have been associated to the volume occupied by the protein in the pore[80,200–202] and will be further discussed in Chapter 3. The detection of proteins with a nanopore is a challenging task. In 2013, Plesa *et al.* have presented the detection of a range of proteins from 6 to 660 kDa in 10 to 57 nm diameter solid-state nanopores[195]. They highlighted the difficulties to detect small proteins due to the high signal-to-noise ratio and the limited temporal resolution of the measurements. They suggested that the observed events originate from the proteins that interact with the pore's walls while the other events are too fast and lost (Figure 1.11). This loss of events has since been described in other studies[203,204].

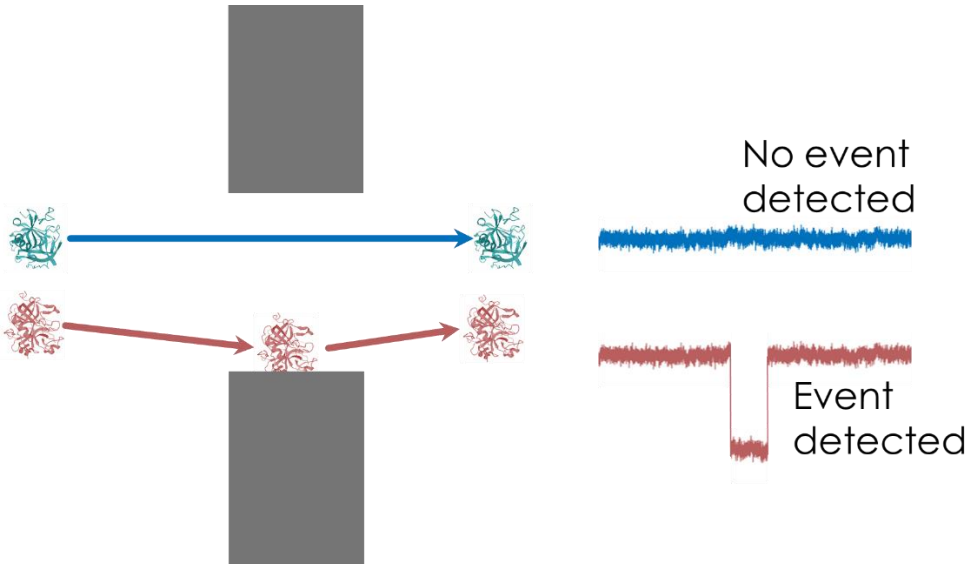

Figure 1.11: Proteins going straight into the nanopore might not be sensed because of the high signal-to-noise ratio and the limited temporal resolution[195], the observed events are the ones resulting from the proteins interacting with the pore's walls. Illustration adapted from reference[203].

In 2017, Yusko *et al*. have used lipid bilayer coated solid-state nanopores to determine the shape, volume, charge, rotational diffusion, and dipole moment of proteins bound to a lipid anchor[47]. They used a theoretical model to estimate the shape and volume based on the proportionality between the current drops caused by the protein going through the pore and an electrical shape factor. Those models will be discussed in this thesis work to experimentally retrieve the volume of proteins and discriminate them. In a later study, they successfully determined the shape, volume and dipole of proteins that are not anchored to the nanopore[205].

An important challenge regarding protein research is the study of its conformation and structural properties such as its size or charge which is directly linked to its activity in cells[60,180,206]. As mentioned

in the previous part, the mechanisms of protein structural deformation or complete unfolding have been intensively studied[188,207–209]. It has also been used to assess the stiffness of proteins[210] or conformational changes[56,211,212]. Nanopores have also been used to characterize oligomeric states of proteins[213–216,108] (their quaternary structure) or post-translational modifications such as phosphorylation[217–219] or ubiquitination[57,213]. Those dynamic studies show potential applications of protein detection with a nanopore toward drug discovery[220] and the understanding of diseases such as cancers[221] or neurodegenerative mechanisms[222–224].

There are other applications of nanopores for the study of proteins, such as the study of DNA-protein complexes[202,225–232] or protein-protein interactions[233–237]. There is notably an increasing interest toward the use of nanopores for enzymology[218,238–242]. Therefore, nanopore sensing is a promising tool for a real-time and label-free detection technique to characterize protein's structure and dynamics in their native form as well as their interactions with other proteins or DNA.

1.4 Nanopores and Aptamers: a Winning Combination

1.4.1 Aptamer Structure and Aptamer-Target Studies using Naked Nanopores

Aptamer's specificity is based on the 3D spatial conformation of the DNA or RNA sequence for the recognition of targets. Several teams have worked on the fundamental understanding of this conformation and the parameters involved for its stability with nanopores. In 2007, Thomson *et al.* assessed the structure of different aptamers in the vestibule of an α-hemolysin nanopore[243,244]. They worked on "Y-shaped" aptamers (TATA sequences for the specific binding of TATA binding proteins) and DNA hairpins. They proposed a statistical analysis method of the current blockage occurring while the aptamer interacts with another molecule, with the channel only, or from undergoing conformational changes[244]. G-quadruplex is a secondary DNA structure formed by interactions between at least four guanines G around a cation. They are notably found in thrombin binding aptamers and are an essential component for the recognition of the target. α-Hemolysin nanopores have been used as a tool for the structural studies of a G-quadruplex, its kinetics of folding and unfolding and the effects of cation selectivity over the stability of the quadruplex[245–249] (Figure 1.12 A). Shim *et al.* have demonstrated with the capture and linearization of a thrombin binding aptamer in a nanopore that the structure is more stable in presence of K^+ ions than other monovalent cations[249].

In 2014, Mahmood *et al.* have proposed a molecular dynamics simulation of a thrombin aptamer in a 6 nm diameter SiN_x nanopore[225]. They showed that the 3D structure of the aptamer is more stable under low voltage. Moreover, they worked on the interaction of the aptamer with its thrombin ligand into the nanopore when the aptamer is free or grafted on the nanopore's wall. They observed with the simulation that the binding affinity is impacted by the applied voltage and that the thrombin translocation time in the nanopore is greater when the aptamer is grafted on the walls. More and more experimental studies assess the interactions between an aptamer and its specific ligands in a nanopore. The thrombin-aptamer association rates have been discussed in several studies[250,251]. Moreover, conformational heterogeneity of the thrombin-aptamer complex has been demonstrated with a ClyA biological nanopore[252]. They showed with the current blockade amplitudes and dwell-times that the complex had two different isomeric conformations, which originate from the aptamer being able to bind two different areas of the thrombin protein (Figure 1.12 B). This proves the opportunity to probe conformational heterogeneity at a single-molecular level of protein-aptamer interactions with a nanopore. Other interactions of proteins with their specific aptamers have been investigated with nanopores, such as nucleocapsid protein 7[253], a protein biomarker of the HIV-1 virus, or TATA binding protein and HIV DNA integrase[243].

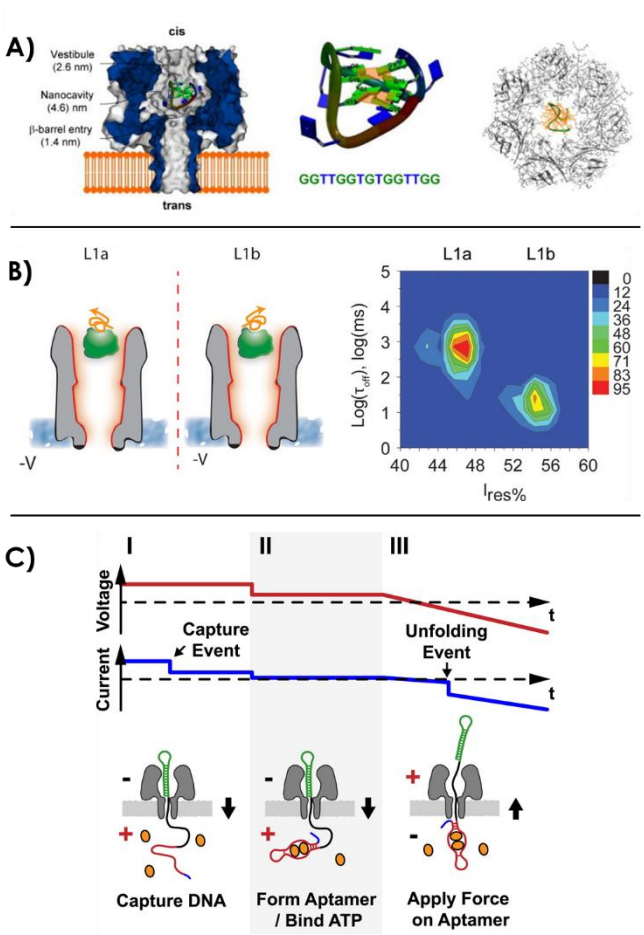

Figure 1.12: A) Capture of the folded G-quadruplex aptamer in the α-hemolysin nanopore cavity. When linearized, the aptamer is able to go through the narrowest region of the pore and translocates[245]. B) Aptamer-ligand conformation study of thrombin-binding aptamer and two possible isomeric configurations demonstrated with a ClyA nanopore[252]. C) Nanopore force spectroscopy of an ATP-aptamer complex[254].

Several other biomolecular interactions with their aptamer have been studied with nanopore technology. Adenosine triphosphate (ATP) interactions with its binding aptamer and the conformation changes with competitive molecules have been assessed[255]. In 2013, Arnaut *et al.* have used a nanopore as a force spectroscopy device for probing the interactions of the ATP binding aptamer and its target[254]. They used a backward translocation technique (Figure 1.12 C). They pulled the aptamer-ligand system by one strand captured in the nanopore, the strand can only fully translocate when the complex has been disrupted by the pulling force. Then, they could determine the dissociation constant $K_d \approx 0.1$ mM and the voltage dependence of unfolding rates. The higher the ligand concentration, the higher the voltage needed for unfolding of the aptamer-ATP complex, which was called the "critical unzipping voltages of the complexes". A limit of this force spectroscopy was drawn to attention in this study while doing the same test with the stable thrombin G-quadruplex aptamer. They showed that

aptamers with a strong secondary structure could not be tested by this pulling technique because of their highly stable nature.

The differentiation between the interaction of an aptamer and two photo-isomeric forms of a molecule have also been demonstrated[256]. Spiropyran and merocyanine are isomers of the same molecule respectively under visible light and ultraviolet light. The spiropyran specific aptamer generates two specific current signatures when going through a nanopore when it is bound to spiropyran or free. It does not interact with the merocyanine form of the molecule. When inserting the aptamer and the spiropyran molecule under visible light, typical current trace of aptamer-ligand complex were observed. Under ultraviolet light, the aptamer dissociated from its target. Finally, the structure and stability of aptamers complexed with chemical compounds targets such as lead[257,258] and mercury[258] ions have also been assessed.

Single-molecule studies with nanopores represent a great tool for the structural study of aptamers when captured in the vestibule of biological nanopores, for example. New strategies for studying the stability of aptamers and aptamer-ligand complexes, their association and dissociation constants as well as their structures under various conditions are being developed, such as the force microscopy reverse pulling technique presented by Arnaut *et al*.[254]. We can probably expect that nanopore popularity amongst scientists will probably increase for the next years, improving the fundamental studies in the field of aptamers.

1.4.2 Aptamers as Carrier Probes for Nanopore Sensing

Nanopore sensing and aptamers have been used in numerous studies for the specific detection of target molecules and proteins. A strategy for the detection of specific targets consists in the single-event detection of aptamer-ligand complexes going through the nanopore. The aptamer and its target are inserted into the solution and freely associate before going through the nanopore. We can categorize this technique in two approaches: free aptamers in solution and the use of aptamer-functionalized nanoparticles.

Aptamers as Carriers for Nanopore Sensing of their Target

This category appears as the most straightforward approach of using nanopores and aptamers for the specific detection of targets. Free aptamers in solution have been used for the specific nanopore detection of proteins such as vascular endothelial growth factor (VEGF)[259], thrombin[259] or viruses protein biomarkers[260]. Nucleocapsid protein 7 (NCp7) is a protein biomarker of the human immunodeficiency virus (HIV-1). In a study, NCp7 protein was specifically detected with three different aptamers variants (high, medium and no affinities with the target)[260]. They analyzed single-events of current blockades when the protein-aptamer complex went through the SiN_x nanopore and assessed the effect of nanopore dimension (< 6 nm or 7-15 nm diameters in a 40 nm thick membrane). As a result, they showed that the detection sensitivity is optimal when the nanopore's diameter is comparable to the target's size, hence the cross-sectional size of the NCp7-aptamer complex.

Other research works involving a nanopore detection of a target with an aptamer in solution concerns small molecules such as ions[257,261], ATP[262], or sensitive compounds such as cocaine[259,263–265] or pesticides[266–268]. In 2011, Kawano *et al*. presented an embedded device for a rapid aptamer-based detection of 1 µM cocaine in solution with an α-hemolysin nanopore[263,264]. With the study of current blockades through the nanopore, they observed the difference between the cocaine complexed with the folded aptamer, too large to go through the pore and thus captured, and the free unfolded aptamer when cocaine is not present (Figure 1.13 A). The size of the nanopore compared to the analyte is a key parameter in this study. In the absence of cocaine, the aptamer stays in a linear single-stranded DNA conformation and goes through the 1.5 nm constriction of the biological nanopore. They performed the detection of cocaine within a minute on multiple nanopores at the same time, showing that this device could be used for massive and parallel drug detection. A similar approach has been performed by Rauf *et al.* with an aptamer hybridized with a short complementary DNA[265]. When the aptamer binds to its target, the complementary strand is released and generates a specific current output when going through the nanopore. They could quantify cocaine with a concentration range from 50 nM to 100 µM and proved the selectivity of their device with control molecules (ATP, adenosine diphosphate ADP, dopamine, and theophylline). Moreover, they performed the detection of 50 nM cocaine in

human serum and saliva samples, which ensures a great potential practical application of this technique.

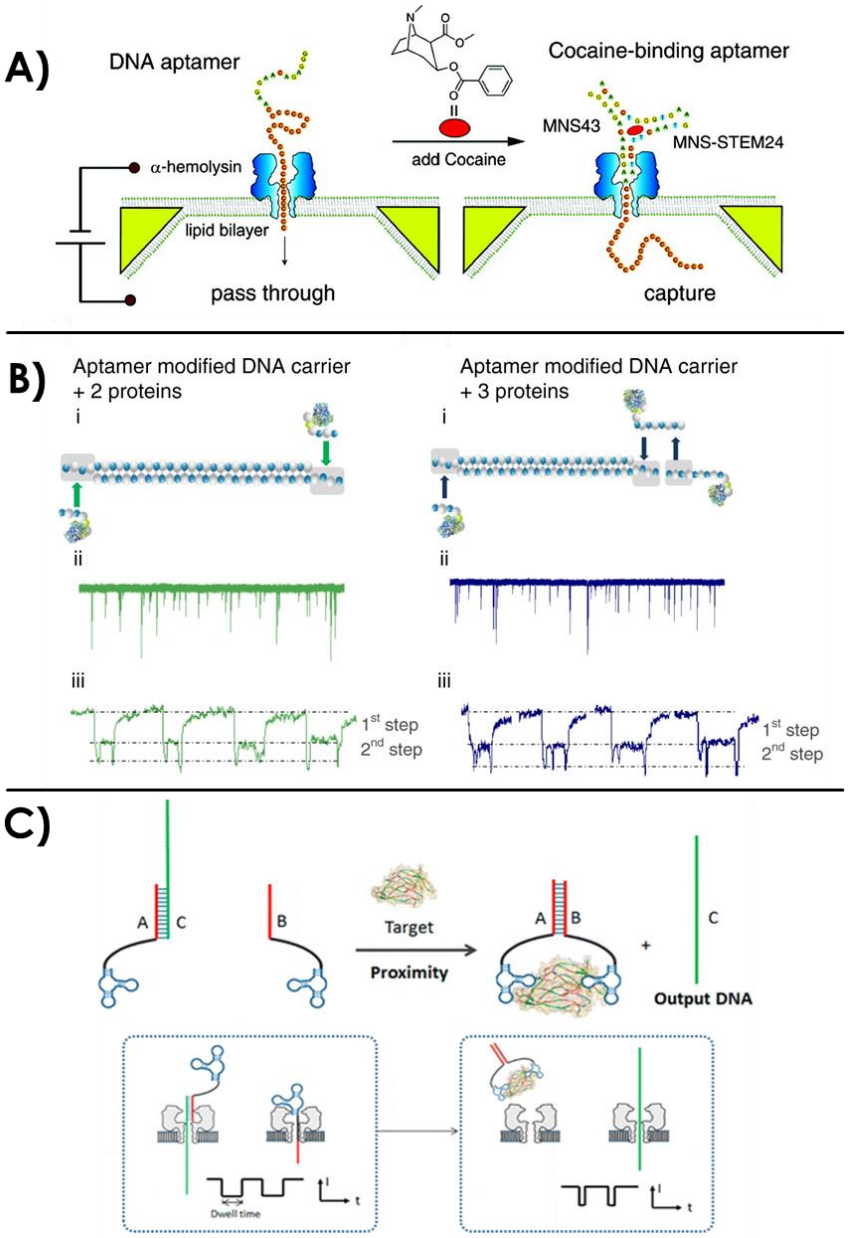

Figure 1.13: A) Nanopore detection of cocaine with aptamers in solution[263]. B) "DNA bar-coding" of a DNA carrier with several aptamers for the specific detection of proteins thanks to the analysis of intra-events[269]. C) Detection of a relatively big target with the release of an intermediate DNA sequence during the aptamer recognition of the target[270].

Another potential application of the combination of nanopore detection with aptamers is the detection of pesticides in environmental samples. In 2015, Nobukawa *et al.* presented a strategy for the detection of the pesticide vapor omethoate with an α-hemolysin nanopore and a specific aptamer[266]. They used the same strategy as the previously described cocaine sensor. When the

aptamer in solution is bound to its target, it is too large to go through the nanopore and clogs the entry, thus generating a specific current signature. Later, the same group has added a hydrogel to absorb and detect the organic volatile compounds from the vapor phase[268]. They exposed the hydrogel to vaporized omethoate at a concentration of 100 ppb (part per billion) for 10 minutes, resulting in an absorption of 600 nM vaporized omethoate and its detection with the aptamer and the nanopore. The same device could detect a concentration down to 4.8 nM of omethoate in solution. Then, they notably improved the permeation of the vapor compound into the analyzed solution while keeping the same detection strategy of the pesticide[267].

The size ratio between the target bound to the aptamer and the nanopore diameter is a key parameter to consider for the nanopore detection of aptamer-ligand complexes. In the past few years, several new strategies emerged to cast off this constraint, such as the "DNA bar-coding" technique[271]. It consists in the labeling of long DNA strands with spatially controlled markers, giving a specific current signal with recognizable intra-events. The combination of this technique with aptamers has allowed the detection of ATP[272,273] and proteins[269,273]. In 2017, a double-stranded DNA scaffold assembly with an aptamer protrusion has been used for the specific detection of ATP[272]. Therefore, when going through the 3 nm diameter SiN_x nanopore, the DNA strands generate a unique signature when ATP is bound to the aptamer protrusion. The same year, another study has shown the possibility to use an aptamer-modified DNA carrier for the "bar-code" detection of different proteins[269]. λ-DNA, a long double-stranded DNA with a standardized sequence have been used as the DNA carrier for its rigidity and reproducible current signature. It has been modified with aptamers onto specific spatial locations. When the target thrombin protein bound to the aptamers, sub-peaks in the current blockade with up to three targets on the same carrier could be observed (Figure 1.13 B). A thrombin concentration down to 1.6 nM could be detected. Moreover, this technique has been extended to multiple target proteins in the same solution on the DNA carrier. Different aptamers on the same carrier were combined (thrombin aptamer and an enzyme acetylcholinesterase aptamer). One must notice that they needed to adapt the size of the nanopore to the desired target. Finally, they performed this strategy in human serum, demonstrating the flexibility and the efficiency of this bar-coding aptamer detection even in complex sample. Another study has shown the feasibility of using this technique for the simultaneous detection of three different targets on the DNA carrier: ATP, thrombin and lysozyme[273].

Another strategy involving aptamers and an intermediate DNA sequence is emerging as a solution to the size ratio challenge between the nanopore and the analyte. The detection is achieved indirectly by the quantification of the intermediate sequence released when the aptamer and the target form a complex. This represents the great advantage to offer a detection independent from the target's size and based on the already well-established detection of single-stranded DNA through nanopores[45].

Zhang *et al.* have demonstrated this strategy with an α-hemolysin nanopore for the detection of platelet-derived growth factor with two B subunits PDGF-BB[270]. The specific aptamer can bind the target on two distinct protein emplacements. An intermediate DNA, called the output DNA was designed to partially hybridize with the aptamer. When the target was added into the solution, the aptamer would bind it and release the output intermediate DNA, which offered a very specific current signature when going through the pore (Figure 1.13 C). With this strategy, they were able to detect PDGF-BB with a limit of detection of 500 fM. They tested the selectivity of the detection with other control proteins (BSA, thrombin, human immunoglobulins G, and glucose oxidase) and further validated the results in 10% diluted human serum. This DNA intermediate strategy has also been used for the detection of a larger target: *Bacillus thuringiensis* spores[274]. In this study, the problem of sensing a large target was overcome by the use of intermediate DNA hairpins that binds the spore-specific aptamers. The unique current signature of the released DNA hairpin in an α-hemolysin nanopore allowed the specific detection of the spores. They reported an enhancement of the signal-to-noise ratio thanks to the sample preparation and the analysis of the solution containing only the unbound DNA hairpin intermediates.

The nanopore detection of specific targets with free aptamers beholds great promises for applications in the healthcare domain (detection of drug compound in human samples) or in environmental safety (detection of pesticides). With the inventive bar-coding approach, it is notably possible to sense multiple targets at the same time with a great sensitivity. However, this approach is limited to the detection of small molecules or specific care must be taken into the ratio between the target size and the nanopore diameter. If the desired target is relatively large, another approach has emerged with the sensing of an intermediate DNA sequence released when the aptamer-ligand complex is formed, this allows the sensing technique to be freed from this size limitation.

Aptamer-Functionalized Nanoparticles as Carrier Probes for Nanopore Sensing

Another strategical approach for the detection of specific targets with an aptamer consists in the use of a nanostructure holding the aptamers. The detection *via* aptamer-coated nanostructures (nanobeads, nanorods) can sometimes require a setup with a relatively larger nanopore (several hundreds of nanometers).

In 2012, proteins with aptamer-functionalized particles aggregates were specifically detected with a nanopore[275]. 300 nm thick and 1 µm long rods with gold and nickel segments were functionalized with PDGF-BB aptamers in a spatially controlled way. Therefore, they could obtain a precise agglutination pattern between the aptamer-rods after addition of the target PDGF-BB protein. They could detect the target with a concentration down to 10 fM and validated the specificity with BSA as a control protein. Later, they detected 128 nm superparamagnetic beads coated with streptavidin and biotin bound thrombin-specific aptamers[250]. After addition of thrombin in a range of concentration from 0.1 nM to 1 µM, they observed a decrease in the event rates sensed in the nanopore. The specific binding of thrombin on the beads resulted in a shielding effect of the negative charges that drives the beads through the nanopore. They also employed another technique to detect thrombin *via* the monitoring of aggregates disruption[276]. A mix of superparamagnetic beads of 1 µm coated with thrombin aptamers and 400 nm-beads coated with the complementary aptamers forms aggregates. After addition of thrombin down to sub-picomolar concentrations, the aggregates were disrupted and specific single-event signals were observed with the nanopore. In another study, they used 120 nm diameter streptavidin coated beads functionalized with biotin-bound VEGF aptamer to detect VEGF proteins with a concentration down to 18 pM[117]. In 2015, they developed a strategy for the simultaneous detection of PDGF and VEGF[277]. They grafted VEGF aptamers and PDGF aptamers to 120 nm and 300 nm superparamagnetic beads, respectively. After addition of VEGF and PDGF at the nanomolar scale, the frequency of bead translocation through the nanopore and the current blockade level of each event could be related to each type of protein and their concentration (Figure 1.14 A). This study proved the possibility of simultaneous label-free detection of proteins with aptamer coated nanoparticles.

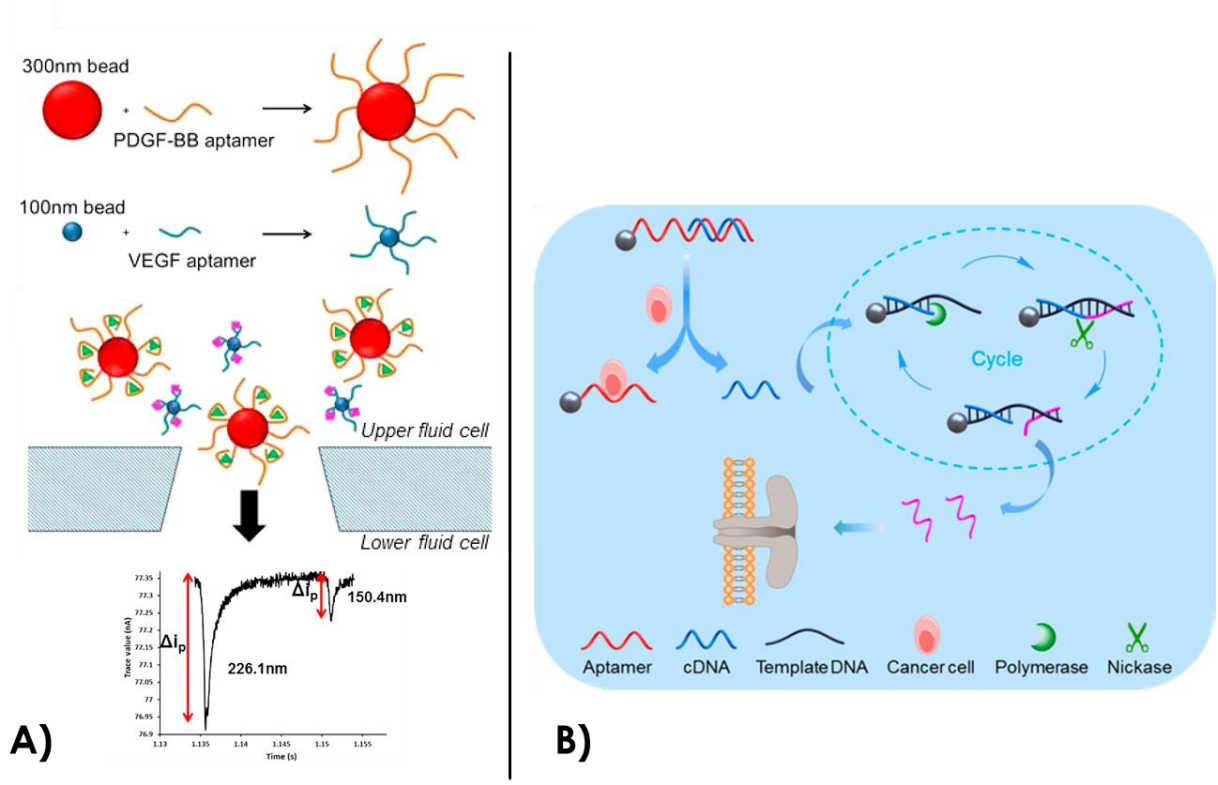

Figure 1.14: A) Multiplexed Tunable Resistive Pulse Sensing of aptamer coated beads for the detection of PDGF-BB and VEGF on 300 nm and 100 nm beads, respectively[277]. B) Detection of human lymphoma cancer cells by combination of aptamer-coated particles, enzymatic amplification of DNA and biological nanopore detection[278].

Other groups have worked on aptamer-functionalized nanoparticles for the detection of biomolecules. In 2017, nanopore sensing of lysozyme was performed using 21 nm diameter quartz nanopipettes and 5 nm aptamer-functionalized gold nanoparticles[279]. They detected lysozyme with a concentration of 250 nM in a solution with background control proteins cytochrome C and trypsin. Alsager *et al.* have sensed 17β-estradiol hormone by using 217 nm-sized carboxylated polystyrene nanoparticles coated with aptamers[280]. Thanks to the analysis of single-events amplitude, they observed the diameter increase of the nanoparticles after grafting of the aptamer. Then, they also observed the diameter decrease resulting from the conformational change of the aptamer bound to its specific ligand. They reported a detection of 17β-estradiol in the nanomolar range.

Nanopores and aptamer-coated nanoparticles have also been investigated for the detection of polluting agents in water. Microcystin-LR is a lethal cyanotoxin produced by cyanobacteria in fresh or saline water. He *et al.* have developed a strategy in 2018 to detect this toxin with two different sizes of gold nanoparticles coated with aptamers and a 20 nm diameter SiN_x nanopore[281]. They grafted Microcystin-LR specific aptamers on 5 nm gold nanoparticles and the complementary sequence on 20

nm gold nanoparticles. Those two kinds of particles formed aggregates by complementary hybridization of the aptamers. After addition of the target toxin, the aggregates were disrupted and the 5 nm particles with the captured toxin were sensed through the nanopore. They tested this strategy with a concentration range of Microcystin-LR from of 0.1 nM to 20 µM. Additionally, they proved the specificity of their approach with a mixture containing Microcystin-LR, other congener toxins and chlorophyll that abundantly coexists in water. The same year, Mayne *et al.* have designed aptamer-modified nanoparticles for the detection of mercury (Hg^{2+}) and lead (Pb^{2+}) ions which are agents of metal pollution in sea-water[258]. With a study of translocation velocities, driven by the aptamer charge density around the 150 and 300 nm particles when bound to their target or not, they could simultaneously detect the two targets in a concentration range between 10 to 200 nM. They also engineered a dual aptamer aiming to detect both Hg^{2+} and Pb^{2+} at the same time.

Recently, there has been an increase of interest toward aptamer-coated nanoparticles and nanopores sensing for biomedical and diagnostic applications. Healey *et al.* have developed a system for a rapid quantification of prion PrP^C proteins[282], which are involved in neurological diseases. After functionalization of 125 nm superparamagnetic beads with PrP^C specific aptamers, they specifically detected PrP^C proteins (50 nM concentration) with the monitoring of particle velocities. They also added 200 nM albumin, fibrinogen or γ-globulin as control proteins to show the specificity of their detection. The entire workflow from cellular extraction to the quantification of prion proteins takes less than an hour and offers a great promise toward the use of nanopore and aptamer coated particles for rapid diagnostics. Another biomedical application concerns the detection of cancer biomarkers. Li *et al.* modified magnetic nanoparticles with aptamers that target carcinoembryonic antigen (CEA)[283], a cancer biomarker. After addition of the magnetic aptamer-nanoparticles (~5 nm diameter) in a complex human sample containing 1 nM of CEA, the nanoparticles could be magnetically separated for the analysis. Then, a nanopore analysis was performed with a 30 nm diameter quartz nanopipette. By analysis of single-events current blockades of particles going through the pore, they could discriminate the presence of CEA on the nanoparticles. Indeed, aptamer-nanoparticles with bound target CEA are three times larger in volume than aptamer-nanoparticles only and could easily be distinguished in the current signal. They tested this strategy in different human serums and compared the results with classical ELISA assays. This technique obtained the same level of performance and could be used for early diagnosis of cancer. In 2020, another study has shown the simultaneous nanopore detection of VEGF, PDGF-BB and thrombin (that are cancer lung biomarkers when overexpressed) with three different nanoparticle-aptamer and complementary DNA constructs[284]. This approach has been further developed in the same group by Xi *et al.* for an ultrasensitive detection of cancer Ramos cells, which are involved in human lymphoma[278]. They coated 1 µm-diameter beads with

aptamers that specifically target Ramos cells. The sequence was hybridized with a short complementary DNA. When the aptamer specifically recognizes the cancer cell, the short complementary strand of DNA is released. Afterward, this sequence is specifically amplified *via* enzymatic cycling with phi29 DNA polymerase and the collected solution is further detected in an aerolysin biological nanopore. The illustration of their strategy is found on Figure 1.14 B. The output DNA going through the nanopore produced characteristic single-events of current blockades and permitted a detection of the Ramos cells with an excellent sensitivity. Down to five Ramos cells could be detected in 100 µL, they also successfully performed the detection into human serum. This approach of sensing an intermediate product released with the target-aptamer binding allows an emancipation from the target size dependence of nanopore sensing. Moreover, this is a good example of selective and precise detection of cancer cells in human serum, which offers a powerful tool for biomedical research and diagnosis.

Aptamer-coated nanostructures have been used for various applications such as water pollution and contaminant detection or advanced biomedical diagnostics. In most of the cases, the ligand-aptamer nanostructure is relatively large (~ 100 nm). The single-events of particles going through the pore are analyzed to discriminate the size and the velocity of the nanoparticles according to the presence of the target or not.

Even though monitoring the nanoparticle functionalization can be a technological challenge, using a nanoparticle-coated aptamer instead of a free aptamer in solution could allow an easier nanopore detection thanks to larger objects. Nevertheless, there is still no study that thoroughly compares those two approaches and further examination would be required.

1.4.3 Gating with Aptamer-Functionalized Nanopores

Nanopore or nanochannel gating has raised interest as nanofluidic valves or biomimetic selective transport tools. Mimicking the selectivity of gating functions from the biological ion channels can allow a controllable release of molecules into a fabricated system. A lot of different approaches already exist for stimuli-responsive gating of nanopores[98]. Aptamer-coated nanochannels represent a new strategy for the precise control of gating systems responding to biomolecule stimuli.

In 2012, Jiang *et al.* presented an array of nanochannels of ~60 nm diameter in alumina membranes with an aptamer structure allowing a closed and open state[285]. The inner surface of the nanochannel had been grafted with a first capture ATP aptamer probe. Then, two other sequences could hybridize on this probe, forming an aptamer super-sandwich structure that obstructed the channel as a perfect electric seal (~GΩ). After addition of ATP in the system, the aptamer assembly into the channel was disrupted by the ATP-aptamer recognition and the ionic current was established. The channel was then in its open state (Figure 1.15). With those open and close states, they were able to perform logical operations with eight parallel structures, showing the opportunities for complex nanofluidic architectures and manipulations. Later, the same group studied the effects of asymmetric exposure of this system to ATP both experimentally and theoretically[286].

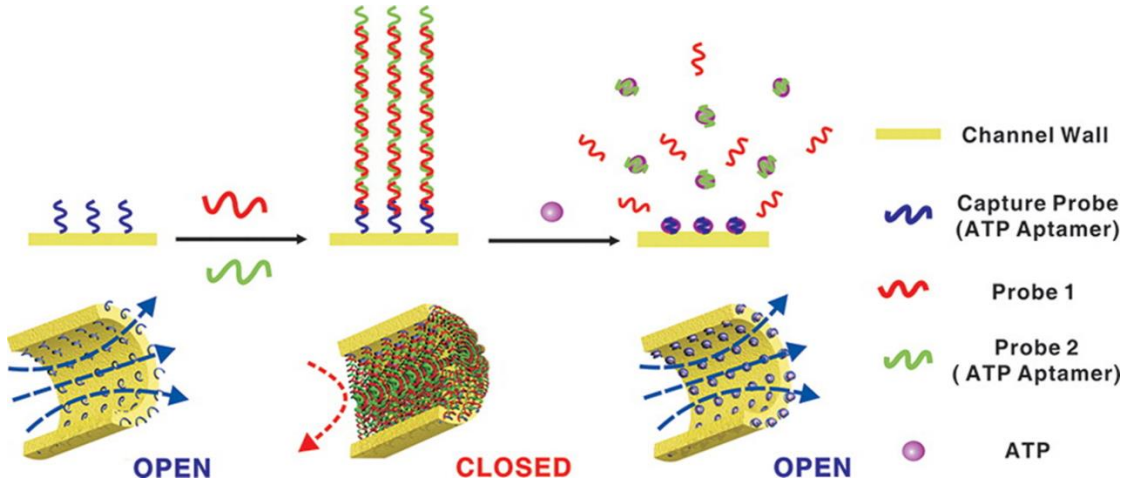

Figure 1.15: Highly-efficient gating with two ATP aptamers forming a super-sandwich structure in a nanochannel[285].

Recently, Acar *et al.* reproduced potassium selectivity inside a solid-state nanopore using crown ether and single-stranded DNA grafting[287]. The device was tested using nanopores of different diameters, at different salt concentrations and under a 1V voltage range. Current measurements with a mixture of KCl and NaCl at different ratios showed that the functionalized nanopore acted as a gate towards sodium ions, selectively letting potassium ions through.

Other aptamer-coated channels have been reported to respond to small molecules such as cocaine[288] or adenosine[289] in a reversible manner. In the latter case, the study was inspired by natural adenosine receptors found on the cell's membrane and responsible for cellular signaling pathways. Polymer membranes with ion-track etched nanopores (20 nm) were coated with adenosine aptamers[289] that filled the inside of the channel. After addition of adenosine, the aptamers folded in a compact way, allowing the flow of the ionic current. They could reverse the process and close the channel again by addition of adenosine deaminase, an enzyme which converts adenosine into inosine molecules that are no more recognized by the aptamers.

Synthetic ions channels and stimuli responsive gates are one of the first steps toward nanoscale sensors and actuators. The aptamer gates and setting of nanometric logic operations represent good candidates for potential advanced structures called molecular robots[290] or nanoscale power generator[291]. Those molecular robots could represent a promising tool for environmental monitoring or healthcare applications such as *in vivo* diagnosis or drug delivery. The high selectivity brought by aptamers could also serve in separation membranes[292,293] for water desalination[294–296] or wastewater treatment[297]. Those are only few directions where biomimetic nanoporous membranes could be useful in the future[298].

1.4.4 Target Specific Detection with Aptamer-Functionalized Nanopores

Over the past years, the grafting of aptamers inside nanopores has been an extensively used approach to detect specific molecules, proteins or dangerous substances such as drugs or toxic molecules. Solid-state nanopores are mainly employed but several cases of genetically or molecularly engineered biological nanopores combined with aptamers have also been reported.

The main physical phenomenon employed for measurements with aptamer-coated nanopores is ionic current rectification (ICR). Nanopores usually exhibit a linear current-voltage (I-V) curve following an ohmic behavior. However, it has been shown that this I-V curve is no more linear when the pore is conical (asymmetric) or has a non-homogeneous fixed charge distribution on the pore walls[286,299,300]. This phenomenon will be further discussed in Chapter 3. Such ICR phenomenon is used as an indicator for the modification of nanopore's surface and grafting of charged biomolecules.

Specific detection of lysozyme protein with aptamers was performed in a single conical glass 20 nm nanopore thanks to ICR[301]. After the grafting of lysozyme binding aptamers on the inside of the nanopore, ICR was observed due to the negatively charged walls. After the binding of the protein, the global surface charges were partially neutralized and the ICR effects decreased (Figure 1.16 A). Thanks to this, Cai *et al.* could specifically detect lysozyme amongst other control proteins (BSA, cytochrome c and pepsin) with a limit of detection of 0.5 pM. A similar approach was performed on a 20 nm track-etched nanopore in polyethylene terephthalate (PET) membranes for the specific detection of lysozyme down to 70 µM[302].

Several studies show the interest of aptamer-coated nanopores for the specific detection of thrombin proteins[111,303,304]. A 30 nm diameter glass conical nanopore has been functionalized with thrombin binding aptamers and tested with 50 pM of target thrombin in undiluted serum[303]. Successive decreases in the current level has shown the consecutive binding of thrombin proteins on the aptamers. With a probabilistic model, they showed that this device can be efficiently used for quantification of the target with a response time of 10 minutes. Another group has presented a similar device with a 50 nm quartz conical nanopore coated with thrombin binding aptamers[111]. With a measurement of ICR, thrombin could be detected at a concentration of 270 nM in phosphate buffered saline (PBS) while the control protein bovine serum albumin (BSA) did not affect the current levels. They reported that using undiluted serum would clog their device. Another approach has been performed by Zhao *et al*.[304] with the use of a 100 nm thick porous anodic alumina membrane with an array of nanopore (~ 40 nm average diameter). After grafting of thrombin aptamers on its surface, they monitored ICR induced by thrombin binding in 1 mM KCl with different pH conditions. They obtained a limit of detection of 0.22 fM for specific pH conditions. Moreover, they showed that in human serum

they could detect thrombin with a concentration down to 0.111 nM. This could indicate that using nanopore arrays and nanoporous membranes instead of single nanopores could be an alternative to enhance the measurements when using ICR as an indicator for protein detection. However, with arrays instead of single nanopore, the possibility for single-molecule sensitivity is lost. Blundell *et al.* have used both ICR and single-event measurements in the same study for the aptamer detection of VEGF[117] in a relatively large nanopore (800 nm). In one part of the study, they coated the nanopore with VEGF aptamer and measured ICR to monitor VEGF concentrations down to 5 pM.

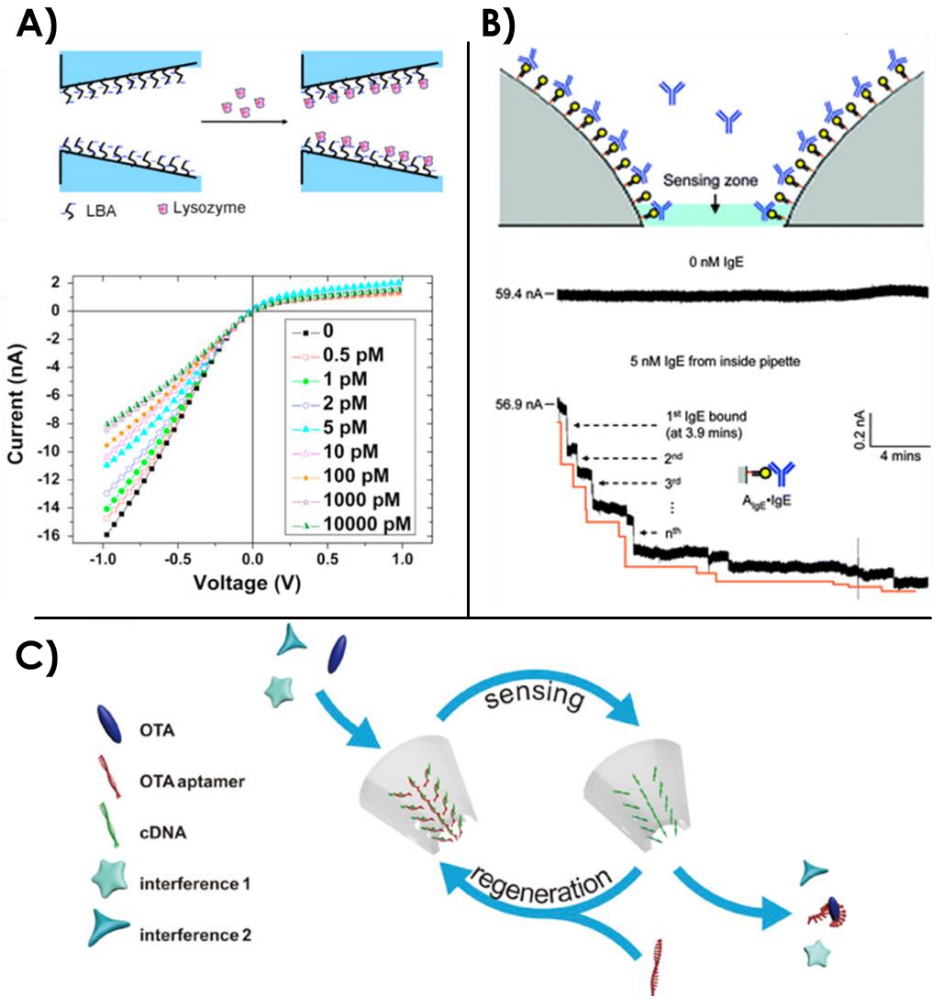

Figure 1.16: A) Illustration of lysozyme binding aptamer grafting on a 20 nm conical glass nanopores and induced ICR after addition of various concentrations of lysozyme protein[301]. B) Consecutive current decrease steps with immunoglobulin binding on the surface aptamers from reference[134]. C) Strategy for OTA toxin detection with DNA direct immobilization of aptamers from reference[305].

Aptamer-coated nanopores are also employed for the detection of proteins such as immunoglobulin[134,306] or the extremely toxic ricin protein[134,307]. Gao *et al*. have focused their works on the detection of ricin[134] that can be used as a bioterrorist agent. They also used the same kind of device

in their study for the detection of immunoglobulin proteins. They functionalized a 56 nm glass nanopore with ricin binding aptamers. After addition of ricin at a concentration of 100 nM, they could monitor the decrease of current when each protein bound to the aptamers. They performed the same experiments with immunoglobulin E specific aptamers (Figure 1.16 B) and could detect the protein with a concentration down to 5 nM. This particular example shows the possibility to use aptamer-coated nanopores as a versatile tool for both diagnostic purposes and environmental detection of dangerous substances.

In this applied field of research, nanopores coated with aptamers has also been used to detect small toxic molecules: cocaine[288,308] and Ochratoxin A (OTA)[305], a dangerous product of fungi species that can be found in agricultural products. Wang *et al*. have performed cocaine detection over a wide range of concentration down to 1 nM[308] in a 30 nm diameter track-etched nanochannel in PET. They used a couple of cocaine specific aptamers that enclosed the target between the two DNA strands. One of the aptamers was immobilized inside the nanochannel, while the second aptamer was inserted simultaneously with cocaine in the solution. They monitored cocaine capture on the surface of the nanochannel thanks to ICR measurements and validated the specificity of their detection with other small control molecules (glucose, atropine, and tropinone). Recently, Zhang *et al.* have developed a different strategy for the detection of OTA toxins with an aptamer coated nanopore[305]. In a 90 nm diameter glass conical nanopore, they grafted a first DNA sequence that is partially complementary to the OTA binding aptamer. The latter aptamer is hybridized with the pre-immobilized sequence, following the principle of DNA-directed immobilization[309]. After addition of the OTA, the aptamer that partially pairs with the immobilized DNA sequence will bind to OTA and subsequently dissociate from the nanopore surface (see illustration on Figure 1.16 C). Therefore, ICR is generated by the aptamer dissociation that causes a negative charge reduction on the nanopore inner surface. An interesting point for this method is that the ICR measurement is independent from the charge of the target biomolecule, which is an undeniable advantage for this type of detection. Moreover, they showed a simple regeneration of the device by adding a solution containing the OTA binding aptamer for its immobilization on the grafted partially complementary DNA sequence.

Other aptamer coated solid-state nanopores have been used for the detection of ATP[310,311], potassium[310] or TATA box binding protein[312]. Nevertheless, the grafting of aptamers on the surface of a nanopore for the detection of a target is not restricted to solid-state nanopores. Genetic and molecular engineering allows the modification of biological nanopores as well.

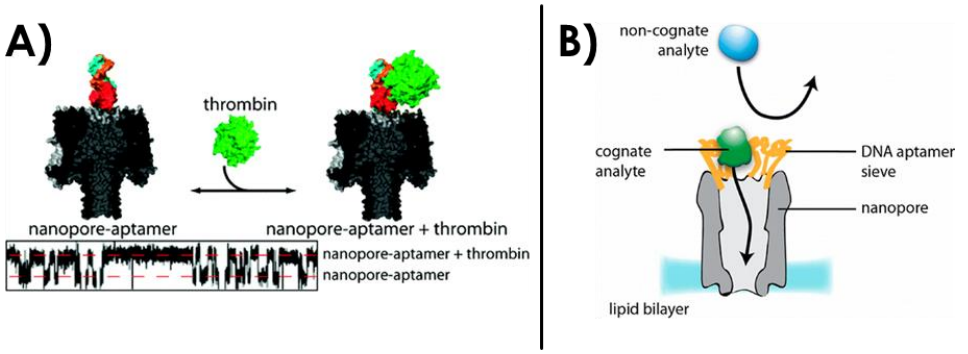

Figure 1.17 : A) α-hemolysin biological nanopore engineered by Rotem *et al.* [313] to specifically detect thrombin with a thrombin aptamer at its entrance. B) Engineered ClyA nanopore with an aptamer sieve for the specific detection of proteins from Soskine *et al.*[314].

In 2012, an α-hemolysin biological nanopore was engineered by Rotem *et al.* to specifically detect thrombin with an aptamer[313] (Figure 1.17 A). With the analysis of current blockades, they showed that the insertion of thrombin with a concentration down to 20 nM could generate a specific current signature. They also defined specific equilibrium dissociation constants K_d that are consistent with the ones obtained using standard approaches. The selectivity of this sensor toward the natively folded thrombin protein was proved using a denatured form and BSA as negative controls.

Later the same year, Soskine *et al.* have reported an engineered ClyA biological nanopore that exhibited a sieve of aptamers for the specific recognition of proteins (thrombin or lysozyme)[314]. They grafted aptamers to the ClyA monomers, resulting in an assembled nanopore that contains 12 aptamers at its entrance that are ~ 2 nm apart from each other (Figure 1.17 B). By analysis of the single-events of current blockage through the nanopore, the decorated nanopore showed an excellent specificity toward the target analyte even when another protein was introduced. For example, with a thrombin aptamer decorated ClyA nanopore, a control protein was added in large excess concentration compared to the specific human thrombin target (2.2 nM) but they managed to record twice as much thrombin specific events compared to the control protein. With this nanopore, they succeeded in mimicking the nuclear pore complex selectivity of translocated molecules, which is one of the goals of engineering nanopores for biomimetic applications. Another study using aptamer-functionalized nanopipettes in combination with surface-enhanced Raman scattering showed localization of cancer biomarkers inside single-cells[315].

As a conclusion, specific detections of targets have been performed on aptamer-functionalized nanopores thanks to ICR measurements and successive current decreases when each target binds the inside of the nanopore. ICR is a great indicator but is generally dependent on the target's charge. An interesting variation of this sensing strategy was presented by Zhang *et al.* with DNA-directed

immobilization of the aptamer for the detection of OTA toxin[305]. With the release of the aptamer-OTA complex from the nanopore walls, the ICR measurement was independent from the target's charge and the device could be easily regenerated for further experiments. There are some examples of aptamers grafted on biological nanopores. In this case, the monitoring of single-events of biomolecules going through the nanopore is then used for the specific recognition of a target.

Either free in solution or grafted onto the nanopore, the aptamers are generally used as recognition elements to improve the sensibility and/or the selectivity of nanopores to detect a target. Thanks to the versatility of the aptamers, the range of accessible targets is large: from simple ions, pesticides, hormones or proteins to name a few. This wide range of targets allows for applications in various domains like health (diagnostics or drug discovery), environment (water pollution) and security (drug detection). The ease of production and molecular modifications along with the low cost of aptamer chemical synthesis and the huge stability of aptamers are good assets for the industrialization of functionalized nanopore devices. The combination of aptamer sensing with nanopore technology is therefore a winning association promised to numerous developments.

1.5 Focus of this Project

The objective of this thesis project is to use an aptamer-functionalized nanopore for the specific detection and discrimination of closely related proteins.

The studied protein is thrombin, an enzyme involved in the blood coagulation cascade[316,317]. This protein converts fibrinogen, a blood-clotting element dissolved in blood, into long stranded fibrin that helps coagulation. Thrombin exerts a multitude of regulated actions on the blood and vessel wall. It is involved in diverse physiological and pathological processes such as bleeding disorders, atherosclerosis, or cancer[318–322]. Thrombin is the product of the cleaving of its precursor prothrombin by another enzyme called factor Xa[323].

Thrombin is an extensively studied target for aptamer sensing. In 1992, thrombin aptamer was the first aptamer designed to target a protein that does not interact with nucleic acid as its basic function[324]. It has been since widely used with aptamer-based assays and biosensors[111,303,304,325–328]. It should be highlighted that in those assays, thrombin is often used as a model protein to demonstrate the proof-of-concept of a developed technique[325]. In this work, we also decided to study thrombin with the thrombin binding aptamer as a first approach. Further studies might consider using other proteins and aptamer models.

Three different proteins are used in this study to take advantage of the nanopore capabilities to differentiate proteins with different volumes, as well as the aptamer properties to interact with a specific protein. The protein that is specifically detected by our selected aptamer is α-thrombin[324,329], a 5 nm diameter globular protein with an approximate volume of 65 nm^3. Its molecular weight is 36 700 Da. ɣ-thrombin is a modified α-thrombin lacking the aptamer binding epitope[330,331]. It is also a 5 nm diameter globular protein with the same volume as α-thrombin. Its molecular weight is 34 300 Da. Finally, prothrombin, the precursor of α-thrombin, is a 9 nm x 5 nm pear-shaped protein with a volume of 212 nm^3 and a molecular weight of 72 000 Da. The different protein 3D configurations are presented on Figure 1.18.

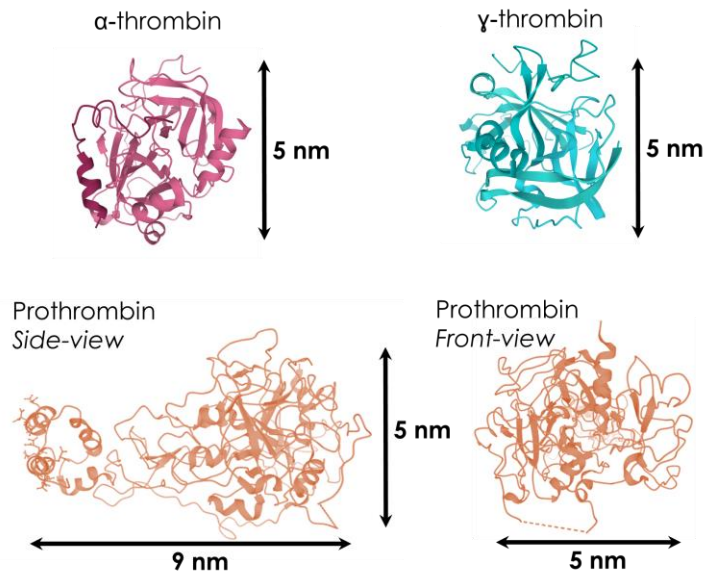

Figure 1.18: Representation of target proteins α-thrombin (PDB entry 1D3T, 36.7 kDa), ɣ-thrombin (PDB entry 2HNT, 34.3 kDa) and prothrombin (PDB entry 6BJR, 72 kDa). Representations made on the RCSB Protein Data Bank website 3D viewer, and measurements done with Swiss-PdbViewer 4.1.0 software.

The aim of this thesis is to detect and discriminate the aforementioned proteins thanks to nanopore technology. With a classical solid-state nanopore setup, we can expect to discriminate α-thrombin and prothrombin because their excluded volume in the pore is different; hence prothrombin might generate a deeper current blockage in the signal. However, due to their similar size, α-thrombin and ɣ-thrombin cannot be differentiated by this approach. Therefore, we decided to benefit from the recognition capabilities of aptamers to differentiate α-thrombin, which interacts with the aptamers, from ɣ-thrombin which lacks the recognition site. To do so, we aim to functionalize the surface of the nanopore with aptamers recognizing α-thrombin. The surface functionalization technique chosen is silanization. Moreover, we expect surface functionalization to increase the probability of proteins interacting with the pore's walls and facilitate the observation of single-events of proteins going through the pore[195].

On Figure 1.19 is illustrated the expected outcome of the three different proteins going through a bare solid-state nanopore (top) and through an aptamer-functionalized nanopore (bottom). With a bare nanopore, α-thrombin and ɣ-thrombin are expected to generate the same single-events signature dwell-time δt and current blockade amplitudes ΔI. Prothrombin is expected to have a deeper ΔI. After functionalization with the aptamers, we expect to be able to differentiate α-thrombin from ɣ-thrombin because of the increased interaction of α-thrombin with the surface aptamers; hence a longer dwell-time.

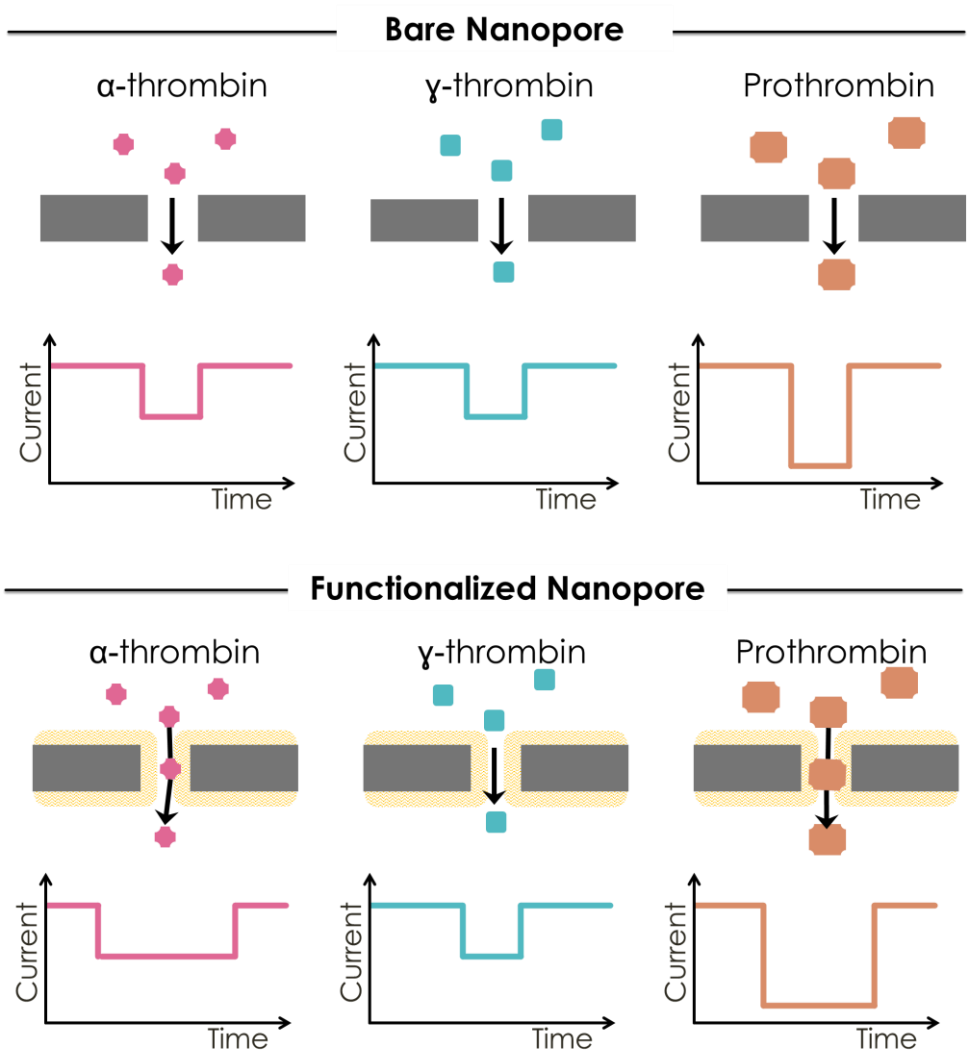

Figure 1.19: Scheme of the targeted results regarding single-event detection of the closely related proteins α-thrombin, ɣ-thrombin and prothrombin. (Top) With a bare nanopore we expect α-thrombin and ɣ-thrombin to have a similar current drop and dwell-time signature because of their similar volume (~65 nm^3). Prothrombin is expected to have a greater impact on current drop because of its bigger size (~212 nm^3). (Bottom) After functionalization, we expect α-thrombin to interact with the aptamers at the surface of the pore and have a longer dwell-time than ɣ-thrombin. Prothrombin might also interact with the aptamers and present a longer dwell -time.

On Figure 1.20 is depicted an illustration of the expected results when all single-events from an experiments are plotted with their δt and ΔG (=ΔI/applied voltage) on a scatter plot. We expect to have a localized point cloud for each protein, represented on the figure by a colored disc. This figure represents the synthesis of all experiments for each protein depicted previously on Figure 1.19. The functionalization would allow the time discrimination of α-thrombin and ɣ-thrombin.

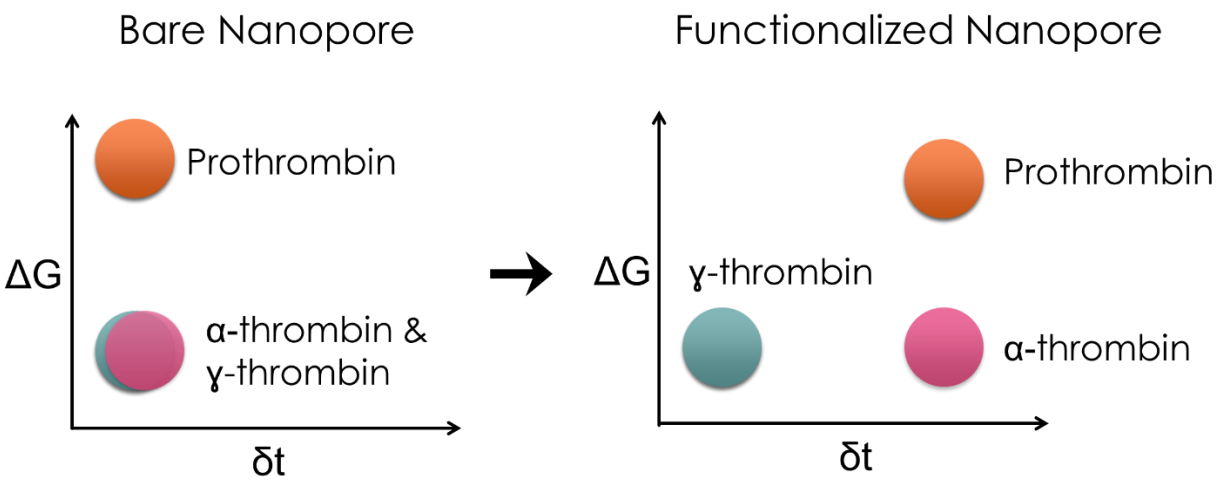

Figure 1.20: Scheme of the targeted results for this study. The single-events are plotted with their dwell-time δt and conductance blockade amplitudes ΔG. All the points corresponding to one protein (scatter plot) are represented here by a colored disc. The functionalization of the nanopore would allow the discrimination of the three proteins thanks to a δt and ΔG separation.

In order to obtain such results, there are several milestones that will be described in this thesis manuscript. First, the solid-state nanopore chips need to be designed and fabricated. In Chapter 2 will be described a process flow to fabricate single-nanopore chips at a wafer scale, as well as another faster technique using commercial membranes and a transmission electron microscope (TEM). Then, the Chapter 3 will relate to the building of an experimental bench for nanopore sensing. The theory and physics behind this technique will be described. Finally, the experimental steps for the grafting of aptamers on the nanopore and membrane surface will be depicted. In Chapter 4, the bench will be validated thanks to pilot experiments such as the characterization of a nanopore or the translocation of a biomolecule with a well-known current signature. The surface chemistry will also be validated in nanopores. Finally, the detection of closely related proteins in a bare and functionalized nanopore will be performed.

1.6 References

1. Paluch, E. K. Biophysics across time and space. *Nat. Phys.* **14**, 646–647 (2018).
2. Vogenberg, F. R., Isaacson Barash, C. & Pursel, M. Personalized Medicine. *Pharm. Ther.* **35**, 560–576 (2010).
3. Hood, L. & Friend, S. H. Predictive, personalized, preventive, participatory (P4) cancer medicine. *Nat. Rev. Clin. Oncol.* **8**, 184–187 (2011).
4. Wang, D. & Bodovitz, S. Single cell analysis: the new frontier in 'omics'. *Trends Biotechnol.* **28**, 281–290 (2010).
5. Zhao, Y., Chen, D., Yue, H., French, J. B., Rufo, J., Benkovic, S. J. & Huang, T. J. Lab-on-a-chip technologies for single-molecule studies. *Lab. Chip* **13**, 2183–2198 (2013).
6. Ha, T. Single-molecule methods leap ahead. *Nat. Methods* **11**, 1015–1018 (2014).
7. Gooding, J. J. & Gaus, K. Single-Molecule Sensors: Challenges and Opportunities for Quantitative Analysis. *Angew. Chem. Int. Ed.* **55**, 11354–11366 (2016).
8. Watson, J. D. & Crick, F. H. C. Molecular Structure of Nucleic Acids: A Structure for Deoxyribose Nucleic Acid. *Nature* **171**, 737–738 (1953).
9. Alberts, B., Johnson, A., Lewis, J., Raff, M., Roberts, K. & Walter, P. The Shape and Structure of Proteins. *Mol. Biol. Cell 4th Ed.* (New York: Garland Science, 2002).
10. Alberts, B., Johnson, A., Lewis, J., Raff, M., Roberts, K. & Walter, P. Protein Function. *Mol. Biol. Cell 4th Ed.* (New York: Garland Science, 2002).
11. Li, C. M., Dong, H., Zhou, Q. & Goh, K. H. CHAPTER 11 - Biochips – fundamentals and applications. in *Electrochemical Sensors, Biosensors and their Biomedical Applications* (eds. Zhang, X., Ju, H. & Wang, J.) 307–383 (Academic Press, 2008).
12. Clark, L. C. & Lyons, C. Electrode Systems for Continuous Monitoring in Cardiovascular Surgery. *Ann. N. Y. Acad. Sci.* **102**, 29–45 (1962).
13. Temiz, Y., Lovchik, R. D., Kaigala, G. V. & Delamarche, E. Lab-on-a-chip devices: How to close and plug the lab? *Microelectron. Eng.* **132**, 156–175 (2015).

14. Jain, K. K. Chapter Two - Role of Proteomics in the Development of Personalized Medicine. in *Advances in Protein Chemistry and Structural Biology* (ed. Donev, R.) **102** 41–52 (Academic Press, 2016).

15. Weinrich, D., Jonkheijm, P., Niemeyer, C. M. & Waldmann, H. Applications of Protein Biochips in Biomedical and Biotechnological Research. *Angew. Chem. Int. Ed Engl.* **48**, 7744–7751 (2009).

16. Chen, Z., Dodig-Crnković, T., Schwenk, J. M. & Tao, S. Current applications of antibody microarrays. *Clin. Proteomics* **15**, 7 (2018).

17. Chevolot, Y., Laurenceau, E., Phaner-Goutorbe, M., Monnier, V., Souteyrand, E., Meyer, A., Géhin, T., Vasseur, J.-J. & Morvan, F. DNA directed immobilization glycocluster array: applications and perspectives. *Curr. Opin. Chem. Biol.* **18**, 46–54 (2014).

18. Ventimiglia, G. & Petralia, S. Recent Advances in DNA Microarray Technology: an Overview on Production Strategies and Detection Methods. *BioNanoScience* **3**, 428–450 (2013).

19. Jung, S.-H. & Ha, K.-S. Protein arrays for quantitative enzymatic profiling and serodiagnosis. *BioChip J.* **9**, 269–277 (2015).

20. Duarte, J. G. & Blackburn, J. M. Advances in the development of human protein microarrays. *Expert Rev. Proteomics* **14**, 627–641 (2017).

21. Huang, W., Luo, S., Burgess, R., Yi, Y.-H., Huang, G. F. & Huang, R.-P. New Insights into the Tumor Microenvironment Utilizing Protein Array Technology. *Int. J. Mol. Sci.* **19**, 559 (2018).

22. Jonkheijm, P., Weinrich, D., Schröder, H., Niemeyer, C. M. & Waldmann, H. Chemical Strategies for Generating Protein Biochips. *Angew. Chem. Int. Ed.* **47**, 30 (2008).

23. Yan, S.-R., Foroughi, M. M., Safaei, M., Jahani, S., Ebrahimpour, N., Borhani, F., Rezaei Zade Baravati, N., Aramesh-Boroujeni, Z. & Foong, L. K. A review: Recent advances in ultrasensitive and highly specific recognition aptasensors with various detection strategies. *Int. J. Biol. Macromol.* **155**, 184–207 (2020).

24. Hassan, E. M. & DeRosa, M. C. Recent advances in cancer early detection and diagnosis: Role of nucleic acid based aptasensors. *TrAC Trends Anal. Chem.* **124**, 115806 (2020).

25. Zhu, C., Li, L., Wang, Z., Irfan, M. & Qu, F. Recent advances of aptasensors for exosomes detection. *Biosens. Bioelectron.* **160**, 112213 (2020).

26. Negahdary, M. Electrochemical aptasensors based on the gold nanostructures. *Talanta* **216**, 120999 (2020).

27. Tuerk, C. & Gold, L. Systematic evolution of ligands by exponential enrichment: RNA ligands to bacteriophage T4 DNA polymerase. *Science* **249**, 505–510 (1990).

28. Stoltenburg, R., Reinemann, C. & Strehlitz, B. SELEX—A (r)evolutionary method to generate high-affinity nucleic acid ligands. *Biomol. Eng.* **24**, 381–403 (2007).

29. Wolter, O. & Mayer, G. Aptamers as Valuable Molecular Tools in Neurosciences. *J. Neurosci.* **37**, 2517–2523 (2017).

30. Neves, M. M. P. da S. & Martín-Yerga, D. Advanced Nanoscale Approaches to Single-(Bio)entity Sensing and Imaging. *Biosensors* **8**, 100 (2018).

31. Akkilic, N., Geschwindner, S. & Höök, F. Single-molecule biosensors: Recent advances and applications. *Biosens. Bioelectron.* **151**, 111944 (2020).

32. Rissin, D. M., Kan, C. W., Campbell, T. G. & Duffy, D. C. Single-molecule enzyme-linked immunosorbent assay detects serum proteins at subfemtomolar concentrations. *Nat. Biotechnol.* **28**, 595–599 (2010).

33. Sun, B. & Wang, M. D. Chapter Three - Single-Molecule Optical-Trapping Techniques to Study Molecular Mechanisms of a Replisome. in *Methods in Enzymology* (eds. Spies, M. & Chemla, Y. R.) **582** 55–84 (Academic Press, 2017).

34. Arbore, C., Perego, L., Sergides, M. & Capitanio, M. Probing force in living cells with optical tweezers: from single-molecule mechanics to cell mechanotransduction. *Biophys. Rev.* **11**, 765–782 (2019).

35. Zhang, X., Zhang, B., Miao, W. & Zou, G. Molecular-Counting-Free and Electrochemiluminescent Single-Molecule Immunoassay with Dual-Stabilizers-Capped CdSe Nanocrystals as Labels. *Anal. Chem.* **88**, 5482–5488 (2016).

36. Zrimsek, A. B., Chiang, N., Mattei, M., Zaleski, S., McAnally, M. O., Chapman, C. T., Henry, A.-I., Schatz, G. C. & Van Duyne, R. P. Single-Molecule Chemistry with Surface- and Tip-Enhanced Raman Spectroscopy. *Chem. Rev.* **117**, 7583–7613 (2017).

37. Taylor, A. B. & Zijlstra, P. Single-Molecule Plasmon Sensing: Current Status and Future Prospects. *ACS Sens.* **2**, 1103–1122 (2017).

38. Ying, Y.-L. & Long, Y.-T. Nanopore-Based Single-Biomolecule Interfaces: From Information to Knowledge. *J. Am. Chem. Soc.* **141**, 15720–15729 (2019).

39. Bezrukov, S. M. Ion Channels as Molecular Coulter Counters to Probe Metabolite Transport. *J. Membr. Biol.* **174**, 1–13 (2000).

40. Coulter, W. H. Means for counting particles suspended in a fluid. Patent US2656508A (1953).

41. Hladky, S. B. & Haydon, D. A. Discreteness of Conductance Change in Bimolecular Lipid Membranes in the Presence of Certain Antibiotics. *Nature* **225**, 451–453 (1970).

42. Kasianowicz, J. J., Brandin, E., Branton, D. & Deamer, D. W. Characterization of individual polynucleotide molecules using a membrane channel. *Proc. Natl. Acad. Sci.* **93**, 13770–13773 (1996).

43. Li, J., Stein, D., McMullan, C., Branton, D., Aziz, M. J. & Golovchenko, J. A. Ion-beam sculpting at nanometre length scales. *Nature* **412**, 166–169 (2001).

44. Wang, Z., Liu, Y., Yu, L., Li, Y., Qian, G. & Chang, S. Nanopipettes: a potential tool for DNA detection. *Analyst* **144**, 5037–5047 (2019).

45. Wanunu, M. Nanopores: A journey towards DNA sequencing. *Phys. Life Rev.* **9**, 125–158 (2012).

46. Oukhaled, A., Bacri, L., Pastoriza-Gallego, M., Betton, J.-M. & Pelta, J. Sensing Proteins through Nanopores: Fundamental to Applications. *ACS Chem. Biol.* **7**, 1935–1949 (2012).

47. Yusko, E. C., Bruhn, B. R., Eggenberger, O. M., Houghtaling, J., Rollings, R. C., Walsh, N. C., Nandivada, S., Pindrus, M., Hall, A. R., Sept, D., Li, J., Kalonia, D. S. & Mayer, M. Real-time shape approximation and fingerprinting of single proteins using a nanopore. *Nat. Nanotechnol.* **12**, 360 (2017).

48. Kasianowicz, J. J., Balijepalli, A. K., Ettedgui, J., Forstater, J. H., Wang, H., Zhang, H. & Robertson, J. W. F. Analytical applications for pore-forming proteins. *Biochim. Biophys. Acta BBA - Biomembr.* **1858**, 593–606 (2016).

49. Beck, M. & Hurt, E. The nuclear pore complex: understanding its function through structural insight. *Nat. Rev. Mol. Cell Biol.* **18**, 73–89 (2017).

50. Song, L., Hobaugh, M. R., Shustak, C., Cheley, S., Bayley, H. & Gouaux, J. E. Structure of Staphylococcal α-Hemolysin, a Heptameric Transmembrane Pore. *Science* **274**, 1859–1865 (1996).

51. Shi, W., Friedman, A. K. & Baker, L. A. Nanopore Sensing. *Anal. Chem.* **89**, 157–188 (2017).

52. Fahie, M., Chisholm, C. & Chen, M. Resolved Single-Molecule Detection of Individual Species within a Mixture of anti-Biotin Antibodies Using an Engineered Monomeric Nanopore. *ACS Nano* **9**, 1089–1098 (2015).

53. Laszlo, A. H., Derrington, I. M. & Gundlach, J. H. MspA nanopore as a single-molecule tool: From sequencing to SPRNT. *Methods* **105**, 75–89 (2016).

54. Piguet, F., Ouldali, H., Pastoriza-Gallego, M., Manivet, P., Pelta, J. & Oukhaled, A. Identification of single amino acid differences in uniformly charged homopolymeric peptides with aerolysin nanopore. *Nat. Commun.* **9**, 966 (2018).

55. Cao, C., Cirauqui, N., Marcaida, M. J., Buglakova, E., Duperrex, A., Radenovic, A. & Dal Peraro, M. Single-molecule sensing of peptides and nucleic acids by engineered aerolysin nanopores. *Nat. Commun.* **10**, 1–11 (2019).

56. Van Meervelt, V., Soskine, M., Singh, S., Schuurman-Wolters, G. K., Wijma, H. J., Poolman, B. & Maglia, G. Real-Time Conformational Changes and Controlled Orientation of Native Proteins Inside a Protein Nanoreactor. *J. Am. Chem. Soc.* **139**, 18640–18646 (2017).

57. Wloka, C., Van Meervelt, V., van Gelder, D., Danda, N., Jager, N., Williams, C. P. & Maglia, G. Label-Free and Real-Time Detection of Protein Ubiquitination with a Biological Nanopore. *ACS Nano* **11**, 4387–4394 (2017).

58. Haque, F., Lunn, J., Fang, H., Smithrud, D. & Guo, P. Real-time sensing and discrimination of single chemicals using the channel of phi29 DNA packaging nanomotor. *ACS Nano* **6**, 3251–3261 (2012).

59. Ji, Z., Wang, S., Zhao, Z., Zhou, Z., Haque, F. & Guo, P. Fingerprinting of Peptides with a Large Channel of Bacteriophage Phi29 DNA Packaging Motor. *Small* **12**, 4572–4578 (2016).

60. Varongchayakul, N., Song, J., Meller, A. & W. Grinstaff, M. Single-molecule protein sensing in a nanopore: a tutorial. *Chem. Soc. Rev.* **47**, 8512–8524 (2018).

61. Haque, F., Li, J., Wu, H.-C., Liang, X.-J. & Guo, P. Solid-State and Biological Nanopore for Real-Time Sensing of Single Chemical and Sequencing of DNA. *Nano Today* **8**, 56–74 (2013).

62. Wang, S., Zhao, Z., Haque, F. & Guo, P. Engineering of protein nanopores for sequencing, chemical or protein sensing and disease diagnosis. *Curr. Opin. Biotechnol.* **51**, 80–89 (2018).

63. Howorka, S. & Siwy, Z. Nanopore analytics: sensing of single molecules. *Chem. Soc. Rev.* **38**, 2360–2384 (2009).

64. Franssila, S. *Introduction to Microfabrication, 2nd Edition*. (Wiley, 2010).

65. Storm, A. J., Chen, J. H., Ling, X. S., Zandbergen, H. W. & Dekker, C. Fabrication of solid-state nanopores with single-nanometre precision. *Nat. Mater.* **2**, 537–540 (2003).

66. Kennedy, E., Dong, Z., Tennant, C. & Timp, G. Reading the primary structure of a protein with 0.07 nm 3 resolution using a subnanometre-diameter pore. *Nat. Nanotechnol.* **11**, 968–976 (2016).

67. Graf, M., Lihter, M., Thakur, M., Georgiou, V., Topolancik, J., Ilic, B. R., Liu, K., Feng, J., Astier, Y. & Radenovic, A. Fabrication and practical applications of molybdenum disulfide nanopores. *Nat. Protoc.* **14**, 1130–1168 (2019).

68. Kwok, H., Briggs, K. & Tabard-Cossa, V. Nanopore fabrication by controlled dielectric breakdown. *PloS One* **9**, e92880 (2014).

69. Goyal, G., Lee, Y. B., Darvish, A., Ahn, C. W. & Kim, M. J. Hydrophilic and size-controlled graphene nanopores for protein detection. *Nanotechnology* **27**, 495301 (2016).

70. Wilson, J., Sloman, L., He, Z. & Aksimentiev, A. Graphene Nanopores for Protein Sequencing. *Adv. Funct. Mater.* **26**, 4830–4838 (2016).

71. Larkin, J., Henley, R., Bell, D. C., Cohen-Karni, T., Rosenstein, J. K. & Wanunu, M. Slow DNA Transport through Nanopores in Hafnium Oxide Membranes. *ACS Nano* **7**, 10121–10128 (2013).

72. Clarke, R. W., White, S. S., Zhou, D., Ying, L. & Klenerman, D. Trapping of Proteins under Physiological Conditions in a Nanopipette. *Angew. Chem. Int. Ed.* **44**, 3747–3750 (2005).

73. Steinbock, L. J., Otto, O., Chimerel, C., Gornall, J. & Keyser, U. F. Detecting DNA Folding with Nanocapillaries. *Nano Lett.* **10**, 2493–2497 (2010).

74. Steinbock, L. J., Steinbock, J. F. & Radenovic, A. Controllable Shrinking and Shaping of Glass Nanocapillaries under Electron Irradiation. *Nano Lett.* **13**, 1717–1723 (2013).

75. Li, W., Bell, N. A. W., Hernández-Ainsa, S., Thacker, V. V., Thackray, A. M., Bujdoso, R. & Keyser, U. F. Single Protein Molecule Detection by Glass Nanopores. *ACS Nano* **7**, 4129–4134 (2013).

76. Terejánszky, P., Makra, I., Fürjes, P. & Gyurcsányi, R. E. Calibration-Less Sizing and Quantitation of Polymeric Nanoparticles and Viruses with Quartz Nanopipets. *Anal. Chem.* **86**, 4688–4697 (2014).

77. Y. Sze, J. Y., Kumar, S., P. Ivanov, A., Oh, S.-H. & B. Edel, J. Fine tuning of nanopipettes using atomic layer deposition for single molecule sensing. *Analyst* **140**, 4828–4834 (2015).

78. Youn, Y., Lee, C., Kim, J. H., Chang, Y. W., Kim, D. Y. & Yoo, K.-H. Selective Detection of Single-Stranded DNA Molecules Using a Glass Nanocapillary Functionalized with DNA. *Anal. Chem.* **88**, 688–694 (2016).

79. Kudr, J., Skalickova, S., Nejdl, L., Moulick, A., Ruttkay–Nedecky, B., Adam, V. & Kizek, R. Fabrication of solid-state nanopores and its perspectives. *Electrophoresis* **36**, 2367–2379 (2015).

80. Yusko, E. C., Johnson, J. M., Majd, S., Prangkio, P., Rollings, R. C., Li, J., Yang, J. & Mayer, M. Controlling protein translocation through nanopores with bio-inspired fluid walls. *Nat. Nanotechnol.* **6**, 253–260 (2011).

81. Hall, A. R., Scott, A., Rotem, D., Mehta, K. K., Bayley, H. & Dekker, C. Hybrid pore formation by directed insertion of alpha hemolysin into solid-state nanopores. *Nat. Nanotechnol.* **5**, 874–877 (2010).

82. Cabello-Aguilar, S., Balme, S., Chaaya, A. A., Bechelany, M., Balanzat, E., Janot, J.-M., Pochat-Bohatier, C., Miele, P. & Dejardin, P. Slow translocation of polynucleotides and their discrimination by α-hemolysin inside a single track-etched nanopore designed by atomic layer deposition. *Nanoscale* **5**, 9582–9586 (2013).

83. Bentin, J., Balme, S. & Picaud, F. Polynucleotide differentiation using hybrid solid-state nanopore functionalizing with α-hemolysin. *Soft Matter* **16**, 1002–1010 (2020).

84. Jovanovic-Talisman, T., Tetenbaum-Novatt, J., McKenney, A. S., Zilman, A., Peters, R., Rout, M. P. & Chait, B. T. Artificial nanopores that mimic the transport selectivity of the nuclear pore complex. *Nature* **457**, 1023–1027 (2009).

85. Kowalczyk, S. W., Kapinos, L., Blosser, T. R., Magalhães, T., van Nies, P., Lim, R. Y. H. & Dekker, C. Single-molecule transport across an individual biomimetic nuclear pore complex. *Nat. Nanotechnol.* **6**, 433–438 (2011).

86. Cressiot, B., Greive, S. J., Mojtabavi, M., Antson, A. A. & Wanunu, M. Thermostable virus portal proteins as reprogrammable adapters for solid-state nanopore sensors. *Nat. Commun.* **9**, 4652 (2018).

87. Wang, P., Meyer, T. A., Pan, V., Dutta, P. K. & Ke, Y. The Beauty and Utility of DNA Origami. *Chem* **2**, 359–382 (2017).

88. Hernández-Ainsa, S. & Keyser, U. F. DNA origami nanopores: an emerging tool in biomedicine. *Nanomed.* **8**, 1551–1554 (2013).

89. Bell, N. A. W., Engst, Christian. R., Ablay, M., Divitini, G., Ducati, C., Liedl, T. & Keyser, U. F. DNA Origami Nanopores. *Nano Lett.* **12**, 512–517 (2012).

90. Wei, R., Martin, T. G., Rant, U. & Dietz, H. DNA Origami Gatekeepers for Solid-State Nanopores. *Angew. Chem. Int. Ed.* **51**, 4864–4867 (2012).

91. Barati Farimani, A., Dibaeinia, P. & Aluru, N. R. DNA Origami–Graphene Hybrid Nanopore for DNA Detection. *ACS Appl. Mater. Interfaces* **9**, 92–100 (2017).

92. Balasubramanian, R., Pal, S., Joshi, H., Rao, A., Naik, A., Varma, M., Chakraborty, B. & Maiti, P. K. DNA Translocation through Hybrid Bilayer Nanopores. *J. Phys. Chem. C* **123**, 11908–11916 (2019).

93. Wanunu, M. & Meller, A. Chemically Modified Solid-State Nanopores. *Nano Lett.* **7**, 1580–1585 (2007).

94. Eggenberger, O. M., Leriche, G., Koyanagi, T., Ying, C., Houghtaling, J., Schroeder, T. B. H., Yang, J., Li, J., Hall, A. & Mayer, M. Fluid surface coatings for solid-state nanopores: comparison of phospholipid bilayers and archaea-inspired lipid monolayers. *Nanotechnology* **30**, 325504 (2019).

95. Li, X., Hu, R., Li, J., Tong, X., Diao, J. J., Yu, D. & Zhao, Q. Non-sticky translocation of bio-molecules through Tween 20-coated solid-state nanopores in a wide pH range. *Appl. Phys. Lett.* **109**, 143105 (2016).

96. Shan, Y. P., Tiwari, P. B., Krishnakumar, P., Vlassiouk, I., Li, W. Z., Wang, X. W., Darici, Y., Lindsay, S. M., Wang, H. D., Smirnov, S. & He, J. Surface modification of graphene nanopores for protein translocation. *Nanotechnology* **24**, 495102 (2013).

97. Roman, J., Jarroux, N., Patriarche, G., Français, O., Pelta, J., Le Pioufle, B. & Bacri, L. Functionalized Solid-State Nanopore Integrated in a Reusable Microfluidic Device for a Better Stability and Nanoparticle Detection. *ACS Appl. Mater. Interfaces* **9**, 41634–41640 (2017).

98. Lepoitevin, M., Ma, T., Bechelany, M., Janot, J.-M. & Balme, S. Functionalization of single solid state nanopores to mimic biological ion channels: A review. *Adv. Colloid Interface Sci.* **250**, 195–213 (2017).

99. Eggenberger, O. M., Ying, C. & Mayer, M. Surface coatings for solid-state nanopores. *Nanoscale* **11**, 19636–19657 (2019).

100. Ding, D., Gao, P., Ma, Q., Wang, D. & Xia, F. Biomolecule-Functionalized Solid-State Ion Nanochannels/Nanopores: Features and Techniques. *Small* **15**, 1804878 (2019).

101. George, S. M. Atomic Layer Deposition: An Overview. *Chem. Rev*. **110**, 111-113 (2009).

102. Hampden-Smith, M. J. & Kodas, T. T. Chemical vapor deposition of metals: Part 1. An overview of CVD processes. *Chem. Vap. Depos.* **1**, 8–23 (1995).

103. Asatekin, A. & Gleason, K. K. Polymeric Nanopore Membranes for Hydrophobicity-Based Separations by Conformal Initiated Chemical Vapor Deposition. *Nano Lett.* **11**, 677–686 (2011).

104. Chen, P., Mitsui, T., Farmer, D. B., Golovchenko, J., Gordon, R. G. & Branton, D. Atomic Layer Deposition to Fine-Tune the Surface Properties and Diameters of Fabricated Nanopores. *Nano Lett.* **4**, 1333–1337 (2004).

105. Wang, C., Fu, Q., Wang, X., Kong, D., Sheng, Q., Wang, Y., Chen, Q. & Xue, J. Atomic Layer Deposition Modified Track-Etched Conical Nanochannels for Protein Sensing. *Anal. Chem.* **87**, 8227–8233 (2015).

106. Chou, Y.-C., Masih Das, P., Monos, D. S. & Drndić, M. Lifetime and Stability of Silicon Nitride Nanopores and Nanopore Arrays for Ionic Measurements. *ACS Nano* **14**, 6715-6728 (2020).

107. Yamazaki, H., Hu, R., Zhao, Q. & Wanunu, M. Photothermally Assisted Thinning of Silicon Nitride Membranes for Ultrathin Asymmetric Nanopores. *ACS Nano* **12**, 12472–12481 (2018).

108. Hu, R., Diao, J., Li, J., Tang, Z., Li, X., Leitz, J., Long, J., Liu, J., Yu, D. & Zhao, Q. Intrinsic and membrane-facilitated α-synuclein oligomerization revealed by label-free detection through solid-state nanopores. *Sci. Rep.* **6**, 1–11 (2016).

109. Schneider, G. F., Xu, Q., Hage, S., Luik, S., Spoor, J. N. H., Malladi, S., Zandbergen, H. & Dekker, C. Tailoring the hydrophobicity of graphene for its use as nanopores for DNA translocation. *Nat. Commun.* **4**, 1–7 (2013).

110. Umehara, S., Pourmand, N., Webb, C. D., Davis, R. W., Yasuda, K. & Karhanek, M. Current Rectification with Poly-l-Lysine-Coated Quartz Nanopipettes. *Nano Lett.* **6**, 2486–2492 (2006).

111. Actis, P., Rogers, A., Nivala, J., Vilozny, B., Seger, R. A., Jejelowo, O. & Pourmand, N. Reversible thrombin detection by aptamer functionalized STING sensors. *Biosens. Bioelectron.* **26**, 4503–4507 (2011).

112. Actis, P., Jejelowo, O. & Pourmand, N. UltraSensitive Mycotoxin Detection by STING Sensors. *Biosens. Bioelectron.* **26**, 333–337 (2010).

113. Alem, H., Blondeau, F., Glinel, K., Demoustier-Champagne, S. & Jonas, A. M. Layer-by-Layer Assembly of Polyelectrolytes in Nanopores. *Macromolecules* **40**, 3366–3372 (2007).

114. Ali, M., Yameen, B., Cervera, J., Ramírez, P., Neumann, R., Ensinger, W., Knoll, W. & Azzaroni, O. Layer-by-Layer Assembly of Polyelectrolytes into Ionic Current Rectifying Solid-State Nanopores: Insights from Theory and Experiment. *J. Am. Chem. Soc.* **132**, 8338–8348 (2010).

115. Ma, T., Gaigalas, P., Lepoitevin, M., Plikusiene, I., Bechelany, M., Janot, J.-M., Balanzat, E. & Balme, S. Impact of Polyelectrolyte Multilayers on the Ionic Current Rectification of Conical Nanopores. *Langmuir* **34**, 3405–3412 (2018).

116. Lepoitevin, M., Jamilloux, B., Bechelany, M., Balanzat, E., Janot, J.-M. & Balme, S. Fast and reversible functionalization of a single nanopore based on layer-by-layer polyelectrolyte self-assembly for tuning current rectification and designing sensors. *RSC Adv.* **6**, 32228–32233 (2016).

117. Blundell, E. L. C. J., Mayne, L. J., Lickorish, M., Christie, S. D. R. & Platt, M. Protein detection using tunable pores: resistive pulses and current rectification. *Faraday Discuss.* **193**, 487–505 (2016).

118. He, H., Xu, X., Wang, P., Chen, L. & Jin, Y. The facile surface chemical modification of a single glass nanopore and its use in the nonenzymatic detection of uric acid. *Chem. Commun.* **51**, 1914–1917 (2015).

119. Wei, R., Gatterdam, V., Wieneke, R., Tampé, R. & Rant, U. Stochastic sensing of proteins with receptor-modified solid-state nanopores. *Nat. Nanotechnol.* **7**, 257–263 (2012).

120. Siwy, Z., Trofin, L., Kohli, P., Baker, L. A., Trautmann, C. & Martin, C. R. Protein Biosensors Based on Biofunctionalized Conical Gold Nanotubes. *J. Am. Chem. Soc.* **127**, 5000–5001 (2005).

121. Emilsson, G., Xiong, K., Sakiyama, Y., Malekian, B., Gagnér, V. A., Schoch, R. L., Lim, R. Y. H. & Dahlin, A. B. Polymer brushes in solid-state nanopores form an impenetrable entropic barrier for proteins. *Nanoscale* **10**, 4663–4669 (2018).

122. Emilsson, G., Sakiyama, Y., Malekian, B., Xiong, K., Adali-Kaya, Z., Lim, R. Y. H. & Dahlin, A. B. Gating Protein Transport in Solid State Nanopores by Single Molecule Recognition. *ACS Cent. Sci.* **4**, 1007–1014 (2018).

123. Guo, W., Xia, H., Xia, F., Hou, X., Cao, L., Wang, L., Xue, J., Zhang, G., Song, Y., Zhu, D., Wang, Y. & Jiang, L. Current Rectification in Temperature-Responsive Single Nanopores. *ChemPhysChem* **11**, 859–864 (2010).

124. Schroeder, T. B. H., Houghtaling, J., Wilts, B. D. & Mayer, M. It's Not a Bug, It's a Feature: Functional Materials in Insects. *Adv. Mater.* **30**, 1705322 (2018).

125. Bouchet, A., Descamps, E., Mailley, P., Livache, T., Chatelain, F. & Haguet, V. Contactless Electrofunctionalization of a Single Pore. *Small* **5**, 2297–2303 (2009).

126. Liu, J., Pham, P., Haguet, V., Sauter-Starace, F., Leroy, L., Roget, A., Descamps, E., Bouchet, A., Buhot, A., Mailley, P. & Livache, T. Polarization-Induced Local Pore-Wall Functionalization for Biosensing: From Micropore to Nanopore. *Anal. Chem.* **84**, 3254–3261 (2012).

127. Ismail, A., Voci, S., Pham, P., Leroy, L., Maziz, A., Descamps, L., Kuhn, A., Mailley, P., Livache, T., Buhot, A., Leichlé, T., Bouchet-Spinelli, A. & Sojic, N. Enhanced Bipolar Electrochemistry at Solid-State Micropores: Demonstration by Wireless Electrochemiluminescence Imaging. *Anal. Chem.* **91**, 8900–8907 (2019).

128. Bouchet-Spinelli, A., Descamps, A., Liu, J., Ismail, A., Pham, P., Chatelain, F., Leïchlé, T., Leroy, L., Marche, P. N., Raillon, C., Roget, A., Roupioz, Y., Sojic, N., Buhot, A., Haguet, V., Livache, T. & Mailley, P. Polarization Induced Electro-Functionalization of Pore Walls: A Contactless Technology. *Biosensors* **9**, 121 (2019).

129. Ma, Q., Si, Z., Li, Y., Wang, D., Wu, X., Gao, P. & Xia, F. Functional solid-state nanochannels for biochemical sensing. *TrAC Trends Anal. Chem.* **115**, 174–186 (2019).

130. Brzoska, J. B., Azouz, I. B. & Rondelez, F. Silanization of Solid Substrates: A Step Toward Reproducibility. *Langmuir* **10**, 4367–4373 (1994).

131. To, T. D., Nguyen, A. T., Phan, K. N. T., Truong, A. T. T., Doan, T. C. D. & Dang, C. M. Modification of silicon nitride surfaces with GOPES and APTES for antibody immobilization: computational and experimental studies. *Adv. Nat. Sci. Nanosci. Nanotechnol.* **6**, 045006 (2015).

132. Nilsson, J., Lee, J. R. I., Ratto, T. V. & Létant, S. E. Localized Functionalization of Single Nanopores. *Adv. Mater.* **18**, 427–431 (2006).

133. Iqbal, S. M., Akin, D. & Bashir, R. Solid-state nanopore channels with DNA selectivity. *Nat. Nanotechnol.* **2**, 243–248 (2007).

134. Ding, S., Gao, C. & Gu, L.-Q. Capturing Single Molecules of Immunoglobulin and Ricin with an Aptamer-Encoded Glass Nanopore. *Anal. Chem.* **81**, 6649–6655 (2009).

135. Mussi, V., Fanzio, P., Repetto, L., Firpo, G., Stigliani, S., Tonini, G. P. & Valbusa, U. "DNA-Dressed NAnopore" for complementary sequence detection. *Biosens. Bioelectron.* **29**, 125–131 (2011).

136. Liu, G.-C., Gao, M.-J., Chen, W., Hu, X.-Y., Song, L.-B., Liu, B. & Zhao, Y.-D. pH-modulated ion-current rectification in a cysteine-functionalized glass nanopipette. *Electrochem. Commun.* **97**, 6–10 (2018).

137. Liebes-Peer, Y., Rapaport, H. & Ashkenasy, N. Amplification of Single Molecule Translocation Signal Using β-Strand Peptide Functionalized Nanopores. *ACS Nano* **8**, 6822–6832 (2014).

138. Zhang, S., Liu, G., Chai, H., Zhao, Y.-D., Yu, L. & Chen, W. Detection of alkaline phosphatase activity with a functionalized nanopipette. *Electrochem. Commun.* **99**, 71–74 (2019).

139. Zhang, L.-X., Cai, S.-L., Zheng, Y.-B., Cao, X.-H. & Li, Y.-Q. Smart Homopolymer Modification to Single Glass Conical Nanopore Channels: Dual-Stimuli-Actuated Highly Efficient Ion Gating. *Adv. Funct. Mater.* **21**, 2103–2107 (2011).

140. Fu, Y., Tokuhisa, H. & Baker, L. A. Nanopore DNA sensors based on dendrimer-modified nanopipettes. *Chem. Commun.* 4877–4879 (2009).

141. Lee, S. B., Mitchell, D. T., Trofin, L., Nevanen, T. K., Söderlund, H. & Martin, C. R. Antibody-Based Bio-Nanotube Membranes for Enantiomeric Drug Separations. *Science* **296**, 2198–2200 (2002).

142. Wang, G., Bohaty, A. K., Zharov, I. & White, H. S. Photon Gated Transport at the Glass Nanopore Electrode. *J. Am. Chem. Soc.* **128**, 13553–13558 (2006).

143. Ananth, A., Genua, M., Aissaoui, N., Díaz, L., Eisele, N. B., Frey, S., Dekker, C., Richter, R. P. & Görlich, D. Reversible Immobilization of Proteins in Sensors and Solid-State Nanopores. *Small* **14**, 1703357 (2018).

144. Branton, D. & Schloss, J. A. The potential and challenges of nanopore sequencing. *Nat. Biotechnol.* **26**, 1146–1153 (2008).

145. Kasianowicz, J. J. & Bezrukov, S. M. On 'three decades of nanopore sequencing'. *Nat. Biotechnol.* **34**, 481-482 (2016).

146. Yuan, Z., Wang, C., Yi, X., Ni, Z., Chen, Y. & Li, T. Solid-State Nanopore. *Nanoscale Res. Lett.* **13**, 56 (2018).

147. Feng, Y., Zhang, Y., Ying, C., Wang, D. & Du, C. Nanopore-based Fourth-generation DNA Sequencing Technology. *Genomics Proteomics Bioinformatics* **13**, 4–16 (2015).

148. Akeson, M., Branton, D., Kasianowicz, J. J., Brandin, E. & Deamer, D. W. Microsecond Time-Scale Discrimination Among Polycytidylic Acid, Polyadenylic Acid, and Polyuridylic Acid as Homopolymers or as Segments Within Single RNA Molecules. *Biophys. J.* **77**, 3227–3233 (1999).

149. Meller, A., Nivon, L., Brandin, E., Golovchenko, J. & Branton, D. Rapid nanopore discrimination between single polynucleotide molecules. *Proc. Natl. Acad. Sci. U. S. A.* **97**, 1079–1084 (2000).

150. Stoddart, D., Heron, A. J., Mikhailova, E., Maglia, G. & Bayley, H. Single-nucleotide discrimination in immobilized DNA oligonucleotides with a biological nanopore. *Proc. Natl. Acad. Sci.* **106**, 7702–7707 (2009).

151. Stoddart, D., Heron, A. J., Klingelhoefer, J., Mikhailova, E., Maglia, G. & Bayley, H. Nucleobase Recognition in ssDNA at the Central Constriction of the α-Hemolysin Pore. *Nano Lett.* **10**, 3633–3637 (2010).

152. Manrao, E. A., Derrington, I. M., Laszlo, A. H., Langford, K. W., Hopper, M. K., Gillgren, N., Pavlenok, M., Niederweis, M. & Gundlach, J. H. Reading DNA at single-nucleotide resolution with a mutant MspA nanopore and phi29 DNA polymerase. *Nat. Biotechnol.* **30**, 349–353 (2012).

153. Eisenstein, M. Oxford Nanopore announcement sets sequencing sector abuzz. *Nat. Biotechnol.* **30**, 295–296 (2012).

154. Oxford Nanopore. https://app.acuityscheduling.com/schedule.php?owner=13373598.

155. Jain, M., Fiddes, I., Miga, K. H., Olsen, H. E., Paten, B. & Akeson, M. Improved data analysis for the MinION nanopore sequencer. *Nat. Methods* **12**, 351–356 (2015).

156. Keller, M. W., Rambo-Martin, B. L., Wilson, M. M., Ridenour, C. A., Shepard, S. S., Stark, T. J., Neuhaus, E. B., Dugan, V. G., Wentworth, D. E. & Barnes, J. R. Direct RNA Sequencing of the Coding Complete Influenza A Virus Genome. *Sci. Rep.* **8**, 14408 (2018).

157. Garalde, D. R. & Turner, D. J. Highly parallel direct RNA sequencing on an array of nanopores. *Nat. Methods* **15**, 201–206 (2018).

158. Montel, F. Séquençage de l'ADN par nanopores: Résultats et perspectives. *médecine/sciences* **34**, 161–165 (2018).

159. Jain, M., Tyson, J. R., Loose, M. & Olsen, H. E . MinION Analysis and Reference Consortium: Phase 2 data release and analysis of R9.0 chemistry. *F1000Research* **6**, 760 (2017).

160. De Roeck, A. & Sleegers, K. Deleterious ABCA7 mutations and transcript rescue mechanisms in early onset Alzheimer's disease. *Acta Neuropathol. (Berl.)* **134**, 475–487 (2017).

161. Scientists from the Wellcome Trust Centre for Human Genetics (WTCHG) have used Oxford Nanopore Technologies MinION. *Oxford Genomics Centre* https://www.well.ox.ac.uk/ogc/scientists-from-the-wellcome-trust-centre-for-human-genetics-wtchg-have-used-oxford-nanopore-technologies-minion/ (2017).

162. Kono, N. & Arakawa, K. Nanopore sequencing: Review of potential applications in functional genomics. *Dev. Growth Differ.* **61**, 316–326 (2019).

163. Minervini, C. F., Cumbo, C., Orsini, P., Anelli, L., Zagaria, A., Specchia, G. & Albano, F. Nanopore Sequencing in Blood Diseases: A Wide Range of Opportunities. *Front. Genet.* **11**, 1-10 (2020).

164. Wang, Y., Tian, K., Shi, R., Gu, A., Pennella, M., Alberts, L., Gates, K. S., Li, G., Fan, H., Wang, M. X. & Gu, L.-Q. Nanolock−Nanopore Facilitated Digital Diagnostics of Cancer Driver Mutation in Tumor Tissue. *ACS Sens.* **2**, 975–981 (2017).

165. Helmersen, K. & Aamot, H. V. DNA extraction of microbial DNA directly from infected tissue: an optimized protocol for use in nanopore sequencing. *Sci. Rep.* **10**, 2985 (2020).

166. Hall, C. L., Zascavage, R. R., Sedlazeck, F. J. & Planz, J. V. Potential Applications of Nanopore Sequencing for Forensic Analysis. *Forensic. Sci. Rev*. **32**, 23-54 (2020).

167. Wang, M., & Liu, T. Nanopore Targeted Sequencing for the Accurate and Comprehensive Detection of SARS-CoV-2 and Other Respiratory Viruses. *Small* **16**, 2002169 (2020).

168. Filloux, D., Fernandez, E., Loire, E., Claude, L., Galzi, S., Candresse, T., Winter, S., Jeeva, M. L., Makeshkumar, T., Martin, D. P. & Roumagnac, P. Nanopore-based detection and characterization of yam viruses. *Sci. Rep.* **8**, 17879 (2018).

169. Oh, S., Lee, M.-K. & Chi, S.-W. Single-Molecule-Based Detection of Conserved Influenza A Virus RNA Promoter Using a Protein Nanopore. *ACS Sens.* **4**, 2849–2853 (2019).

170. Ji, P., Aw, T. G., Van Bonn, W. & Rose, J. B. Evaluation of a portable nanopore-based sequencer for detection of viruses in water. *J. Virol. Methods* **278**, 113805 (2020).

171. Truelove, N. K., Andruszkiewicz, E. A. & Block, B. A. A rapid environmental DNA method for detecting white sharks in the open ocean. *Methods Ecol. Evol.* **0**, 1-8 (2019).

172. Leidenfrost, R. M., Bänsch, S., Prudnikow, L., Brenig, B., Westphal, C. & Wünschiers, R. Analyzing the Dietary Diary of Bumble Bee. *Front. Plant Sci.* **11**, 1-9 (2020).

173. Niedzwiecki, D. J., Chou, Y.-C., Xia, Z., Thei, F. & Drndić, M. Detection of single analyte and environmental samples with silicon nitride nanopores: Antarctic dirt particulates and DNA in artificial seawater. *Rev. Sci. Instrum.* **91**, 031301 (2020).

174. Rezzonico, F. Nanopore-Based Instruments as Biosensors for Future Planetary Missions. *Astrobiology* **14**, 344–351 (2014).

175. Saboda, K., Moeller, R. & Carr, C. E. Enabling Measurement of Darwinian Evolution in Space. in *2019 IEEE Aerospace Conference* 1–10 (2019).

176. Bhattaru, S. A., Tani, J., Saboda, K., Borowsky, J., Ruvkun, G., Zuber, M. T. & Carr, C. E. Development of a Nucleic Acid-Based Life Detection Instrument Testbed. in *2019 IEEE Aerospace Conference* 1–10 (2019).

177. Maggiori, C., Stromberg, J., Blanco, Y., Goordial, J., Cloutis, E., García-Villadangos, M., Parro, V. & Whyte, L. The Limits, Capabilities, and Potential for Life Detection with MinION Sequencing in a Paleochannel Mars Analog. *Astrobiology* **20**, 375–393 (2020).

178. Chen, K., Zhu, J., Bošković, F. & Keyser, U. F. Nanopore-Based DNA Hard Drives for Rewritable and Secure Data Storage. *Nano Lett.* **20**, 3754–3760 (2020).

179. Callahan, N., Tullman, J., Kelman, Z. & Marino, J. Strategies for Development of a Next-Generation Protein Sequencing Platform. *Trends Biochem. Sci.* **45**, 76–89 (2020).

180. Luo, Y., Wu, L., Tu, J. & Lu, Z. Application of Solid-State Nanopore in Protein Detection. *Int. J. Mol. Sci.* **21**, 2808 (2020).

181. Howorka, S. & Siwy, Z. S. Reading amino acids in a nanopore. *Nat. Biotechnol.* **38**, 159–160 (2020).

182. Chinappi, M. & Cecconi, F. Protein sequencing via nanopore based devices: a nanofluidics perspective. *J. Phys. Condens. Matter* **30**, 204002 (2018).

183. Cressiot, B., Bacri, L. & Pelta, J. The Promise of Nanopore Technology: Advances in the Discrimination of Protein Sequences and Chemical Modifications. *Small Methods*, 2000090 (2020).

184. Firnkes, M., Pedone, D., Knezevic, J., Döblinger, M. & Rant, U. Electrically Facilitated Translocations of Proteins through Silicon Nitride Nanopores: Conjoint and Competitive Action of Diffusion, Electrophoresis, and Electroosmosis. *Nano Lett.* **10**, 2162–2167 (2010).

185. Moriyama, Y., Watanabe, E., Kobayashi, K., Harano, H., Inui, E. & Takeda, K. Secondary Structural Change of Bovine Serum Albumin in Thermal Denaturation up to 130 °C and Protective Effect of Sodium Dodecyl Sulfate on the Change. *J. Phys. Chem. B* **112**, 16585–16589 (2008).

186. Freedman, K. J., Jürgens, M., Prabhu, A., Ahn, C. W., Jemth, P., Edel, J. B. & Kim, M. J. Chemical, Thermal, and Electric Field Induced Unfolding of Single Protein Molecules Studied Using Nanopores. *Anal. Chem.* **83**, 5137–5144 (2011).

187. Payet, L., Martinho, M., Pastoriza-Gallego, M., Betton, J.-M., Auvray, L., Pelta, J. & Mathé, J. Thermal Unfolding of Proteins Probed at the Single Molecule Level Using Nanopores. *Anal. Chem.* **84**, 4071–4076 (2012).

188. Freedman, K. J., Haq, S. R., Edel, J. B., Jemth, P. & Kim, M. J. Single molecule unfolding and stretching of protein domains inside a solid-state nanopore by electric field. *Sci. Rep.* **3**, 1638 (2013).

189. Wu, L., Liu, H., Zhao, W., Wang, L., Hou, C., Liu, Q. & Lu, Z. Electrically facilitated translocation of protein through solid nanopore. *Nanoscale Res. Lett.* **9**, 140 (2014).

190. Restrepo-Pérez, L., John, S., Aksimentiev, A., Joo, C. & Dekker, C. SDS-assisted protein transport through solid-state nanopores. *Nanoscale* **9**, 11685–11693 (2017).

191. Pastoriza-Gallego, M., Breton, M.-F., Discala, F., Auvray, L., Betton, J.-M. & Pelta, J. Evidence of Unfolded Protein Translocation through a Protein Nanopore. *ACS Nano* **8**, 11350–11360 (2014).

192. Restrepo-Pérez, L., Joo, C. & Dekker, C. Paving the way to single-molecule protein sequencing. *Nat. Nanotechnol.* **13**, 786–796 (2018).

193. Asandei, A., Muccio, G. D., Schiopu, I., Mereuta, L., Dragomir, I. S., Chinappi, M. & Luchian, T. Nanopore-Based Protein Sequencing Using Biopores: Current Achievements and Open Challenges. *Small Methods*, 1900595 (2020).

194. Dong, Z., Kennedy, E., Hokmabadi, M. & Timp, G. Discriminating Residue Substitutions in a Single Protein Molecule Using a Sub-nanopore. *ACS Nano* **11**, 5440–5452 (2017).

195. Plesa, C., Kowalczyk, S. W., Zinsmeester, R., Grosberg, A. Y., Rabin, Y. & Dekker, C. Fast Translocation of Proteins through Solid State Nanopores. *Nano Lett.* **13**, 658–663 (2013).

196. Ouldali, H., Sarthak, K., Ensslen, T., Piguet, F., Manivet, P., Pelta, J., Behrends, J. C., Aksimentiev, A. & Oukhaled, A. Electrical recognition of the twenty proteinogenic amino acids using an aerolysin nanopore. *Nat. Biotechnol.* **38**, 176–181 (2020).

197. Chinappi, M., Luchian, T. & Cecconi, F. Nanopore tweezers: Voltage-controlled trapping and releasing of analytes. *Phys. Rev. E* **92**, 032714 (2015).

198. Asandei, A., Chinappi, M., Lee, J., Ho Seo, C., Mereuta, L., Park, Y. & Luchian, T. Placement of oppositely charged aminoacids at a polypeptide termini determines the voltage-controlled braking of polymer transport through nanometer-scale pores. *Sci. Rep.* **5**, 10419 (2015).

199. Luchian, T., Park, Y., Asandei, A., Schiopu, I., Mereuta, L. & Apetrei, A. Nanoscale Probing of Informational Polymers with Nanopores. Applications to Amyloidogenic Fragments, Peptides, and DNA–PNA Hybrids. *Acc. Chem. Res.* **52**, 267–276 (2019).

200. Fologea, D., Ledden, B., McNabb, D. S. & Li, J. Electrical characterization of protein molecules by a solid-state nanopore. *Appl. Phys. Lett.* **91**, 053901 (2007).

201. Han, A., Schürmann, G., Mondin, G., Bitterli, R. A., Hegelbach, N. G., de Rooij, N. F. & Staufer, U. Sensing protein molecules using nanofabricated pores. *Appl. Phys. Lett.* **88**, 093901 (2006).

202. Raillon, C., Cousin, P., Traversi, F., Garcia-Cordero, E., Hernandez, N. & Radenovic, A. Nanopore Detection of Single Molecule RNAP–DNA Transcription Complex. *Nano Lett.* **12**, 1157–1164 (2012).

203. Balme, S., Coulon, P. E., Lepoitevin, M., Charlot, B., Yandrapalli, N., Favard, C., Muriaux, D., Bechelany, M. & Janot, J.-M. Influence of Adsorption on Proteins and Amyloid Detection by Silicon Nitride Nanopore. *Langmuir* **32**, 8916–8925 (2016).

204. Larkin, J., Henley, R. Y., Muthukumar, M., Rosenstein, J. K. & Wanunu, M. High-Bandwidth Protein Analysis Using Solid-State Nanopores. *Biophys. J.* **106**, 696–704 (2014).

205. Houghtaling, J., Ying, C., Eggenberger, O. M., Fennouri, A., Nandivada, S., Acharjee, M., Li, J., Hall, A. R. & Mayer, M. Estimation of Shape, Volume, and Dipole Moment of Individual Proteins Freely Transiting a Synthetic Nanopore. *ACS Nano* **13**, 5231–5242 (2019).

206. Gao, R., Lin, Y., Ying, Y.-L. & Long, Y.-T. Nanopore-based sensing interface for single molecule electrochemistry. *Sci. China Chem.* **62**, 1576-1587 (2019).

207. Talaga, D. S. & Li, J. Single-Molecule Protein Unfolding in Solid State Nanopores. *J. Am. Chem. Soc.* **131**, 9287–9297 (2009).

208. Cressiot, B., Oukhaled, A., Bacri, L. & Pelta, J. Focus on Protein Unfolding Through Nanopores. *BioNanoScience* **4**, 111–118 (2014).

209. Si, W. & Aksimentiev, A. Nanopore Sensing of Protein Folding. *ACS Nano* **11**, 7091–7100 (2017).

210. Waduge, P., Hu, R., Bandarkar, P., Yamazaki, H., Cressiot, B., Zhao, Q., Whitford, P. C. & Wanunu, M. Nanopore-Based Measurements of Protein Size, Fluctuations, and Conformational Changes. *ACS Nano* **11**, 5706–5716 (2017).

211. Goyal, G. & Kim, M. J. Use of Solid-State Nanopores to Detect Different Conformational States of Transferrin. in *18th International Conference on Miniaturized Systems for Chemistry and Life Sciences (μTAS)* (2014).

212. Li, X., Lee, K. H., Shorkey, S., Chen, J. & Chen, M. Different Anomeric Sugar Bound States of Maltose Binding Protein Resolved by a Cytolysin A Nanopore Tweezer. *ACS Nano* **14**, 1727–1737 (2020).

213. Nir, I., Huttner, D. & Meller, A. Direct Sensing and Discrimination among Ubiquitin and Ubiquitin Chains Using Solid-State Nanopores. *Biophys. J.* **108**, 2340–2349 (2015).

214. Niedzwiecki, D. J., Lanci, C. J., Shemer, G., Cheng, P. S., Saven, J. G. & Drndić, M. Observing Changes in the Structure and Oligomerization State of a Helical Protein Dimer Using Solid-State Nanopores. *ACS Nano* **9**, 8907–8915 (2015).

215. Varongchayakul, N., Huttner, D., Grinstaff, M. W. & Meller, A. Sensing Native Protein Solution Structures Using a Solid-state Nanopore: Unraveling the States of VEGF. *Sci. Rep.* **8**, 1–9 (2018).

216. Wang, S., Zhou, Z., Zhao, Z., Zhang, H., Haque, F. & Guo, P. Channel of viral DNA packaging motor for real time kinetic analysis of peptide oxidation states. *Biomaterials* **126**, 10–17 (2017).

217. Rosen, C. B., Rodriguez-Larrea, D. & Bayley, H. Single-molecule site-specific detection of protein phosphorylation with a nanopore. *Nat. Biotechnol.* **32**, 179–181 (2014).

218. Harrington, L., Alexander, L. T., Knapp, S. & Bayley, H. Single-Molecule Protein Phosphorylation and Dephosphorylation by Nanopore Enzymology. *ACS Nano* **13**, 633–641 (2019).

219. Restrepo-Pérez, L., Wong, C. H., Maglia, G., Dekker, C. & Joo, C. Label-Free Detection of Post-translational Modifications with a Nanopore. *Nano Lett.* **19**, 7957-7964 (2019).

220. Wang, X., Wilkinson, M. D., Lin, X., Ren, R., Willison, K. R., Ivanov, A. P., Baum, J. & Edel, J. B. Single-molecule nanopore sensing of actin dynamics and drug binding. *Chem. Sci.* **11**, 970–979 (2020).

221. Jetha, N. N., Semenchenko, V., Wishart, D. S., Cashman, N. R. & Marziali, A. Nanopore Analysis of Wild-Type and Mutant Prion Protein (PrPC): Single Molecule Discrimination and PrPC Kinetics. *PLoS ONE* **8**, e54982 (2013).

222. Giamblanco, N., Coglitore, D., Gubbiotti, A., Ma, T., Balanzat, E., Janot, J.-M., Chinappi, M. & Balme, S. Amyloid Growth, Inhibition, and Real-Time Enzymatic Degradation Revealed with Single Conical Nanopore. *Anal. Chem.* **90**, 12900–12908 (2018).

223. Wang, H.-Y., Ying, Y.-L., Li, Y., Kraatz, H.-B. & Long, Y.-T. Nanopore Analysis of β-Amyloid Peptide Aggregation Transition Induced by Small Molecules. *Anal. Chem.* **83**, 1746–1752 (2011).

224. Yusko, E. C., Prangkio, P., Sept, D., Rollings, R. C., Li, J. & Mayer, M. Single-Particle Characterization of Aβ Oligomers in Solution. *ACS Nano* **6**, 5909–5919 (2012).

225. Mahmood, M. A. I., Ali, W., Adnan, A. & Iqbal, S. M. 3D Structural Integrity and Interactions of Single-Stranded Protein-Binding DNA in a Functionalized Nanopore. *J. Phys. Chem. B* **118**, 5799–5806 (2014).

226. Frykholm, K., K. Nyberg, L. & Westerlund, F. Exploring DNA–protein interactions on the single DNA molecule level using nanofluidic tools. *Integr. Biol.* **9**, 650–661 (2017).

227. Ding, T., Yang, J., Pan, V., Zhao, N., Lu, Z., Ke, Y. & Zhang, C. DNA nanotechnology assisted nanopore-based analysis. *Nucleic Acids Res.* **48**, 2791–2806 (2020).

228. Kaur, H., Nandivada, S., Acharjee, M. C., McNabb, D. S. & Li, J. Estimating RNA Polymerase Protein Binding Sites on λ DNA Using Solid-State Nanopores. *ACS Sens.* **4**, 100-109 (2018).

229. Celaya, G., Perales-Calvo, J., Muga, A., Moro, F. & Rodriguez-Larrea, D. Label-Free, Multiplexed, Single-Molecule Analysis of Protein–DNA Complexes with Nanopores. *ACS Nano* **11**, 5815–5825 (2017).

230. Yang, W., Restrepo-Pérez, L., Bengtson, M., Heerema, S. J., Birnie, A., van der Torre, J. & Dekker, C. Detection of CRISPR-dCas9 on DNA with Solid-State Nanopores. *Nano Lett.* **18**, 6469-6474 (2018).

231. Bell, N. A. W. & Keyser, U. F. Digitally encoded DNA nanostructures for multiplexed, single-molecule protein sensing with nanopores. *Nat. Nanotechnol.* **11**, 645–651 (2016).

232. Hornblower, B., Coombs, A., Whitaker, R. D., Kolomeisky, A., Picone, S. J., Meller, A. & Akeson, M. Single-molecule analysis of DNA-protein complexes using nanopores. *Nat. Methods* **4**, 315–317 (2007).

233. Harrer, S., Kim, S. C., Schieber, C., Kannam, S., Gunn, N., Moore, S., Scott, D., Bathgate, R., Skafidas, S. & Wagner, J. M. Label-free screening of single biomolecules through resistive pulse sensing technology for precision medicine applications. *Nanotechnology* **26**, 182502 (2015).

234. Thakur, A. K. & Movileanu, L. Real-time measurement of protein-protein interactions at single-molecule resolution using a biological nanopore. *Nat. Biotechnol.* **37**, 96-101 (2018).

235. Chae, H., Kwak, D.-K., Lee, M.-K., Chi, S.-W. & Kim, K.-B. Solid-state nanopore analysis on conformation change of p53TAD–MDM2 fusion protein induced by protein–protein interaction. *Nanoscale* **10**, 17227–17235 (2018).

236. Han, A., Creus, M., Schürmann, G., Linder, V., Ward, T. R., de Rooij, N. F. & Staufer, U. Label-Free Detection of Single Protein Molecules and Protein−Protein Interactions Using Synthetic Nanopores. *Anal. Chem.* **80**, 4651–4658 (2008).

237. Kwak, D.-K., Chae, H., Lee, M.-K., Ha, J.-H., Goyal, G., Kim, M. J., Kim, K.-B. & Chi, S.-W. Probing the Small-Molecule Inhibition of an Anticancer Therapeutic Protein-Protein Interaction Using a Solid-State Nanopore. *Angew. Chem. Int. Ed Engl.* **55**, 5713–5717 (2016).

238. Willems, K., Van Meervelt, V., Wloka, C. & Maglia, G. Single-molecule nanopore enzymology. *Philos. Trans. R. Soc. B Biol. Sci.* **372**, 20160230 (2017).

239. Sheng, Y., Zhang, S., Liu, L. & Wu, H.-C. Measuring Enzymatic Activities with Nanopores. *ChemBioChem* **21**, 2089-2097 (2020).

240. Meng, F.-N., Ying, Y.-L., Yang, J. & Long, Y.-T. A Wild-Type Nanopore Sensor for Protein Kinase Activity. *Anal. Chem.* **91**, 9910–9915 (2019).

241. Giamblanco, N., Janot, J.-M., Gubbiotti, A., Chinappi, M. & Balme, S. Characterization of Food Amyloid Protein Digestion by Conical Nanopore. *Small Methods*, 1900703 (2020).

242. Harrington, L., Alexander, L. T., Knapp, S. & Bayley, H. Pim Kinase Inhibitors Evaluated with a Single-Molecule Engineered Nanopore Sensor. *Angew. Chem. Int. Ed.* **54**, 8154–8159 (2015).

243. Winters-Hilt, S., Davis, A., Amin, I. & Morales, E. Nanopore current transduction analysis of protein binding to non-terminal and terminal DNA regions: analysis of transcription factor binding, retroviral DNA terminus dynamics, and retroviral integrase-DNA binding. *BMC Bioinformatics* **8**, S10 (2007).

244. Thomson, K., Amin, I., Morales, E. & Winters-Hilt, S. Preliminary nanopore cheminformatics analysis of aptamer-target binding strength. *BMC Bioinformatics* **8**, S11 (2007).

245. Shim, J. W. & Gu, L.-Q. Encapsulating a Single G-Quadruplex Aptamer in a Protein Nanocavity. *J. Phys. Chem. B* **112**, 8354–8360 (2008).

246. Gu, L.-Q. & Wook Shim, J. Single molecule sensing by nanopores and nanopore devices. *Analyst* **135**, 441–451 (2010).

247. Renner, S., Geltinger, S. & Simmel, F. C. Nanopore Translocation and Force Spectroscopy Experiments in Microemulsion Droplets. *Small* **6**, 190–194 (2010).

248. Shim, J. & Gu, L.-Q. Single-molecule investigation of G-quadruplex using a nanopore sensor. *Methods San Diego Calif* **57**, 40–46 (2012).

249. Shim, J. W., Tan, Q. & Gu, L.-Q. Single-molecule detection of folding and unfolding of the G-quadruplex aptamer in a nanopore nanocavity. *Nucleic Acids Res.* **37**, 972–982 (2009).

250. Billinge, E. R., Broom, M. & Platt, M. Monitoring Aptamer–Protein Interactions Using Tunable Resistive Pulse Sensing. *Anal. Chem.* **86**, 1030–1037 (2014).

251. Zhao, X.-P., Cao, J., Nie, X.-G., Wang, S.-S., Wang, C. & Xia, X.-H. Label-free monitoring of the thrombin–aptamer recognition reaction using an array of nanochannels coupled with electrochemical detection. *Electrochem. Commun.* **81**, 5–9 (2017).

252. Van Meervelt, V., Soskine, M. & Maglia, G. Detection of Two Isomeric Binding Configurations in a Protein–Aptamer Complex with a Biological Nanopore. *ACS Nano* **8**, 12826–12835 (2014).

253. Mohammad, M. M., Iyer, R., Howard, K. R., McPike, M. P., Borer, P. N. & Movileanu, L. Engineering a Rigid Protein Tunnel for Biomolecular Detection. *J. Am. Chem. Soc.* **134**, 9521–9531 (2012).

254. Arnaut, V., Langecker, M. & Simmel, F. C. Nanopore Force Spectroscopy of Aptamer–Ligand Complexes. *Biophys. J.* **105**, 1199–1207 (2013).

255. Ying, Y.-L., Wang, H.-Y., Sutherland, T. C. & Long, Y.-T. Monitoring of an ATP-Binding Aptamer and its Conformational Changes Using an α-Hemolysin Nanopore. *Small* **7**, 87–94 (2011).

256. Zhang, X., Zhang, J., Ying, Y.-L., Tian, H. & Long, Y.-T. Single molecule analysis of light-regulated RNA:spiropyran interactions. *Chem. Sci.* **5**, 2642–2646 (2014).

257. Wang, H.-Y., Song, Z.-Y., Zhang, H.-S. & Chen, S.-P. Single-molecule analysis of lead(II)-binding aptamer conformational changes in an α-hemolysin nanopore, and sensitive detection of lead(II). *Microchim. Acta* **183**, 1003–1010 (2016).

258. Mayne, L., Lin, C.-Y., Christie, S. D. R., Siwy, Z. S. & Platt, M. The Design and Characterization of Multifunctional Aptamer Nanopore Sensors. *ACS Nano* **12**, 4844–4852 (2018).

259. Li, T., Liu, L., Li, Y., Xie, J. & Wu, H.-C. A Universal Strategy for Aptamer-Based Nanopore Sensing through Host–Guest Interactions inside α-Hemolysin. *Angew. Chem. Int. Ed.* **54**, 7568–7571 (2015).

260. Niedzwiecki, D. J., Iyer, R., Borer, P. N. & Movileanu, L. Sampling a Biomarker of the Human Immunodeficiency Virus across a Synthetic Nanopore. *ACS Nano* **7**, 3341–3350 (2013).

261. Zeng, T., Li, T., Li, Y., Liu, L., Wang, X., Liu, Q., Zhao, Y. & Wu, H.-C. DNA-based detection of mercury(II) ions through characteristic current signals in nanopores with high sensitivity and selectivity. *Nanoscale* **6**, 8579–8584 (2014).

262. Zhang, S., Bao, A., Sun, T., Wang, E. & Wang, J. PEI/Zr4+-coated nanopore for selective and sensitive detection of ATP in combination with single-walled carbon nanotubes. *Biosens. Bioelectron.* **63**, 287–293 (2015).

263. Kawano, R., Osaki, T., Sasaki, H., Takinoue, M., Yoshizawa, S. & Takeuchi, S. Rapid Detection of a Cocaine-Binding Aptamer Using Biological Nanopores on a Chip. *J. Am. Chem. Soc.* **133**, 8474–8477 (2011).

264. Kawano, R., Osaki, T., Sasaki, H., Takinoue, M., Yoshizawa, S. & Takeuchi, S. 25 second cocaine sensing by membrane protein channel integrated in a microfluidic device. in *2011 IEEE 24th International Conference on Micro Electro Mechanical Systems* 1333–1336 (2011)..

265. Rauf, S., Zhang, L., Ali, A., Liu, Y. & Li, J. Label-Free Nanopore Biosensor for Rapid and Highly Sensitive Cocaine Detection in Complex Biological Fluids. *ACS Sens.* **2**, 227–234 (2017).

266. Nobukawa, A., Osaki, T., Tonooka, T., Morimoto, Y. & Takeuchi, S. Electrical detection of pesticide vapors by biological nanopores with DNA aptamers. in *2015 28th IEEE International Conference on Micro Electro Mechanical Systems (MEMS)* 596–599 (2015).

267. Fujii, S., Misawa, N., Kamiya, K., Osaki, T. & Takeuchi, S. Breathable fabric meets a lipid bilayer system for rapid vapor detection. in *2018 IEEE Micro Electro Mechanical Systems (MEMS)* 276–277 (2018).

268. Fujii, S., Nobukawa, A., Osaki, T., Morimoto, Y., Kamiya, K., Misawa, N. & Takeuchi, S. Pesticide vapor sensing using an aptamer, nanopore, and agarose gel on a chip. *Lab. Chip* **17**, 2421–2425 (2017).

269. Sze, J. Y. Y., Ivanov, A. P., Cass, A. E. G. & Edel, J. B. Single molecule multiplexed nanopore protein screening in human serum using aptamer modified DNA carriers. *Nat. Commun.* **8**, 1552 (2017).

270. Zhang, L., Zhang, K., Liu, G., Liu, M., Liu, Y. & Li, J. Label-Free Nanopore Proximity Bioassay for Platelet-Derived Growth Factor Detection. *Anal. Chem.* **87**, 5677–5682 (2015).

271. Bell, N. A. W. & Keyser, U. F. Specific Protein Detection Using Designed DNA Carriers and Nanopores. *J. Am. Chem. Soc.* **137**, 2035–2041 (2015).

272. Beamish, E., Tabard-Cossa, V. & Godin, M. Identifying Structure in Short DNA Scaffolds Using Solid-State Nanopores. *ACS Sens.* **2**, 1814–1820 (2017).

273. Kong, J., Zhu, J., Chen, K. & Keyser, U. F. Specific Biosensing Using DNA Aptamers and Nanopores. *Adv. Funct. Mater.* **29**, 1807555 (2018).

274. Park, J., Lim, M.-C., Ryu, H., Shim, J., Kim, S. M., Kim, Y.-R. & Jeon, T.-J. Nanopore based detection of Bacillus thuringiensis HD-73 spores using aptamers and versatile DNA hairpins. *Nanoscale* **10**, 11955–11961 (2018).

275. Platt, M., Willmott, G. R. & Lee, G. U. Resistive Pulse Sensing of Analyte-Induced Multicomponent Rod Aggregation Using Tunable Pores. *Small* **8**, 2436–2444 (2012).

276. Billinge, E. R. & Platt, M. Aptamer based dispersion assay using tunable resistive pulse sensing (TRPS). *Anal. Methods* **7**, 8534–8538 (2015).

277. Billinge, E. R. & Platt, M. Multiplexed, label-free detection of biomarkers using aptamers and Tunable Resistive Pulse Sensing (AptaTRPS). *Biosens. Bioelectron.* **68**, 741–748 (2015).

278. Xi, D., Li, Z., Liu, L., Ai, S. & Zhang, S. Ultrasensitive Detection of Cancer Cells Combining Enzymatic Signal Amplification with an Aerolysin Nanopore. *Anal. Chem.* **90**, 1029–1034 (2018).

279. Lin, X., P. Ivanov, A. & B. Edel, J. Selective single molecule nanopore sensing of proteins using DNA aptamer-functionalised gold nanoparticles. *Chem. Sci.* **8**, 3905–3912 (2017).

280. Alsager, O. A., Kumar, S., Willmott, G. R., McNatty, K. P. & Hodgkiss, J. M. Small molecule detection in solution via the size contraction response of aptamer functionalized nanoparticles. *Biosens. Bioelectron.* **57**, 262–268 (2014).

281. He, F., Liang, L., Zhou, S., Xie, W., He, S., Wang, Y., Tlili, C., Tong, S. & Wang, D. Label-Free Sensitive Detection of Microcystin-LR via Aptamer-Conjugated Gold Nanoparticles Based on Solid-State Nanopores. *Langmuir* **34**, 14825–14833 (2018).

282. Healey, M. J., Sivakumaran, M. & Platt, M. Rapid quantification of prion proteins using resistive pulse sensing. *Analyst* **145**, 2595–2601 (2020).

283. Tang, H., Wang, H., Yang, C., Zhao, D., Qian, Y. & Li, Y. Nanopore-based Strategy for Selective Detection of Single Carcinoembryonic Antigen (CEA) Molecules. *Anal. Chem.* **92**, 3042–3049 (2020).

284. Fang, Z., Liu, L., Wang, Y., Xi, D. & Zhang, S. Unambiguous Discrimination of Multiple Protein Biomarkers by Nanopore Sensing with Double-Stranded DNA-Based Probes. *Anal. Chem.* **92**, 1730–1737 (2020).

285. Jiang, Y., Liu, N., Guo, W., Xia, F. & Jiang, L. Highly-Efficient Gating of Solid-State Nanochannels by DNA Supersandwich Structure Containing ATP Aptamers: A Nanofluidic IMPLICATION Logic Device. *J. Am. Chem. Soc.* **134**, 15395–15401 (2012).

286. Jiang, Y., Feng, Y., Su, J., Nie, J., Cao, L., Mao, L., Jiang, L. & Guo, W. On the Origin of Ionic Rectification in DNA-Stuffed Nanopores: The Breaking and Retrieving Symmetry. *J. Am. Chem. Soc.* **139**, 18739–18746 (2017).

287. Acar, E. T., Buchsbaum, S. F., Combs, C., Fornasiero, F. & Siwy, Z. S. Biomimetic potassium-selective nanopores. *Sci. Adv.* **5**, eaav2568 (2019).

288. Abelow, A. E., Schepelina, O., White, R. J., Vallée-Bélisle, A., Plaxco, K. W. & Zharov, I. Biomimetic glass nanopores employing aptamer gates responsive to a small molecule. *Chem. Commun.* **46**, 7984–7986 (2010).

289. Li, P., Kong, X.-Y., Xie, G., Xiao, K., Zhang, Z., Wen, L. & Jiang, L. Adenosine-Activated Nanochannels Inspired by G-Protein-Coupled Receptors. *Small* **12**, 1854–1858 (2016).

290. Kawano, R. Synthetic Ion Channels and DNA Logic Gates as Components of Molecular Robots. *ChemPhysChem* **19**, 359–366 (2018).

291. Feng, J., Graf, M., Liu, K., Ovchinnikov, D., Dumcenco, D., Heiranian, M., Nandigana, V., Aluru, N. R., Kis, A. & Radenovic, A. Single-layer MoS 2 nanopores as nanopower generators. *Nature* **536**, 197–200 (2016).

292. Liu, G., Jin, W. & Xu, N. Two-Dimensional-Material Membranes: A New Family of High-Performance Separation Membranes. *Angew. Chem. Int. Ed.* **55**, 13384–13397 (2016).

293. Wang, L., Boutilier, M. S. H., Kidambi, P. R., Jang, D., Hadjiconstantinou, N. G. & Karnik, R. Fundamental transport mechanisms, fabrication and potential applications of nanoporous atomically thin membranes. *Nat. Nanotechnol.* **12**, 509–522 (2017).

294. Surwade, S. P., Smirnov, S. N., Vlassiouk, I. V., Unocic, R. R., Veith, G. M., Dai, S. & Mahurin, S. M. Water desalination using nanoporous single-layer graphene. *Nat. Nanotechnol.* **10**, 459–464 (2015).

295. Heiranian, M., Farimani, A. B. & Aluru, N. R. Water desalination with a single-layer MoS 2 nanopore. *Nat. Commun.* **6**, 8616 (2015).

296. Yang, Y., Yang, X., Liang, L., Gao, Y., Cheng, H., Li, X., Zou, M., Ma, R., Yuan, Q. & Duan, X. Large-area graphene-nanomesh/carbon-nanotube hybrid membranes for ionic and molecular nanofiltration. *Science* **364**, 1057–1062 (2019).

297. Dervin, S., Dionysiou, D. D. & Pillai, S. C. 2D nanostructures for water purification: graphene and beyond. *Nanoscale* **8**, 15115–15131 (2016).

298. Zhang, Z., Wen, L. & Jiang, L. Bioinspired smart asymmetric nanochannel membranes. *Chem. Soc. Rev.* **47**, 322–356 (2018).

299. Siwy, Z., Heins, E., Harrell, C. C., Kohli, P. & Martin, C. R. Conical-Nanotube Ion-Current Rectifiers: The Role of Surface Charge. *J. Am. Chem. Soc.* **126**, 10850–10851 (2004).

300. Wen, C., Zeng, S., Li, S., Zhang, Z. & Zhang, S.-L. On Rectification of Ionic Current in Nanopores. *Anal. Chem.* **91**, 14597–14604 (2019).

301. Cai, S.-L., Cao, S.-H., Zheng, Y.-B., Zhao, S., Yang, J.-L. & Li, Y.-Q. Surface charge modulated aptasensor in a single glass conical nanopore. *Biosens. Bioelectron.* **71**, 37–43 (2015).

302. Ali, M., Nasir, S. & Ensinger, W. Bioconjugation-induced ionic current rectification in aptamer-modified single cylindrical nanopores. *Chem. Commun.* **51**, 3454–3457 (2015).

303. Das, N., Ray, R., Ray, S. & Roychaudhuri, C. Intelligent Quantification of Picomolar Protein Concentration in Serum by Functionalized Nanopores. *IEEE Sens. J.* **18**, 10183–10191 (2018).

304. Zhao, X.-P., Zhou, Y., Zhang, Q.-W., Yang, D.-R., Wang, C. & Xia, X.-H. Nanochannel–Ion Channel Hybrid Device for Ultrasensitive Monitoring of Biomolecular Recognition Events. *Anal. Chem.* **91**, 1185–1193 (2019).

305. Zhang, S., Chai, H., Cheng, K., Song, L., Chen, W., Yu, L., Lu, Z., Liu, B. & Zhao, Y.-D. Ultrasensitive and regenerable nanopore sensing based on target induced aptamer dissociation. *Biosens. Bioelectron.* **152**, 112011 (2020).

306. Varga, M., Bérczes, Zs., Illés, L., Sáfrány, Gy., Bársony, I., Fürjes, P., Gyurcsányi, R. E. & Jágerszki, Gy. Fluidically and electrically integrated solid state nanopore arrays for biochemical sensing. in *2014 IEEE SENSORS* 870–872 (2014).

307. Gu, L.-Q., Ding, S. & Gao, C. Aptamer-encoded nanopore for ultrasensitive detection of bioterrorist agent ricin at single-molecule resolution. *2009 Annu. Int. Conf. IEEE Eng. Med. Biol. Soc.* 6699–6702 (2009).

308. Wang, J., Hou, J., Zhang, H., Tian, Y. & Jiang, L. Single Nanochannel-Aptamer-Based Biosensor for Ultrasensitive and Selective Cocaine Detection. *ACS Appl. Mater. Interfaces* **10**, 2033–2039 (2018).

309. Meyer, R., Giselbrecht, S., Rapp, B. E., Hirtz, M. & Niemeyer, C. M. Advances in DNA-directed immobilization. *Curr. Opin. Chem. Biol.* **18**, 8–15 (2014).

310. Yu, J., Zhang, L., Xu, X. & Liu, S. Quantitative Detection of Potassium Ions and Adenosine Triphosphate via a Nanochannel-Based Electrochemical Platform Coupled with G-Quadruplex Aptamers. *Anal. Chem.* **86**, 10741–10748 (2014).

311. Liu, N., Jiang, Y., Zhou, Y., Xia, F., Guo, W. & Jiang, L. Two-Way Nanopore Sensing of Sequence-Specific Oligonucleotides and Small-Molecule Targets in Complex Matrices Using Integrated DNA Supersandwich Structures. *Angew. Chem. Int. Ed.* **52**, 2007–2011 (2013).

312. Liu, N., Yang, Z., Lou, X., Wei, B., Zhang, J., Gao, P., Hou, R. & Xia, F. Nanopore-Based DNA-Probe Sequence-Evolution Method Unveiling Characteristics of Protein–DNA Binding Phenomena in a Nanoscale Confined Space. *Anal. Chem.* **87**, 4037–4041 (2015).

313. Rotem, D., Jayasinghe, L., Salichou, M. & Bayley, H. Protein Detection by Nanopores Equipped with Aptamers. *J. Am. Chem. Soc.* **134**, 2781–2787 (2012).

314. Soskine, M., Biesemans, A., Moeyaert, B., Cheley, S., Bayley, H. & Maglia, G. An Engineered ClyA Nanopore Detects Folded Target Proteins by Selective External Association and Pore Entry. *Nano Lett.* **12**, 4895–4900 (2012).

315. Hanif, S., Liu, H.-L., Ahmed, S. A., Yang, J.-M., Zhou, Y., Pang, J., Ji, L.-N., Xia, X.-H. & Wang, K. Nanopipette-Based SERS Aptasensor for Subcellular Localization of Cancer Biomarker in Single Cells. *Anal. Chem.* **89**, 9911–9917 (2017).

316. Davie, E. W. & Ratnoff, O. D. Waterfall Sequence for Intrinsic Blood Clotting. *Science* **145**, 1310–1312 (1964).

317. Macfarlane, R. G. An Enzyme Cascade in the Blood Clotting Mechanism, and its Function as a Biochemical Amplifier. *Nature* **202**, 498–499 (1964).

318. Negrier, C., Shima, M. & Hoffman, M. The central role of thrombin in bleeding disorders. *Blood Rev.* **38**, 100582 (2019).

319. Jaberi, N., Soleimani, A., Pashirzad, M., Abdeahad, H., Mohammadi, F., Khoshakhlagh, M., Khazaei, M., Ferns, G. A., Avan, A. & Hassanian, S. M. Role of thrombin in the pathogenesis of atherosclerosis. *J. Cell. Biochem.* **120**, 4757–4765 (2019).

320. Reddel, C. J., Tan, C. W. & Chen, V. M. Thrombin Generation and Cancer: Contributors and Consequences. *Cancers* **11**, 100 (2019).

321. Krenzlin, H., Lorenz, V. & Alessandri, B. The involvement of thrombin in the pathogenesis of glioblastoma. *J. Neurosci. Res.* **95**, 2080–2085 (2017).

322. Ebrahimi, S., Rahmani, F., Behnam-Rassouli, R., Hoseinkhani, F., Parizadeh, M. R., Keramati, M. R., Khazaie, M., Avan, A. & Hassanian, S. M. Proinflammatory signaling functions of thrombin in cancer. *J. Cell. Physiol.* **232**, 2323–2329 (2017).

323. Krishnaswamy, S. The Transition of Prothrombin to Thrombin. *J. Thromb. Haemost. JTH* **11**, 265–276 (2013).

324. Bock, L. C., Griffin, L. C., Latham, J. A., Vermaas, E. H. & Toole, J. J. Selection of single-stranded DNA molecules that bind and inhibit human thrombin. *Nature* **355**, 564–566 (1992).

325. Deng, B., Lin, Y., Wang, C., Li, F., Wang, Z., Zhang, H., Li, X.-F. & Le, X. C. Aptamer binding assays for proteins: The thrombin example—A review. *Anal. Chim. Acta* **837**, 1–15 (2014).

326. Avino, A., Fabrega, C., Tintore, M. & Eritja, R. Thrombin Binding Aptamer, More than a Simple Aptamer: Chemically Modified Derivatives and Biomedical Applications. *Curr. Pharm. Des.* **18**, 2036–2047 (2012).

327. Musumeci, D. & Montesarchio, D. Polyvalent nucleic acid aptamers and modulation of their activity: a focus on the thrombin binding aptamer. *Pharmacol. Ther.* **136**, 202–215 (2012).

328. Russo Krauss, I., Merlino, A., Giancola, C., Randazzo, A., Mazzarella, L. & Sica, F. Thrombin–aptamer recognition: a revealed ambiguity. *Nucleic Acids Res.* **39**, 7858–7867 (2011).

329. Schultze, P., Macaya, R. F. & Feigon, J. Three-dimensional solution structure of the thrombin-binding DNA aptamer d(GGTTGGTGTGGTTGG). *J. Mol. Biol.* **235**, 1532–1547 (1994).

330. PaborskyS, L. R. & McCurdy, S. N. The Single-stranded DNA Aptamer-binding Site of Human Thrombin. *J. Biol. Chem.* **268**, 20808–20811 (1993).

331. Gosai, A., Hau Yeah, B. S., Nilsen-Hamilton, M. & Shrotriya, P. Label free thrombin detection in presence of high concentration of albumin using an aptamer-functionalized nanoporous membrane. *Biosens. Bioelectron.* **126**, 88–95 (2019).

2

Nanopore Fabrication

Synopsis

In this chapter, we will briefly review the principal techniques used for solid-state nanopore fabrication. Being fully independent for the fabrication of nanopores is an interesting promise for further studies in our group. Therefore, a process flow for cleanroom fabrication of single nanopore chips at wafer scale has been developed and will be discussed in this chapter. Then, the fabrication of nanopores on commercial silicon nitride membranes with a transmission electron microscope will be described.

Table of Contents

2.1 State of the Art: Solid-State Nanopore Fabrication

Solid-state nanopores offer a good stability over time, tunable dimensions and geometries and can be integrated into microfluidic devices for added functionality[1,2]. A nanopore device usually consists in a pore (~5-30 nm diameter) fabricated in a suspended thin dielectric membrane (from a few nanometers to ~100 nm thick). The membrane is typically supported by a rigid substrate and is either made from polymeric or inorganic materials. Commonly used polymers are polyethylene terephthalate (PET), polycarbonate and polyimide[3]. Typical inorganic membrane materials are silicon nitride (SiN_x)[4], silicon dioxide[5], aluminum oxide[6,7], boron nitride[8,9] or graphene[10–12]. Pulled glass nanopipettes are also an increasingly popular type of solid-state nanopores[13–16]. Silicon substrate nanopore technology has been broadly used in the nanopore research community thanks to the already standardized semiconductor fabrication technologies in cleanrooms and the possibility to develop a massive production of devices on wafers[1,11,17–19]. Advances in nanopore fabrication development are made every year on various kinds of substrates[1,17,20]. Low stress SiN_x is one of the most popular materials for a dielectric membrane thanks to its advantageous properties[17] such as a high resistivity (in the order of 10^{16} Ω/cm)[21], a good thermal stability and mechanical robustness, and it is chemically inert over a wide range of electrolyte conditions[3,17,22] (pH, temperature, etc.).

Fabrication of nanopores in polymeric membranes is usually carried out with the ion track etching method[3,23–25]. The membrane is irradiated by heavy ions (Xe, Au, or Pb), which go through the membrane and locally damage it. Then, a chemical wet etching attack those weak zones, revealing the nanopores. Tuning the wet etching solution allows a control over the geometry and size of the nanopores. The first SiN_x solid-state nanopore has been fabricated by Li *et al.* in 2001 with the technique of focused ion beam (FIB)[26] (Figure 2.1 A). To do so, a first etching was made with reactive ion etching (RIE) to form a bowl-shaped cavity into the backside of the SiN_x membrane. Then, a focused Ar^+ ion beam was used to sputter the membrane on the other side until a nanopore was formed. They showed that the ion beam can be used to later reduce the pore diameter. Nanopores with a diameter down to 1.8 nm could be formed. Since then, FIB fabricated nanopores have been popular in the nanopore research field. Pores have been fabricated with FIB into various materials such as SiO_2, Cr or Al[27] by using a variety of ions[28] such as Ga^+, Ar^+, Ne^+, Kr^+ or Xe^+. The most commonly used ions are Ga^+. However, those ions can alter pore surface charge[3]. Moreover, it has been proven difficult to fabricate nanopores with a diameter below 20 nm without ultrathin membranes due to the scattering effects of incoming ions and redeposition of sputtered material[29,30]. An alternative is the use of He^+ ions beams because the low mass of the ion diminishes those scattering effects and enhance pore size resolution[31,32]. Nevertheless, another technique is commonly used for ~10 nm diameter nanopores and below: the Transmission Electron Microscope (TEM). It is the technique used in this thesis work

for the fabrication of nanopores for single-event translocation experiments. Storm *et al*. have first demonstrated the convenience to use a TEM in 2003[18] (Figure 2.1 B). They fabricated nanopores with a diameter below 10 nm in a 10 nm thick SiO_2 membrane with a high intensity electron beam. Moreover, they demonstrated that with a wide field of electrons at a lower intensity, the nanopore could shrink or increase its diameter depending on its initial dimensions. If the initial pore diameter were smaller than the membrane thickness, then it would shrink. This phenomenon is thought to be caused by the partial melting of membrane material and its local fluidization. One of the main advantages of TEM drilling is the immediate visual feedback over nanopore fabrication. It has been widely used for nanopore fabrication and extended to other membrane materials such as aluminum oxide[6], graphene[10] and SiN_x[33].

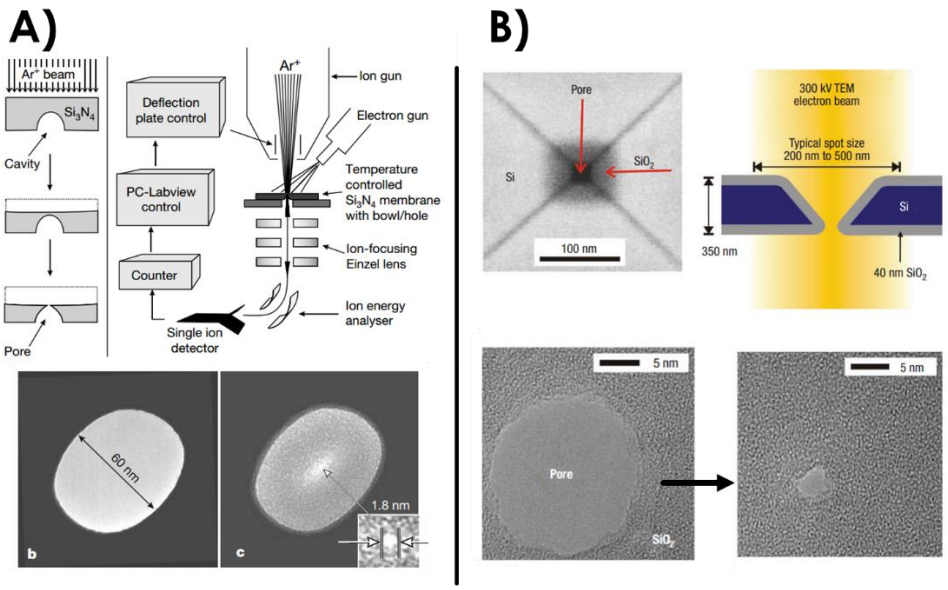

Figure 2.1: A) Nanopore fabrication technique using FIB first presented by Li *et al.*[26] Ion beam irradiation causes nanopore shrinking. B) Top view and cross section of the nanopore device by Storm et al.[18], electron irradiation in TEM causes nanopore shrinking.

Another recent and increasingly popular technique for nanopore fabrication is controlled dielectric breakdown[19,34,35]. With this technique, it is possible to fabricate a nanopore in a SiN_x membrane (5 nm to 30 nm thick) directly in an electrolyte by the simple application of a constant potential difference. This potential difference induces an electric field in the range of 0.5-1 V/nm[34] and a leakage current is observed in response to this high electric field. It has been hypothesized that ions contained in the electrolyte transfer charges through the dielectric membranes with trap-assisted tunneling[19]. Accumulation of these charges form structural defects and a localized conductive path with a sudden current increase, indicating that a nanopore has been formed. The applied voltage is stopped directly after sensing this current increase thanks to a feedback control loop. It is possible to tune the threshold

current triggering the end of the applied voltage and then finely control the size of the resulting nanopore. Since the wetting procedure is sometimes a difficult step in nanopore experiments, this technique presents the advantage to fabricate a nanopore directly in aqueous conditions. It also gives the possibility to fabricate a nanopore directly into an embedded fluidic device[35]. There are several other ways to fabricate nanopores[1,20,36], such as the fishing technique[37] or the superposition of two perpendicular capillaries[38]. In this chapter, we will later present another technique using electron beam lithography and RIE for the fabrication of wafer-scale nanopores devices (See section 2.2).

An alternative type of solid-state device is metallic oxide nanopores. They are obtained by atomic layer deposition (ALD) of a metallic material over a fabricated nanopore made with the previous techniques[39–43]. The deposited materials are HfO_2, ZnO, TiO_2 or Al_2O_3. They present interesting electrical and mechanical properties. For example, Al_2O_3 nanopores exhibit a better signal-to-noise ratio, and translocated molecules are more easily detected[6,44]. DNA, a negatively charged molecule, interacts with the positively charged Al_2O_3 and translocates for a longer time in the nanopore.

2.2 Cleanroom Process Flow for the Fabrication of Nanopores

Being able to work on entirely homemade nanopore chips with customizable size and geometry is an interesting promise for further studies in the laboratory. Apart from the TEM drilled nanopores on commercial membranes that were used for this study and that will be described in section 2.3, we developed a cleanroom fabrication process that will enable an independent nanopore chip production. This allows a precise tuning of nanopore's dimensions and the fabrication of multiple chips at the same time. This section will detail all the main steps for the nanopore chip cleanroom fabrication. It is important to notice that we did not use nanopore chips from this process flow for experiments and that further development will be needed on those chips.

2.2.1 Requirement Specifications for the Fabrication of Nanopore Chips

Semiconductor processing techniques allow the rapid and controlled fabrication of hundreds of chips per wafer. The development of such a process for nanopore chips is possible thanks to a facilitating environment and access to a research-oriented cleanroom, the Upstream Technological Platform (PTA)[45,46]. We use as a first material 200 mm silicon wafers (crystal orientation <100>) that are 725 µm thick with either 50 nm or 100 nm SiN_x deposited on both sides. Then, we cut two 100 mm silicon wafers out of it for a compatibility with the PTA equipment (Figure 2.2). We work on those 100 mm wafers in order to fabricate around 100 nanopore chips at a time. The objective for each nanopore chip is to open the bulk silicon from one side to release the thin SiN_x membrane, and to drill the nanopore in that membrane from the other side (Figure 2.2). The main challenge is to align those apertures from both sides and make sure that the nanopore will be fabricated in the released membrane. The main steps for this fabrication are going to be described in the next subsections.

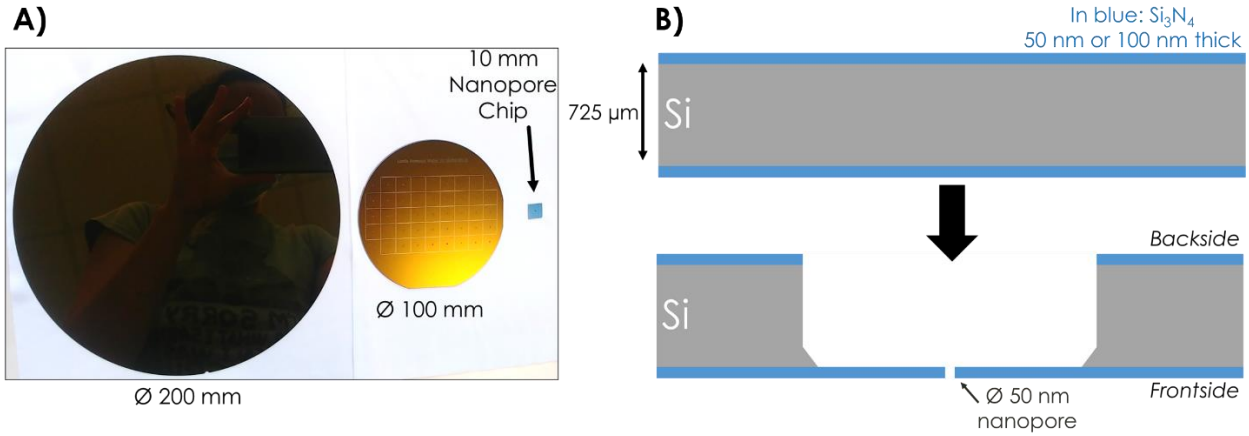

Figure 2.2: A) From a 200 mm diameter wafer to 10 mm square nanopore chip. B) Cross section view of the starting silicon material to the fabricated nanopore chip. For simplification purposes, the schemes are not to scale.

2.2.2 Laser Pre-Opening of Membranes

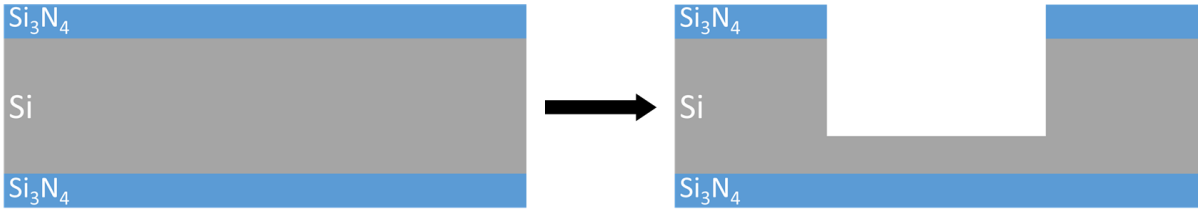

Figure 2.3: Scheme illustrating the membrane "pre-opening" step with a laser. For simplification purposes, the schemes are not to scale.

The 200 mm diameter silicon substrates that we use for the development of the microfabrication process either have a 50 nm or 100 nm silicon nitride (SiN_x or Si_3N_4 on the schemes) layer that is later used as the freestanding membrane. The 50 nm layer has been deposited with a Low Pressure Chemical Vapor Deposition (LPCVD) process[47]. LPCVD is performed at 800 °C for 20 minutes and 30 seconds using ammonia (NH_3) and dichlorosilane (SiH_2Cl_2) gazes. The following chemical reaction occurs at the surface of the silicon wafer:

$$3SiH_2Cl_{2(g)} + 4NH_{3(g)} \rightarrow Si_3N_{4(s)} + 6H_{2(g)} + 6HCl_{(g)}$$

The deposited film is a 50 nm SiN_x layer with a tensile stress of 300 MPa. The 200 mm diameter wafer with 725 µm thick bulk silicon and 50 nm Si_3N_4 layer is then cut down to 100 mm diameter with a laser (Tau Tech, Cielle, Italy[48]). The aim is to be compatible with the cleanroom equipment that are used later. This cutting step has two other purposes in the process flow: the removal of most of the silicon where the future membranes windows will be placed (membrane "pre-opening") and the placement of alignment marks on the backside. Those marks are used later to make sure that the nanopore fabrication on the frontside will be placed in the center of the membrane opened from the backside (Figure 2.2). Concerning the membranes pre-opening (Figure 2.3), squares ranging from 100 µm x 100 µm to 550 µm x 550 µm have been engraved in the silicon bulk with a 625 µm depth. It will allow target membranes ranging from 50 µm x 50 µm to 500 µm x 500 µm (cf. subsection 2.2.5 for more details on the freestanding membrane release). The designs given on Figure 2.4 are further detailed in Appendix V.

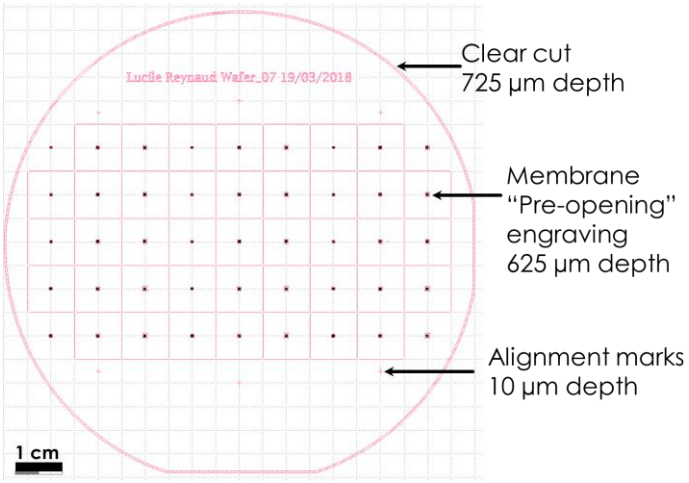

Figure 2.4: Klayout[49] software screenshot of the wafer design for laser cutting and engraving. The different actions are: cutting down a 200 mm wafer into 100 mm diameter wafer, engraving of membranes "pre-openings" and marking of alignment pattern, wafer information and 1 cm square chips delimitation.

2.2.3 Gold Marks Deposition

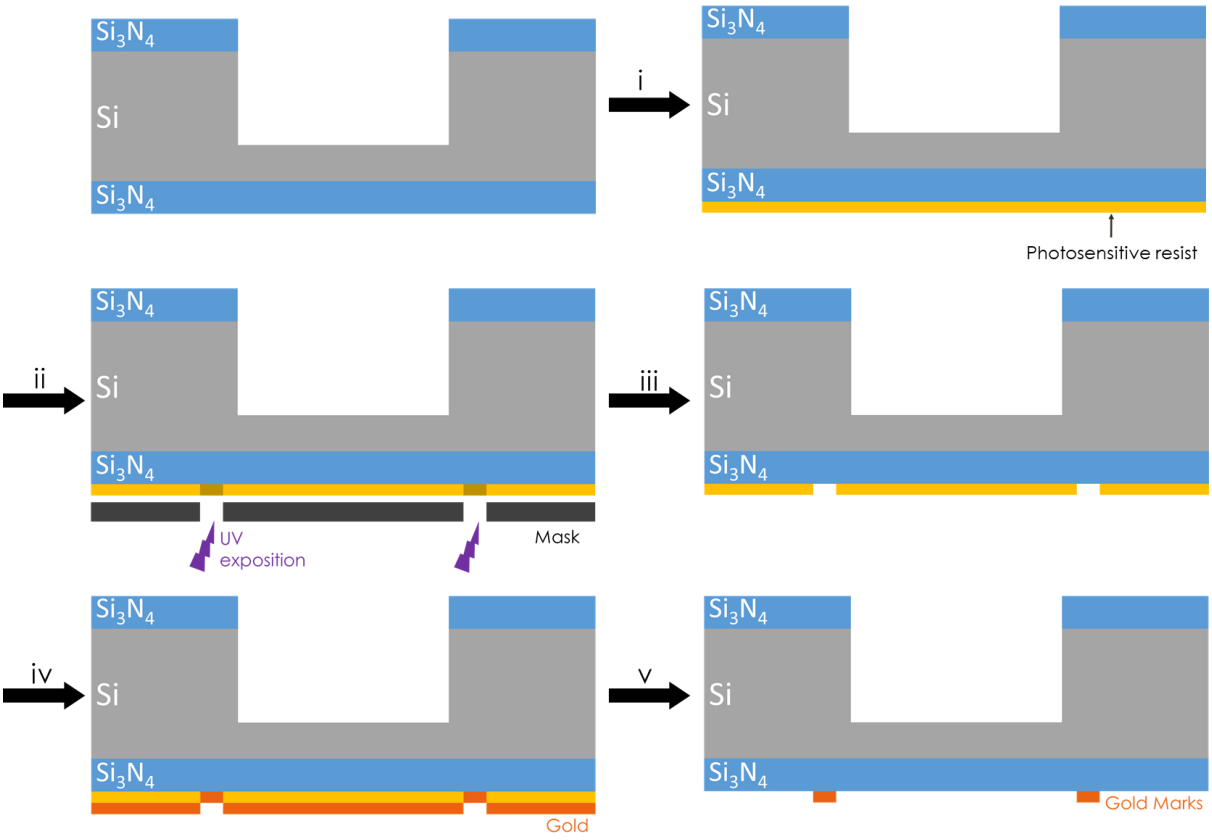

Figure 2.5: Illustration of the microfabrication steps for the frontside and backside alignments of patterns and deposition of gold marks for further guiding of nanopore fabrication: (i) Photosensitive resist deposition (ii) backside and frontside alignments with a mask for exposition of the resist in place of the future gold marks (iii) resist development (iv) gold layer deposition (v) resist removal, only the desired aligned gold marks remain. For simplification purpose, the schemes are not to scale.

Deposition of gold marks is necessary for the alignment of the nanopore in the membrane. Therefore, they must be positioned on the frontside of the wafer in alignment with the backside windows pattern obtained in the previous part (Figure 2.5). To do so, we perform photolithography with a custom chrome photomask made with the equipment Laser µPG 101 (Heidelberg Instruments, Germany). The mask displays the pattern for frontside and backside alignments (Figure 2.6) as well as the pattern for gold marks deposition.

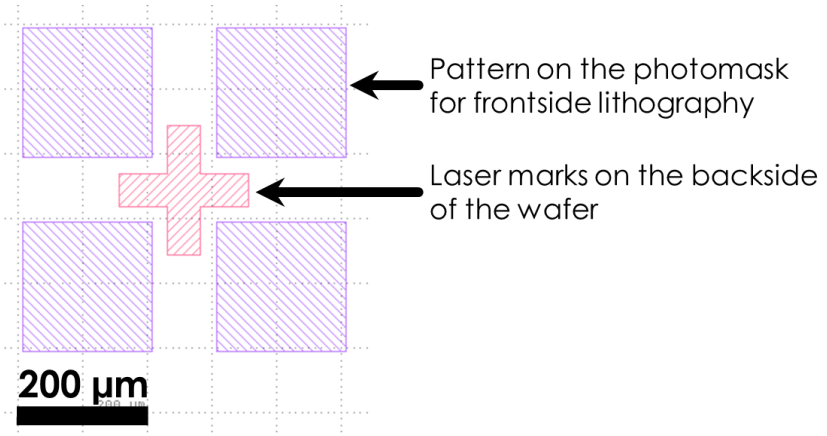

Figure 2.6: Design of the pattern for frontside and backside alignments: cross marks on the backside of the wafer and squares on the frontside mask for the photolithography.

The photolithography process is as follows. AZ1512HS photosensitive positive resist is spin-coated on the frontside of the wafer (step i). Then, the wafer and the photomask with the desired pattern are inserted in the mask aligner MA8 (Suss MicroTec, Germany) to perform alignment with micrometric precision. The resist is insolated with ultraviolet (UV) light through the mask (step ii). Then, the resist is developed into a bath of AZ Developer diluted at 50 % with deionized water for two minutes in order to lift off the pattern (step iii).

The next step consists in the deposition of a thin gold layer to form the desired marks on the SiN_x where the resist has been removed (step iv). To do so, we use the MEB550 (Plassys, France) metal evaporator that uses an intense electron beam to vaporize metal under high vacuum and permits a controlled deposition of thin layers on the substrate. A 10 nm adhesive layer of titanium is first deposited on the SiN_x, followed by a 50 nm layer of gold. Then, the resist is totally removed from the wafer thanks to a 10 min acetone bath, followed by a 10 min isopropanol bath and a 10 min distilled water bath (step v). The only remaining things are the desired gold marks that permit the nanopore fabrication (cf. subsection 2.2.4).

2.2.4 Nanopore Opening

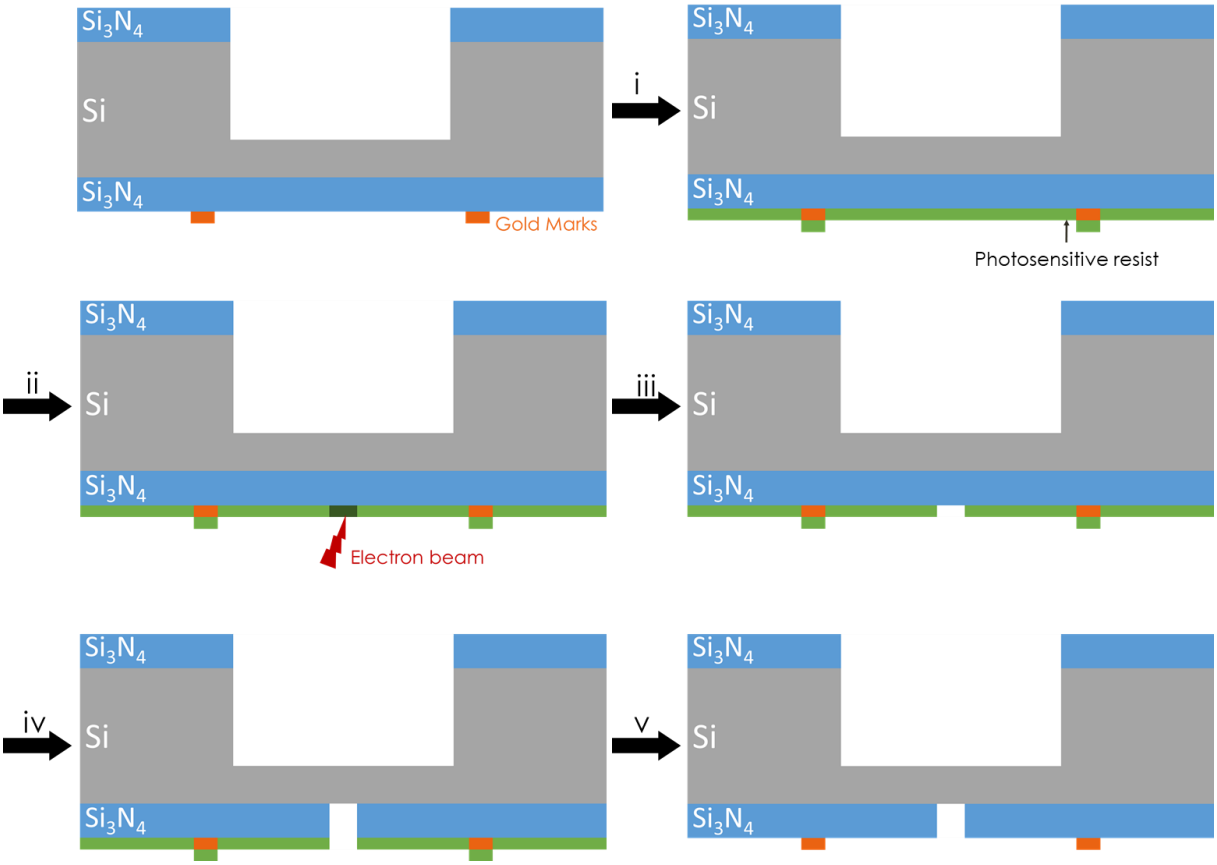

Figure 2.7: Scheme of the different microfabrication steps for nanopore etching: (i) photosensitive resist deposition (ii) electron beam insulation of the resist following nanopore patterning (iii) resist development (iv) etching of the SiN_x to form nanopores (v) removal of the resist. For simplification purpose, the schemes are not to scale.

With the gold marks, a specific lithography with nanometric precision can be performed to form a nanopore where the future membrane will be (Figure 2.7). A ZEP520A photosensitive resist is spin-coated on the frontside of the wafer (step i). Then, it is inserted in the electron beam lithography equipment 6300FS (JEOL, Japan) that enables a precise insolation of the resist with a 10 nm resolution (step ii). The beam is precisely positioned thanks to the optically retrieved gold marks and a .GDS format file (KLayout software) containing all the coordinates of the nanopores. Afterward, the resist is developed in a solution of methyl isobutyl ketone (MIBK) and isopropanol (IPA) in order to remove the insolated resist (step iii).

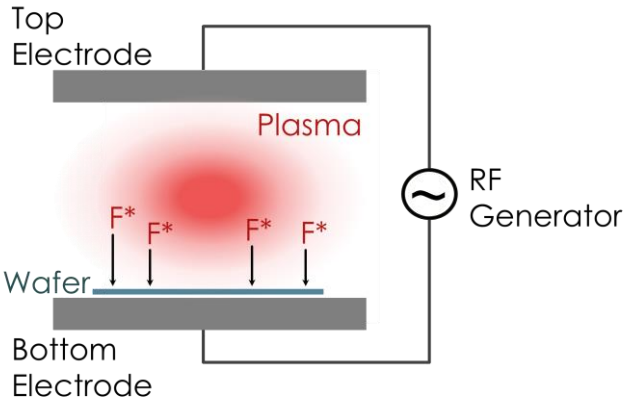

Figure 2.8: Scheme of RIE process inside the vacuum chamber (adapted from reference[47]).

The next step consists in the selective etching of SiN_x to form the nanopores (step iv). The previous lithographic step allows the covering of the whole nitride with a protective resist mask with the nanopore pattern. The exposed SiN_x is removed thanks to RIE, a plasma etching technique that combines a chemical reaction (reactive ionized gas) and a physical phenomenon (directional ion bombardment)[47,50]. The chemical process is isotropic (no specific direction) while the physical process is anisotropic (specific direction). Therefore, the balance between those two phenomena must be tuned in order to form a nanopore with straight walls. The substrate is placed inside a vacuum chamber with electrodes at the top and the bottom (Figure 2.8). Sulfur hexafluoride (SF_6), a fluorine gas highly reactive with silicon is introduced in the vacuum chamber. Plasma is generated by applying an oscillating electric field RF (Radio Frequency, 13.56 MHz). Upon impacts with electrons within the plasma, SF_6 gas is converted into excited reactive species via the following reaction:

$$e^- + SF_6 \rightarrow e^- + SF_5^* + F^*$$

Exposed SiN_x is etched by the excited fluorine F* with the following equation[47]:

$$Si_3N_{4(s)} + 24\,F^*_{(g)} \rightarrow 3\,SiF_{4(g)} + 4\,NF_{3(g)}$$

RIE is performed in the equipment PLASMALAB100 (Oxford, United Kingdom) at a 20 mTorr pression, with a SF_6 flow rate of 50 sccm (standard cubic centimeters per minute) and a power of 50 W for 2 minutes and 50 seconds. In these conditions the SiN_x etch rate is 40 nm/min. We decided for this preliminary work to etch for a longer time to be sure that the 100 nm layer is etched all the way through. After the RIE step, the wafer is immersed into a bath of resist remover (AR 300 76) at 50 °C for 20 minutes and in a final bath of distilled water for 5 minutes (step v). From this point, the wafer can either be characterized with microscopy (cf. subsection 2.2.6) or go through the final microfabrication step (cf. subsection 2.2.5).

2.2.5 KOH Wet Etching for Opening the Membranes

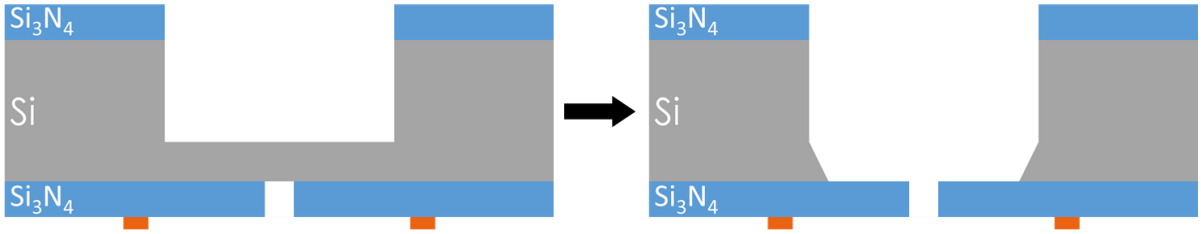

Figure 2.9: Scheme of the final step of nanopore chip fabrication: KOH wet etching for the release of SiN_x membranes. For simplification purpose, the schemes are not to scale.

The final step of our cleanroom fabrication process consists in the release of the freestanding SiN_x membranes thanks to a potassium hydroxide (KOH) wet etch (Figure 2.9). It has been developed on wafers right after the laser engraving step (subsection 2.2.2) but not on wafers with the nanopore opening on the other side. Due to a change in the nanopore fabrication strategy for this thesis (from a cleanroom process flow to a TEM fabrication with commercial membranes), we did not perform this wet etch on chips with the opened nanopore in the SiN_x layer (Figure 2.10). To do the wet etching, the wafer is immersed for two hours and a half in a solution at 85 °C of KOH diluted at 15 % v/v in distilled water. The SiN_x acts as a protective layer and the silicon accessible in the "pre-opened" membranes is etched via the following chemical reaction[51]:

$$Si_{(s)} + 2OH^-_{(l)} + 2H_2O_{(l)} \rightarrow SiO_2(OH)^{2-}_{2\ (l)} + 2H_{2(g)}$$

KOH wet etching is anisotropic along the <111> crystal plane for a <100> silicon surface. The angle of the etching slope is θ = arctan$\sqrt{2}$ = 54.74 ° (Figure 2.10). This allows calculating the size of the freestanding SiN_x membrane (Width 1) as a function of the size of the pre-opening window (Width 2) made with the laser (cf. subsection 2.2.2) and the remaining height of SiN_x h (= 100 µm for our application). For silicon membranes, which Width 1 ranges from 50 µm to 500 µm, the silicon bulk is pre-opened as squares with Width 2 ranging from 100 µm to 550 µm.

$$Width1 = Width2 + \frac{2h}{\tan\theta}$$
$$with \quad \theta = \arctan\sqrt{2}$$

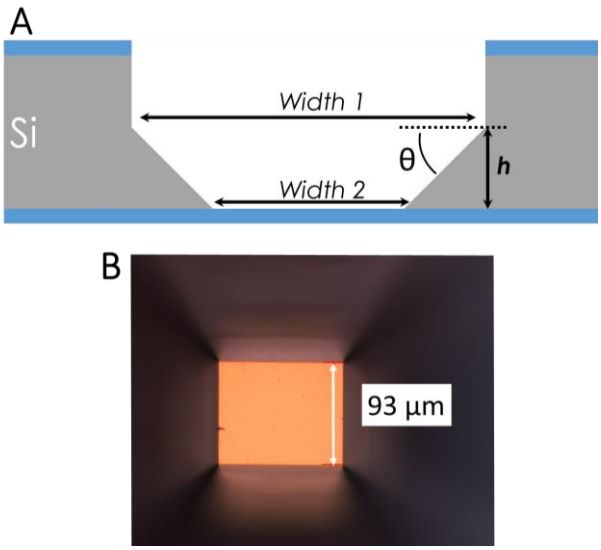

Figure 2.10: A) KOH wet etching geometrical schematic on a <100> oriented silicon substrate coated with SiN_x for the release of freestanding membranes. For simplification purpose, the schemes are not to scale. B) Optical microscopy imaging of a released SiN_x membrane.

2.2.6 Microscopic Characterization of Fabricated Nanopores

Microscopy is used to characterize the membranes and the nanopores at both the micrometer and nanometer scale. Optical microscopy (Microscope DM2500, camera DFC 425, Leica, Germany) is generally used for inspecting the cleanliness of the samples and check the laser pattern on the backside. The nanopores are observed thanks to a ZEISS ULTRA 55 (Zeiss, Germany) Scanning Electron Microscope (SEM). The SEM scans the surface of the sample with a focused electron beam and produces a high-resolution image down to the nanometer[52]. Nanopores are observed after the RIE and before KOH wet etching because freestanding SiN_x membrane charge under the electron beam and the observation is easier with bulk silicon behind. The nanopores are imaged in the SEM with a magnification ranging from 50 000 x to 200 000 x. The images are taken with an Electron High Tension (EHT) of 5 kV and a working distance (WD) of 5 mm. With the software SmartSEM (Zeiss, Germany), it is possible to instantly characterize the size of the nanopores. They are also characterized afterward thanks to the ImageJ software (National Institutes of Health, United States of America).

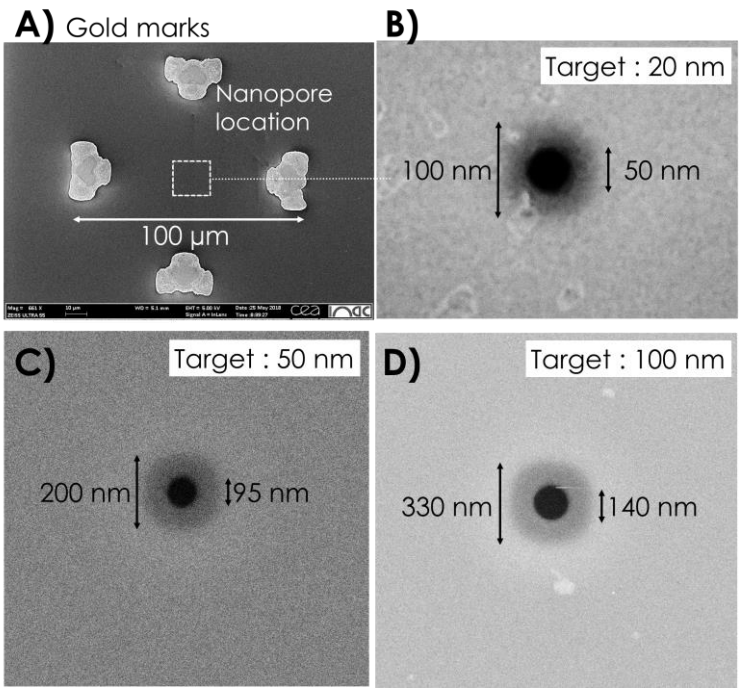

Figure 2.11: SEM images of nanopores on silicon bulk formed by RIE in a 100 nm SiN_x membrane. A) Gold marks deposited on the membrane for the optical retrieval of the nanopore. B) 20 nm target nanopore. C) 50 nm target nanopore. D) 100 nm target nanopore. We can observe a typical RIE conical shape with a bigger upper aperture. For this preliminary work, the nanopores where over-etched during RIE to be sure that the membrane would be drilled all the way through.

On Figure 2.11 are displayed nanopores etched by RIE in a 100 nm SiN_x membrane. The target diameter sizes for the nanopores are 20 nm, 50 nm and 100 nm. For this preliminary work, we over etched the SiN_x during RIE to ensure that the layer is engraved all the way through. Therefore, the resulting nanopores exhibit a larger size than originally designed. Moreover, we can observe a conical shape of the nanopore with a larger diameter at the top. This is a typical RIE profile[47] resulting from the combination of an isotropic chemical reaction and an anisotropic physical phenomenon (cf. subsection 2.2.4). Further developments of this nanopore fabrication process could benefit from the tuning of the RIE parameters in order to obtain straight walls. For example, tetrafluroromethane (CF_4) could be used as the chemical in the plasma chamber instead of sulfur hexafluoride (SF_6). It has already been used to fabricate nanopores with straight walls[53]. This chemical etches Si_3N_4 at a slower pace, allowing the physical anisotropic phenomenon to play a more important role and thus have straight walls. Another improvement could be the use of Deep RIE technique and Bosch process[54] that enables high-rate etching of deep and narrow structures.

2.2.7 Prospect: a PDMS Flow-Cell for Nanopore Experiments

The process flow for wafer-scale nanopore chip fabrication has been described previously, but a final step for nanopore experiments is still yet to be conceived: the flow-cell. In this section, I will suggest a design for encapsulating the nanopore chip between two fluidic channels.

Polydimethylsiloxane (PDMS) is a popular material for microfluidics thanks to its ease of fabrication, low cost, oxygen permeability and optical transparency[55–57]. PDMS microfluidic chips can be fabricated thanks to a master mold with the channel pattern obtained from photolithography on a silicon-based wafer[58]. PDMS is poured onto the mold, reticulated and released. The inlets for electrode insertion and fluidic connection can be perforated with a needle which diameter corresponds to the available tubing. For further works involving the nanopore chip previously described, I suggest a design inspired from the work of Roman *et al.*[59] in which the chip is enclosed between two PDMS layers, each containing a channel (typical dimensions of such channels are between 500 µm and 1 mm). The concepts for those designs are illustrated on Figure 2.12. Each channel is in contact with the nanopore chip on one of its sides and connected to a fluidic inlet and outlets. I recommend that the inlets and outlets are disposed on the same side for an easier insertion of the chip between the PDMS layers. All dimensions will need to be tuned and mounting steps will need to be defined for an optimal utilization.

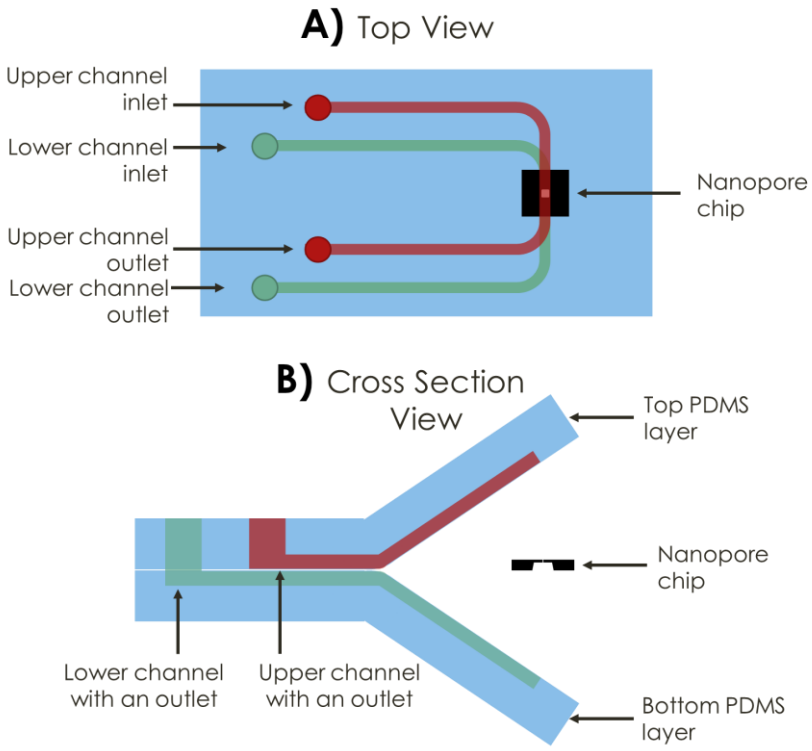

Figure 2.12: Illustration of a possible PDMS flow-cell for nanopore experiments with the previously described nanopore chip. The designs are inspired from reference[59]. A) Top view of the proposed set-up. B) Cross section view of the set-up before enclosing the chip between the two layers.

2.3 TEM Fabrication of Nanopores on Commercial Membranes

Using a TEM for drilling ~10 nm nanopores in freestanding SiN_x membrane is a popular approach[18]. The opportunity to use this technique on commercial membranes occurred while we were developing the cleanroom process flow described previously. This allowed us to quickly move on nanopore experiments and that is the reason why the development of cleanroom fabricated nanopore chips has been set aside. In this section, we will describe how we used this equipment to drill our nanopore chips for translocation experiments.

The chosen membrane is a commercial 20 nm thick freestanding SiN_x membrane on 200 µm thick silicon support (see section 3.1 of Chapter 3 for more detailed information). Prior to insertion in the TEM, an oxygen plasma cleaning of the chip is made in order to remove hydrocarbon contamination (Gatan Solarus 950, Ametek, United States of America). The equipment used is a TEM Tecnai Osiris (FEI, United States of America) in the PFNC facilities (PlateForme Nano Caractérisation[60]). All alignment adjustments and corrections of the beam's stigmatism are made prior to insertion of the sample. After that, the sample is inserted in the TEM. The 15 µm x 15 µm SiN_x window is detected with the lower magnification available (SA magnification mode). Then, we must wait for approximately 40 minutes for a complete stabilization of the set-up that we can optically monitor by observation of the membrane surface drift. With this equipment, we found that the most suitable parameters for nanopore drilling are an accelerating voltage of 200 kV, a 70 µm condenser lens and a spot size 5 with a 410 000 x magnification. The resulting current is usually around 1.75 nA.

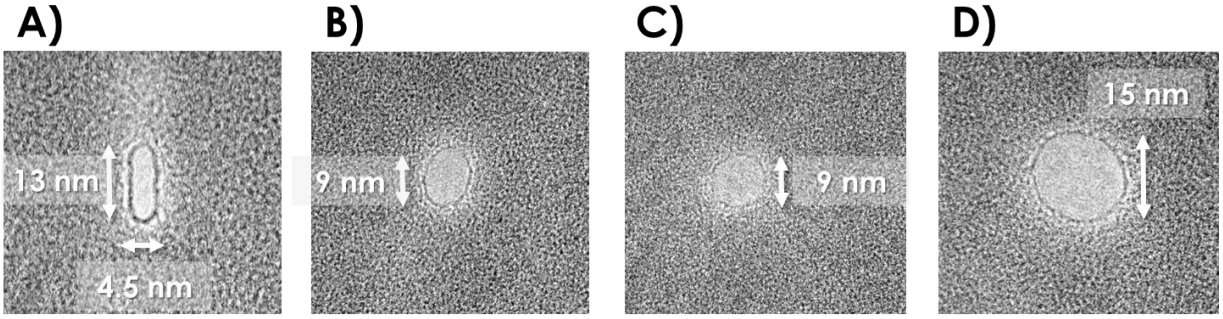

Figure 2.13: Testing out different parameters in order to reach a 15 nm diameter nanopore. A) 13 nm x 4.5 nm pore. The electron beam was focused for 1 minute but the membrane was not yet stable, therefore we could observe the beam drift over the membrane. B) 9 nm diameter pore with 2 minutes 15 seconds of focus. C) 9 nm diammeter pore with 3 minutes 15 seconds of focus. D) 15 nm diameter pore with 2 minutes 20 seconds of focus but the beam is slightly less concentrated. All measures are performed with the software ImageJ.

A desired nanopore size for the project was 15 nm. In order to reach a precise sizing of nanopores with the TEM, the following parameters need to be tuned: the focus duration and intensity of the electron beam. In this work, electron beam intensity ranged between 930 $e^-/Å^2s$ and 2560 $e^-/Å^2s$. On Figure 2.13 A), we can observe the beam drifting during focus that occurs when the set-up has not yet been stabilized. We indeed need to wait 30 to 40 minutes with our equipment after inserting the chip in the chamber for a perfect mechanical stabilization of the membrane, of the electronic components and the electron beam. On Figure 2.13 B and C, we focused finely the beam for respectively 2 minutes 15 seconds and 3 minutes 15 seconds. The obtained nanopores are of the same size. This indicates that the maximum nanopore size for a fine focus of electrons is reached before 2 minutes with our equipment. Therefore, to obtain a large pore, it was necessary to drill the membrane for 2 minutes and 20 seconds but with a less condensed focus (blurrier). Thus, we could fabricate a perfectly sized nanopore of 15 nm for our experiments. The average time required for each nanopore chip to be drilled is one hour, comprising the plasma cleaning of the chip prior to its insertion in the TEM and the stabilization before drilling.

Microfabrication techniques in a cleanroom possess the advantages to offer a wafer-scale production of nanopore chips with highly tunable geometrical properties. However, the development process of all steps is long. Using a TEM to drill nanopores in commercial silicon nitride membranes is fast, with only one step procedure, and provides a direct visual feedback on the fabricated nanopore. However, only one nanopore is fabricated at a time. Regarding those options, the TEM drilling on commercial membrane technique has been selected to provide us with the nanopore chips for experiments of biomolecule translocations.

2.4 References

1. Lee, K., Park, K.-B., Kim, H.-J., Yu, J.-S., Chae, H., Kim, H.-M. & Kim, K.-B. Recent Progress in Solid-State Nanopores. *Adv. Mater.* **30**, 1704680 (2018).
2. Zhang, Y. & Reisner, W. Fabrication and characterization of nanopore-interfaced nanochannel devices. *Nanotechnology* **26**, 455301 (2015).
3. Gibb, T. & Ayub, M. Chapter 5 - Solid-State Nanopore Fabrication. in *Engineered Nanopores for Bioanalytical Applications* 121–140 (William Andrew Publishing, 2013).
4. Li, J., Gershow, M., Stein, D., Brandin, E. & Golovchenko, J. A. DNA molecules and configurations in a solid-state nanopore microscope. *Nat. Mater.* **2**, 611–615 (2003).
5. Storm, A. J., Chen, J. H., Zandbergen, H. W. & Dekker, C. Translocation of double-strand DNA through a silicon oxide nanopore. *Phys. Rev. E* **71**, 051903 (2005).
6. Venkatesan, B. M., Shah, A. B., Zuo, J.-M. & Bashir, R. DNA Sensing Using Nanocrystalline Surface-Enhanced Al2O3 Nanopore Sensors. *Adv. Funct. Mater.* **20**, 1266–1275 (2010).
7. Venkatesan, B. M., Dorvel, B., Yemenicioglu, S., Watkins, N., Petrov, I. & Bashir, R. Highly Sensitive, Mechanically Stable Nanopore Sensors for DNA Analysis. *Adv. Mater. Deerfield Beach Fla* **21**, 2771–2776 (2009).
8. Zhou, Z., Hu, Y., Wang, H., Xu, Z., Wang, W., Bai, X., Shan, X. & Lu, X. DNA Translocation through Hydrophilic Nanopore in Hexagonal Boron Nitride. *Sci. Rep.* **3**, 3287 (2013).
9. Liu, S., Lu, B., Zhao, Q., Li, J., Gao, T., Chen, Y., Zhang, Y., Liu, Z., Fan, Z., Yang, F., You, L. & Yu, D. Boron Nitride Nanopores: Highly Sensitive DNA Single-Molecule Detectors. *Adv. Mater.* **25**, 4549–4554 (2013).
10. Fischbein, M. D. & Drndić, M. Electron beam nanosculpting of suspended graphene sheets. *Appl. Phys. Lett.* **93**, 113107 (2008).
11. Garaj, S., Hubbard, W., Reina, A., Kong, J., Branton, D. & Golovchenko, J. A. Graphene as a subnanometre trans-electrode membrane. *Nature* **467**, 190–193 (2010).

12. Jain, T., Rasera, B. C., Guerrero, R. J. S., Boutilier, M. S. H., O'Hern, S. C., Idrobo, J.-C. & Karnik, R. Heterogeneous sub-continuum ionic transport in statistically isolated graphene nanopores. *Nat. Nanotechnol.* **10**, 1053–1057 (2015).

13. Li, W., Bell, N. A. W., Hernández-Ainsa, S., Thacker, V. V., Thackray, A. M., Bujdoso, R. & Keyser, U. F. Single Protein Molecule Detection by Glass Nanopores. *ACS Nano* **7**, 4129–4134 (2013).

14. Steinbock, L. J., Krishnan, S., Bulushev, R. D., Borgeaud, S., Blokesch, M., Feletti, L. & Radenovic, A. Probing the size of proteins with glass nanopores. *Nanoscale* **6**, 14380–14387 (2014).

15. Actis, P., Mak, A. C. & Pourmand, N. Functionalized nanopipettes: toward label-free, single cell biosensors. *Bioanal. Rev.* **1**, 177–185 (2010).

16. Wang, Z., Liu, Y., Yu, L., Li, Y., Qian, G. & Chang, S. Nanopipettes: a potential tool for DNA detection. *Analyst* **144**, 5037–5047 (2019).

17. Dekker, C. Solid-state nanopores. *Nat. Nanotechnol.* **2**, 209–215 (2007).

18. Storm, A. J., Chen, J. H., Ling, X. S., Zandbergen, H. W. & Dekker, C. Fabrication of solid-state nanopores with single-nanometre precision. *Nat. Mater.* **2**, 537–540 (2003).

19. Kwok, H., Briggs, K. & Tabard-Cossa, V. Nanopore fabrication by controlled dielectric breakdown. *PloS One* **9**, e92880 (2014).

20. Yuan, Z., Wang, C., Yi, X., Ni, Z., Chen, Y. & Li, T. Solid-State Nanopore. *Nanoscale Res. Lett.* **13**, 56 (2018).

21. Gad-el-Hak, M. *MEMS: design and fabrication, The MEMS Handbook*. (CRC/Taylor & Francis, 2006).

22. Miles, B. N., Ivanov, A. P., Wilson, K. A., Doğan, F., Japrung, D. & Edel, J. B. Single molecule sensing with solid-state nanopores: novel materials, methods, and applications. *Chem. Soc. Rev.* **42**, 15–28 (2012).

23. Apel, P. Yu. Heavy particle tracks in polymers and polymeric track membranes. *Radiat. Meas.* **25**, 667–674 (1995).

24. Apel, P. Y., Korchev, Yu. E., Siwy, Z., Spohr, R. & Yoshida, M. Diode-like single-ion track membrane prepared by electro-stopping. *Nucl. Instrum. Methods Phys. Res. Sect. B Beam Interact. Mater. At.* **184**, 337–346 (2001).

25. Spohr, R. Status of ion track technology—Prospects of single tracks. *Radiat. Meas.* **40**, 191–202 (2005).

26. Li, J., Stein, D., McMullan, C., Branton, D., Aziz, M. J. & Golovchenko, J. A. Ion-beam sculpting at nanometre length scales. *Nature* **412**, 166–169 (2001).

27. Howorka, S. & Siwy, Z. Nanopore analytics: sensing of single molecules. *Chem. Soc. Rev.* **38**, 2360–2384 (2009).

28. Cai, Q., Ledden, B., Krueger, E., Golovchenko, J. A. & Li, J. Nanopore sculpting with noble gas ions. *J. Appl. Phys.* **100**, 024914-024914–6 (2006).

29. Schiedt, B., Auvray, L., Bacri, L., Oukhaled, G., Madouri, A., Bourhis, E., Patriarche, G., Pelta, J., Jede, R. & Gierak, J. Direct FIB fabrication and integration of “single nanopore devices” for the manipulation of macromolecules. *Microelectron. Eng.* **87**, 1300–1303 (2010).

30. MoberlyChan, W. J., Adams, D. P., Aziz, M. J., Hobler, G. & Schenkel, T. Fundamentals of Focused Ion Beam Nanostructural Processing: Below, At, and Above the Surface. *MRS Bull.* **32**, 424–432 (2007).

31. Yang, J., Ferranti, D. C., Stern, L. A., Sanford, C. A., Huang, J., Ren, Z., Qin, L.-C. & Hall, A. R. Rapid and precise scanning helium ion microscope milling of solid-state nanopores for biomolecule detection. *Nanotechnology* **22**, 285310 (2011).

32. Marshall, M. M., Yang, J. & Hall, A. R. Direct and Transmission Milling of Suspended Silicon Nitride Membranes With a Focused Helium Ion Beam. *Scanning* **34**, 101–106 (2012).

33. Kim, M. J., Wanunu, M., Bell, D. C. & Meller, A. Rapid Fabrication of Uniformly Sized Nanopores and Nanopore Arrays for Parallel DNA Analysis. *Adv. Mater.* **18**, 3149–3153 (2006).

34. Briggs, K., Kwok, H. & Tabard-Cossa, V. Automated Fabrication of 2-nm Solid-State Nanopores for Nucleic Acid Analysis. *Small* **10**, 2077–2086 (2014).

35. Tahvildari, R., Beamish, E., Tabard-Cossa, V. & Godin, M. Integrating nanopore sensors within microfluidic channel arrays using controlled breakdown. *Lab. Chip* **15**, 1407–1411 (2015).

36. Kudr, J., Skalickova, S., Nejdl, L., Moulick, A., Ruttkay–Nedecky, B., Adam, V. & Kizek, R. Fabrication of solid-state nanopores and its perspectives. *Electrophoresis* **36**, 2367–2379 (2015).

37. Choi, W., Jeon, E.-S., Chun, K.-Y., Kim, Y.-R., Park, K.-B., Kim, K.-B. & Han, C.-S. A low-noise silicon nitride nanopore device on a polymer substrate. *PLOS ONE* **13**, e0200831 (2018).

38. Arjmandi-Tash, H., Bellunato, A., Wen, C., Olsthoorn, R. C., Scheicher, R. H., Zhang, S.-L. & Schneider, G. F. Zero-Depth Interfacial Nanopore Capillaries. *Adv. Mater.* **30**, 1703602 (2018).

39. Chen, P., Mitsui, T., Farmer, D. B., Golovchenko, J., Gordon, R. G. & Branton, D. Atomic Layer Deposition to Fine-Tune the Surface Properties and Diameters of Fabricated Nanopores. *Nano Lett.* **4**, 1333–1337 (2004).

40. Larkin, J., Henley, R., Bell, D. C., Cohen-Karni, T., Rosenstein, J. K. & Wanunu, M. Slow DNA Transport through Nanopores in Hafnium Oxide Membranes. *ACS Nano* **7**, 10121–10128 (2013).

41. Knez, M., Nielsch, K. & Niinistö, L. Synthesis and Surface Engineering of Complex Nanostructures by Atomic Layer Deposition. *Adv. Mater.* **19**, 3425–3438 (2007).

42. Torre, R. dela, Larkin, J., Singer, A. & Meller, A. Fabrication and Characterization of Solid-state Nanopore Arrays for High Throughput DNA Sequencing. *Nanotechnology* **23**, 385308 (2012).

43. Abou Chaaya, A., Le Poitevin, M., Cabello-Aguilar, S., Balme, S., Bechelany, M., Kraszewski, S., Picaud, F., Cambedouzou, J., Balanzat, E., Janot, J.-M., Thami, T., Miele, P. & Dejardin, P. Enhanced Ionic Transport Mechanism by Gramicidin A Confined Inside Nanopores Tuned by Atomic Layer Deposition. *J. Phys. Chem. C* **117**, 15306–15315 (2013).

44. Thangaraj, V., Lepoitevin, M., Smietana, M., Balanzat, E., Bechelany, M., Janot, J.-M., Vasseur, J.-J., Subramanian, S. & Balme, S. Detection of short ssDNA and dsDNA by current-voltage measurements using conical nanopores coated with Al2O3 by atomic layer deposition. *Microchim. Acta* **183**, 1011–1017 (2016).

45. PTA | Upstream Technological Platform. http://pta-grenoble.com/.

46. CEA. Upstream Technological Platform (PTA). *CEA/Interdisciplinary Research Institute of Grenoble (IRIG)* http://www.cea.fr/drf/irig/english/Pages/Platform/PTA.aspx (2018).

47. Franssila, S. *Introduction to Microfabrication, 2nd Edition*. (Wiley, 2010).

48. Tau Tech. http://www.ciellecnc.com/le-nostre-macchine/laser-fibra/tau-tech.html.

49. KLayout Layout Viewer And Editor. https://www.klayout.de/.

50. Etching Process. http://www.memsnet.org/about/processes/etch.html.

51. Janssen, G. & Baumgärtel, H. Anisotropic Etching of Crystalline Silicon in Alkaline Solutions I. Orientation Dependence and Behavior of Passivation Layers. *J. Electrochem. Soc.* **137**, 3612–3626 (1990).

52. *Scanning microscopy for nanotechnology: techniques and applications*. (Springer, 2007).

53. Guzel, F. D., Pitchford, W. H. & Kaur, J. Controlled gradual and local thinning of free-standing nanometer thick Si3N4 films using reactive ion etch. *Microsyst. Technol.* **26**, 1167–1172 (2020).

54. Laermer, F., Franssila, S., Sainiemi, L. & Kolari, K. Chapter 21 - Deep Reactive Ion Etching. in *Handbook of Silicon Based MEMS Materials and Technologies (Second Edition)* (eds. Tilli, M., Motooka, T., Airaksinen, V.-M., Franssila, S., Paulasto-Kröckel, M. & Lindroos, V.) 444–469 (William Andrew Publishing, 2015).

55. Zhou, J., Ellis, A. V. & Voelcker, N. H. Recent developments in PDMS surface modification for microfluidic devices. *Electrophoresis* **31**, 2–16 (2010).

56. Hwang, Y. & N. Candler, R. Non-planar PDMS microfluidic channels and actuators: a review. *Lab. Chip* **17**, 3948–3959 (2017).

57. Torino, S., Corrado, B., Iodice, M. & Coppola, G. PDMS-Based Microfluidic Devices for Cell Culture. *Inventions* **3**, 65 (2018).

58. La microfluidique et les puces microfluidiques. *Elveflow* https://www.elveflow.com/archives-fr/histoire-de-la-microfluidique-et-des-puces-microfluidiques/.

59. Roman, J., Jarroux, N., Patriarche, G., Français, O., Pelta, J., Le Pioufle, B. & Bacri, L. Functionalized Solid-State Nanopore Integrated in a Reusable Microfluidic Device for a Better Stability and Nanoparticle Detection. *ACS Appl. Mater. Interfaces* **9**, 41634–41640 (2017).

60. CEA. The Nanocharacterization Platform (PFNC). *CEA/Interdisciplinary Research Institute of Grenoble (IRIG)* http://www.cea.fr/drf/irig/english/Pages/Platform/PFNC.aspx (2018).

3

Experimental Setup

Synopsis

This chapter relates to the setting up of an experimental bench for nanopore sensing, the theoretical considerations for data analysis and the description of the chosen surface chemistry for grafting aptamers on nanopore surfaces. First, all the different elements constituting an experimental bench will be described, from the selection of the fluidic system and electronic hardware, to the data treatment software. Then, the different physical properties of nanopore sensing used in this work will be theoretically described. Finally, all the experimental steps for the grafting of aptamers on a silicon nitride surface will be depicted.

Table of Contents

3.1 Building the Experimental Bench

3.1.1 Principle

Building an experimental bench for single nanopore sensing was one of the main challenges of this work. It can be divided into several building blocks. Figure 3.1 illustrates a typical nanopore experimental setup.

First of all, the setup contains noise reduction thanks to a Faraday cage and soundproof foam. This protects from external sources of interferences. Another important part of the setup is the fluidic cell for handling the nanopore chip and performing the experiments. It is intended for sealing the chip between two electrolyte solution reservoirs with the nanopore as the only fluidic connection between them. Then, electrodes are needed for the application of a potential across the membrane and the monitoring of the ionic current through the nanopore. The main instrumentation required is the amplifier. It is used to apply the voltage and record the current. The chosen solution is an Axopatch 200B amplifier from Molecular Device. It has a preamplifier called “headstage” that can be placed close to the nanopore inside the Faraday cage. The analog output signal from the amplifier is then processed with an Analog-to-Digital Converter. Thanks to a software, the experimental data are recorded as a digital file that will be further processed. Finally, the data analysis will be performed with an open source MATLAB software.

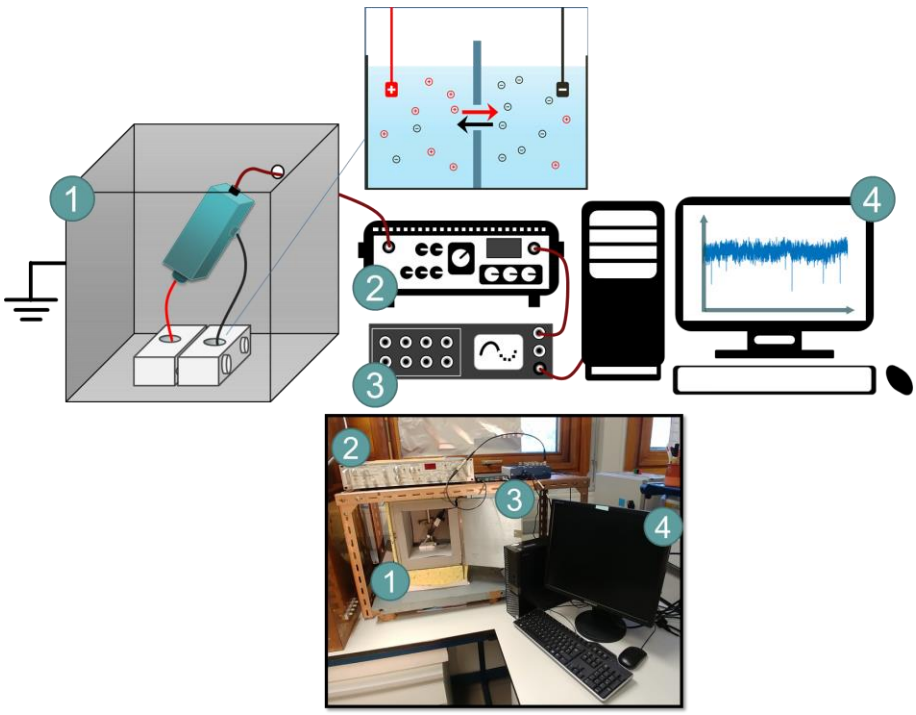

Figure 3.1: Illustration (top) and photography (bottom) of the experimental bench. 1) Faraday cage enclosing the fluidic cell holding the nanopore chip, 2) Amplifier, 3) Analog-to-Digital Converter, 4) Computer for data recording and treatment.

3.1.2 Shielding of the Setup

Avoiding vibrations and surrounding electrical noise in nanopore experiments is key for successful measurements with a good signal-to-noise ratio (see subsection 3.2.2 for noises in solid-state nanopores). The traditional electrophysiologist's refuge from vibrations is the following: experimenting at midnight in the basement room[1]. Fortunately, this solution can be avoided by a careful sound, vibration and electrical insulation design.

The electrical insulation consists in a grounded Faraday cage. It shields the headstage circuitry from external electrical interferences. Those can be categorized into three different categories[1]: radiative electrical pickup ("hum" noise from lights and power sockets as well as high-frequency noise from computers), magnetically-induced pickup (magnetic flux through wires forming a loop), and ground-loop noise (when the setup is grounded at more than one place). Therefore, the Faraday cage we use in this work (Figure 3.2) is grounded with the common ground of the Axopatch amplifier (that will be presented subsection 3.1.6).

For the vibration isolation, a heavy lead slab (around 200 kg) supported by four tennis balls is used to hold the Faraday cage. At the first days of the experimental bench, sound was not insulated. It quickly became a problem as the nanopore experiments could record casual noise in the lab. The sound insulation foam was chosen from the retailer Panasorb[2] and the products chosen according to their advises. There are two basic acoustic applications for foam: reverberation reduction within rooms (with the well-known pyramidal pattern foam in music sound studios) and sound insulation between rooms. The foam (Verbund200-1cm and AV40G, Panasorb, Germany) was cut in order to fit perfectly in the Faraday cage and shield the nanopore fluidic cell and the headstage.

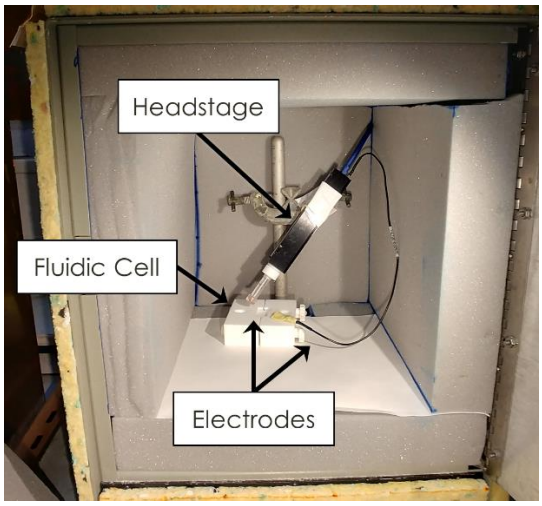

Figure 3.2: Photography of the Faraday cage's inside with sounding insulation foam, the amplifier's headstage, the electrodes and the fluidic cell.

3.1.3 Nanopore Chip

The chips used for nanopore experiments in this work originate from a small company called Nanopore Solutions[3] (Portugal). We ordered 3 mm circular chips that consist in 200 µm thick silicon bulk support and a 20 nm thin silicon nitride (Si_3N_4 or SiN_x) membrane deposited by Low Pressure Chemical Vapor Deposition (LPCVD). An opening is located on one side in the precise center, releasing a free-standing 15 µm x 15 µm SiN_x dielectric membrane (Figure 3.3). The chip with the membrane is designed to fit in a TEM holder; therefore we can drill a nanopore of any desired size in its center. The description of nanopore drilling in the TEM has been described in Chapter 2. In the eventuality of Nanopore Solutions ceasing to sell the membranes, another retailer called Norcada[4] could decently replace this product.

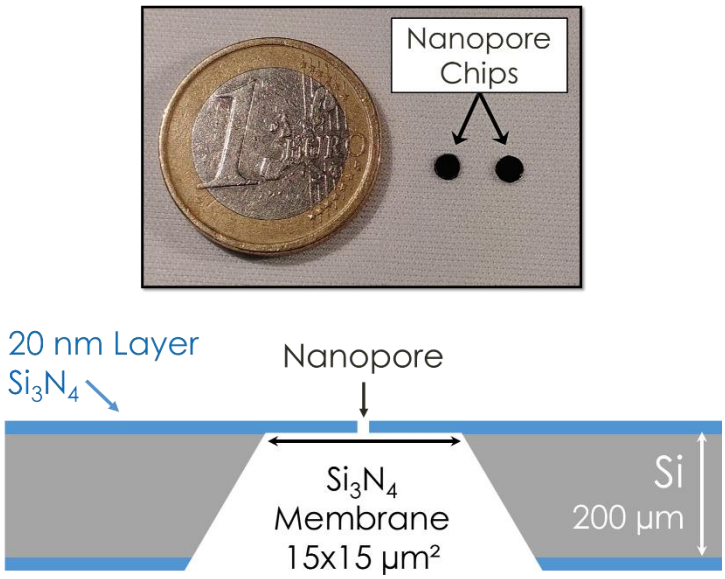

Figure 3.3: Photography of Nanopore Solutions chips close to a 1 € coin (top) and cross-sectional view schematic of the chip (bottom). For simplification purpose, the scheme is not to scale.

3.1.4 Fluidic Cell

Nanopore experiments require a hermetic setup to ensure that the measured current originates only from the nanopore. The objective of the fluidic cell is to provide a practical way of handling the nanopore chip while ensuring a tight seal between the electrolyte reservoirs. The company Nanopore Solutions provides a very practical flow-cell designed for 3 mm diameter chips. The fluidic cell is shown on Figure 3.4. It is made from Teflon (Polytetrafluoroethylene, PTFE), which is chemically inert. This fluidic cell enables *in situ* cleaning and treatment with Piranha solution (Appendix II).

The nanopore chip is tightened between two O-rings that fit in a small cassette closed with small Teflon screws (Figure 3.4). The chip is accessible through conical openings on each side of the cassette. Those openings are convenient as the surface tension always keeps a small drop of liquid against the chip. This allows us to keep the pore "wet" while manipulating it. It is indeed a difficult step to make sure that the liquid is in the nanopore and that there are no bubbles or nanocrystals of salt blocking the passage of the current. Those conical apertures also provide a way of flowing in a new buffer and washing the chip with a pipette between each experiment. They can hold up to 20 µL of solution. Another advantage of this cassette system is that the mounted nanopore chip in the cassette can be stored in a 50 mL Eppendorf tube filled with storing solution (Appendix II). Thus, it can be reused on demand without the need of "wetting" again the nanopore. This is particularly interesting for the nanopore chips with functionalized surfaces that need to remain in aqueous solution. The cassette is enclosed into a flow-cell between two other O-rings (Figure 3.4). The flow-cell contains the two reservoirs that can be filled with electrolyte solution volumes ranging from 300 to 1000 µL. Two small openings allow an easy insertion of the electrodes.

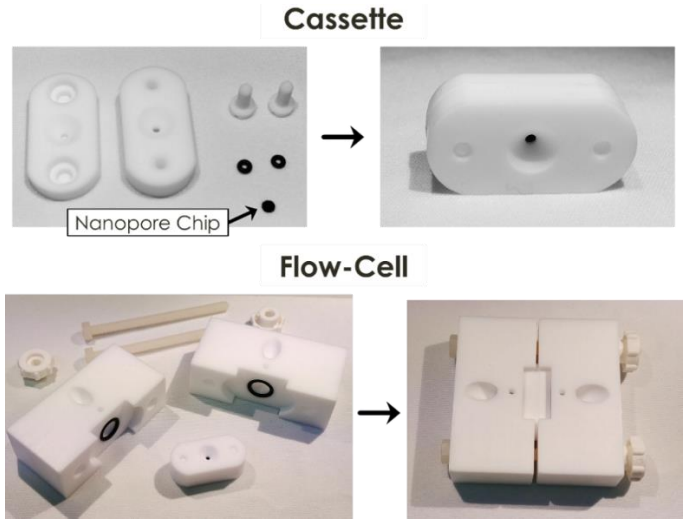

Figure 3.4: Fluidic cell setup with the Cassette containing the nanopore chip (top) and the Flow-cell holding the cassette (bottom).

3.1.5 Electrodes

The ionic current going through the nanopore is generated thanks to the application of a voltage between the electrodes immersed in electrolyte solutions on each side of the dielectric membrane. The most widely used electrodes in electrophysiological patch-clamp measurements are silver/silver chloride electrodes (Ag/AgCl)[1]. They work in solutions with chloride ions and possess the advantage of being non-polarizable. They cause no capacitive current at their interface with the electrolyte. One of the two electrodes is coated with chlorine by soaking it for 10 minutes into sodium hypochlorite solution (bleach) at 5 %. When an electrical potential difference is applied across the nanopore *via* the electrodes, the following two electrochemical reactions occur:

At the anode: $Ag_{solid} + Cl^- \rightarrow AgCl_{solid} + e^-$

At the cathode: $AgCl_{solid} + e^- \rightarrow Ag_{solid} + Cl^-$

At the positive electrode, the anode, an oxidative electrochemical reaction occurs. The Cl^- anions in the electrolyte solution react on the silver electrode and a free electron migrates through the wires to the electrometer in the amplifier[5]. The generated charge imbalance results in the migration toward the membrane of cations in the solution (generally Na^+ or K^+). At the cathode, the reverse electrochemical reaction occurs. An electron arrives from the electric circuit and a chlorine anion Cl^- is released in the solution. For nanopore experiments in typical KCl electrolyte solutions, the voltage range used does not exceed ± 1 V under which the nanopore has an ideal ohmic resistive behavior. At larger voltage values, pH is unstable due to oxidation and reduction of water, which is a reason why typical nanopore experiments are performed under 1 V[6].

3.1.6 Amplifier

The amplifier must be able to acquire ultra-low noise current and detect current changes at a picoamper scale. The Axopatch 200B is a well-known amplifier used for patch-clamp experiments (recording current through a pore with an applied voltage)[7]. It can apply a voltage up to ± 1 V and measure current up to 200 nA with a sub-pA sensitivity.

This precise current measurement is possible thanks to a headstage placed in the Faraday cage. It is internally cooled down at -15°C in order to prevent thermal noise (this will further be discussed in subsection 3.2.2). The current is converted into a measurable voltage signal thanks to a capacitor-feedback circuit[7]. Moreover, the voltage output is low-pass filtered through a 4-pole Bessel filter in order to reduce high frequency noise. This filter has the cut-off frequency of 10 kHz, which is the one used for all our experiments. The output voltage is amplified thanks to a gain tuned with α and β parameters. In this work the α and β parameters are respectably set to 1 and 0.1. Therefore the voltage output of the amplifier is read as the following:

$$Gain = \alpha \times \beta \quad (mV / pA)$$

$$\Rightarrow Voltage\ Output = Gain \times Nanopore\ Current \tag{1}$$

$$\Rightarrow Nanopore\ Current = \frac{1}{\alpha \times \beta} \times Voltage\ Output = 10 \times Voltage\ Output$$

3.1.7 Analog-to-Digital Converter

Digitization is the process of converting an electrical analog signal into a digital signal that a computer can process and read. For this experimental bench, the voltage signal at the output of the Axopatch 200B amplifier must be digitized. The Analog-to-Digital (A/D) converter that has been chosen is a NI USB 6361 from National Instruments.

In order to find the appropriate A/D converter, the characteristics of the voltage output signal of the amplifier for nanopore experiments must be considered. On Figure 3.5, a typical signal for a translocation event is depicted (λDNA going through a 12 nm diameter SiN_x nanopore at + 200 mV). The current drop magnitude is ~400 pA and the dwell-time is ~ 500 µs.

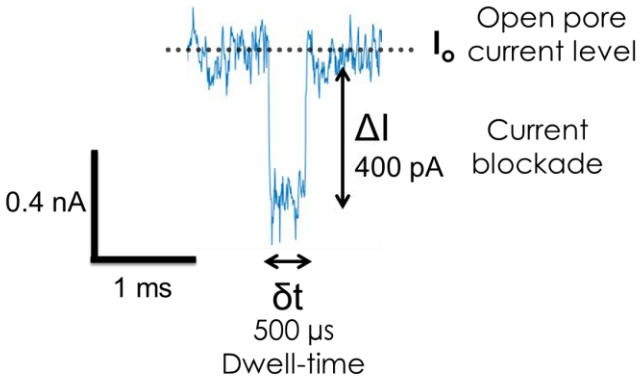

Figure 3.5: An example of current data for a translocation signal event of λDNA in a 12 nm diameter SiN_x nanopore at + 200 mV (1 M KCl, 1 mM Tris/HCl, 0.1 mM EDTA buffer).

The dynamic voltage output of the amplifier is up to ± 10 V[7], it depends on the α*β gain described previously. Therefore, the input range of the A/D converter must fit those values and handle up to ± 10 V. The NI USB 6361 can provide this input range, it is also possible to lower this input range down to ± 0,1 V. For nanopore translocating events, we wish to observe current changes with a pA order of magnitude. The number of bits of the A/D converter corresponds to the resolution of the digitized signal. For our application, 16 bits are used. It means that for a ± 10 V input range (20 V in total), the signal is divided into 2^{16}=65536 values called bins. Thus, the resolution provided is 0,305 mV per bin (20 V range divided by 2^{16} bins). In our case the Axopatch 200B output gain α*β is equal to 0,1 mV/pA (cf. previous section). As the baseline current in the nanopore does not strongly vary during translocation experiments, an A/D converter input range of ± 0,5 V is more than adequate to record the single-events. The resolution of one bin is therefore equal to 15 µV (1 V range divided by 2^{16}), which corresponds to a resolution of 0,15 pA (cf. equation (1) Voltage output (mV) * (1/α*β) = current measured (pA) → 0,015 mV * (1/0,1) = 0,15 pA). The resolution of the A/D converter USB 6361 is then sufficient to observe current drops triggered by a biomolecule translocating through the nanopore.

The reduction of the continuous analog signal into a discrete digital signal is called sampling. The sampling frequency is the number of samples per second. The Nyquist sampling theorem states that the sampling frequency must be at least twice the frequency of the targeted signal in order to retrieve interesting information[8]. In practice, it is preferable to oversample the signal. In nanopore experiments, sampling frequency is often 100 kHz[9] (corresponding to 10 µs intervals) which is 10X the cut-off frequency defined previously. That will be the frequency used in all the translocation experiments of this study. A higher frequency (for example 1 MHz) provides a more relevant signal over the translocation and can indicate subtle information on the molecule itself such as submolecular DNA configurations[10–13]. However, high frequencies complicate the measurements as the overall system noise increases. This is the reason why another solution is to slow down the biomolecules as they travel through the nanopore.

An interesting feature of the NI USB 6361 is that it can work with a free acquisition software called DAQExpress. This software allows us to easily record data as a .tdms format (National Instruments Technical Data Management Streaming) while tuning the input voltage range and the sampling frequency. There is also a basic analysis panel tool that lets the user intuitively navigate through the recorded data.

For an experimental characterization of nanopores, different voltages are applied and the resulting current is measured in order to observe the ohmic behavior and retrieve the pore's conductance (see section 3.2.1). The voltage values are applied thanks to the work of Mr. Argentier Loïc who implemented during his internship a Python programmed oscilloscope (Handyscope HS5, TiePie engineering)[14]. The program enables the application of different voltage steps for a defined time on a nanopore. The voltage value alternates between positive and negative values in order to avoid a possible accumulation of charges on the membrane's surface that could affect the conductance's value.

Data from experiments of biomolecules translocation in a nanopore will further be analyzed in a MATLAB software that has been developed by Raillon *et al.*[15] at EPFL (Switzerland). In order to use this software, the data acquired with our setup must be converted from the .tdms format (National Instrument) to the .mat format. We can either use the Matlab function *TDMS_getStruct* or *TDMS_readTDMSFile* to this intend.

3.1.8 Data Analysis using Open Nanopore MATLAB Software

The experimental data of translocating events of biomolecules through a single nanopore is analyzed thanks to an open source MATLAB software called Open Nanopore developed in the EPFL Laboratory of Nanoscale Biology[15,16]. This software detects abrupt changes in the current (translocation events) and uses an algorithm called cumulative sums algorithm (CUSUM) that fits different levels of current blockage inside an event (Figure 3.6). In this work, the CUSUM part of the software has only been used for experiments where the translocation events exhibited several levels.

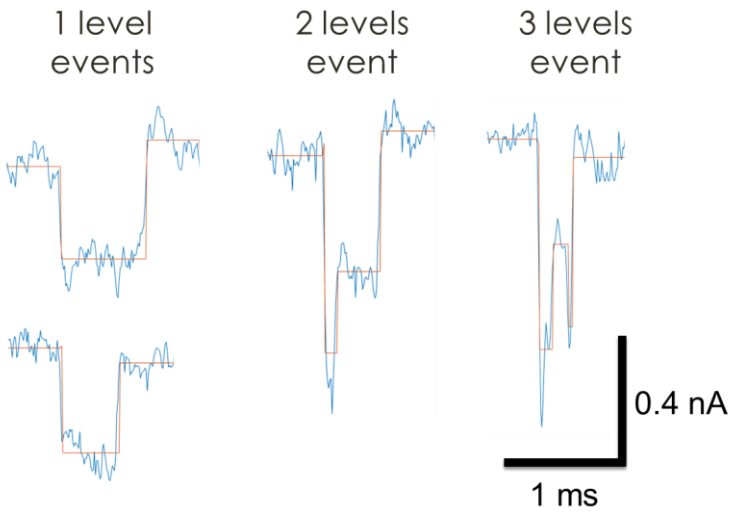

Figure 3.6: Example of Open Nanopore data fitting for λDNA going through a 12 nm nanopore (+200 mV, buffer: 1 M KCl, 1 mM Tris-HCl, 0.1 mM EDTA, pH 8). Several events with one to three levels in one event are depicted. In blue is the raw current data trace, in orange are the fitted levels of currents by the software.

The Open Nanopore overall structure[15] can be described as follows (Figure 3.7). A first step consists in the rough detection of events location in the signal data. It is made thanks to an adaptive threshold recursive filter based on local estimates of mean current values and standard deviation. When a point or a series of points is beyond the adapted threshold, it is localized as a rough event. A file of concatenated events is obtained. After that, the events are manually checked in order to decide whether we use the CUSUM algorithm part of the software or not. If the events are only one level, we decided not to use the software and perform the statistical analysis on the concatenated events. If the events present several levels, the file is processed through the other part of the OpenNanopore software with the CUSUM algorithm. In the latter case, the events are treated according to their length following three scenarii. First case: if only one change point is detected, it is not considered as an event. Second case: if the event's length is smaller than a value defined by the user (usually 10 points), the event is considered as a one-level event (too short to be segmented in different levels). Its level is fitted

as the minimal value of the current drop. Third case: if the event length is greater than this value, the CUSUM algorithm is applied to that event and all the different levels are fitted to their current drop values. All the information from those events are registered in a database that comprises the start and end-point of the event in the signal, the number of current levels in the event, and for each level their current drop values and dwell-time. The database is manually checked in order to verify the accuracy of the fitted events.

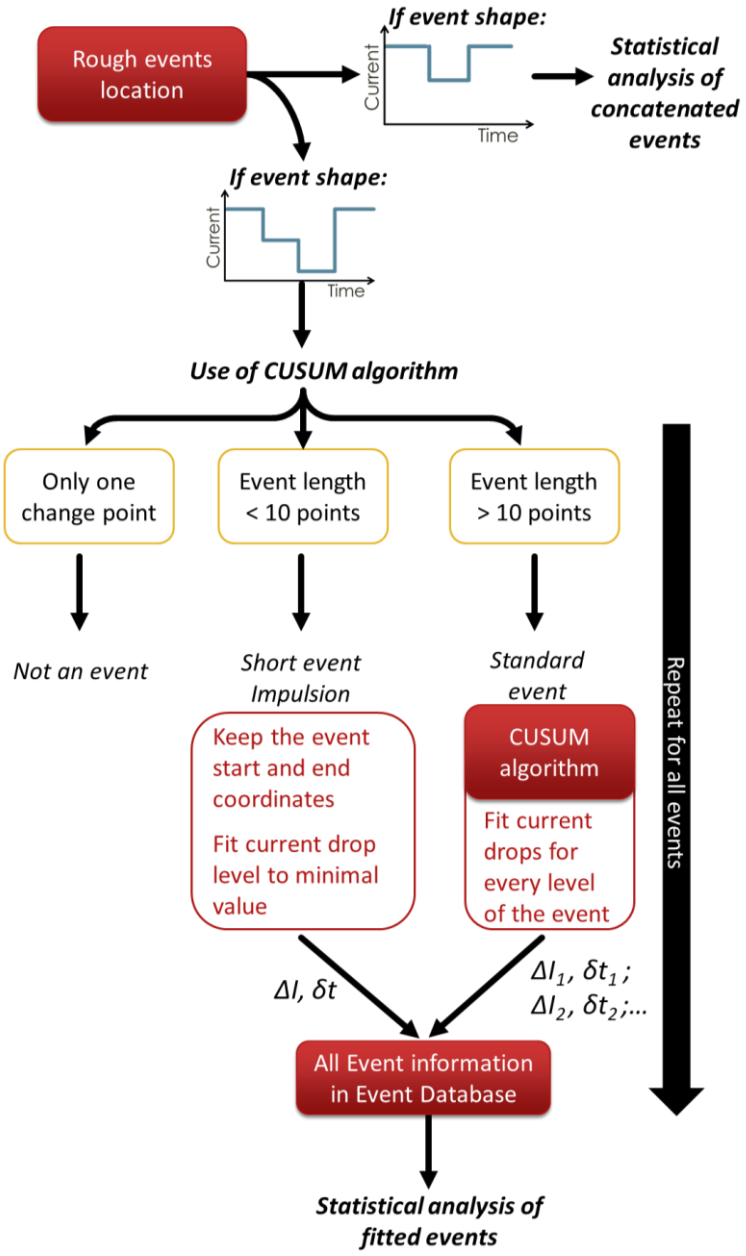

Figure 3.7: Block diagram of the Open Nanopore software, adapted from reference[15].

The dwell-times and current drops of the events are displayed as histograms with the MATLAB function *hist* and as scatter plots with the function *scatter*, respectively. For fitting the histograms and finding

peaks, the MATLAB data are converted in .txt files with the functions *table* and *writetable* and the software Origin (OriginLab, USA) is used.

3.2 Physical Properties of Nanopores

3.2.1 Ionic Conduction in Nanopores

Understanding the effects of ionic transportation in nanopores is crucial for their experimental characterization. The aim of this part will be to understand the physics beneath and learn how to extract information from its measured conductance such as diameter or surface charge changes.

Theoretical Open Pore Conductance

The conductivity σ of an electrolyte solution is its ability to conduct electricity. It is expressed in Siemens per meter (S/m). We can extrapolate the nanopore as a resistance in an electrical circuit. The nanopore is then characterized by its conductance G_{pore} (=1/R_{pore}) which is by definition the slope of the ionic current flowing through as a function of the applied voltage (Ohm's Law). G_{pore} is dependent on the number of free charge carriers in a solution. When an electric field is applied across the nanopore, all the anions are driven to the anode while the cations are driven to the cathode. The following part will theoretically detail how the pore diameter can be extracted from the measured conductance. The line of thought is inspired from the work of Santoshi Nandivada[17].

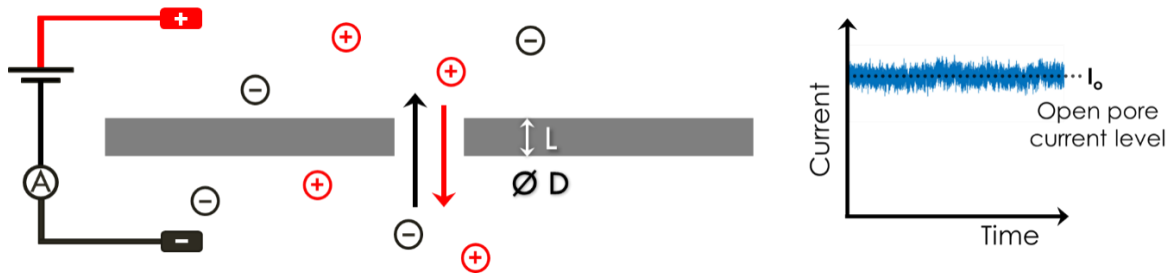

Figure 3.8 : Scheme of a nanopore of thickness L and diameter D. When a voltage is applied a current I_o is established in the nanopore corresponding to the open pore current level.

Let us consider a nanopore of length L (the membrane thickness) and diameter D as a cylinder connecting the two electrolyte reservoirs (Figure 3.8). The nanopore is the only connection between those reservoirs, they are filled with a uniform electrolyte solution of conductivity σ. When an electric potential V is applied, a current I is established in the nanopore of conductance G_{pore} following Ohm's law:

(2) $$V = R_{pore} \times I = \frac{I}{G_{pore}} \Leftrightarrow I = G_{pore} \times V$$

This equation can be derived, giving an alternate form of Ohm's law:

(3) $$J = \sigma \times E$$

Where J is the current density (current per unit area) and E is the applied electric field (voltage per unit length). The current density J inside the nanopore can be written as follows:

(4) $$J = \frac{Current}{Area} = \frac{I}{A} \quad (nA/nm^2)$$

With a cylindrical nanopore, we have a disc of area $A = \pi D^2/4$.

The current density from equation (4) becomes: $J = \frac{4 \times I}{\pi \times D^2}$

Applied to the electric field from equation (3) we obtain:

(5) $$\sigma \times E = \frac{4 \times I}{\pi \times D^2}$$

The electric field E is calculated in first approximation by the applied potential drop inside the nanopore neglecting the applied potential drop inside the two electrolyte solutions besides the membrane. We consider the electric field in this cylinder to be uniform. Then, $E = V_{applied}/L$ with L the length of the nanopore. We can now modify equation (5):

(6) $$V_{applied} = (\frac{4L}{\sigma \pi D^2}) \times I$$

By analogy with Ohm's law (equation (2)), we extract the resistance of the nanopore and its conductance:

(7) $$R_{pore} = \frac{4L}{\sigma \pi D^2}$$
$$\Leftrightarrow G_{pore} = \frac{1}{R_{pore}} = \frac{\sigma \pi D^2}{4L}$$

This equation considers the nanopore as a cylindrical tube. However, TEM drilled nanopores often exhibit an hourglass shape (cf. Figure 3.9). This geometry is taken into consideration with the following equation[18]:

(8) $$G_{pore} = \frac{\pi D^2}{4} \sigma (\frac{\delta \tan \alpha + 1}{L + L_{eff} \delta \tan \alpha})$$

Where L_{eff} is the width of the cylindrical region in the nanopore, α is the cone half-angle and δ=(L-L_{eff})/D. For this thesis work, a theoretical conductance range is calculated in order to check that the

nanopore experimental conductance is comprised in between those values. The range is given by the previous equation with the extreme geometrical values α = 0 ° and L_{eff}=L or α = 45 ° and L_{eff}=0.

(9)
$$\begin{cases} \alpha = 0° \text{ and } L_{eff} = L \quad \Rightarrow G_{theory1} = \dfrac{\sigma\pi D^2}{4L} \\ \alpha = 45° \text{ and } L_{eff} = 0 \quad \Rightarrow G_{theory2} = (L + D)\dfrac{\sigma\pi D}{4L} \end{cases}$$

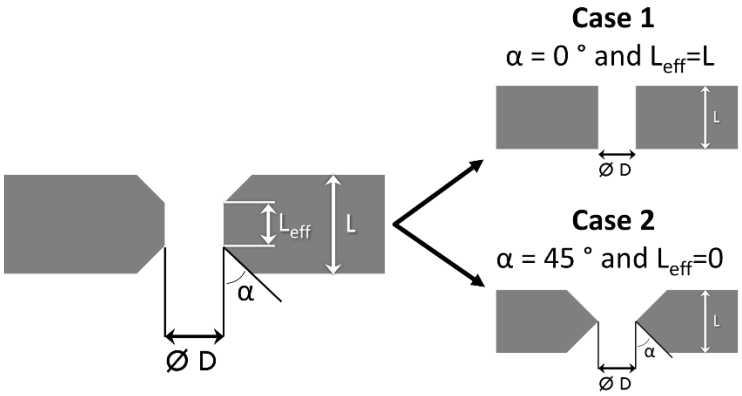

Figure 3.9: Geometrical considerations regarding the calculation of G_{pore}[18]. The theoretical conductance range used in this work is given when α = 0 ° and L_{eff}=L (case 1), or α = 45 ° and L_{eff}=L (case 2).

Moreover, we focus during this work on nanopore diameter reductions and fluctuations in order to monitor the surface functionalization. In order to approximate an experimental diameter, we consider the conductance of a nanopore assuming a cylindrical geometry (equation (7)). By measuring the experimental conductance of the nanopore G_{exp} , we assume an experimental diameter of the pore obtained with the equation:

(10)
$$D_{\exp} = \sqrt{\frac{4LG_{\exp}}{\sigma\pi}}$$

Ionic Current Rectification

Previously described ionic transportation depicts ideal symmetrical nanopores. In this case, I-V curves are linear and symmetrical. However, in some cases the experimental I-V curves do not exhibit a linear profile and are similar to a nanofluidic diode[19,20] (Figure 3.10). This behavior is called Ionic Current Rectification[21] (ICR). It is triggered by two different parameters: an asymmetric geometry of the pore[22,23] or a non-homogeneous charged surface of the pore[24,25] .

For asymmetric nanopores (an opening wider than the other), ICR comes from the accumulation of ions inside the pore and the simultaneous accumulation of opposite polarity ions outside the narrow opening of the pore[22]. Concerning pores with a non-homogeneously charged surface[24,25], the current appears to have a preferential flow direction. The effect of surface charge has been described with the work of Siwy *et al*.[26] where the electrolyte pH influenced the surface charge of a PET nanopore. When the PET nanopore was negatively or positively charged, the I-V curve was nonlinear and ionic current rectification observed, while at pH 3.8 (when the PET surface charge was 0), the I-V curve showed a linear behavior.

ICR is an interesting phenomenon to consider for our project because the surface functionalization with DNA of the nanopores brings negatively charged walls. It can be used as a tool for monitoring the process of chemical modification on the inner surface of the nanopore[27–29].

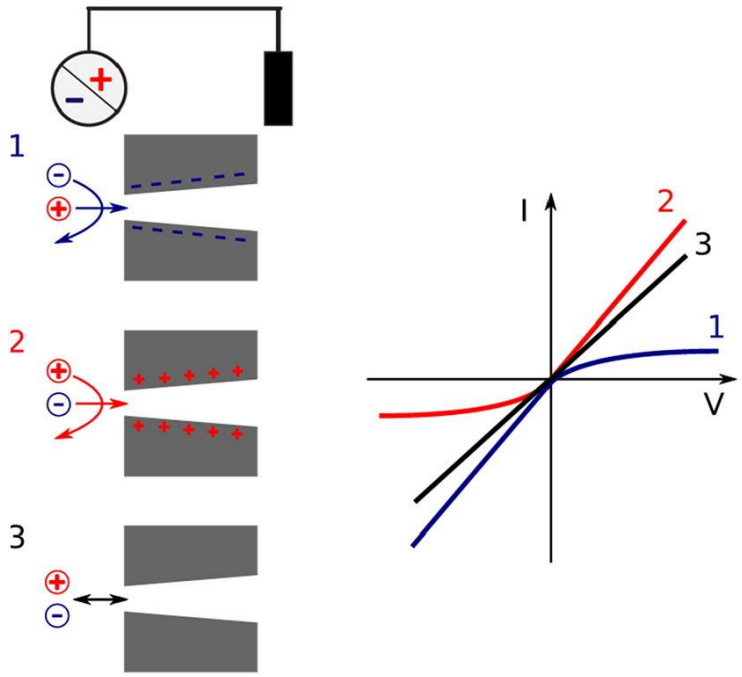

Figure 3.10: Illustration of ionic current rectification phenomenon on I-V curves for a negatively charged, positively charged or non-charged nanopore, from reference[30].

3.2.2 Noise in Solid-State Nanopores

When a potential V is applied on the nanopore, noise arises with the current I. The root-mean square current noise $I_{noise,RMS}$ is defined as $I_{noise,RMS} = \sqrt{\langle I^2 \rangle - \langle I \rangle^2}$. Signal-to-Noise Ratio (SNR) is the comparison between the level of the desired signal (the current drop ΔI occurring during biomolecule translocation) and the level of the background current noise. SNR is defined as[31]:

$$SNR = \frac{|\Delta I|}{I_{noise,RMS}}$$

For our experiments, $I_{noise,RMS}$ reading is given thanks to the Axopatch Amplifier panel meter display or can be calculated from recordings.

Contributions of noise in solid-state nanopore experiments are categorized according to their frequencies[10,32]. In the low-frequency range, the flicker noise (<100 Hz), and the thermal and shot noise (~0.1-2 kHz) prevail. At high frequencies, we can observe the dielectric noise (~1-10 kHz) and the capacitive noise (>10 kHz). Those dominant sources of noise can be visualized on a Power Spectral Density (PSD) obtained from a Fourier transform of experimental current data. Figure 3.11 is a scheme of this PSD for a solid-state nanopore experiment. Each contribution of the different noises is now going to be described.

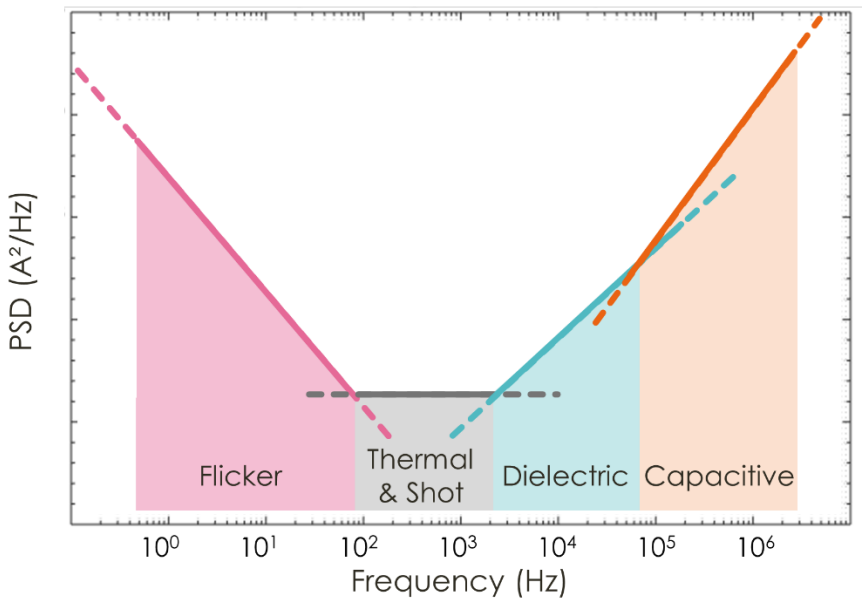

Figure 3.11: This scheme adapted from references[10,32] represents the different sources of noise in the Power Spectral Density (PSD) of current recording in a solid-state nanopore, as a function of frequency.

Flicker Noise

Also known as 1/f noise or Pink noise, the Flicker noise dominates the low-frequency part of the PSD spectrum. Its origins in solid-state nanopores is still under discussion[32]. The surface properties of a nanopore have been shown to play an important role in the flicker noise. The formation of nanobubbles and poor wettability of the pore have been associated in high 1/f noise in SiN_x pores[33]. Moreover, Tabard-Cossa *et al.* associated this noise with surface contamination and inhomogeneity of the pore surface[34]. Thus, the irregular surface results in fluctuations of the number and the mobility of charge carriers due to their trapping at the pore surface. We expect surface functionalization of the nanopore to strongly affect this noise contribution. The PSD of the Flicker Noise is described as follows[32]:

$$S_{flicker} = \frac{\alpha_H I^2}{N_c f^{\beta}} \quad (A^2 / Hz)$$

Where α_H is the Hooge's constant, an empirical parameter that quantifies the magnitude of 1/f noise fluctuations, I the ionic current (A), N_c is the number of charge carriers inside the nanopore, f is the frequency and β ($\approx$1) is another empirical parameter.

Thermal Noise and Shot Noise

In electronic circuits, thermal noise, also known as Johnson noise or Nyquist noise, corresponds to the thermal agitation of charge carriers inside an electrical conductor. It happens regardless of any applied voltage. As an approximation, the overall pore structure can be considered as a simple resistive element. The agitation of charge carriers inside the pore triggers the thermal noise. Moreover, the electronic circuitry of the current amplifier also generates thermal noise. At equilibrium, the PSD of the thermal noise is given by the following equation[11]:

$$S_{thermal} = \frac{4kT}{R} \quad (A^2 / Hz)$$

Where k ($m^2.kg/(K.s^2)$) is the Boltzmann constant, T (K) is the absolute temperature, and R (Ω) is the sum of the resistance of the nanopore and the resistor in the amplifier. Therefore, to minimize thermal noise one must consider using a small sized pore with a higher resistance. Moreover, the circuitry in the Axopatch headstage preamplifier is actively cooled at -15°C in order to significantly reduce thermal noise[7]. Concerning shot noise, it arises from discrete and random fluctuation of charge carriers in an electrical conducting medium such as ions in our electrolyte solution. With q (C) the charge of a single carrier and I (A) the average current, its contribution to the PSD of a nanopore experiment is as follows[32]:

$$S_{shot} = 2Iq \quad (A^2 / Hz)$$

Dielectric Noise

SiN_x membrane is a dielectric membrane. However, dielectric materials are not ideal insulators. Therefore, after application of potential voltage across the membrane and the nanopore, some current can leak through the membrane. It is dissipated in the membrane through dipolar relaxation and charge carrier migration. This phenomenon is called dielectric loss and results in dielectric noise[32] . The PSD of this noise is written as:

$$S_{dielectric} = 8\pi kTDC_{chip} f \quad (A^2/Hz)$$

Where k ($m^2.kg/(K.s^2)$) is the Boltzmann constant, T is the absolute temperature (K), D is a dissipation factor of the dielectric material, C_{chip} (Farad) is the parasitic capacitance of the membrane and *f* (Hz) the frequency[32].

Capacitive Noise

Above 10 kHz in the PSD, the largest noise contribution is Capacitive Noise. It comes from an electrolytic capacitor made of the lineup of ions and counterions on each side of the membrane[10]. The contribution of Capacitive Noise to the PSD is as follows:

$$S_{capacitance} = 4\pi^2 C_{tot}^{\ 2} v_n^{\ 2} f^2 \quad (A^2/Hz)$$

Where C_{tot} (Farad) is the sum of several capacitances, such as the capacitance of the membrane, capacitances that can be present in any wiring, and the input capacitance by the amplifier, v_n (V/Hz) is the input voltage noise. With our amplifier, the Axopatch 200B from Molecular Devices, the value of the input voltage noise is 3 nV/Hz[7,32].

The total current noise of a solid-state nanopore experiment is the sum of all previously cited contributions (Figure 3.11). For further information about noises origins in nanopores and a comparison between solid-state and biological nanopore's noises, I suggest reading respectively the Axon Guide[1] and the excellent review from Fragasso *et al.*[32]. In Chapter 4 of this work, the PSD of a bare nanopore at different voltage values and the PSD of a bare and a functionalized solid-state nanopore will be given for their comparison.

3.2.3 Single-Molecule Sensing: Principles

Single-event detection is going to be discussed by looking at the different parameters accessible from the recorded current. As shown in Figure 3.12, when individual biomolecules such as a DNA strand or a protein translocate through the nanopore, disruptions in the recorded current are observed. The statistical analysis of those current drops provides information about the biomolecule. The first parameter that will be discussed here is the Event Amplitude ΔI which can be linked to the volume of the molecule. Then, we will talk about the Event Duration δt that corresponds to the time spent in the nanopore and may possibly be linked to the interactions with the pore walls. Finally, the capture rate, which corresponds to the time between events, will be debated with a discussion about the capture radius at the entrance of a pore.

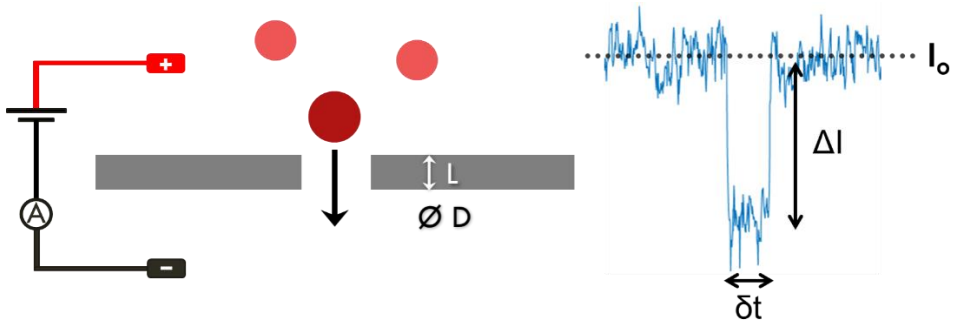

Figure 3.12 : Typical current trace for translocation events. When a biomolecule enters the nanopore of diameter D and thickness L, the current drops (ΔI) from its open pore current level I_o for a specific duration δt.

Event Amplitude

During a biomolecule translocation, the nanopore resistance is not the only one that must be taken into account. An important role is played by the "Access Resistance"[35,36] R_{access} of the electrolyte in the hemispheres at the pore entry and exit:

(11) $$R_{access} = \frac{1}{\sigma D}$$

Where D is the nanopore diameter and σ is the electrolyte conductivity. This access resistance plays a significant role especially for low aspect ratio nanopores (small Length/Diameter values)[37,38] such as the SiN_x nanopores used in our study. By adding the contribution of access resistance to pore resistance (equation (7) from subsection 3.2.1) we can express the total resistance of the nanopore:

(12) $$R_{total} = R_{pore} + R_{access} = \frac{4L}{\sigma \pi D^2} + \frac{1}{\sigma D}$$

We can deduce the total conductance of the pore[18]:

(13) $$G_{total} = \frac{\sigma \pi D^2}{4L + \pi D} \approx \frac{\sigma \pi D^2}{4(L + 0.8D)}$$

When a potential V is applied, I_o corresponds to the open pore current (Figure 3.12). The event amplitude ΔI originates from a decrease in the pore conductance ΔG because of the excluded electrolyte solution corresponding to the occupied volume of the biomolecule. It is therefore possible to estimate a protein volume from its current drop amplitude ΔI.

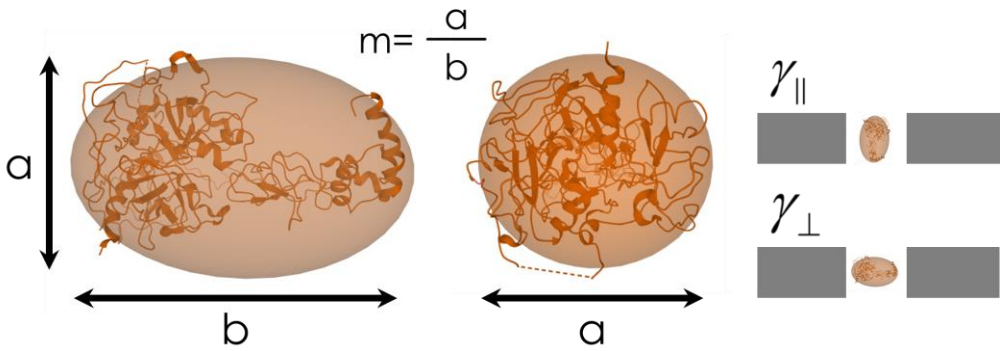

Figure 3.13: Scheme of a protein (Prothrombin, PDB entry 6BJR) approximated as an oblate spheroid with axes a and b and m=a/b <1 for the calculation of the shapes factors $\gamma_{||}$ and $\gamma_{\perp}$.

Extracting volumetric information from resistive pulse measurements is a technique that has been developed in the 70s with the theory of DeBlois and Bean[39]. This model has later on been adapted to nanopore sensing[12,40–42] with the introduction of a shape factor *γ*:

(14) $$\Delta G = \gamma \sigma \frac{V_{excluded}}{{L_{eq}}^2}$$
$$with \quad L_{eq} = L + 0.8D$$

With *γ* the shape factor, $V_{excluded}$ the volume of the protein and L_{eq} an equivalent nanopore thickness taking into account the resistance access. For a spherical protein, *γ*=1.5[41–43].For an oblate spheroid of principal axes a and b and with m=a/b<1, *γ* takes two values according to its orientation in the nanopore (Figure 3.13). They can can be calculated as follow[41,43]:

(15) $$\begin{cases} \frac{1}{\gamma_{\perp}} = \frac{m \times \arccos(m)}{(1-m^2)^{\frac{3}{2}}} - \frac{m^2}{1-m^2} \\ \gamma_{||} = \frac{2\gamma_{\perp}}{2\gamma_{\perp} - 1} \end{cases}$$

Figure 3.14: Model of a spherical protein of radius r going through a nanochannel of length L.

In the case depicted on Figure 3.14 of a spherical protein of radius r going through a nanochannel (length of the nanopore L significantly larger than the radius of the protein), the following equation is employed to express the current drop as a function of the excluded volume[43,44]:

(16) $$\Delta G = \frac{2\pi r^3}{L^2}\sigma = \frac{3V_{excluded\ sphere}}{2L^2}\sigma$$

This equation considers the shape factor γ=1.5 for a sphere, and L_{eq}=L. However, the exact relationship between a protein's geometry and the current drop amplitude remain ambiguous[9]. The proteins are generally non-homogeneously charged molecules and their charge can influence the ionic conduction in the nanopore.

Event Duration

The event duration, or dwell-time, of a translocating event corresponds to the time that the biomolecule spends in the sensing zone of the nanopore. The length of the sensing zone depends on the pore's geometry and its electric field distribution. Several models exist for the dwell-time distribution of DNA. For charged proteins, the dwell-time depends on the applied voltage[12], the higher the voltage across the nanopore, the faster the biomolecules go through it. For small nanopores, the translocation can be seen as an energy barrier crossing[9]. The dwell-time decreases exponentially with the applied voltage which reduces the barrier by zV (z is the total protein charge and V the applied voltage). The salt concentration in the electrolyte (charge carriers) does not appear to affect the event duration[45]. Specific care must be taken while talking about the dwell-time. The physical models proposed[9,12,46] rely on approximations and parameters such as the protein diffusion constant and mobility which can largely be influenced by interactions with the pore walls[47]. It is even more important in the case of pore wall functionalization as will be considered in this study.

3.3 Nanopore Surface Functionalization with Aptamers

3.3.1 Principle

One of the objectives of this work is to combine nanopore technology with aptamer sensing in order to discriminate closely-related proteins. This part will describe the surface chemistry process for the grafting of aptamers on a SiN_x surface. The different steps are schematized on Figure 3.15. The surface is silanized using silanes bearing reactive groups which are able to react with thiolated aptamers. The chip is then ready to be used for experiments or further steps are performed in order to validate the grafting of the aptamers. To do so, a biotinylated oligonucleotide with a complementary sequence to the aptamer is hybridized with the aptamer on the surface. Then a revelation is performed using fluorescence microscopy thanks to a protein complex (Streptavidin-Associated Phycoerythrin, SAPE) that specifically binds to biotin groups.

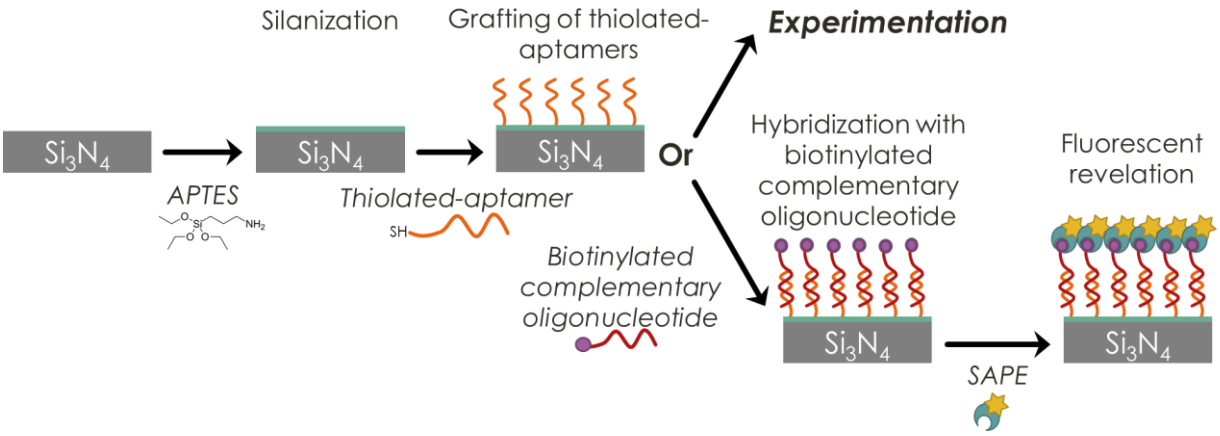

Figure 3.15 : Different steps of the surface functionalization of SiN_x with aptamers. First, the surface is silanized in order to graft aptamers. Then, the chip can either be used for protein sensing experimentations or be hybridized with the biotinylated complementary oligonucleotide for a further fluorescent revelation using SAPE.

3.3.2 Coupling oligonucleotides with Thiol or Biotin Groups

Table shows all the oligonucleotide sequences[48] (Eurogentec, Belgium). They are functionalized with an amine group (NH_2) at their 5' extremity. The aptamer thr1 recognizes specifically α-thrombin and thr1c is its complementary strand. At the 5' end is a poly thymine spacer that keeps the surface at a certain distance from the aptamer. It provides to the aptamer an appropriate spatial mobility for its folding and accessibility for the specific recognition of proteins[49–52]. The aptamer thr2 is later used as a negative control.

Sequence name	Sequence (5'→3')	Desired 5' modification
Thr1	TTT-TTT-TTT-TGG-TTG-GTG-TGG-TTG-G	-thiol
Thr1c	TTT-TTT-TTT-TCC-AAC-CAC-ACC-AAC-C	-biotin
Thr2	TTT-TTT-TTT-TAG-TCC-GTG-GTA-GGG-CAG-GTT-GGG-GTG-ACT	-biotin

Table i: Sequences of α-thrombin specific aptamer thr1 and its complementary sequence oligonucleotide thr1c. Thr2 sequence is used latter as a negative control. Reagents used in this work are from Eurogentec (Belgium). They have a poly-T spacer in 5'.

The protocol for coupling the oligonucleotides in 5' with a thiol or biotin group molecule (Figure 3.16) is inspired from references[49,53,54]. Spacers bearing either a thiol or a biotin on the one side, and a N-hydroxysuccinimide (NHS) activated ester at the other side, are used so that the primary amine group at the 5' extremity of the oligonucleotide reacts with the NHS moiety.

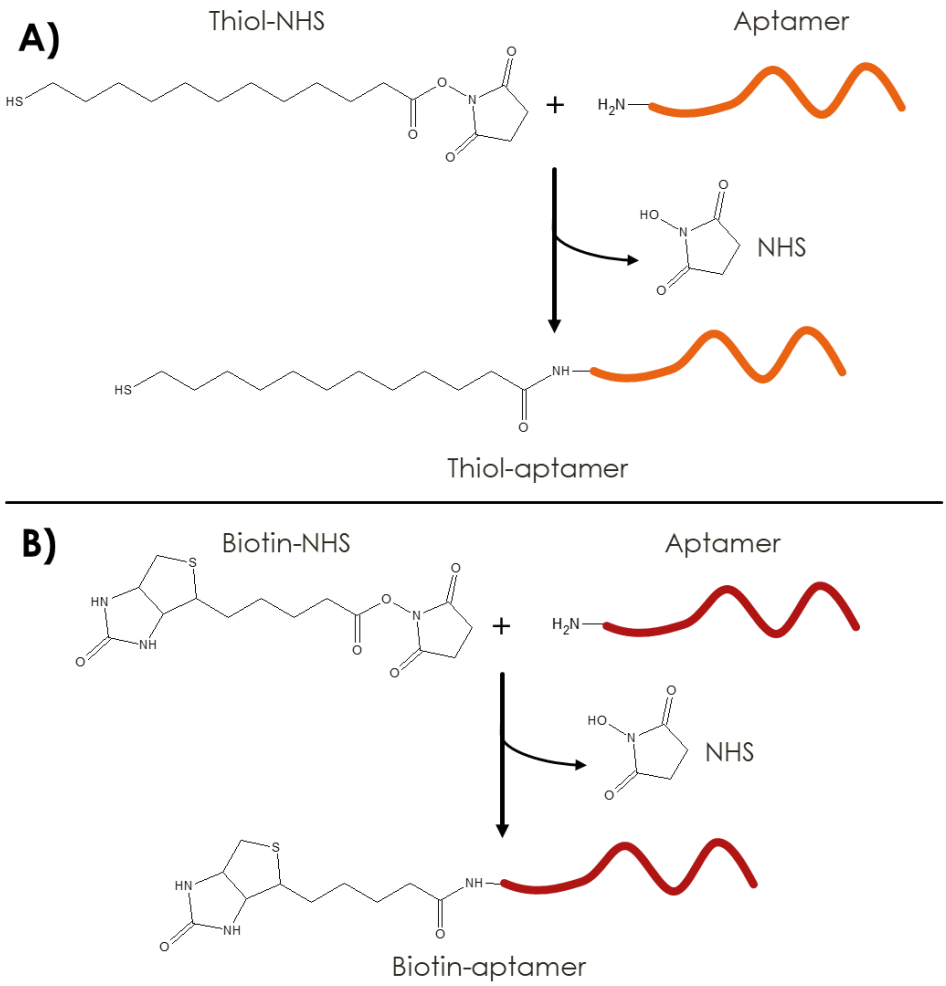

Figure 3.16: A) Thiolation of aptamers. B) Biotinylation of the complementary sequence. In both strategies, the final product results from the reaction between an amine group at the 5' end of the oligonucleotide and a N-HydroxySuccinimide (NHS) activated ester.

As a first step, a solution of spacers (thiol-NHS or biotin-NHS, 1.6 mM) are mixed in large excess with the aminated oligonucleotide (20 µM) in 200 µL PBS (pH 8) . The mixture is then vortexed, centrifuged and left at room temperature for 60 min. Then, the medium is purified using an Illustra Nap-5 column[55] (GE Healthcare, UK). In order to obtain a 100 µM final concentration for the modified oligonucleotides, the concentration of the collected samples is measured with a NanoDrop 2000C spectrophotometer (ThermoFischer Scientific, USA). We gather the two or three most concentrated samples, making sure that the sample purity is correct by checking that the absorbance ratio 260/280 is above 1.8[56]. The obtained aptamer solution is dryed using a SpeedVac Concentrator (ThermoFischer Scientific, USA) and a new stock solution is fabricated at 100 µM in water for storage at -20°C.

3.3.3 Surface Silanization with APTES

Silanization is a widely-used strategy for the chemical functionalization of biochips[57]. A lot of silane derivatives are commercially available bearing different chemical groups for further reactions. The first step of the silanization protocol is the generation of silanol groups on the surface by pretreatment with piranha solution (Appendix II) or oxygen plasma. Then, silanes are added. In this work, we use (3-Aminopropyl)triethoxysilane (APTES) (Figure 3.17 A)), an amino-terminated silane, which has widely been employed for surface functionalization of biochips[58–64]. The silanization process takes place thanks to the hydrolysis of the reactive siloxanes and the formation of covalent bonds with the surface's silanol groups. The last step is the thermal curing that allows crosslinking between silanes on the surface. The different chemical steps are described on Figure 3.17.

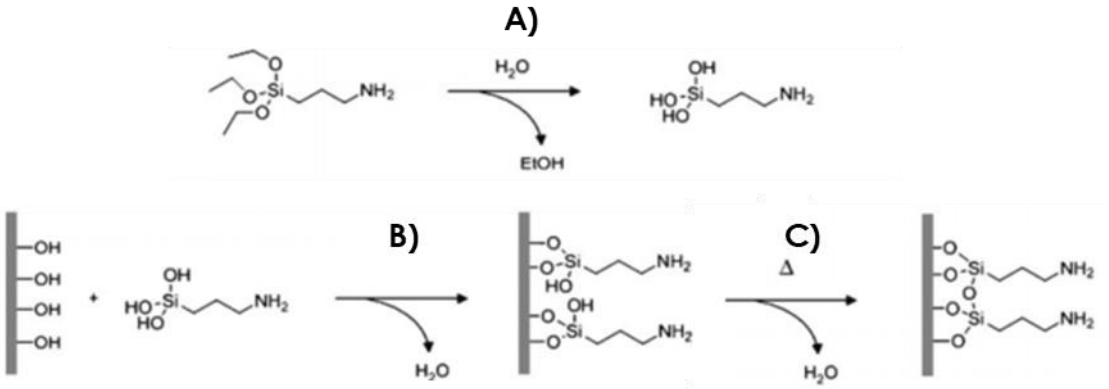

Figure 3.17: Silanization using APTES, adapted from reference[57]. A) Hydrolysis of the reactive siloxanes on the APTES molecule. B) Condensation on the silanol groups at the substrate's surface. C) Cross-linking of the APTES molecule thanks to thermal curing.

The silanization protocol is as follows. First, the SiN_x chip's surface is activated (formation of silanol groups) using an oxygen plasma. The equipment used is a Femto plasma (Diener Electronic, Germany) with a gas composed of dioxygen (75%) and argon (25%) at a 0.6 mbar pressure. The plasma is applied for 3 minutes with a power of 40 W. Then, the sample is immediately immersed in an APTES solution at 2.5% (v/v) in toluene (Sigma Aldrich, USA). The chip is incubated in the solution in a closed dry chamber with calcium crystals for 5 hours. Afterward, the sample is successively rinsed in different bathes. First the sample is rinsed in a toluene bath for 2 minutes, then in an absolute ethanol (VWR, USA) bath for 2 minutes, in an ethanol at 96° (Carlo Erba Reagents, France) bath for another 2 minutes and finally in a bath of distilled water for 2 minutes. The chip is then dried with compressed air and placed in an oven at 110°C for an hour. The silanized surface is now prepared for the functionalization with aptamers.

3.3.4 Surface Functionalization with Thiol Aptamers

Once the SiN_x surface is silanized, the next step is to graft the aptamers. For this purpose, a maleimide-NHS linker (GMBS, N-[γ-maleimidobutyryloxy]succinimide ester) is used. The chemical reaction occurring at the chip surface is described on Figure 3.18. The linker is first added and its NHS moiety reacts with the amino-groups on the surface leading to a maleimide functionalized surface, which allows the grafting of thiolated aptamers.

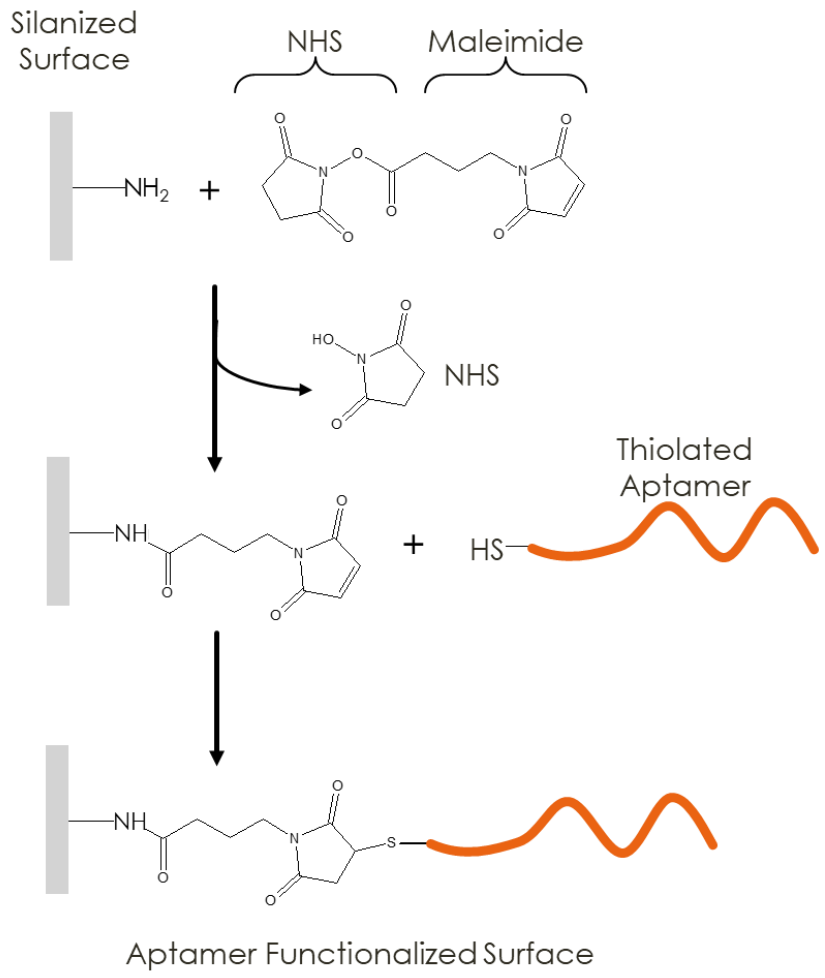

Figure 3.18: Aptamer grafting on the SiN_x aminated silanized surface *via* amaleimide-NHS linker.

The first step is the incubation for 1 hour at room temperature of the silanized chip with a maleimide-NHS crosslinker solution at 0.1 mM in PBS at pH 7.4. Then, several washing steps are necessary to remove the excess of linker. First, the chip is washed five times with PBS at pH 7.4. Then, the sample is rinsed 10 times with distilled water. Finally, the chip is dried with compressed air.

The second step consists in the incubation of the chip in a 10 µM solution of thiolated aptamers in PBS at pH 7.4. 1 µL-droplets of this solution are deposited on the surface and the sample is left for 1 hour in a wet chamber to avoid evaporation. Afterward, the chip is washed 5 times with rinsing buffer

(composition in Appendix II). The following step depends on the purpose of the experiment. If the surface functionalization must be checked, the hybridization with the complementary strand of the aptamer and further fluorescent revelation are performed (cf. next subsection 3.3.5). If the chip is intended to be used as an aptasensor, the experiments can start right away. In the case of nanopore chip functionalization, the procedure must be slightly adapted to functionalize both sides of the chip as well as the inner walls of the nanopore (cf. subsection 3.3.6).

3.3.5 Hybridization with Complementary Strands for Fluorescent Revelation

In order to validate the surface chemistry and prove that aptamers are grafted on the silanized SiN_x surface, hybridization with the complementary strands of the aptamer and fluorescent revelation are performed (cf. Figure 3.15). To do so, biotinylated complementary strands of the aptamers (see subsection 3.3.2 for preparation) are added and SAPE, a fluorescent biotin-binding protein complex is used to specifically reveal the hybridized spots using fluorescence microscopy. Its absorption maximum is at 565 nm and emission maximum at 578 nm.

The biotinylated-oligonucleotides are diluted at 1 µM in hybridization buffer (composition in Appendix II). The whole surface of the chip is covered with this solution and the sample let for 15 min in a humid chamber placed in an incubator at 37°C (Thermostat plus MTP, Eppendorf, Germany). Afterward, the chip is washed 10 times with rinsing buffer (Appendix II). A 5 % (v/v) SAPE solution (initially at 1 mg/mL in commercial medium 0.1 M NaPi, 0.1 M NaCl, 5 mM azide pH 7.5) in rinsing buffer is added on the chip which is placed in a dark humid chamber for 5 minutes. After this incubation, rinsing buffer is used to wash the chip (several times), a glass coverslip is deposited, and the sample is directly observed under a fluorescence microscope (BX60, Olympus, Japan) with a gain parameter of 4, and 0.4 ms acquisition time. The validation of this surface functionalization of SiN_x and the fluorescent revelation will be depicted in Chapter 4.

3.3.6 Specific Experimental Adaptations for a Nanopore Chip

The previously detailed protocol for the surface functionalization of SiN_x with aptamers must be slightly adapted when working on a nanopore chip. The objective is to functionalize the inner walls of the nanopore, the surrounding membrane will also be functionalized (Figure 3.19).

The first step described in subsection 3.3.2 about the aptamer coupling with thiol or biotin remains unchanged. The surface silanisation with APTES (cf. subsection 3.3.3) must be adapted in order to silanize both faces. A 5 mL glass container with a conical sharp bottom (Supelco, USA) allows APTES solution to be in contact with both sides of the chip during the 5-hour incubation (Figure 3.19). The incubation with the cross-linker solution of maleimide-NHS (same concentration as in subsection 3.3.4) is also carried out in the same type of glass container. Then, after drying, the surface functionalization with the aptamers is performed with the chip already mounted in the cassette described in subsection 3.1.4. The 1 µL droplets of 10 µM thiol-aptamers in PBS are deposited in the cones of the cassette on each side of the chip for the incubation. After that, all washing steps are achieved by adding 20 µL of rinsing buffer directly in the cassette on both sides.

At this point, the functionalized nanopore chip can either be used right away for experiments or be stored at 4°C in a 50 mL of storing solution (composition solution in Appendix II).

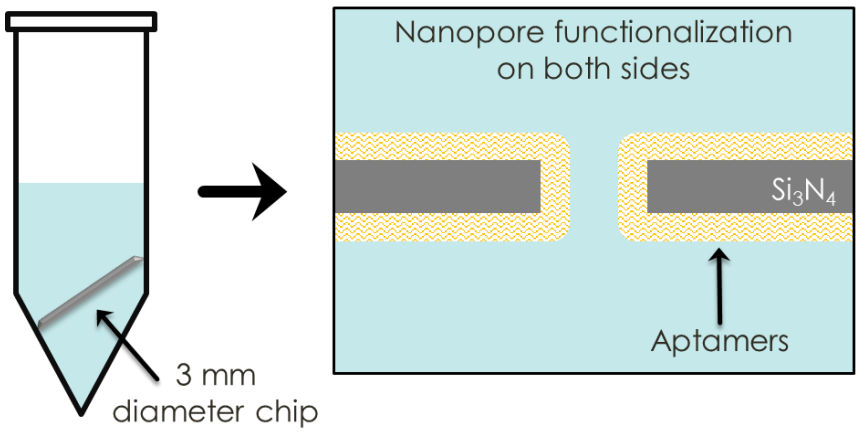

Figure 3.19: Surface functionalization protocol adaptation to a nanopore chip. The APTES silanization and cross-linker maleimide-NHS incubation are performed in a sharp-ended glass container allowing the solution to flow on both sides.

3.4 References

1. Molecular Devices. The Axon Guide: Electrophysiology and Biophysics Laboratory Techniques. 302 (2012).
2. Panasorb - The Foam Company - Foam, Mousse, Espanso. https://www.panasorb.eu/index.php?language=en.
3. Yates, J. Nanopore Solutions. http://www.nanoporesolutions.com/nano/.
4. Norcada Nanopore Products. https://www.norcada.com/products/nanopore-products/.
5. Buck, R. P. Electrochemistry of Ion-Selective Electrodes. in *Comprehensive Treatise of Electrochemistry: Volume 8 Experimental Methods in Electrochemistry* (eds. White, R. E., Bockris, J. O., Conway, B. E. & Yeager, E.) 137–248 (Springer US, 1984).
6. Wanunu, M. Nanopores: A journey towards DNA sequencing. *Phys. Life Rev.* **9**, 125–158 (2012).
7. Molecular Devices. Axon Axopatch 200B Microelectrode Amplifier Datasheet. (2012).
8. Oshana, R. 4 - Overview of Digital Signal Processing Algorithms. in *DSP Software Development Techniques for Embedded and Real-Time Systems* (ed. Oshana, R.) 59–121 (Newnes, 2006).
9. Varongchayakul, N., Song, J., Meller, A. & W. Grinstaff, M. Single-molecule protein sensing in a nanopore: a tutorial. *Chem. Soc. Rev.* **47**, 8512–8524 (2018).
10. Rosenstein, J. K., Wanunu, M., Merchant, C. A., Drndic, M. & Shepard, K. L. Integrated nanopore sensing platform with sub-microsecond temporal resolution. *Nat. Methods* **9**, 487–492 (2012).
11. Uram, J. D., Ke, K. & Mayer, M. Noise and Bandwidth of Current Recordings from Submicrometer Pores and Nanopores. *ACS Nano* **2**, 857–872 (2008).
12. Larkin, J., Henley, R. Y., Muthukumar, M., Rosenstein, J. K. & Wanunu, M. High-Bandwidth Protein Analysis Using Solid-State Nanopores. *Biophys. J.* **106**, 696–704 (2014).
13. Shekar, S., Niedzwiecki, D. J., Chien, C.-C., Ong, P., Fleischer, D. A., Lin, J., Rosenstein, J. K., Drndić, M. & Shepard, K. L. Measurement of DNA Translocation Dynamics in a Solid-State Nanopore at 100 ns Temporal Resolution. *Nano Lett.* **16**, 4483–4489 (2016).
14. Argentier, L. Python Programming to Streaming Data from a PC Oscilloscope. *ENSE*^{3} (2019).

15. Raillon, C., Granjon, P., Graf, M., J. Steinbock, L. & Radenovic, A. Fast and automatic processing of multi-level events in nanopore translocation experiments. *Nanoscale* **4**, 4916–4924 (2012).

16. Laboratory of Nanoscale Biology (LBEN). OpenNanopore software ressources (Matlab). *EPFL* https://www.epfl.ch/labs/lben/page-79460-en-html/.

17. Nandivada, S. Characterization of Nanoparticles Using Solid State Nanopores. *University of Arkansas* (2017).

18. Kim, M. J., Wanunu, M., Bell, D. C. & Meller, A. Rapid Fabrication of Uniformly Sized Nanopores and Nanopore Arrays for Parallel DNA Analysis. *Adv. Mater.* **18**, 3149–3153 (2006).

19. Vlassiouk, I., Kozel, T. R. & Siwy, Z. S. Biosensing with Nanofluidic Diodes. *J. Am. Chem. Soc.* **131**, 8211–8220 (2009).

20. Ma, T., Gaigalas, P., Lepoitevin, M., Plikusiene, I., Bechelany, M., Janot, J.-M., Balanzat, E. & Balme, S. Impact of Polyelectrolyte Multilayers on the Ionic Current Rectification of Conical Nanopores. *Langmuir* **34**, 3405–3412 (2018).

21. Wen, C., Zeng, S., Li, S., Zhang, Z. & Zhang, S.-L. On Rectification of Ionic Current in Nanopores. *Anal. Chem.* **91**, 14597–14604 (2019).

22. Krems, M. & Di Ventra, M. Ionic Coulomb Blockade in Nanopores. *J. Phys. Condens. Matter Inst. Phys. J.* **25**, 065101 (2013).

23. Ramírez, P., Apel, P. Y., Cervera, J. & Mafé, S. Pore structure and function of synthetic nanopores with fixed charges: tip shape and rectification properties. *Nanotechnology* **19**, 315707 (2008).

24. Ali, M., Nasir, S. & Ensinger, W. Bioconjugation-induced ionic current rectification in aptamer-modified single cylindrical nanopores. *Chem. Commun.* **51**, 3454–3457 (2015).

25. Jiang, Y., Feng, Y., Su, J., Nie, J., Cao, L., Mao, L., Jiang, L. & Guo, W. On the Origin of Ionic Rectification in DNA-Stuffed Nanopores: The Breaking and Retrieving Symmetry. *J. Am. Chem. Soc.* **139**, 18739–18746 (2017).

26. Siwy, Z. & Fuliński, A. A nanodevice for rectification and pumping ions. *Am. J. Phys.* **72**, 567–574 (2004).

27. Cai, X.-H., Cao, S.-H., Cai, S.-L., Wu, Y.-Y., Ajmal, M. & Li, Y.-Q. Reversing current rectification to improve DNA-sensing sensitivity in conical nanopores. *Electrophoresis* **40**, 2098–2103 (2019).

28. Cai, S.-L., Zhang, L.-X., Zhang, K., Zheng, Y.-B., Zhao, S. & Li, Y.-Q. A single glass conical nanopore channel modified with 6-carboxymethyl-chitosan to study the binding of bovine serum albumin due to hydrophobic and hydrophilic interactions. *Microchim. Acta* **183**, 981–986 (2016).

29. Lin, C.-Y., Ma, T., Siwy, Z. S., Balme, S. & Hsu, J.-P. Tunable Current Rectification and Selectivity Demonstrated in Nanofluidic Diodes through Kinetic Functionalization. *J. Phys. Chem. Lett.* **11**, 60–66 (2020).

30. Lepoitevin, M., Ma, T., Bechelany, M., Janot, J.-M. & Balme, S. Functionalization of single solid state nanopores to mimic biological ion channels: A review. *Adv. Colloid Interface Sci.* **250**, 195–213 (2017).

31. Smeets, R. M. M., Keyser, U. F., Dekker, N. H. & Dekker, C. Noise in solid-state nanopores. *Proc. Natl. Acad. Sci.* **105**, 417–421 (2008).

32. Fragasso, A., Schmid, S. & Dekker, C. Comparing Current Noise in Biological and Solid-State Nanopores. *ACS Nano* **14**, 1338–1349 (2020).

33. Smeets, R. M. M., Keyser, U. F., Wu, M. Y., Dekker, N. H. & Dekker, C. Nanobubbles in Solid-State Nanopores. *Phys. Rev. Lett.* **97**, 088101 (2006).

34. Tabard-Cossa, V., Trivedi, D., Wiggin, M., Jetha, N. N. & Marziali, A. Noise analysis and reduction in solid-state nanopores. *Nanotechnology* **18**, 305505 (2007).

35. Hall, J. E. Access resistance of a small circular pore. *J. Gen. Physiol.* **66**, 531–532 (1975).

36. Kowalczyk, S. W., Grosberg, A. Y., Rabin, Y. & Dekker, C. Modeling the conductance and DNA blockade of solid-state nanopores. *Nanotechnology* **22**, 315101 (2011).

37. Hyun, C., Rollings, R. & Li, J. Probing Access Resistance of Solid-State Nanopores with a Scanning-Probe Microscope Tip. *Small* **8**, 385–392 (2012).

38. Davenport, M., Healy, K., Pevarnik, M., Teslich, N., Cabrini, S., Morrison, A. P., Siwy, Z. S. & Létant, S. E. The Role of Pore Geometry in Single Nanoparticle Detection. *ACS Nano* **6**, 8366–8380 (2012).

39. DeBlois, R. W. & Bean, C. P. Counting and Sizing of Submicron Particles by the Resistive Pulse Technique. *Rev. Sci. Instrum.* **41**, 909–916 (1970).

40. Yusko, E. C., Johnson, J. M., Majd, S., Prangkio, P., Rollings, R. C., Li, J., Yang, J. & Mayer, M. Controlling protein translocation through nanopores with bio-inspired fluid walls. *Nat. Nanotechnol.* **6**, 253–260 (2011).

41. Raillon, C., Cousin, P., Traversi, F., Garcia-Cordero, E., Hernandez, N. & Radenovic, A. Nanopore Detection of Single Molecule RNAP–DNA Transcription Complex. *Nano Lett.* **12**, 1157–1164 (2012).

42. Yusko, E. C., Bruhn, B. R., Eggenberger, O. M., Houghtaling, J., Rollings, R. C., Walsh, N. C., Nandivada, S., Pindrus, M., Hall, A. R., Sept, D., Li, J., Kalonia, D. S. & Mayer, M. Real-time shape approximation and fingerprinting of single proteins using a nanopore - SI. *Nat. Nanotechnol.* **12**, 360–367 (2017).

43. Grover, N. B., Naaman, J., Ben-Sasson, S. & Doljanski, F. Electrical Sizing of Particles in Suspensions: I. Theory. *Biophys. J.* **9**, 1398–1414 (1969).

44. Grover, N. B., Naaman, J., Ben-Sasson, S., Doljanski, F. & Nadav, E. Electrical Sizing of Particles in Suspensions: II. Experiments with Rigid Spheres. *Biophys. J.* **9**, 1415–1425 (1969).

45. Smeets, R. M. M., Keyser, U. F., Krapf, D., Wu, M.-Y., Dekker, N. H. & Dekker, C. Salt Dependence of Ion Transport and DNA Translocation through Solid-State Nanopores. *Nano Lett.* **6**, 89–95 (2006).

46. Talaga, D. S. & Li, J. Single-Molecule Protein Unfolding in Solid State Nanopores. *J. Am. Chem. Soc.* **131**, 9287–9297 (2009).

47. Muthukumar, M. Communication: Charge, diffusion, and mobility of proteins through nanopores. *J. Chem. Phys.* **141**, 081104 (2014).

48. Bock, L. C., Griffin, L. C., Latham, J. A., Vermaas, E. H. & Toole, J. J. Selection of single-stranded DNA molecules that bind and inhibit human thrombin. *Nature* **355**, 564–566 (1992).

49. Daniel, C., Roupioz, Y., Gasparutto, D., Livache, T. & Buhot, A. Solution-Phase vs Surface-Phase Aptamer-Protein Affinity from a Label-Free Kinetic Biosensor. *PLOS ONE* **8**, e75419 (2013).

50. Zammatteo, N., Jeanmart, L., Hamels, S., Courtois, S., Louette, P., Hevesi, L. & Remacle, J. Comparison between Different Strategies of Covalent Attachment of DNA to Glass Surfaces to Build DNA Microarrays. *Anal. Biochem.* **280**, 143–150 (2000).

51. Halperin, A., Buhot, A. & Zhulina, E. B. Hybridization at a Surface: The Role of Spacers in DNA Microarrays. *Langmuir* **22**, 11290–11304 (2006).

52. Balamurugan, S., Obubuafo, A., Soper, S. A. & Spivak, D. A. Surface immobilization methods for aptamer diagnostic applications. *Anal. Bioanal. Chem.* **390**, 1009–1021 (2008).

53. Daniel, C., Roupioz, Y., Livache, T. & Buhot, A. On the use of aptamer microarrays as a platform for the exploration of human prothrombin/thrombin conversion. *Anal. Biochem.* **473**, 66–71 (2015).

54. Grosjean, L., Cherif, B., Mercey, E., Roget, A., Levy, Y., Marche, P. N., Villiers, M.-B. & Livache, T. A polypyrrole protein microarray for antibody–antigen interaction studies using a label-free detection process. *Anal. Biochem.* **347**, 193–200 (2005).

55. NAP DNA Purification Columns. *GE Healthcare Life Sciences* https://www.gelifesciences.com/en/us/shop/molecular-biology/purification/gel-filtration-columns/illustra-nap-columns-p-00045.

56. Pureté de l'échantillon | Plateforme d'extraction et de qualification des ressources biologiques. https://cit.ligue-cancer.net/bioresources/index.php/la-qualification/la-purete-de-lechantillon/.

57. Jonkheijm, P., Weinrich, D., Schröder, H., Niemeyer, C. M. & Waldmann, H. Chemical Strategies for Generating Protein Biochips. *Angew. Chem. Int. Ed.* **47**, 30 (2008).

58. To, T. D., Nguyen, A. T., Phan, K. N. T., Truong, A. T. T., Doan, T. C. D. & Dang, C. M. Modification of silicon nitride surfaces with GOPES and APTES for antibody immobilization: computational and experimental studies. *Adv. Nat. Sci. Nanosci. Nanotechnol.* **6**, 045006 (2015).

59. Acres, R. G., Ellis, A. V., Alvino, J., Lenahan, C. E., Khodakov, D. A., Metha, G. F. & Andersson, G. G. Molecular Structure of 3-Aminopropyltriethoxysilane Layers Formed on Silanol-Terminated Silicon Surfaces. *J. Phys. Chem. C* **116**, 6289–6297 (2012).

60. Zhu, M., Lerum, M. Z. & Chen, W. How To Prepare Reproducible, Homogeneous, and Hydrolytically Stable Aminosilane-Derived Layers on Silica. *Langmuir* **28**, 416–423 (2012).

61. Ben Haddada, M., Blanchard, J., Casale, S., Krafft, J.-M., Vallée, A., Méthivier, C. & Boujday, S. Optimizing the immobilization of gold nanoparticles on functionalized silicon surfaces: amine- vs thiol-terminated silane. *Gold Bull.* **46**, 335–341 (2013).

62. Sarkar, A. & Daniels-Race, T. Electrophoretic Deposition of Carbon Nanotubes on 3-Amino-Propyl-Triethoxysilane (APTES) Surface Functionalized Silicon Substrates. *Nanomaterials* **3**, 272–288 (2013).

63. Le, T. T. T., Pham, V. T., Phan, T. N. K., Pham, V. B., Le, V. T. & Tong, D. H. Detecting the golgi protein 73 of liver cancer with micro cantilever. *Adv. Nat. Sci. Nanosci. Nanotechnol.* **5**, 045016 (2014).

64. Blinka, E., Loeffler, K., Hu, Y., Gopal, A., Hoshino, K., Lin, K., Liu, X., Ferrari, M. & Zhang, J. X. J. Enhanced microcontact printing of proteins on nanoporous silica surface. *Nanotechnology* **21**, 415302 (2010).

4

Experimental Results

Synopsis

Detecting closely-related proteins in an aptamer-functionalized nanopore with a new experimental bench requires several steps. In this chapter, the bench will be experimentally assessed with pilot experiments such as nanopore characterization and single-event detection of a widely studied target. The surface functionalization by aptamers on the surface of silicon nitride will be validated with fluorescent revelation and then with experimental conductance decrease in the nanopore. Finally, the detection of three closely-related proteins will be performed in a bare nanopore and in a functionalized nanopore. The discrimination between those proteins will be performed either using their global current blockage signature or using their single-event signatures.

Table of Contents

4.1 Experimental Objectives

This chapter combines all the relevant experimental milestones and results that are needed for the objective of detecting and discriminating closely-related proteins in an aptamer-functionalized solid-state nanopore.

First, the experimental bench is tested and validated thanks to pilot experiments such as conductance measurements of nanopore. The noise is then characterized in order to check whether the experimental bench setup is appropriate for single-event detection of biomolecule going through a nanopore. A final pilot experiment of single-event detection is performed with the translocation of λDNA in a nanopore.

Surface functionalization with aptamers is first assessed on plane silicon nitride (SiN_x) with fluorescent revelation, and then in a solid-state nanopore with the measurement of a nanopore's conductance and diameter monitoring before and after functionalization. Noise is also compared before and after functionalization to check the effect of aptamer grafting at the surface of the nanopore.

The single-event detection of closely-related proteins, prothrombin, α-thrombin and ɣ-thrombin, is then performed. First in a bare SiN_x nanopore and after, in a nanopore bearing aptamers specific for α-thrombin. Prothrombin is expected to be discriminated from α-thrombin and ɣ-thrombin because of its bigger size and thus bigger current drop amplitude. ɣ-Thrombin is a modified α-thrombin protein lacking the aptamer binding epitope and is not expected to interact with the aptamers. We don't expect to be able to discriminate α-thrombin from ɣ-thrombin in naked nanopore as they are proteins with a similar volume. With a dwell-time analysis of proteins going through the aptamer-functionalized nanopore, we expect to be able to discriminate α-thrombin from ɣ-thrombin. Finally, measuring I-V curves of the functionalized nanopore before and after insertion of α-thrombin is expected to enable a specific detection of this protein thanks to the monitoring of a diameter decrease.

4.2 Pilot Experiments

4.2.1 Experimental Conductance and Diameter of a Solid-State Nanopore

Figure 4.1 depicts a typical I-V measurement of a 12 nm diameter nanopore for its characterization with our experimental bench. Different voltages are applied, and the current is measured. Plotting the current as a function of the voltage allows the retrieval of a linear domain of the I-V curve due to the resistive properties of the nanopore (cf. subsection 3.2.1 of chapter 3). Therefore, the slope of the I-V curve gives access to a conductance of 0.0121 nA/mV = 12.1 nS. The coefficient of determination R^2 = 0.995 is given for the linear fitting of the curve. R^2 =0.99 means that the I-V curve is close to a perfect linear fit.

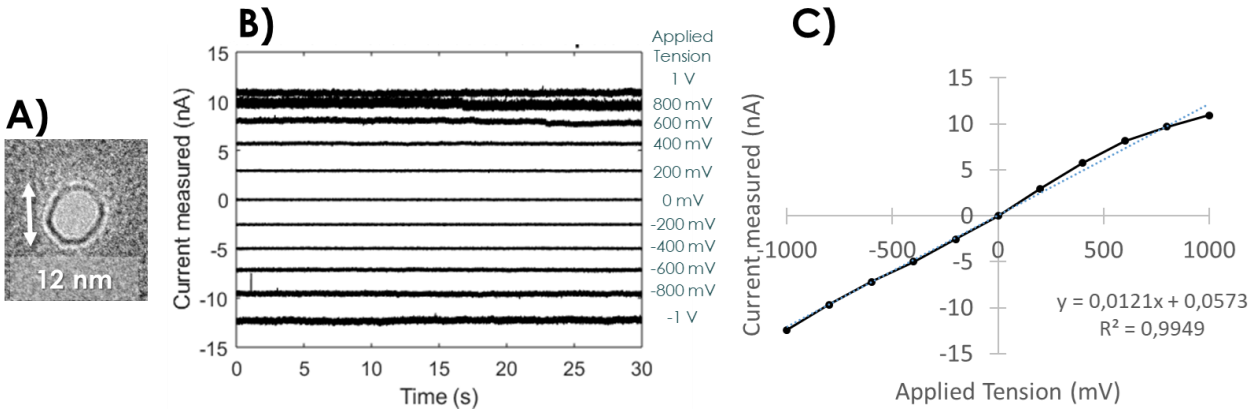

Figure 4.1: Experimental determination of the conductance of a 12 nm diameter nanopore in the buffer for protein and aptamer experiments (Tris-HCl 20 mM, $MgCl_2$ 1 mM, NaCl 120 mM, KCl 10 mM, pH7.4). A) TEM image of the pore. B) Measured current as a function of time for an applied voltage range of [-1 V; +1 V] with a 200 mV voltage step. C) I-V curve of the same nanopore, with current values extracted from B), the slope of this curve fitted by the dotted line gives the nanopore experimental conductance G_{exp}=12.1 nS.

As explained in part 3 of Chapter 3 about the physical properties of ionic conduction in nanopores, we can calculate a range for the theoretical conductance of the pore. G_{th1} is a lower limit considering a cylindrical nanopore and G_{th2} is an upper limit considering an hourglass shaped nanopore. They are given by the following equations:

(9)
$$\begin{cases} G_{th1} = \dfrac{\sigma \pi D^2}{4L} \\ G_{th2} = (L + D)\dfrac{\sigma \pi D}{4L} \end{cases}$$

Where D is the nanopore diameter (12 nm), L is the nanopore thickness (20 nm) and σ is the electrolyte conductivity (0.953 S/m). The obtained theoretical conductance range is [5.4 - 14.4] nS and the experimental conductance G_{exp}=12.1 nS is consistent with it.

Retrieving an experimental diameter is an important step in this work. It is a key for monitoring whether the surface functionalization of the nanopore has been successful or not via observed diameter reduction. Combining the experimental nanopore conductance and the equation (10) considering a perfectly cylindrical nanopore allows the determination of an estimated pore diameter.

(10) $$D_{\exp} = \sqrt{\frac{4LG_{exp}}{\sigma\pi}}$$

With the previously-cited example, we had an experimental conductance of G_{exp} = 12.1 nS (Figure 4.1). Therefore, the experimental diameter measured is 18 nm, which is larger than the TEM measurement of 12 nm. It is important to notice that this measurement is subject to approximations and errors. First, the geometry of the nanopore is not perfectly consistent for each drilled nanopore and can affect the conductance measurement[1], we chose to use a cylindrical pore model as an approximation. Moreover, the solution conductivity has been measured only once for each type of electrolyte because of equipment availability. It is prone to variations due to solution preparation. For the sake of accuracy, it would be beneficial to acquire a conductivity measurement instrument such as the conductometer CDM210 (Radiometer Analytical, France) and measure the electrolyte experimental conductivity σ_{exp} before each nanopore experiment. Another possible approximation source when measuring the experimental diameter of a functionalized nanopore is the membrane thickness L and the contribution of the surface chemistry onto this thickness. The calculations performed for the functionalized nanopores in section 4.4.2 were also performed with the thickness L+2x (with x the size of an aptamer) in order to approximate the contribution of this layer on both sides of the membrane but no significant impact were observed on the result. Therefore, the calculation in this section are made taking into account the thickness L. Those errors and approximations must be kept in mind while studying nanopore's diameter variations. For each of our experiments, diameters will be compared only for the same nanopore in the same electrolyte solution in order to observe variations within the same pore in the same conditions.

4.2.2 Experimental Noise of a Solid-State Nanopore

Noise is an important characteristic for nanopore sensing (cf. Chapter 3). It can be experimentally assessed on a Power Spectral Density (PSD) obtained from a Fourier transform of experimental current data. On Figure 4.2 are the PSD of the 30 seconds current measurements described in the previous part for voltages varying between 0 and 800 mV on the 12 nm diameter nanopore in the buffer for protein and aptamer experiments (Tris-HCl 20 mM, $MgCl_2$ 1 mM, NaCl 120 mM, KCl 10 mM, pH 7.4). The PSD calculus is inspired from Raillon *et al.*[2]. They were calculated on 3 000 000 sample long data with the MATLAB function *pwelch* using a 225 504 sample long Hanning window with 75 % overlap.

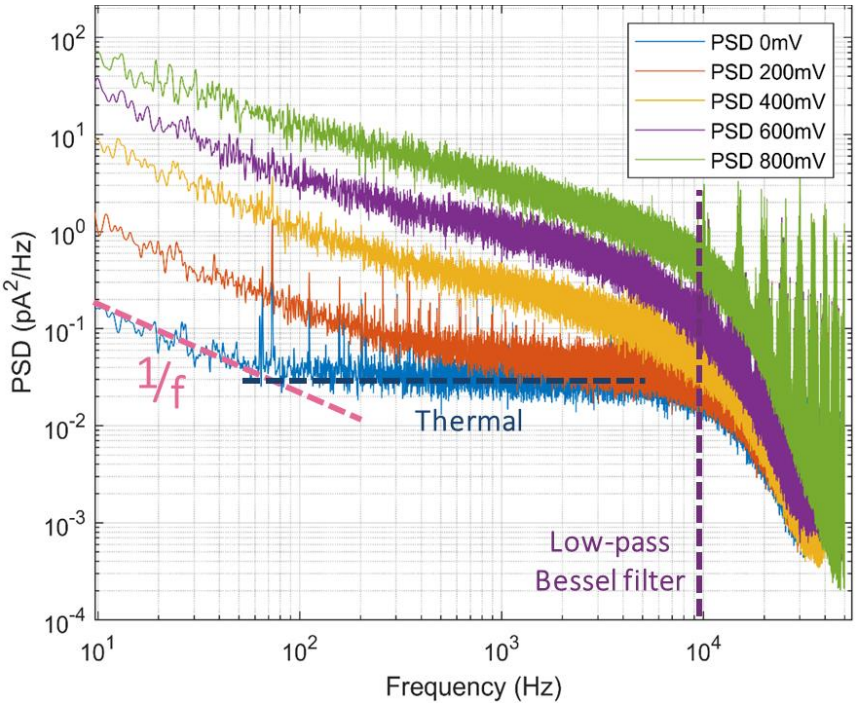

Figure 4.2: Power Spectral Density (PSD) for a 12 nm nanopore at different applied voltages in the buffer for protein and aptamer experiments (Tris-HCl 20 mM, $MgCl_2$ 1 mM, NaCl 120 mM, KCl 10 mM, pH 7.4).

The values of the obtained PSD are in good agreement with the literature[2–6]. When the applied voltage increases, the overall noise increases. It can be up to several orders of magnitudes higher when a voltage is applied compared to when the voltage is equal to 0 mV. In the low frequency range below 1 kHz, we can observe the 1/f dependency of the Flicker noise. This type of noise, as well as the shot noise, is dependent on the current (cf. Chapter 3), which is the reason why the amplitude of the PSD increases with the voltage under 1 kHz. At 0 mV we observe between 100 and 10 kHz a plateau corresponding to the thermal and shot noise. Above 10 kHz, we can observe the noise reduction resulting from the low-pass Bessel filter in the amplifier set to 10 kHz, which reduces the dielectric and capacitive noise contributions to the PSD.

4.2.3 Single-Events Detection of λDNA

Validation of single-events detection with the nanopore experimental setup has been performed first using λDNA. This biomolecule is a 48 502 bp linear double-stranded DNA extracted from a bacteriophage (*cI857 Sam7*)[7]. It has been widely used as a sensing target for nanopore experiments and has well-defined current signatures when going through a nanopore[1,2,8,9] . On Figure 4.3 is presented the TEM image of the 12 nm nanopore used for this experiment as well as its I-V curve characterization. The experimental conductance of the nanopore is equal to 61.9 nS in the buffer used for λDNA translocations (1 M KCl, 1 mM Tris-HCl, 0.1 mM EDTA, pH 8, conductivity 9.78 S/m), which is in the acceptable range of theoretical conductance [55.3 - 147.5] nS calculated with equation (9). Even though the same nanopore is used as for subsection 4.2.1, this measured conductance and theoretical range are different. It is because the conductance is dependent on conductivity of the buffer used.

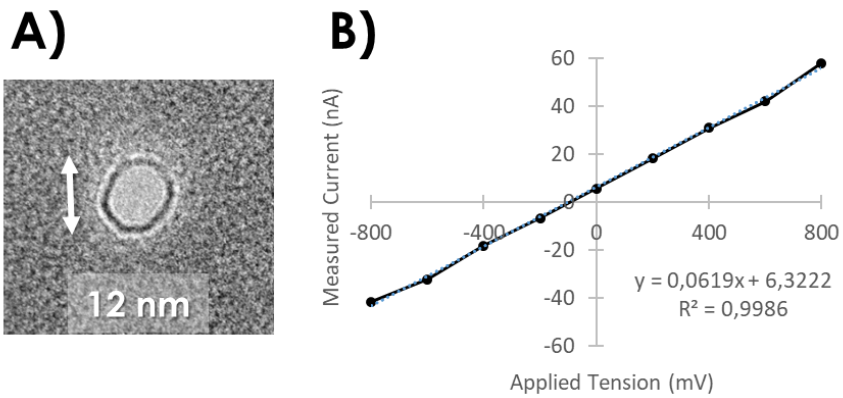

Figure 4.3: A) TEM image of the drilled SiN_x nanopore (12 nm diameter in 20 nm thick membrane). B) I-V curve characterization of the nanopore in the buffer for λDNA translocations (1 M KCl, 1 mM Tris-HCl, 0.1 mM EDTA, pH 8). The experimental conductance Gexp is equal 61.9 nS, obtained with a linear fit (dotted line).

Prior to translocation experiments, the nanopore chip is placed for 3 minutes on each side in a 100°C oven to remove residual humidity and 3 min on each side in an oxygen plasma (Femto, Diener Electronic, Germany) for the removal of organic contaminants. The flow cell and cassette are cleaned with ethanol and deionized water before mounting the chip. λDNA is inserted in the reservoirs at a concentration of 3 ng/µL in the buffer for λDNA translocations (1 M KCl, 1 mM Tris-HCl, 0.1 mM EDTA pH 8.0[8]). The current is measured by placing Ag/AgCl electrodes in each reservoir. The amplifier is used with gain parameters β = 0.1 and α = 1. The 4-pole Bessel low-pass analog filter is set to 10 kHz. The signal is acquired at a 100 kHz sampling frequency. A 200 mV voltage is applied, resulting in an open-pore current of 20 nA. The translocation of λDNA molecules through the nanopore is observed as stepwise decreases in the open pore current level. On Figure 4.4 A) is presented the recorded current

for this 3-minute experiment with roughly 280 events. On Figure 4.4 B) and C) are presented recurrent current shapes of events of λDNA going through the pore in a linear or folded conformation. Those current signatures are typical for λDNA translocation experiments and in good agreement with the literature[9,10]. Current drops are linearly proportional to the applied voltage (see Chapter 3). We observe currents drops at roughly -0.4 nA and -0.8 nA at -200 mV, which are similar to the -0.2 nA and -0.4 nA measured by Raillon *et al.* at -100 mV[2]. The different levels observed inside the events make this dataset a good candidate for an analysis with the CUSUM algorithm in the software OpenNanopore (presented in Chapter 3).

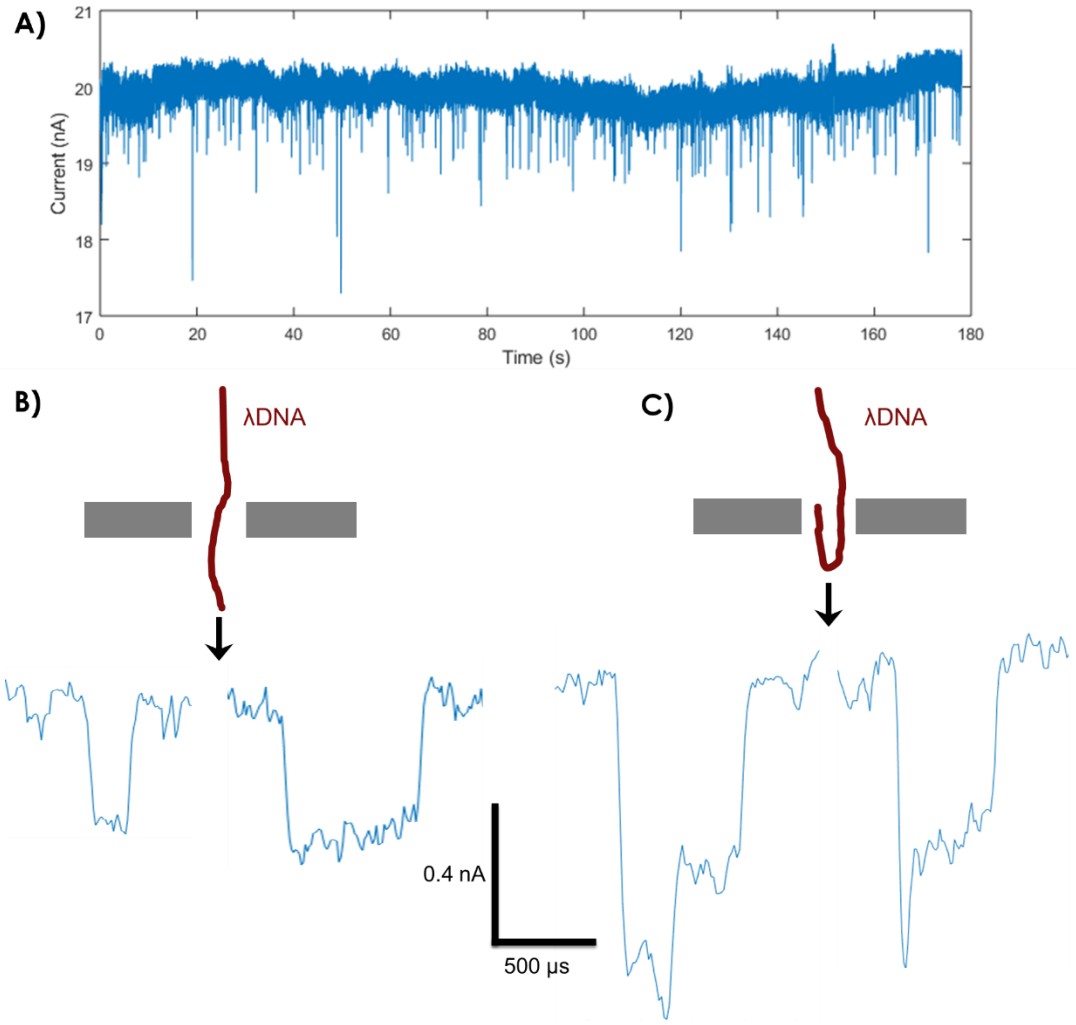

Figure 4.4: A) 3-minute recording of single-events detection of λDNA in a 12 nm diameter SiN_x nanopore. λDNA at 3 ng/µL in the buffer for λDNA translocations (1 M KCl, 1 mM Tris-HCl, 0.1 mM EDTA pH 8.0). B) Illustration and focus on two typical single-events of λDNA going linearly into the pore. C) Illustration and focus on two typical single-events of λDNA going partially folded into the pore.

OpenNanopore software is used with the parameters delta = 0.4 nA, which is a rough approximation of standard current drop observed for the adaptive threshold, and sigma = 0.0639 nA, which is the standard deviation of the signal when there is no event. It has been calculated with the MATLAB *std* function. On Figure 4.5 is displayed a zoom in the concatenated signal of detected events (blue line) and the fitted levels for each event (orange line). With 280 events detected by the software, ~ 75 % are one level events (λDNA going through the pore linearly), ~ 20 % are two level events (λDNA going through the pore with one of its ends folded) and ~ 5% are three levels events (λDNA going through the pore with its middle part folded or both its ends folded).

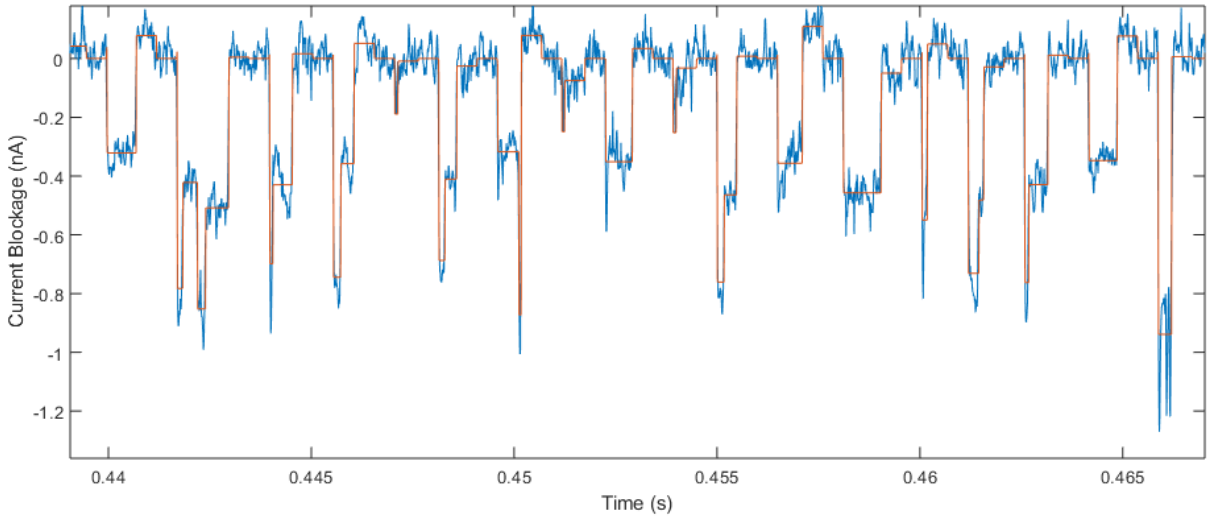

Figure 4.5: Events fitting of λDNA going through the nanopore with OpenNanopore MATLAB software. The current trace is in blue and the fitted levels are in orange. Events have been concatenated.

On Figure 4.6 is presented the statistical analysis of the fitted events by the CUSUM algorithm in OpenNanopore. The histogram A) displays the number of levels fitted for each current blockage, the histogram B) displays the dwell time fitted for each level and on C) is presented the scatter plot of dwell-times and current blockage for each level. Histograms are fitted with a multiple peak Gaussian curve on Origin software in order to find the mean value of the peaks. We find that the most probable current blockages are 0.37 nA (linear DNA) and 0.77 nA (folded DNA) and the most probable dwell times are 90 µs and 450 µs. On the scatter plot, we observe that the longer events are those with the smallest current blockage, hence when the DNA goes linearly through the pore with its full length and spend more time in the nanopore.

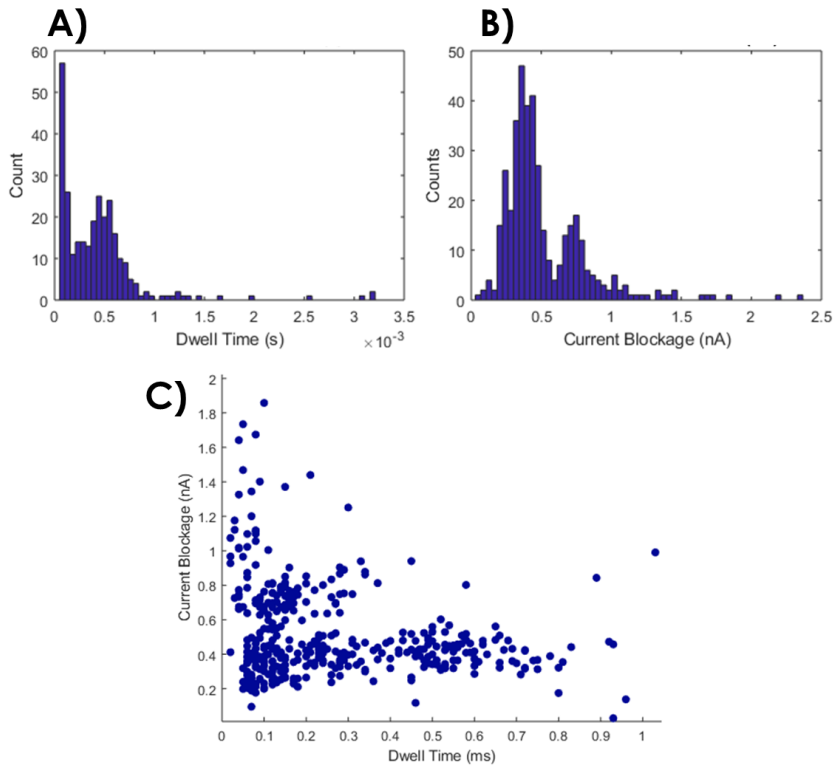

Figure 4.6: A) Current Blockage and B) Dwell Time Histograms for levels of λDNA going through the nanopore fitted with the CUSUM algorithm of OpenNanopore. C) Scatter plot of current blockages versus the Dwell Time.

Current drops are converted into conductance drops with a division by the applied voltage value 200 mV. We obtain ΔG_1 = 1,87 nS for λDNA going linearly in the pore and ΔG_2 = 3.86 nS for folded λDNA. Based on geometrical considerations[1,9] (assuming a cylindrical pore and ignoring edge effects), we can compare the ratio of conductance drop over the experimental conductance G_{exp} (=61.9 nS) and the ratio of the cross-sectional area of double-stranded DNA A_{DNA} (disc of diameter 2 nm) over the pore area A_{pore} (disc of diameter 12 nm). We obtain:

$$\frac{\Delta G_1}{G_{\exp}} = \frac{1.87}{61.9} = 0.031 \rightarrow 3.1\% \quad and \quad \frac{A_{DNA}}{A_{pore}} = \frac{\pi \times 1^2}{\pi \times 6^2} = 0.028 \rightarrow 2.8\%$$

Therefore, the conductance drop is in accordance with the space occupied by double-stranded DNA going linearly in the pore (ratio of conductances = 3.1 % and ratio of cross-sections = 2.8 %). The same concordance of ratio is obtained for ΔG_2 and considering the cross-sectional area of two double-stranded DNA.

The results of the single-event detection of λDNA are concordant with theory (shape of the signal, value of conductance drops). Therefore, we validated that the mounted experimental bench and the TEM fabrication solid-state SiN_x nanopores are suitable for translocation experiments.

4.3 Surface Functionalization

One of the main objectives of this work is to functionalize the membrane and the inner walls of solid-state nanopores with aptamers for the specific recognition of proteins. The grafting protocol has been described in Chapter 3. Briefly, the SiN_x surface is silanized and aptamers are grafted thanks to a cross-linker.

4.3.1 Surface Chemistry on Plane Silicon Nitride

The aim is to validate the aptamer-based surface chemistry on planar SiN_x before transposing it on a nanopore chip. The experimental protocol described previously in Chapter 3 is applied on a 2 cm x 2 cm square plane SiN_x chip (50 nm SiN_x deposited by LPCVD on 725 µm thick silicon substrate). The characterization of the functionalization is achieved using fluorescence microscopy. Briefly, hybridization with biotinylated complementary strand is fluorescently revealed by the addition of SAPE. In order to test the grafting specificity of the aptamer, we use another aptamer sequence called thr2 as a negative control during the hybridization step (sequence in Appendix I). This sequence is not complementary to the surface aptamer thr1.

The results are presented on Figure 4.7. The fluorescence profile is defined as the grey values on a straight line across the dots. The measurement is made on ImageJ software with the "plot profile" tool. A grey value of 0 represents perfect black and 255 a perfect white pixel. We considered spots with a fluorescence grey value above 150 to have thr1 aptamer correctly hybridized with its complementary aptamer thr1c. By comparison, the negative controls spots with thr2 in the hybridization buffer gave gray values of roughly 30. With a fluorescence 5 times superior to the negative controls, we consider that we effectively grafted the thr1 aptamers on the planar SiN_x surface and that we can apply this protocol on nanopore chips.

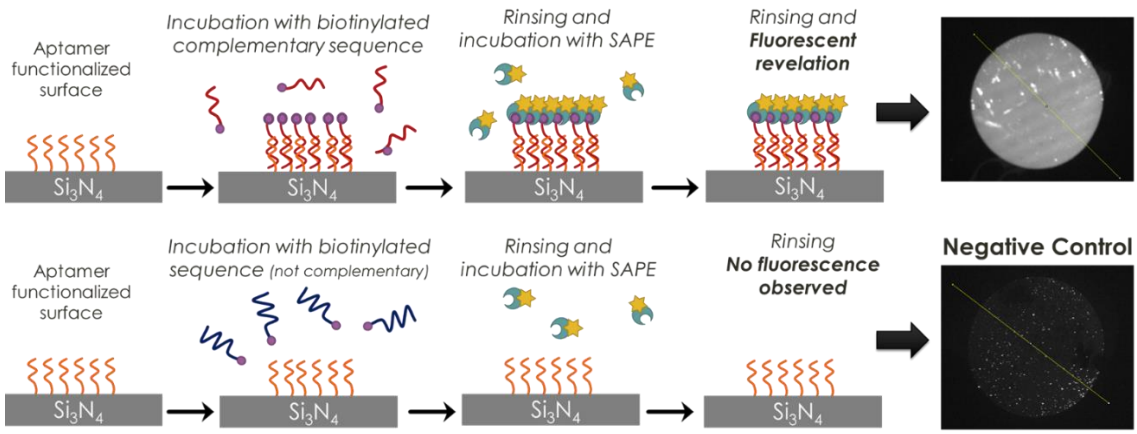

Figure 4.7: Fluorescence results of SiN_x surface functionalization with aptamers. Scheme of the different steps and fluorescent revelation with complementary strands (top) and negative control with non-complementary strands (bottom).

4.3.2 Validation of Nanopore Surface Functionalization

In this work, the surface functionalization of a nanopore is assessed by measuring the experimental conductance decrease and comparing the experimental diameters of the bare and functionalized nanopore. The experimental diameter is given by equation (10) used in subsection 4.2.1. It has been assessed on a ~50 nm diameter commercial nanopore from Nanopore Solutions (Portugal). A TEM representative picture of the ~50 nm diameter nanopores provided by this seller is shown on Figure 4.8 A). We do not have the exact dimensions of the pore. Therefore, we chose to only compare relative experimental conductances and diameters in the same buffer conditions to monitor changes.

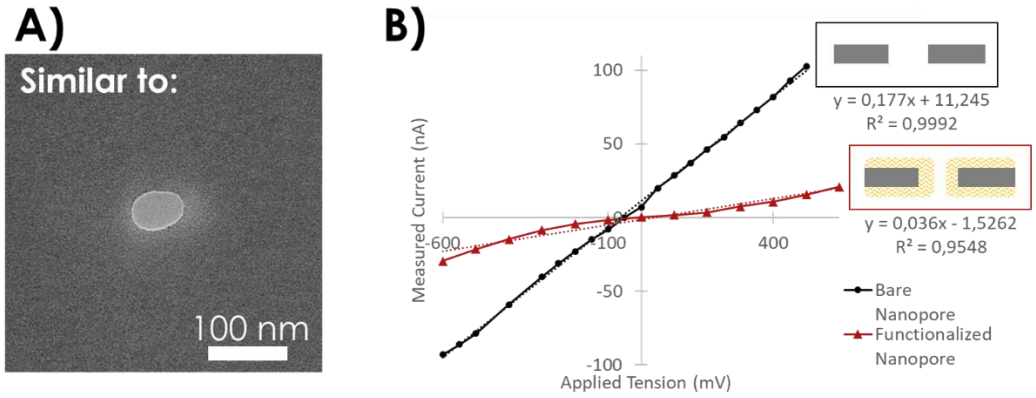

Figure 4.8: Comparison of a ~50 nm diameter nanopore conductance before and after functionalization. A) Representative TEM picture of the nanopore from Nanopore Solutions. B) I-V conductance curves before and after surface functionalization with aptamers (buffer for λDNA translocations: 1 M KCl, 1 mM Tris-HCl, 0,1 mM EDTA, pH 8). Nanopore schemes not to scale.

The experimental I-V curves for the characterization of this nanopore before and after its functionalization are given on Figure 4.8 B). It has been performed in the same buffer as the one for the translocation of λDNA (1 M KCl, 1 mM Tris-HCl, 0,1 mM EDTA, pH 8). For the bare nanopore, an experimental conductance of 177 nS is measured, leading to an experimental diameter of 21 nm (equation (10)). After the functionalization with aptamers, the experimental conductance was lowered to 36 nS, leading to an experimental diameter of 10 nm and thus a decrease of 11 nm. With this experimental decrease in conductance, the functionalization of the inside of the nanopore is confirmed. We have expected a decrease of at least twice the size of the thrombin aptamer[11] (~2 nm x 2 nm). Considering the contribution of the surface silanes, the linkers, the thiol extremity and the poly-T tail of the aptamer sequence (that have not been assessed in this work), the 11 nm diameter decrease seems coherent with the surface chemistry applied in the nanopore.

Ionic Current Rectification (ICR) has been observed in this functionalized nanopore while performing the I-V characterization in a different buffer at a lower salinity and pH (Tris-HCl 20 mM, $MgCl_2$ 1 mM,

NaCl 120 mM, KCl 10 mM, pH 5.2). It is depicted in Figure 4.9. We unfortunately do not have an I-V curve in this buffer before the nanopore functionalization. As explained in Chapter 3 part 2, ICR is triggered by an asymmetry of the pore and a charged surface. In the literature, ICR has been associated with the functionalization of nanopores with DNA[12]. Therefore, observing ICR in this pore suggests that it has been effectively functionalized with the aptamers. This result also suggests that the commercial nanopore is not perfectly symmetrical or more probably that the surface functionalization has not been performed in a symmetrical way. Some hypotheses are made regarding the fact that ICR has mostly been observed in this buffer. The first buffer used (Figure 4.8) is at pH 8, while the second buffer (Figure 4.9) is at pH 5.2. In some studies, ICR has been shown to be pH-dependent[13]. Here, at a low pH, there are more positive charges that can accumulate in the negatively charged nanopore and trigger a bigger rectification[14]. Moreover, Krems *et al.* have suggested that highly charged heavier ions, such as Mg^{2+} in this buffer, could increase ICR[14]. ICR is a good indicator that we successfully functionalized the nanopore with the aptamers that are negatively charged nucleotides. However, the question of the asymmetry remains. It would be interesting to assess the functionalization profile in the nanopore and also to calculate the theoretical Gouy-Chapman length to understand the phenomena.

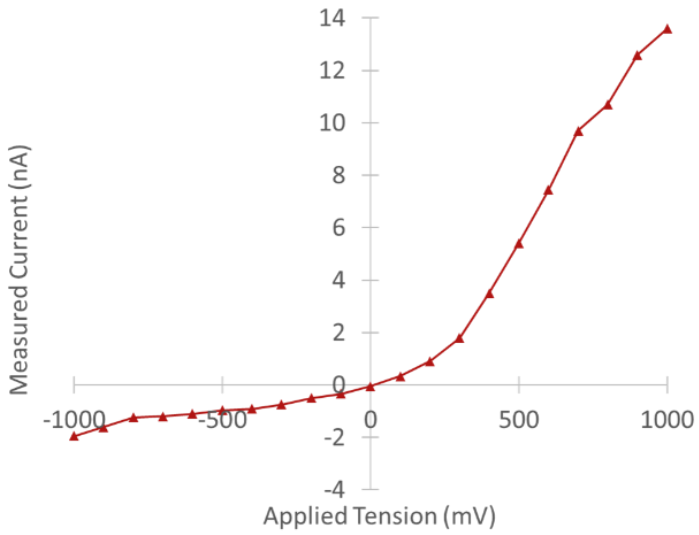

Figure 4.9: Ionic Current Rectification (ICR) in the ~50 nm diameter nanopore functionalized with aptamers. Measurement in buffer Tris-HCl 20 mM, $MgCl_2$ 1 mM, NaCl 120 mM, KCl 10 mM, pH 5.2.

4.3.3 Noise Comparison Before and After Functionalization

Comparing the noise characteristics of a nanopore before and after its functionalization is necessary to assess the impact of surface functionalization on nanopore sensing. We want to make sure that grafting aptamers results at least in the same noise characteristics. On Figure 4.10 are the Power Spectral Densities (PSD) obtained from current recordings of a 12 nm diameter nanopore at 0 mV in the buffer for protein and aptamer experiments (Tris-HCl 20 mM, $MgCl_2$ 1 mM, NaCl 120 mM, KCl 10 mM, pH7.4) before (black) and after its functionalization with aptamers (red). PSD were obtained in the same way as described in part 4.2.2.

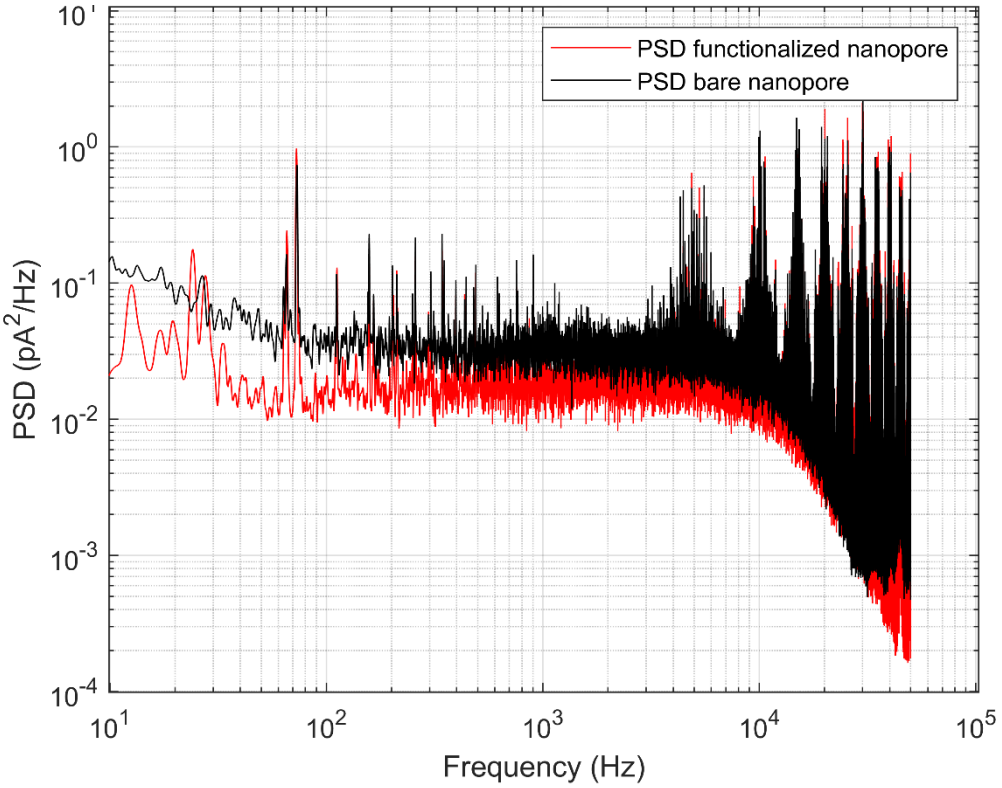

Figure 4.10: Power Spectral Density (PSD) of a 12 nm diameter nanopore measurement at 0 mV in the buffer for protein and aptamer experiments (Tris-HCl 20 mM, $MgCl_2$ 1 mM, NaCl 120 mM, KCl 10 mM, pH7.4) before (black) and after its surface functionalization with aptamers (red).

The functionalized nanopore exhibits a lower level of noise in the low frequency ranges, notably where the 1/f noise and thermal noise prevails. It is hypothesized that 1/f noise in solid-state nanopores originates from a poor wettability and inhomogeneities of its surface[9,15]. Thermal and shot noises (between 10^2 Hz and 10^4 Hz) are dependent on the pore's conductivity and pore's average current (cf. Chapter 3 subsection 3.2.2). Hence, there contribution is lower in the functionalized nanopore thanks to its reduced diameter. Therefore, we can assume that the surface condition of the functionalized nanopore has been improved for nanopore sensing. Surface functionalization of solid-state nanopores

had in some studies the effect to reduce noise and enhance signal-to-noise ratio[16–19] but few have been realized with oligonucleotide functionalized nanopores. In 2011, Mussi *et al*. have demonstrated that grafting oligonucleotides on the surface of their nanopore has improved the signal-to-noise ratio for single-molecule sensing of DNA[19]. It would be interesting for the continuation of this work to further assess the effect of aptamer surface functionalization on noise characteristic, for example in different conditions of pore size and buffer compositions.

4.4 Single-Events Detection of Closely-Related Proteins

The translocation of the three target proteins in the bare solid-state nanopore is expected to give specific current blockade signatures according to the protein's volume. Therefore, we expect to be able to discriminate prothrombin (212 nm^3) from α-thrombin and ɣ-thrombin (both at 65 nm^3). Regarding α-thrombin and ɣ-thrombin, we expect the same current blockade and dwell time distribution. In order to discriminate those two proteins, we will need surface functionalization of the nanopore in order to have an influence on their dwell-time.

The buffer for translocation of proteins (Tris-HCl 20 mM, $MgCl_2$ 1 mM, NaCl 120 mM, KCl 10 mM, pH 7.4) originates from the work of Daniel *et al.*[20] in our team who worked on interactions between the thrombin aptamer and α-thrombin. This buffer has a lower salt concentration than the one used in part 4.2.3 for the detection of λDNA. According to the fact that the conductance drops are dependent with the solution's conductivity and that proteins are smaller objects than λDNA, we expect to observe smaller current blockades than the ones observed in the pilot experiment.

4.4.1 Single-Events in a Bare Nanopore

Experimental Conditions

On Figure 4.11 is presented the TEM image of the 14 nm nanopore used for the translocation of proteins in a bare nanopore and its I-V curve characterization. The same nanopore has been used for the three proteins α-thrombin, ɣ-thrombin, and prothrombin presented in this section. The experimental conductance is equal to 9.9 nS in the protein experiments buffer (Tris-HCl 20 mM, $MgCl_2$ 1 mM, NaCl 120 mM, KCl 10 mM, pH7.4), which is in the acceptable range of theoretical conductance [7.3 – 17.8] nS calculated with equation (9).

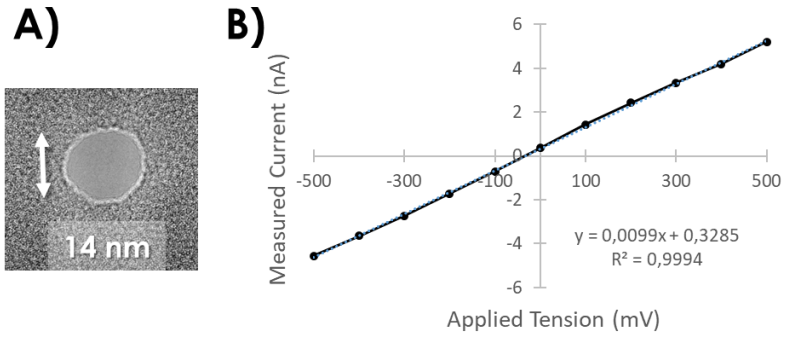

Figure 4.11: A) Figure of the TEM drilled SiN_x nanopore (14 nm diameter, 20 nm thick membrane). B) I-V curve of the nanopore in the buffer (Tris-HCl 20 mM, $MgCl_2$ 1 mM, NaCl 120 mM, KCl 10 mM, pH 7.4). The linear fit (dotted line) gives an experimental conductance Gexp=9.9 nS.

Prior to translocation experiments, the nanopore chip is placed for 3 minutes on each side in a 100°C oven to remove residual humidity and 3 min on each side in an oxygen plasma for the removal of organic contaminants. The flow cell and cassette are cleaned with ethanol and deionized water before mounting the chip. The amplifier is used with gain parameters $\beta = 0.1$ and $\alpha = 1$. The 4-pole Bessel low-pass analog filter is set to 10 kHz. The signal is acquired at a 100 kHz sampling frequency. For each experiment, the proteins are first inserted at a concentration of 1 nM in the buffer for protein and aptamer experiments (Tris-HCl 20 mM, $MgCl_2$ 1 mM, NaCl 120 mM, KCl 10 mM, pH 7.4). If we fail to see single-events in the current trace, the protein concentration is gradually increased until 100 nM. The concentration will be specified for each experiment. Data is recorded until the current baseline is no longer stable, because of pore clogging, for example, or until the number of events is considered as sufficient, in the order of several hundred. Between each experiment, the nanopore is washed with several milliliters of buffer to remove all proteins. Mechanical stirring is added by pipetting up and down in the reservoirs.

Prothrombin

Prothrombin is a 212 nm^3 oblate spheroid protein[21]. Its isoelectric point is 4.8, therefore it is negatively charged at pH 7.4 and we expect it to be electrophoretically driven through the nanopore. It also has a dipole of 1803 Debyes which is oriented perpendicularly to the oblate spheroid (calculated with the protein PDB 6BJR on the online software https://dipole.weizmann.ac.il/dipol/).

A voltage of 200 mV is applied to the bare nanopore described previously, resulting in an open pore current of ~2 nA. Irms is equal to 8.3 pA rms. It is obtained on the amplifier read-out panel. We expect one 212 nm^3 oblate spheroid protein to have a current blockade of ~83 pA or ~55 pA according to its orientation in the nanopore (equation (14) from Chapter 3). Therefore, the signal-to-noise ratio (SNR) is equal to 10 and 6.6 respectively and we expect to be able to observe single-events of prothrombin going through the nanopore. Prothrombin is inserted at a 10 nM concentration in the reservoirs. On Figure 4.12 A) is the current recording of the 3.5 minutes measurement. The data is cut at this duration because almost no more events were observed later. We observe roughly 270 events during this time. However, we observe an unexpected behavior with this sample. With time, the amplitude of the current blockade decreased, from ~200 pA current blockades in the first minute to ~100 pA current blockades in the last minute and almost no events. This was not explained and not observed in other experiments, but some perspectives will be given for further work on this behavior. The single-events current blockage exhibits a peculiar shape with a first deep current blockage (~200 pA) that is only a few points long (~20 µs), and a second level of current blockage which is much smaller (~50 pA) but longer in time (100-200 µs).

The signal is analyzed with the OpenNanopore software for the detection and localization of events in the signal with the parameters delta = 0.1 nA and sigma = 0.0160 nA. We did not use the CUSUM section of the software because it is optimized to detect longer levels into longer events (λDNA typical current signature for example) and was not relevant for this dataset. On Figure 4.12 B) is displayed the concatenated signal of the detected single-events separated with 200 points of the current baseline. Two extracts are presented, one from the first detected events and one from the last detected events. The software detected a total of 269 events. Their mean dwell-time is 130 µs (Figure 4.13 B)).

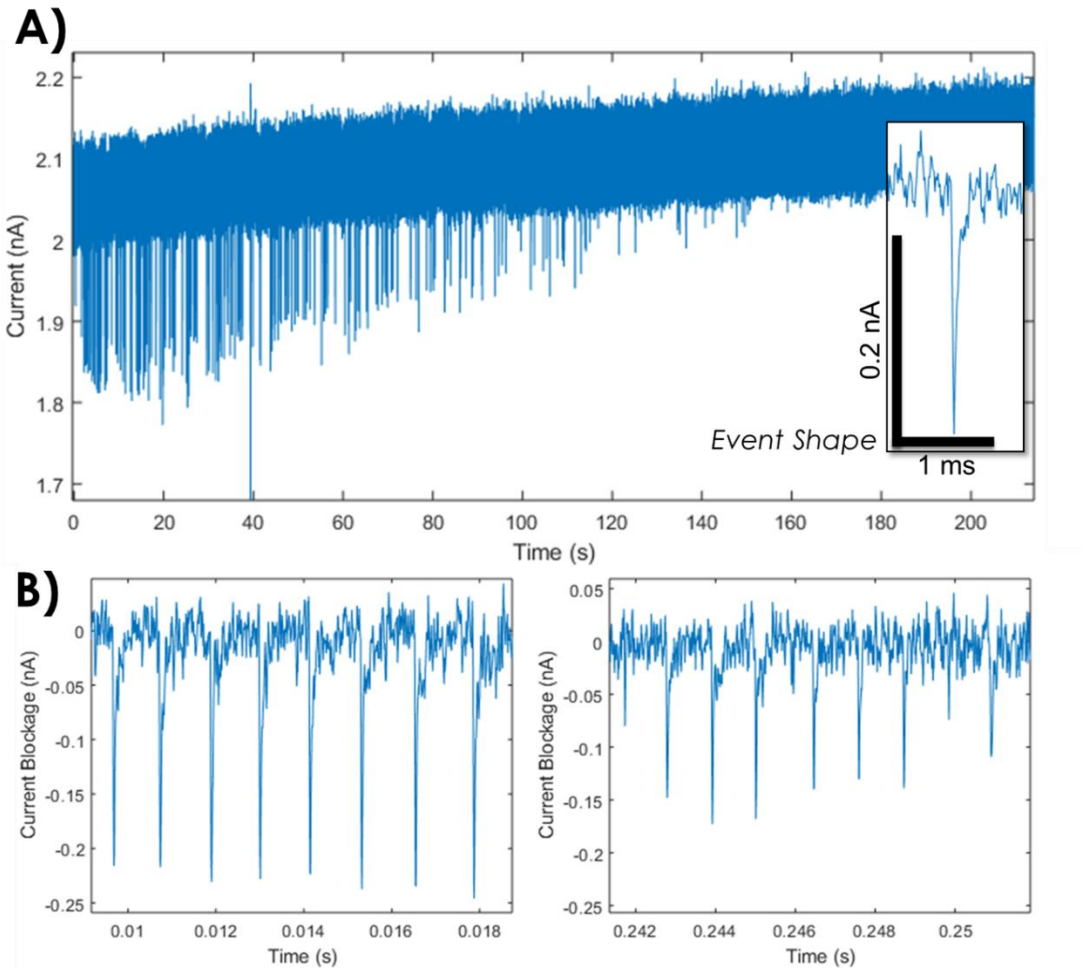

Figure 4.12 : A) 3.5 minutes current recording of 10 nM prothrombin going through a 14 nm diameter bare nanopore at 200 mV in the buffer for protein translocation with an inset of a typical event shape. B) Zoom-in the concatenated signal with only the events detected separated by 200 points of baseline set to 0 nA. Left: firsts events detected in the signal. Right: last events detected in the signal.

Plotting the histogram of the concatenated event's current (without taking the baseline into account) allows the retrieval of the mean current blockage in the nanopore. All current points are represented in this histogram. Therefore, a stronger representation is given on the second small current blockage of each event that is longer and have more points than the deep and short first level. The histogram is

fitted on Origin software with a multi-peak Gaussian analysis. We observe a first current blockage peak ΔI_1 with a mean at 38 pA and a second broader peak ΔI_2 with a mean at 99 pA. The broad 99 pA peak corresponds to the first deep current blockage in an event and the 38 pA peak corresponds to the second smaller and longer current blockage. With a division by the applied voltage 200 mV, those peaks correspond to the conductance drops ΔG_1 = 190 pS and ΔG_2 = 495 pS.

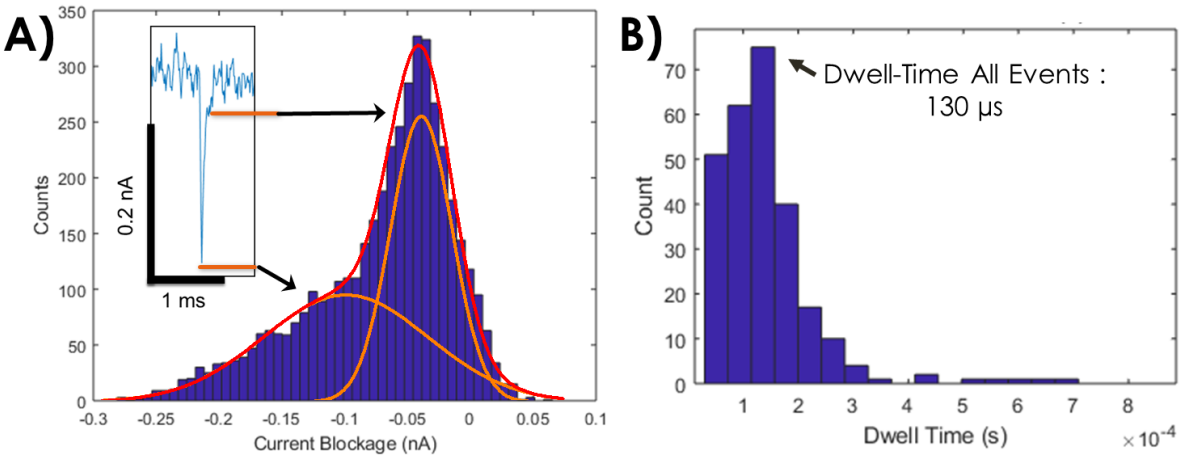

Figure 4.13: A) Current blockages histogram for the concatenated events of prothrombin going through the nanopore. B) Dwell-time histogram of all detected events.

As explained in Chapter 3 part 2, those mean conductance drops can be linked to the volume of the object going through the nanopore. Prothrombin is an oblate spheroid, and two shape factors $\gamma_\perp$ =1.99 (long axis perpendicular to the length of the pore) and $\gamma_\parallel$ =1.34 (long axis parallel to the length of the pore) can be taken into account. As a reminder, the relation linking the conductance drops to the volume of an object going through a nanopore is given by equation (14):

$$\Delta G = \gamma\sigma \frac{V_{excluded}}{{L_{eq}}^2} \quad \text{with} \quad L_{eq} = L + 0.8D \tag{14}$$

With γ the shape factor($\gamma_\perp$ = 1.99 or $\gamma_\parallel$ = 1.34) , σ = 0.953 S/m the conductivity of the solution, L = 20 nm the thickness of the membrane, D = 14 nm the diameter of the pore and $V_{excluded}$ the volume of the object going through the pore. For ΔG_1 = 190 pS, we obtain with $\gamma_\parallel$ a volume corresponding to 145 nm^3 ~ 0.69 x 212 nm^3, which is approximated as the size of one prothrombin (212 nm^3) going through the pore perpendicularly to the pore's length. For ΔG_2 = 495 pS, we obtain with $\gamma_\perp$ a volume corresponding to 254 nm^3 ~ 1.20 x 212 nm^3 which is also approximated as the size of one prothrombin going through the pore in a parallel way.

Reorientation of proteins in nanopores has already been described in the literature[22–27]. Proteins with strong dipolar moments can translocate in a preferred orientation[22]. Prothrombin has a high positive dipole momentum, we hypothesize that it arrives in the nanopore sensing area in an oriented perpendicular position and that its orientation changes to a parallel position while going through the nanopore. The summary of the results and of this hypothesis is given on Figure 4.14.

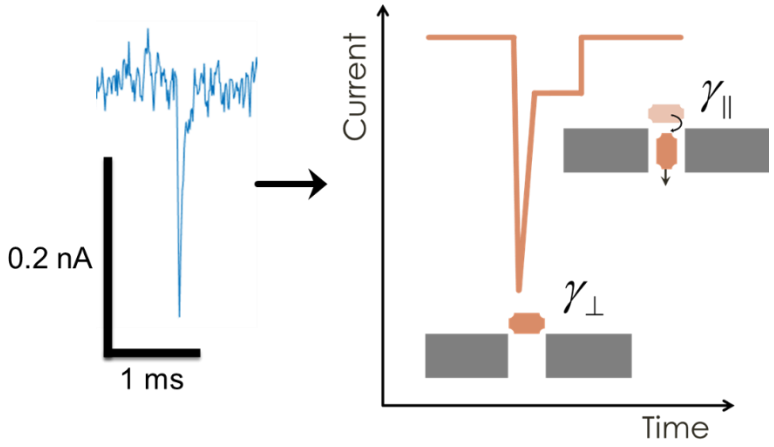

Figure 4.14: Hypothesis for the explanation of the single-events shape for prothrombin going through the nanopore. Prothrombin arrives in a perpendicular way to the pore and is reoriented when going through it.

To go further and understand why the rate of translocation drastically decreased, it would be interesting to calculate the capture radius of the nanopore[28,29] and compare it to the number of prothrombin in the solution within this radius. To do so, we would need the prothrombin diffusion coefficient and electrophoretic mobility in the buffer used for those experiments.

ɣ-Thrombin and α-Thrombin

ɣ-Thrombin[30] and α-thrombin[31] are both 5 nm diameter globular proteins with a volume of 65 nm^3. In the buffer at pH 7.4, ɣ-thrombin's surface is negatively charged (pI=5.63) while α-thrombin's surface is neutral (pI=7.3). This difference makes ɣ-thrombin an easier target because it is electrophoretically driven through the pore thanks to the applied voltage[22]. This section will compare the results of those two different proteins translocation experiments in the same nanopore depicted previously.

For both experiments (ɣ-thrombin and α-thrombin translocation through the nanopore), a 200 mV voltage is applied, in the same manner as presented previously for prothrombin. ɣ-thrombin is inserted at a 1 nM concentration and approximately 540 translocation events are observed during the 15 minutes current recording. In another protein experiment, α-thrombin is inserted at a 10 nM concentration and approximately 600 events are observed during the 20 minutes recording. The signal is analyzed with the OpenNanopore software for the detection and localization of events in the signal with the parameters delta = 0.1 nA, and sigma = 0.02 nA for ɣ-thrombin and 0.0231 nA for α-thrombin. 538 events are detected for ɣ-thrombin experiments, 81 % of which are categorized as impulsions (less than 10 points = 100 µs). 598 events are detected for α-thrombin experiments, with 50 % impulsions. On Figure 4.15 are presented extracts from the concatenated events for both experiments. All are one-level events as expected from globular proteins.

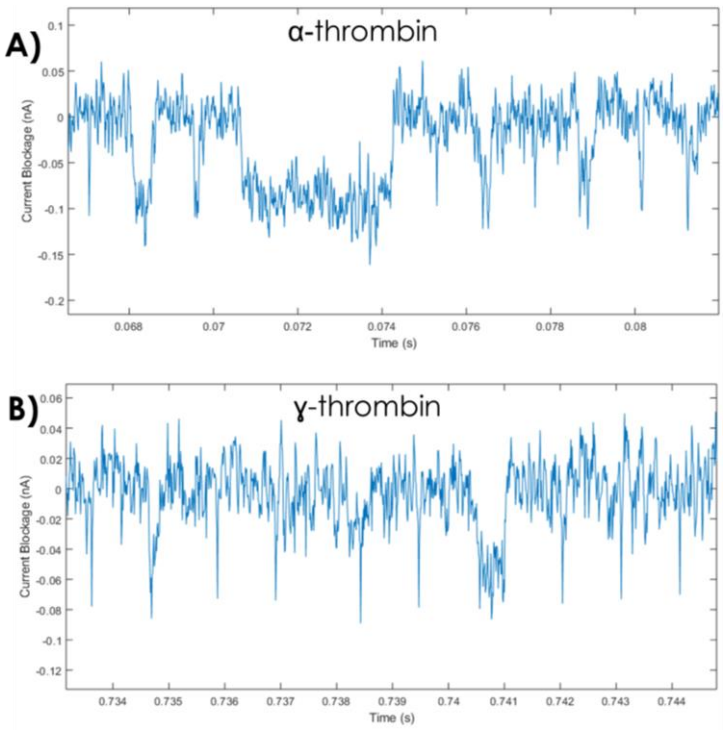

Figure 4.15: Zoom-in the concatenated with only the detected events for A) α-thrombin and B) ɣ-thrombin going through the 14 nm diameter bare nanopore at 200 mV. Baselines set to 0 nA.

On Figure 4.16 are presented the histograms of concatenated event's current without taking the baseline into account. This allows the retrieval of the mean current blockages generated by the translocation of α-thrombin or ɣ-thrombin in the nanopore. A mean current blockage of 74 pA is generated for α-thrombin, and 41 pA for ɣ-thrombin. With a division by the applied voltage 200 mV, the mean conductance drop generated by α-thrombin is 370 pS, and 205 pS for ɣ-thrombin. Those two proteins are approximated as 5 nm diameter spheres (65 nm^3). The nanopore used has a length of 20 nm; therefore the geometrical conformation is closer to the model of a protein in a nanochannel and equation (16) from Chapter 3 is used for the calculation of excluded volumes:

(16) $$\Delta G = \frac{3V_{excluded\ sphere}}{2L^2}\sigma$$

With σ = 0.953 S/m the conductivity of the solution, L = 20 nm the thickness of the membrane. We obtain an excluded volume corresponding to 104 nm^3 ~ 1.6 x 65 nm^3 for α-thrombin and 57 nm^3 ~ 0.9 x 65 nm^3 for ɣ-thrombin. We can approximate that we effectively detected α-thrombin and ɣ-thrombin proteins in the bare nanopore, but as their volume is the same and the conductance drops measured are close, we cannot differentiate those proteins based on conductance drop alone.

The percentage of impulsions among all the detected events is 50 % for α-thrombin and 81 % for ɣ-thrombin. This lower percentage of impulsions for α-thrombin can be explained by the fact that the protein is not charged at pH 7.4 and the voltage applied does not drive the protein in the nanopore. It has been demonstrated in the literature that as the pH approaches the protein's pI, there is an increase in the translocation dwell-time[22,32]. ɣ-thrombin is negatively charged and is quickly drawn across the nanopore. The overall dwell-time distribution for both experiments is given on Figure 4.16. The mean dwell-time for all events (impulsions + standard events) is 75 µs for α-thrombin and 50 µs for ɣ-thrombin. This is in good agreement with protein dwell-times in the literature[33]. The mean dwell time of the two events subcategories is also given. Impulsions (events that are less than 100 µs) are 60 µs and 45 µs long for α-thrombin and ɣ-thrombin, respectively. The overall dwell-time is dominated by the impulsions for both proteins. Standard events are 135 µs long for α-thrombin and 215 µs long for ɣ-thrombin. The fact that standard events are shorter for α-thrombin encounters the discussion held in the beginning of this paragraph and we cannot conclude that the dwell-time allows a discrimination between those two proteins.

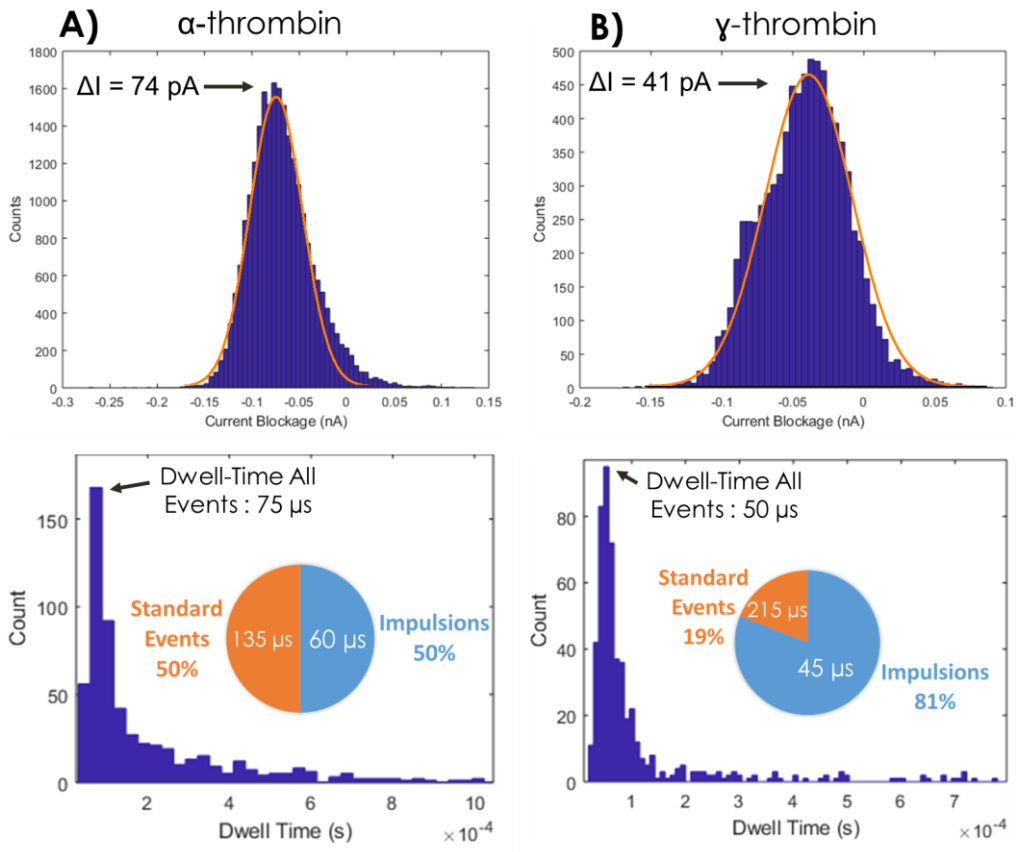

Figure 4.16: Current Blockages histogram of the detected events and dwell-time histogram A) α-thrombin and B) ɣ-thrombin going through the 14 nm diameter bare nanopore at 200 mV.

As a conclusion, the three target proteins have successfully been sensed with the bare nanopore. The current shape of prothrombin was explained by a reorientation of the protein in the nanopore during translocation. Prothrombin's volume is significantly bigger than the one for α-thrombin and ɣ-thrombin. This protein can be discriminated from the two others with the shape and the value of its mean conductance drop (495 pS for prothrombin's deepest conductance drop, 370 pS for α-thrombin and 205 pS for ɣ-thrombin). It would be interesting as a perspective to sense a mixture solution of prothrombin and α-thrombin or ɣ-thrombin in order to validate that they can be discriminated in the same solution. The effects of buffer pH and protein concentrations could be assessed. As expected regarding α-thrombin and ɣ-thrombin, we could not discriminate those proteins with their conductance drops because they have a similar volume. The analysis of their mean dwell-time was not concluding either because their mean dwell-time for all events (75 µs for α-thrombin and 50 µs for ɣ-thrombin) are not significantly different. Surface functionalization is a way to affect the interactions of the proteins with the nanopore's walls, hence a way to increase the dwell-time. In the next part, the results of α-thrombin and ɣ-thrombin sensing in an aptamer-functionalized nanopore will be described. We expect to be able to discriminate those two proteins with their dwell-time.

4.4.2 Single-Events in a Functionalized Nanopore

Experimental Conditions

On Figure 4.17 is presented the TEM image of the same 12 nm diameter nanopore that has been functionalized with aptamers according to the protocol presented in Chapter 3 and that is used for the translocation of α-thrombin and ɣ-thrombin. It is the same nanopore as the one used in part 4.2.3 for the translocation of λDNA. The experimental conductance after functionalization is 1.7 nS in the buffer for protein translocations. It has been measured as an approximation with a linear fitting of the I-V curve, even though this functionalized nanopore does not exhibit an ideally straight I-V curve.

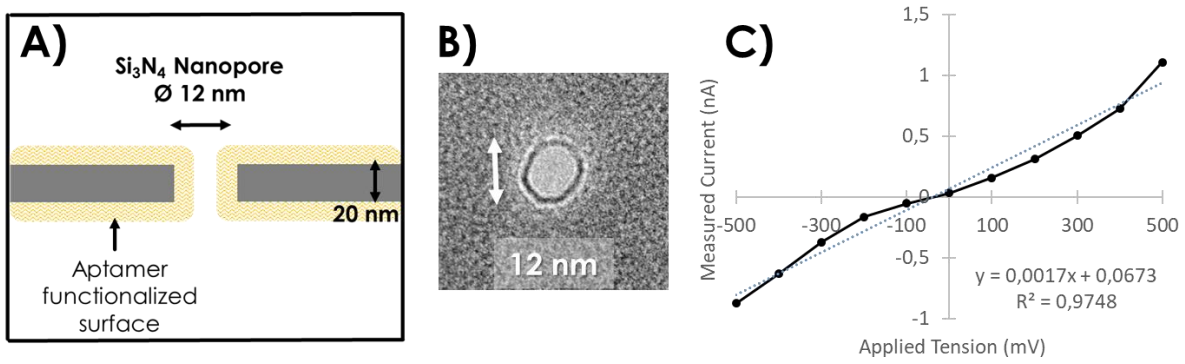

Figure 4.17: A) Scheme of the aptamer-functionalized nanopore. B) Figure of the TEM-drilled SiN_x nanopore before its functionalization (12 nm, 20 nm thick membrane). C) I-V curve of the nanopore in the buffer (Tris-HCl 20 mM, $MgCl_2$ 1 mM, NaCl 120 mM, KCl 10 mM, pH 7.4). The measured conductance Gexp is equal to 1.7 nS.

The nanopore chip is already wet since its functionalization occurs in the cassette. The flow cell is cleaned with ethanol and deionized water before mounting the cassette. The amplifier is used with gain parameters $\beta = 0.1$ and $\alpha = 1$. The 4-pole Bessel low-pass analog filter is set to 10 kHz. The signal is acquired at a 100 kHz sampling frequency. Similarly to the experiments in the bare nanopore, proteins are inserted in the reservoirs with a concentration of 1 nM. If we fail to observe single events, the concentration is gradually increased up until 100 nM. The concentration used for each protein will be specified. In between different protein experiments, nanopore is cleaned at least for 2 hours at a 50 mV voltage with 1 M NaCl buffer for the removal of proteins that interact with the aptamers on the membrane or nanopore's surface. A high NaCl concentration is indeed able to disrupt the G-quadruplex that allows the recognition of the aptamer's target[34]. Nevertheless, α-thrombin experiments are performed last in the case that this would not release all proteins. Between experiments using the same protein, the nanopore is simply washed several times with protein buffer.

ɣ-Thrombin

A 300 mV voltage is applied to the functionalized nanopore described previously, resulting in an open pore current of ~0.6 nA. ɣ-Thrombin is inserted in the reservoirs at a concentration of 1 nM. The current is recorded for 15 minutes and ~220 events are observed. On Figure 4.18 A) is a 3-minute extract of the current recording. The signal is analyzed with the OpenNanopore software for the automatic detection of events with the parameters delta = 0.1 nA and sigma = 0.0208 nA. On Figure 4.18 B) is the obtained concatenated signal with all the detected events. This dataset exhibits relatively long events with different levels, which was not expected from translocations of globular proteins. This makes it an interesting candidate for the use of the CUSUM section of OpenNanopore. Over the 220 detected events ~60 % are then categorized as 1 level events, ~30% are 2-levels events and ~10% are 3-levels events.

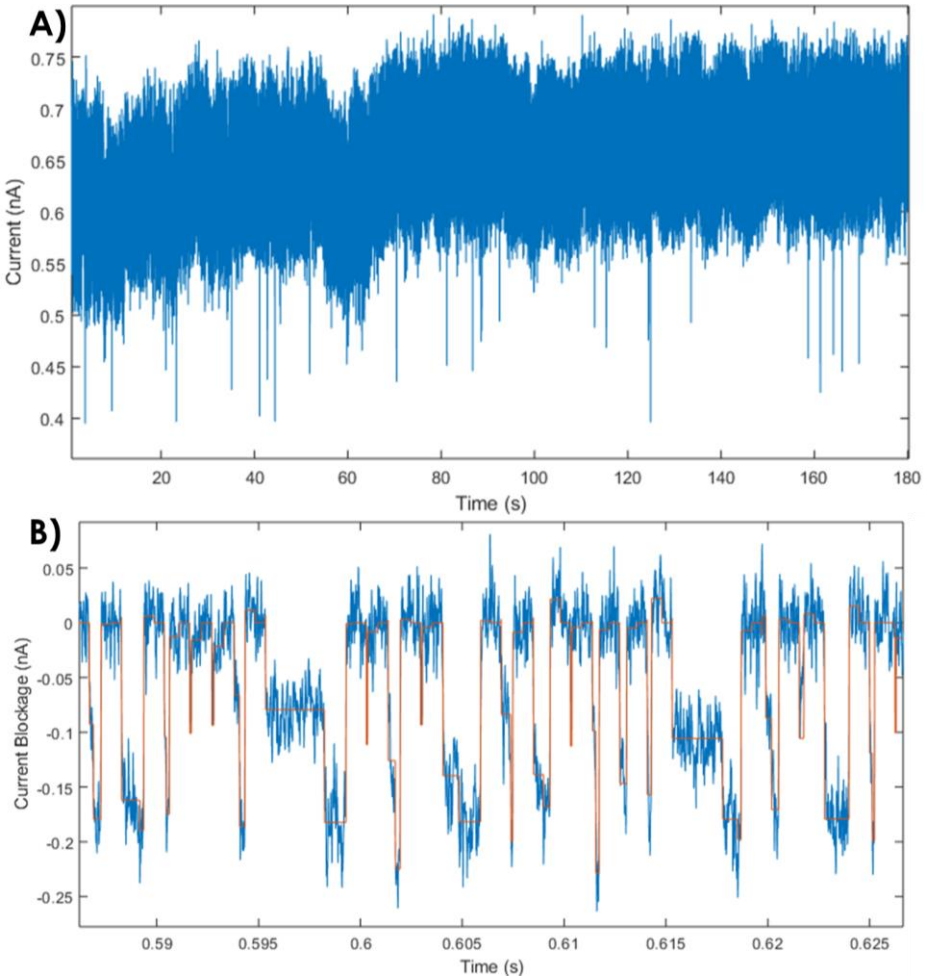

Figure 4.18: A) 3 minutes current recording of 1 nM ɣ-thrombin going through the 12 nm diameter functionalized nanopore at 300 mV in the buffer for protein translocation. B) Zoom-in the concatenated signal with only the events detected separated by 200 points of baseline set to 0 nA. The current trace is in blue and the fitted levels by the CUSUM algorithm are in orange.

The statistical analysis of the fitted levels by the CUSUM algorithm is given on Figure 4.19. Two main populations of current blockages emerge from this graph. With a multiple Gaussian fit on the Origin software, the mean value of the two peaks are ΔI_1 = 99 pA and ΔI_2= 162 pA. When converted into conductance drops, we have ΔG_1 = 330 pS and ΔG_2 = 540 pS. With the model of a globular protein going through a cylindrical nanopore already used in subsection 4.4.1 for α-thrombin and ɣ-thrombin (16), we obtain volumes corresponding to 92 nm^3 ~1.4 x 65 nm^3 and 151 nm^3~2.3 x 65 nm^3, respectively. Therefore, we estimate that those two levels of current blockade correspond to the presence of one and two ɣ-thrombin proteins in the sensing area of the nanopore.

The mean dwell time for all events detected is 160 µs (Figure 4.19). 30 % of all events are categorized as impulsions (less than 10 points), their mean dwell time is 50 µs and they correspond to the smallest current drop ΔI_1. We hypothesize that those current blockages correspond to one protein going through the pore in a fast way without interacting with the walls. The mean dwell time of the 70 % remaining standard events is 413 µs, which is significatively longer. Hence, the standard events correspond to proteins translocating through the pore and interacting with its surface.

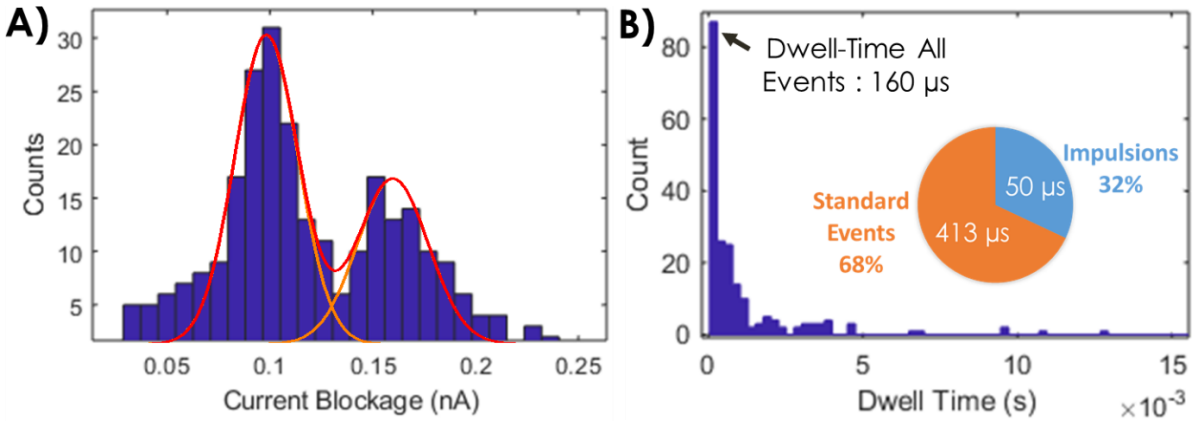

Figure 4.19: A) Histogram count of the current blockage levels fitted by the OpenNanopore CUSUM mode for the 220 events of ɣ-thrombin going through the functionalized nanopore. B) Histogram of the dwell time for all events and repartition of those events between impulsions and standard events.

To go further into the analysis of those two levels of current blockade, we analyze the population of two-level events and observe that 94 % of them exhibit the same feature: the smaller current drop (one protein in the sensing area) is always the first one. Some examples of this shape of two-levels events are present on Figure 4.18 B). This would mean that a first protein arrives in the sensing area of the nanopore and is then followed by a second protein before both translocate fully through the pore. Moreover, the time distribution indicates that ɣ-thrombin's standard events have a longer dwell time in the functionalized nanopore (413 µs) than in the bare nanopore presented previously (215 µs).

It would be more appropriate to compare the translocation of ɣ-thrombin in the same nanopore before and after its functionalization. Nevertheless, we can hypothesize that the negatively charged ɣ-thrombin is electrostatically repulsed by the negatively charged walls of the functionalized nanopore and is slowed down. Hence, those two-level events would be typical of a slowed ɣ-thrombin at the entrance of the pore, which is in turn hit by a second ɣ-thrombin before the two proteins finally translocate along in the pore (Figure 4.20).

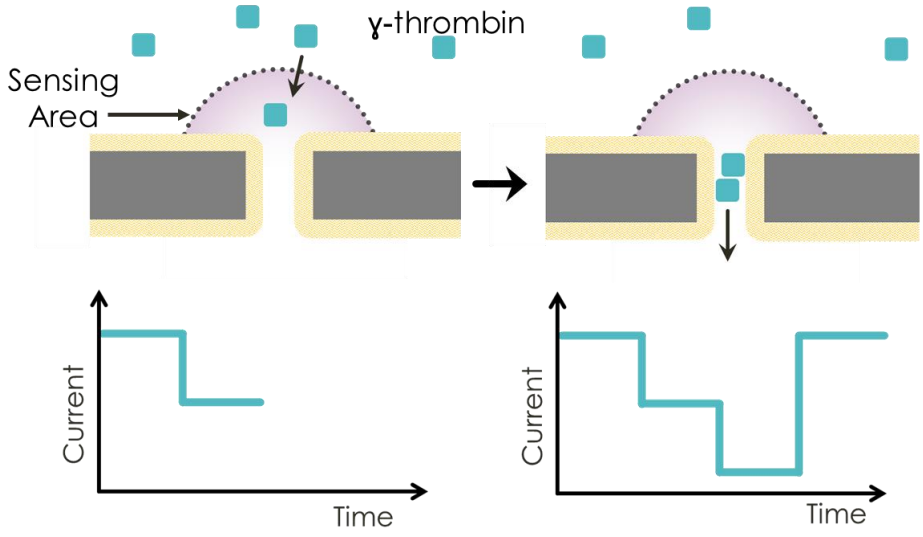

Figure 4.20: Hypothesis of the observed two-level events of ɣ-thrombin going through the functionalized nanopore. A first protein arrives in the sensing zone and is slowed down by the negatively charged walls, before being pushed by another protein and the two translocating through the functionalized nanopore.

α-Thrombin

A 200 mV voltage is applied to the same functionalized nanopore. The reservoirs are filled with 100 nM solution of α-thrombin in the buffer for protein and aptamer experiments. This concentration is 100 times larger than the one used for ɣ-thrombin experiments. An explanation for those large concentrations required to observe single-event translocation might be because α-thrombin binds the aptamers on the membrane's surface, and we need to saturate it before being able to observe single events. Approximately 440 events are observed during the 3 minutes current recording. All the events exhibit a typical 1-level shape that is expected from a globular protein going through a nanopore. The software OpenNanopore is used to detect and locate the events in the current data with the parameters delta= 0.1 nA and sigma = 0.0176 nA. 446 events are detected. As the events do not exhibit different levels, we do not use the CUSUM algorithm section of the software. On Figure 4.21 is an extract of the concatenated events that have been detected. Over all the events, 51 % are classified as impulsions, which is the same value as in the experiment in the bare nanopore.

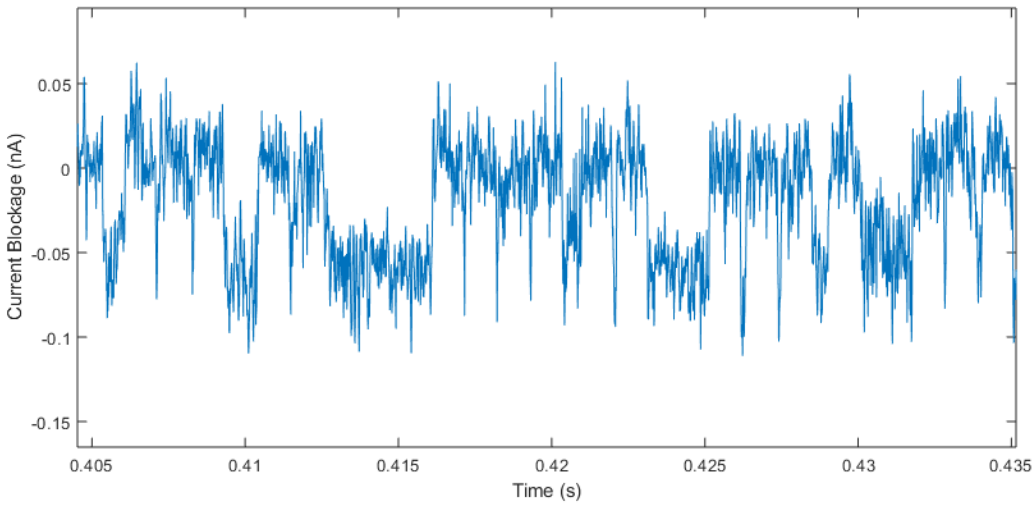

Figure 4.21: α-Thrombin sensing in the aptamer-functionalized nanopore. Zoom-in of the concatenated signal with only the events detected by OpenNanopore (baseline set to 0 nA).

On Figure 4.22 is the current histogram of the concatenated events without the baseline. A Gaussian fit gives a mean value of ΔI = 55 pA for the current blockage of α-thrombin going through the nanopore. The corresponding conductance drop is ΔG = 275 pS (by division with the applied voltage 200 mV). With the model of a globular protein going through a cylindrical nanopore (16), we obtain a corresponding excluded volume of 104 nm^3 ~ 1.2 x 65 nm^3. Therefore, we can estimate that each the events corresponds to one α-thrombin protein effectively sensed by the nanopore.

The dwell-time distribution is given on Figure 4.22 B. The mean dwell-time for all events is 73 µs. Among all those events, 51 % are categorized as impulsions and their mean dwell time is 63 µs. The mean dwell-time of the 49 % standard events is 146 µs.

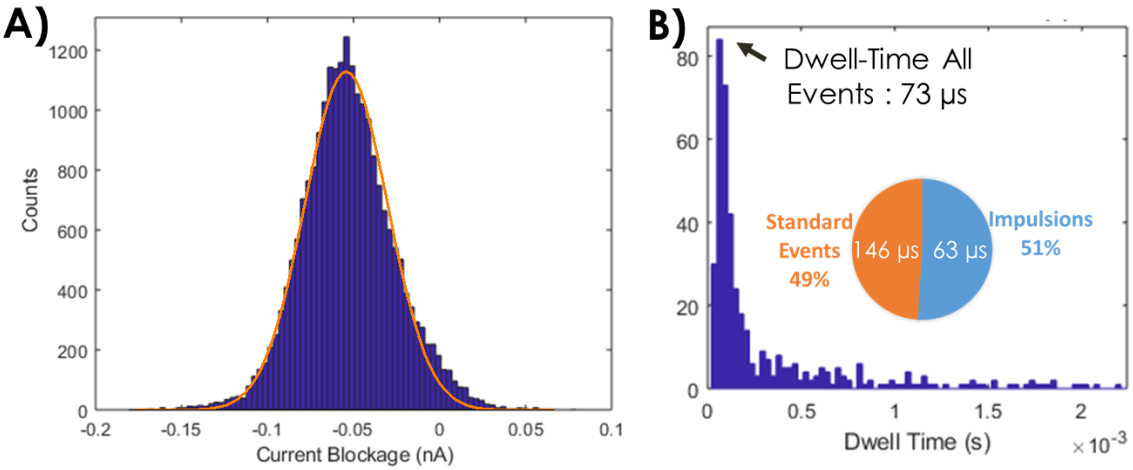

Figure 4.22: A) Current blockages histogram for the concatenated events of α-thrombin going through the functionalized nanopore. B) Dwell-times histogram of all detected events.

The comparison of ɣ-thrombin and α-thrombin dwell-time distributions allows us to check whether the surface functionalization allows a discrimination between the two proteins or not. Surprisingly, ɣ-thrombin is the protein that exhibits a longer dwell-time for all events (160 µs instead of 63 µs for α-thrombin), as well as for the standard events subcategory (413 µs instead of 146 µs for α-thrombin). We were expecting the opposite with α-thrombin interacting with the aptamers grafted in the nanopore. In order to check if there is a competition between the target-aptamer binding and the electrophoretic force applied on α-thrombin, we compare the value from literature of force spectroscopy of α-thrombin-aptamer interaction[35–38] with the calculation of electrophoretic force exerted on the protein[39,40]:

$$F = \frac{qZ \times V}{H_{eq}}$$

With q the elementary charge (1.602 x 10^{-19} C), Z the net charge of the protein, V the applied voltage (= 0.2 V), H_{eq}=H+0.8D with H the thickness of the membrane (20 nm) and D the diameter of the pore (12 nm). We use the diameter value before functionalization as an approximation. α-thrombin is not highly charged at pH 7.4 since its isoelectric point is pI = 7.3. Therefore, in order to calculate the electrophoretic force, we estimate that its net charge is 1 as an approximation. We obtain an electrophoretic force of F= 1.08 pN. The literature gives an aptamer-protein binding force ranging from 4.45 pN to 260 pN in various buffers, which is always higher than the calculated electrophoretic force exerted on α-thrombin. It would be appropriate to measure this force in the buffer used in this work, but it seems that proteins should be able to correctly bind to the surface aptamers and this does not explain why α-thrombin's dwell-time is shorter than ɣ-thrombin. We can hypothesize that the functionalization has a stronger slowing-down effect on negatively charged proteins than uncharged proteins, because of electrostatic interactions with the negatively charged walls such as demonstrated previously with the detection of ɣ-thrombin. As a perspective, it would be interesting to replicate those experiments in the same buffer in order to check the reproducibility of this result, as well as trying in different buffers with different pH in order to observe the effects of protein charge on its dwell-time in functionalized nanopore.

Nevertheless, the detection of ɣ-thrombin has been enhanced in the functionalized nanopore with an overall increase of dwell-time, even though the applied voltage was higher in this experiment (300 mV). This higher voltage should have indeed decreased the translocation time, but we observe the opposite. The percentage of impulsions (very short events of proteins bumping at the surface of the pore or straight and fast into the pore) has decreased from 81 % in the bare nanopore for ɣ-thrombin to 32 % in the functionalized nanopore. The mean dwell-time of the standard events has approximately

doubled from 215 µs in the bare nanopore to 413 µs. Regarding α-thrombin, which is not charged at pH 7.4 and freely diffuse in the buffer without being impacted by the applied voltage, the number of impulsions has remained around 50 % in the bare and functionalized nanopore. The overall dwell-time of all events is 75 µs in the bare nanopore and 73 µs in the functionalized nanopore. The dwell-time of standard events is 135 µs in the bare nanopore and 146 µs in the functionalized nanopore. Those values are close to each other and there is no significant impact of the functionalization on α-thrombin's dwell-time. As a perspective, more studies should be held in buffers at different pH and different salt concentrations in order to observe translocations of charged α-thrombins and non-charged ɣ-thrombins as well.

4.5 Specific Detection of α-Thrombin with Conductance Measurements

Single-event detection is not the only way for functionalized nanopores to detect biomolecules. Several studies use I-V curves in order to monitor surface changes and detect proteins[41–44].

The 50 nm diameter nanopore that has been presented in section 4.3.2 for the validation of surface functionalization with aptamers has also been used for the detection of α-thrombin. On Figure 4.23 is presented its I-V curve characterization in the buffer for protein experiments (Tris-HCl 20 mM, $MgCl_2$ 1 mM, NaCl 120 mM, KCl 10 mM) at pH 5.2 already presented previously. As a reminder, ionic current rectification (ICR) was observed in these conditions due to the negatively charged surface with oligos and probably to a geometrical asymmetry of the nanopore. A 200 nM solution of α-thrombin in the same buffer has been inserted in the reservoirs and an I-V characterization curve have been measured (Figure 4.23). A conductance decrease is observed. We suggest that the diameter of the functionalized nanopore has been reduced due to the binding of α-thrombin proteins with the surface aptamers in the nanopore. Moreover, ICR is no longer observed, which is probably due to the screening effect of α-thrombin that is positively charged at pH 5.2 (pI=7.3) on the negatively charged surface aptamers. Monitoring ICR variations in an aptamer-modified nanopore after the insertion of solutions with different protein concentrations has been used in the literature for the specific detection of proteins[42].

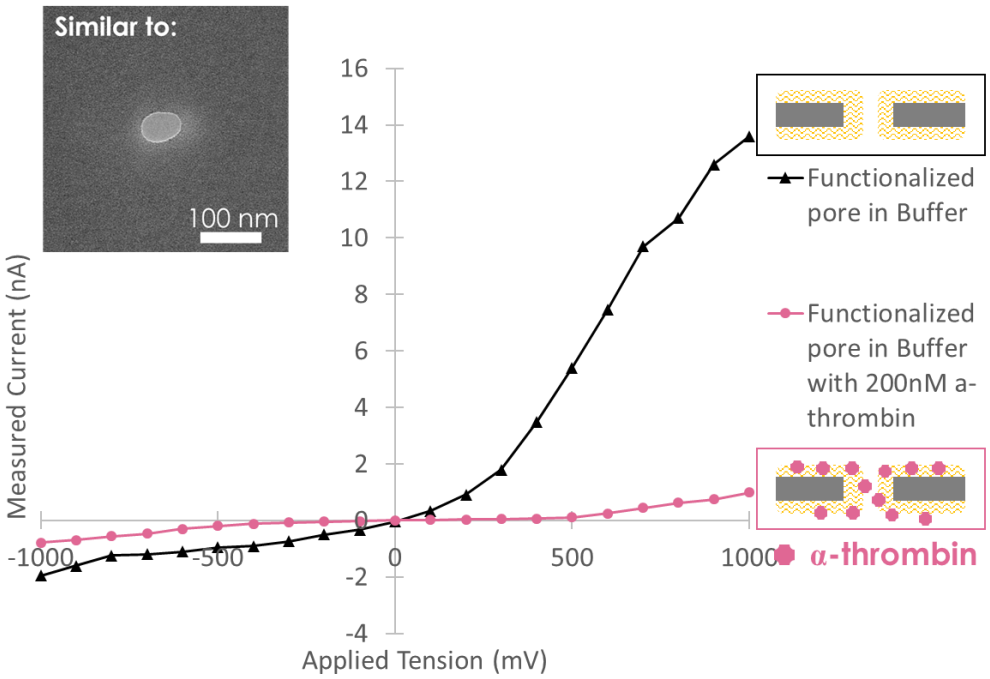

Figure 4.23: I-V characterization of the ~50 nm diameter nanopore functionalized with aptamers before and after insertion of 200 nM α-thrombin in buffer Tris-HCl 20 mM, $MgCl_2$ 1 mM, NaCl 120 mM, KCl 10 mM at pH5.2. Schemes are not to scale.

Extracting the experimental diameter from those experiments would also be a good indicator for the diameter reduction due to α-thrombin binding in the nanopore. Even though it is subject to approximations such as the pore geometry (we consider a cylindrical pore). This has been discussed in part 4.2.1. The experimental conductance of the functionalized nanopore in the 200 nM α-thrombin solution is 0.3 nS, leading to an experimental diameter of 2.3 nm. We cannot extract an experimental conductance from the curve with ICR because of its nonlinear behavior. Previously, in part 4.3.2, an experimental conductance of 36 nS leading to an experimental diameter of 10 nm of this functionalized nanopore had been measured in another buffer that did not trigger ICR (1 M KCl, 1 mM Tris-HCl, 0,1 mM EDTA, pH 8). Keeping in mind all the approximations and the fact that the measurements are made in different buffers, comparing the values of the experimental diameter of the functionalized nanopore before insertion of α-thrombin (10 nm) and after insertion of α-thrombin (2.3 nm) suggests a diameter reduction of ~ 7 nm. This leads us to the conclusion that α-thrombin proteins, which are 5 nm diameter globular proteins, effectively bind the aptamers grafted in the nanopore and that aptamer-functionalized nanopores can be used as a tool for detection of proteins.

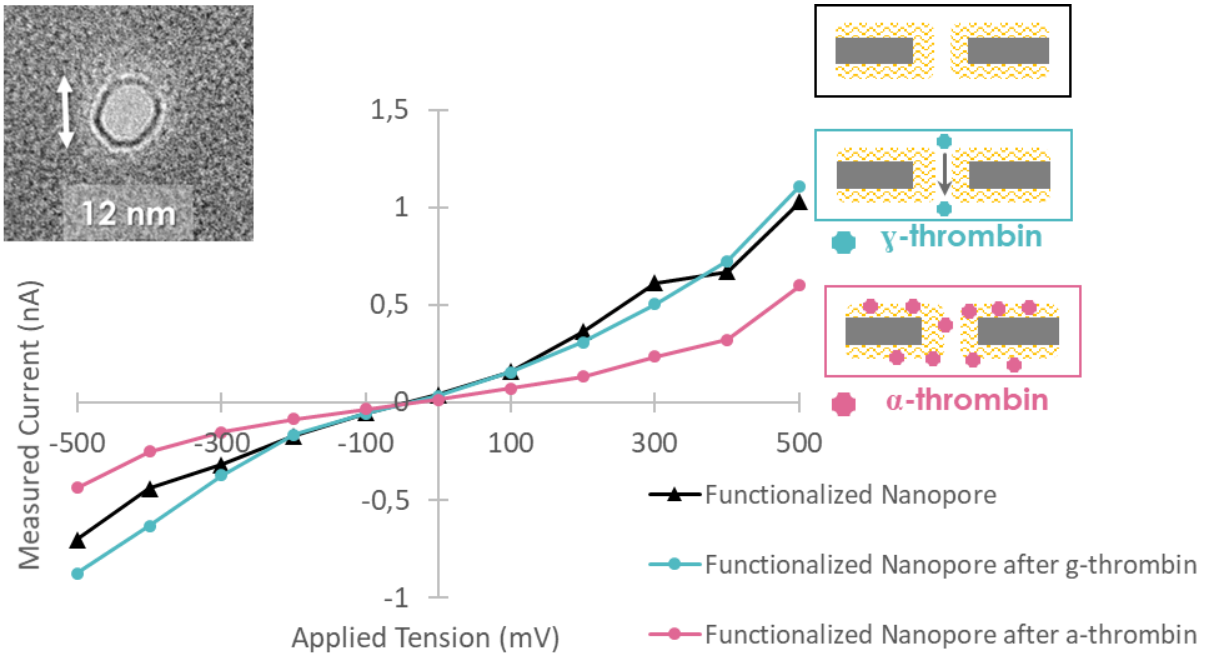

Figure 4.24 : I-V characterization of the 12 nm diameter functionalized nanopore with aptamers in the buffer for protein and aptamer experiments (Tris-HCl 20 mM, $MgCl_2$ 1 mM, NaCl 120 mM, KCl 10 mM, pH 7.4) before insertion of proteins (black), after insertion of 1 nM γ-thrombin (green) and after insertion of 10 nM α-thrombin (pink). Schemes are not to scale.

The specificity of this detection technique is assessed in the 12 nm diameter nanopore that has been functionalized for the single-event detection of α-thrombin and γ-thrombin (section 4.4.2). On Figure

4.24 are different I-V curve characterizations of this functionalized nanopore in the buffer used for protein single-event detection (Tris-HCl 20 mM, $MgCl_2$ 1 mM, NaCl 120 mM, KCl 10 mM, pH 7.4). The curves are linearly fitted even though the functionalized nanopore does not exhibit ideally straight curves. First, one curve is measured in the buffer without proteins, giving an experimental conductance of 1.6 nS and leading to an approximated experimental diameter of 6.6 nm for the functionalized nanopore. A solution containing ɣ-thrombin at a 1 nM concentration in the buffer is inserted in the reservoirs. ɣ-thrombin is the protein that is expected to have no interaction with the aptamer. After 1 hour, I-V curve is measured, giving an experimental conductance of 1.7 nS and an experimental diameter of 6.7 nm. As expected, the overall conductance was not affected by ɣ-thrombin. After rinsing the nanopore with buffer, a solution containing α-thrombin at a 10 nM concentration is inserted. After 1 hour, the experimental conductance has decreased to 0.8 nS, leading to an experimental diameter of 4.6 nm. Therefore, we can hypothesize that one or several α-thrombin proteins have been grafted in or near the entrance of the pore and has triggered this conductance reduction. This highlights the specificity of the aptamer-functionalized nanopore for sensing proteins based on I-V characterization. It would be interesting to perform other experiments in different buffer conditions and with different protein concentrations to assess the detection limit. An I-V characterization can be performed in roughly an hour from sample preparation to the final conductance result. ICR monitoring and conductance decrease in functionalized nanopores can be a good approach for the specific and rapid detection of target proteins.

4.6 Conclusion

The experimental bench built for this thesis work has been effectively tested and validated thanks to pilot experiments. First, the current through a nanopore has been successfully measured with I-V characterization. An estimated experimental pore diameter could be retrieved. Noise has been analyzed and is in good agreement with the literature of solid-state nanopores used for single-molecule detection. Therefore, the setup could be effectively used to sense a widely used biomolecule target: λDNA. Its well-known current signature has been retrieved, with current blockages that coherently match the cross-section area of double-stranded DNA going through the pore. The surface functionalization has been tested on planar SiN_x and validated. Then, it has been tested on nanopores and effectively observed thanks to a conductance decrease. The functionalized nanopore exhibits better noise performances. The single-event detection of prothrombin, α-thrombin and ɣ-thrombin has been performed in a bare nanopore. Prothrombin has been successfully detected with an observed reorientation of this oblate spheroid protein in the nanopore. α-thrombin and ɣ-thrombin have been effectively sensed in the nanopore but could not be differentiated with their current blockage or dwell-time signature. Their detection in an aptamer-functionalized nanopore has allowed a dwell-time discrimination of those two proteins due to different electrostatic interactions with the aptamers. Due to its negatively charged surface, ɣ-thrombin exhibited a longer dwell-time. Finally, another option for the specific detection of α-thrombin has been explored with the monitoring of conductance decrease with α-thrombin interacting with the aptamers on the pore's walls and the observation of ICR behavior changes. On Figure 4.25 is a comparison between the thesis's objectives regarding single-events discrimination of α-thrombin, ɣ-thrombin and prothrombin and the results presented in this chapter. The sensing of prothrombin in a functionalized nanopore is yet to be performed.

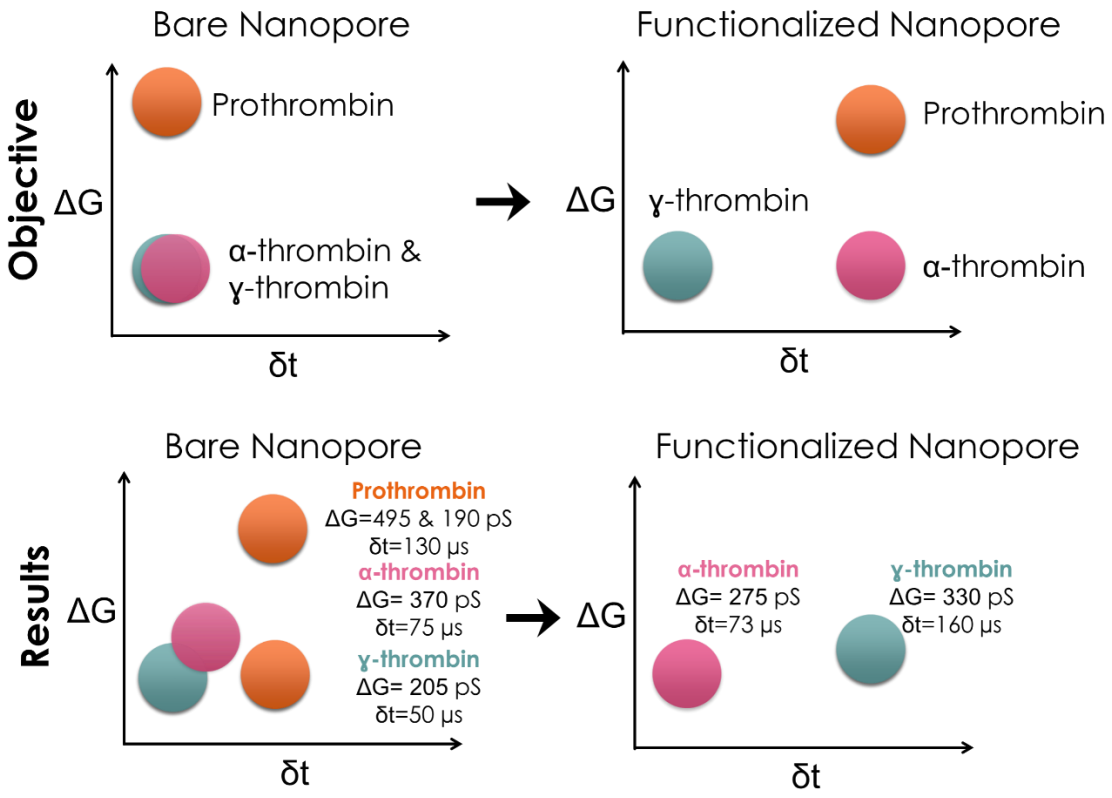

Figure 4.25: Comparison of the thesis's objectives and results regarding the single-event detection of α-thrombin, ɣ-thrombin and prothrombin.

4.7 References

1. Kowalczyk, S. W., Grosberg, A. Y., Rabin, Y. & Dekker, C. Modeling the conductance and DNA blockade of solid-state nanopores. *Nanotechnology* **22**, 315101 (2011).
2. Raillon, C., Granjon, P., Graf, M., J. Steinbock, L. & Radenovic, A. Fast and automatic processing of multi-level events in nanopore translocation experiments. *Nanoscale* **4**, 4916–4924 (2012).
3. Liang, S., Xiang, F., Tang, Z., Nouri, R., He, X., Dong, M. & Guan, W. Noise in nanopore sensors: Sources, models, reduction, and benchmarking. *Nanotechnol. Precis. Eng.* **3**, 9–17 (2020).
4. Fragasso, A., Schmid, S. & Dekker, C. Comparing Current Noise in Biological and Solid-State Nanopores. *ACS Nano* **14**, 1338–1349 (2020).
5. Lee, K., Park, K.-B., Kim, H.-J., Yu, J.-S., Chae, H., Kim, H.-M. & Kim, K.-B. Recent Progress in Solid-State Nanopores. *Adv. Mater.* **30**, 1704680 (2018).
6. Smeets, R. M. M., Keyser, U. F., Dekker, N. H. & Dekker, C. Noise in solid-state nanopores. *Proc. Natl. Acad. Sci.* **105**, 417–421 (2008).
7. Becker, A. & Murialdo, H. Bacteriophage lambda DNA: the beginning of the end. *J. Bacteriol.* **172**, 2819–2824 (1990).
8. Storm, A. J., Storm, C., Chen, J., Zandbergen, H., Joanny, J.-F. & Dekker, C. Fast DNA Translocation through a Solid-State Nanopore. *Nano Lett.* **5**, 1193–1197 (2005).
9. Tabard-Cossa, V., Trivedi, D., Wiggin, M., Jetha, N. N. & Marziali, A. Noise analysis and reduction in solid-state nanopores. *Nanotechnology* **18**, 305505 (2007).
10. Li, J. & Talaga, D. S. The distribution of DNA translocation times in solid-state nanopores. *J. Phys. Condens. Matter* **22**, 454129 (2010).
11. Hidding, J. A therapeutic battle: Antibodies vs. Aptamers. *Nanosci. Master Program* **109**, 20 (2017).
12. Jiang, Y., Feng, Y., Su, J., Nie, J., Cao, L., Mao, L., Jiang, L. & Guo, W. On the Origin of Ionic Rectification in DNA-Stuffed Nanopores: The Breaking and Retrieving Symmetry. *J. Am. Chem. Soc.* **139**, 18739–18746 (2017).

13. Siwy, Z. & Fuliński, A. A nanodevice for rectification and pumping ions. *Am. J. Phys.* **72**, 567–574 (2004).

14. Krems, M. & Di Ventra, M. Ionic Coulomb Blockade in Nanopores. *J. Phys. Condens. Matter Inst. Phys. J.* **25**, 065101 (2013).

15. Smeets, R. M. M., Keyser, U. F., Wu, M. Y., Dekker, N. H. & Dekker, C. Nanobubbles in Solid-State Nanopores. *Phys. Rev. Lett.* **97**, 088101 (2006).

16. Lepoitevin, M., Ma, T., Bechelany, M., Janot, J.-M. & Balme, S. Functionalization of single solid state nanopores to mimic biological ion channels: A review. *Adv. Colloid Interface Sci.* **250**, 195–213 (2017).

17. Eggenberger, O. M., Ying, C. & Mayer, M. Surface coatings for solid-state nanopores. *Nanoscale* **11**, 19636–19657 (2019).

18. Tang, Z., Lu, B., Zhao, Q., Wang, J., Luo, K. & Yu, D. Surface Modification of Solid-State Nanopores for Sticky-Free Translocation of Single-Stranded DNA. *Small* **10**, 4332–4339 (2014).

19. Mussi, V., Fanzio, P., Repetto, L., Firpo, G., Stigliani, S., Tonini, G. P. & Valbusa, U. "DNA-Dressed NAnopore" for complementary sequence detection. *Biosens. Bioelectron.* **29**, 125–131 (2011).

20. Daniel, C., Roupioz, Y., Gasparutto, D., Livache, T. & Buhot, A. Solution-Phase vs Surface-Phase Aptamer-Protein Affinity from a Label-Free Kinetic Biosensor. *PLOS ONE* **8**, e75419 (2013).

21. Chinnaraj, M., Chen, Z., Pelc, L. A., Grese, Z., Bystranowska, D., Di Cera, E. & Pozzi, N. Structure of prothrombin in the closed form reveals new details on the mechanism of activation. *Sci. Rep.* **8**, 2945 (2018).

22. Varongchayakul, N., Song, J., Meller, A. & W. Grinstaff, M. Single-molecule protein sensing in a nanopore: a tutorial. *Chem. Soc. Rev.* **47**, 8512–8524 (2018).

23. Yusko, E. C., Bruhn, B. R., Eggenberger, O. M., Houghtaling, J., Rollings, R. C., Walsh, N. C., Nandivada, S., Pindrus, M., Hall, A. R., Sept, D., Li, J., Kalonia, D. S. & Mayer, M. Real-time shape approximation and fingerprinting of single proteins using a nanopore - SI. *Nat. Nanotechnol.* **12**, 360–367 (2017).

24. Sha, J., Si, W., Xu, B., Zhang, S., Li, K., Lin, K., Shi, H. & Chen, Y. Identification of Spherical and Nonspherical Proteins by a Solid-State Nanopore. *Anal. Chem.* **90**, 13826–13831 (2018).

25. Van Meervelt, V., Soskine, M., Singh, S., Schuurman-Wolters, G. K., Wijma, H. J., Poolman, B. & Maglia, G. Real-Time Conformational Changes and Controlled Orientation of Native Proteins Inside a Protein Nanoreactor. *J. Am. Chem. Soc.* **139**, 18640–18646 (2017).

26. Carlsen, A. & Cossa, V. T. Mapping shifts in nanopore signal to changes in protein and protein-DNA conformation. *bioRxiv Preprint* (2020).

27. Li, Q., Ying, Y.-L., Liu, S.-C., Lin, Y. & Long, Y.-T. Detection of Single Proteins with a General Nanopore Sensor. *ACS Sens.* **4**, 1185-1189 (2019).

28. Wanunu, M., Morrison, W., Rabin, Y., Grosberg, A. Y. & Meller, A. Electrostatic focusing of unlabelled DNA into nanoscale pores using a salt gradient. *Nat. Nanotechnol.* **5**, 160–165 (2010).

29. Plesa, C., Kowalczyk, S. W., Zinsmeester, R., Grosberg, A. Y., Rabin, Y. & Dekker, C. Fast Translocation of Proteins through Solid State Nanopores. *Nano Lett.* **13**, 658–663 (2013).

30. Rydel, T. J., Yin, M., Padmanabhan, K. P., Blankenship, D. T., Cardin, A. D., Correa, P. E., Fenton, J. W. & Tulinsky, A. Crystallographic structure of human gamma-thrombin. *J. Biol. Chem.* **269**, 22000–22006 (1994).

31. Chirgadze, N. Y., Sall, D. J., Briggs, S. L., Clawson, D. K., Zhang, M., Smith, G. F. & Schevitz, R. W. The crystal structures of human alpha-thrombin complexed with active site-directed diamino benzo[b]thiophene derivatives: a binding mode for a structurally novel class of inhibitors. *Protein Sci. Publ. Protein Soc.* **9**, 29–36 (2000).

32. Nir, I., Huttner, D. & Meller, A. Direct Sensing and Discrimination among Ubiquitin and Ubiquitin Chains Using Solid-State Nanopores. *Biophys. J.* **108**, 2340–2349 (2015).

33. Li, W., Bell, N. A. W., Hernández-Ainsa, S., Thacker, V. V., Thackray, A. M., Bujdoso, R. & Keyser, U. F. Single Protein Molecule Detection by Glass Nanopores. *ACS Nano* **7**, 4129–4134 (2013).

34. Hardin, C. C., Perry, A. G. & White, K. Thermodynamic and kinetic characterization of the dissociation and assembly of quadruplex nucleic acids. *Biopolymers* **56**, 147–194 (2000).

35. Basnar, B., Elnathan, R. & Willner, I. Following Aptamer−Thrombin Binding by Force Measurements. *Anal. Chem.* **78**, 3638–3642 (2006).

36. Yu, J., Jiang, Y., Ma, X., Lin, Y. & Fang, X. Energy Landscape of Aptamer/Protein Complexes Studied by Single-Molecule Force Spectroscopy. *Chem. – Asian J.* **2**, 284–289 (2007).

37. Neundlinger, I., Poturnayova, A., Karpisova, I., Rankl, C., Hinterdorfer, P., Snejdarkova, M., Hianik, T. & Ebner, A. Characterization of Enhanced Monovalent and Bivalent Thrombin DNA Aptamer Binding Using Single Molecule Force Spectroscopy. *Biophys. J.* **101**, 1781–1787 (2011).

38. Ma, X., Gosai, A., Balasubramanian, G. & Shrotriya, P. Force spectroscopy of the thrombin-aptamer interaction: Comparison between AFM experiments and molecular dynamics simulations. *Appl. Surf. Sci.* **475**, 462–472 (2019).

39. Heng, J. B., Aksimentiev, A., Ho, C., Marks, P., Grinkova, Y. V., Sligar, S., Schulten, K. & Timp, G. Stretching DNA Using the Electric Field in a Synthetic Nanopore. *Nano Lett.* **5**, 1883–1888 (2005).

40. Raillon, C., Cousin, P., Traversi, F., Garcia-Cordero, E., Hernandez, N. & Radenovic, A. Nanopore Detection of Single Molecule RNAP–DNA Transcription Complex. *Nano Lett.* **12**, 1157–1164 (2012).

41. Cai, S.-L., Cao, S.-H., Zheng, Y.-B., Zhao, S., Yang, J.-L. & Li, Y.-Q. Surface charge modulated aptasensor in a single glass conical nanopore. *Biosens. Bioelectron.* **71**, 37–43 (2015).

42. Ali, M., Nasir, S. & Ensinger, W. Bioconjugation-induced ionic current rectification in aptamer-modified single cylindrical nanopores. *Chem. Commun.* **51**, 3454–3457 (2015).

43. Actis, P., Rogers, A., Nivala, J., Vilozny, B., Seger, R. A., Jejelowo, O. & Pourmand, N. Reversible thrombin detection by aptamer functionalized STING sensors. *Biosens. Bioelectron.* **26**, 4503–4507 (2011).

44. Blundell, E. L. C. J., Mayne, L. J., Lickorish, M., Christie, S. D. R. & Platt, M. Protein detection using tunable pores: resistive pulses and current rectification. *Faraday Discuss.* **193**, 487–505 (2016).

5

Conclusion

5.1 Conclusion

Single-molecule nanopore sensing of proteins with bare and functionalized solid-state nanopore is a promising technique that has been explored during this thesis. First, the description of nanopore sensing technology and the different types of nanopores employed in the literature have been discussed in Chapter 1. Different applications have been described, from the already commercially available DNA sequencing[1] to the more emergent field of protein sensing[2,3]. Differences between those applications have been drawn. Proteins are biomolecules with non-homogeneously charged surfaces that translocate at a high speed in bare nanopores and are challenging to detect[4,5]. A focus has been drawn on the use of aptamers in combination with nanopores. Aptamer-functionalized nanopore emerged as an interesting tool to detect specific targets[6–8]. The aim of this project was indeed the functionalization of a solid-state silicon nitride nanopore for the specific detection of three closely-related proteins involved in the blood coagulation cascade (α-thrombin, ɣ-thrombin and prothrombin).

In Chapter 2, two different approaches for the fabrication of nanopores chips have been described: TEM drilling and a cleanroom microfabrication process. For the latter, all the different steps have been described for the fabrication of nanopores on a 200 mm diameter wafer with a 50 nm thin silicon nitride layer. This process is still under development. A PDMS fluidic design has been suggested for further studies. Another technique has been employed for the fabrication of nanopores used for the translocation of proteins: TEM drilling[9]. This allowed us to get nanopore chips before the cleanroom process flow was complete. Microfabrication techniques in a cleanroom possess the advantages to offer a wafer-scale production of nanopore chips with highly tunable geometrical properties. However, the development process of all steps is long. Using a TEM to drill nanopores in commercial silicon nitride membranes is fast and provides a direct visual feedback on the fabricated nanopore. However, only one nanopore is fabricated at a time and we are limited with the equipment availability. Commercial nanopores were also tested in this work (Chapter 4) but they were too big for our protein sensing applications. Regarding those options, the TEM drilling on commercial membrane technique has been selected to provide us with the nanopore chips for experiments.

In Chapter 3, the experimental bench for nanopore sensing that has been built for this study has been presented. From the selection of the fluidic system for encapsulation of nanopore chips to electronic hardware for the data acquisition, all the different elements have been described. The data treatment methodology has been depicted. The recorded data is analyzed in MATLAB thanks to a software called OpenNanopore[10]. Then, all the different physical properties of nanopores and single-molecule sensing have been described for the further interpretation of results. Finally, this chapter described the surface chemistry chosen for this project. The silicon nitride layer is silanized using silanes bearing reactive maleimide groups which are able to react with thiolated aptamers.

In Chapter 4, the experimental bench built for this thesis work has been effectively tested and validated thanks to different pilot experiments for the I-V characterization of nanopores and single-molecule detection of a widely used biomolecule target: λDNA. Regarding surface functionalization with aptamers that specifically recognize α-thrombin, the first step has been to validate the grafting on planar silicon nitride chips with fluorescent revelation. Then, the same protocol has been tested on nanopores and the grafting of aptamers has been effectively observed thanks to a nanopore's conductance decrease. The ionic current rectification phenomenon after nanopore functionalization also indicates that the surface has been negatively charged with the grafting of aptamers. It also highlighted the fact that the nanopores used are not perfectly symmetrical and that the surface functionalization is not symmetrical either. Finally, noise has been compared before and after functionalization in a same nanopore. The functionalized nanopore exhibited better noise performances in the low frequency range, while at high frequencies it was similar to the bare nanopore. This highlights one of the advantages of surface functionalization which is the enhancement of signal-to-noise ratio and easier single-molecule sensing.

The single-event detection of three proteins, prothrombin, α-thrombin and ɣ-thrombin has been performed first in a bare nanopore. Prothrombin was successfully detected, and the current shape of each translocation indicated a reorientation of this oblate spheroid protein in the nanopore. α-thrombin and ɣ-thrombin are smaller globular proteins with the same volume. They were effectively sensed in the nanopore with single-events but could not be differentiated with their current blockage or dwell-time signature due to their high similarity. The functionalization of the inner walls of a nanopore could be a solution to discriminate such closely related protein, thanks to specific interactions of one protein with grafted probes and then the generation of a specific dwell-time signature. Single-event detection of α-thrombin and ɣ-thrombin has been performed in an aptamer-functionalized nanopore, at pH 7.4. Notably, ɣ-thrombin has generated a specific current signature with different levels in an event that have been linked to the volume of one and two ɣ-thrombin going into the nanopore. The hypothesis that has been emitted is that, at pH 7.4, the negatively charged ɣ-thrombin protein is electrostatically repulsed by the negatively charged surface of the nanopore and is slowed down at the entrance (non specific interaction of ɣ-thrombin with aptamers). Then, another ɣ-thrombin arrives in the sensing zone, collides with the first one and the two proteins translocate along in the nanopore. α-thrombin has exhibited a typical current signature for a globular protein going through the nanopore. We have observed that the dwell-time for the translocation of ɣ-thrombin in the functionalized nanopore is significantly longer than the dwell-time of α-thrombin which was supposed to interact specifically with the surface aptamers. After verification that there is no competition between the electrical force applied on α-thrombin and the binding force between the

aptamer and α-thrombin, we conclude that a balance has to be found for the choice of the pH of the experiment between the charge of the protein (so that it be electrophoretically-driven through the nanopore) and the optimal pH for the aptamer-protein recognition. Further studies should be performed in various buffer compositions and pH to validate this hypothesis. Nevertheless, their dwell-time signatures are different in the functionalized nanopore and the sensing of ɣ-thrombin has been enhanced in the functionalized nanopore with an overall increase of dwell-time and a clear reduction of impulsion percentage (short events from 10 to 100 µs).

Finally, another option for the specific detection of α-thrombin has been explored with the use of conductance curves, at a lower pH (5,2). This allows to specifically detect the target protein in a functionalized nanopore thanks to a decrease in nanopore conductance and a change in the ionic current rectification properties. The specificity of this technique has been assessed with conductance measurements of the aptamer-functionalized nanopore in presence of α-thrombin, which is effectively sensed with a conductance decrease, and in presence of ɣ-thrombin, which is not recognized by the aptamer and had no effect on the pore conductance.

5.2 Perspectives

Perspectives of improvements for the study of α-thrombin, ɣ-thrombin and prothrombin have been suggested along this manuscript. Experiments should be repeated in order to validate the replicability of the results. Protein sensing (from single-events and I-V curve measurements) should be performed in a variety of buffers with different pH and salt concentrations in order to assess the effect of the charge of the protein on its detection. Moreover, it could be interesting to generally improve the detection methodology for single-molecule sensing with various approaches such as the increase of sample frequency and high bandwidth analysis[5], working on the reduction of noise in the current measurements[11,12] or even try different techniques such as molecular crowding which has been used to enhance the detection of DNA and proteins in solid-state nanopores[13].

A long-term perspective would be to adapt the ContactLess ElectroFunctionalization (CLEF) technique from our group on nanopores[14–16]. It has already been validated on micropores and ~200 nm diameter pores and would allow the localized functionalization of the nanopore. We indeed needed a higher concentration of α-thrombin because the proteins would interact will all the surface aptamers on the membrane. The advantage of a localized functionalization would be the reduction of the specific target concentration needed for its sensing with the functionalized nanopore, and probably a more homogenous functionalization in the nanopore. CLEF needs the presence of a (semi) conducting material in the nanopore, which entails supplementary nano-fabrication concerns.

Another long-term perspective would be to adapt the nanopore surface chemistry to DNA-directed immobilization[17] (Figure 5.1). This technique consists in the use of a DNA functionalized surface to generate various kinds of sensors with the complementary DNA strand coupled with a biomolecule such as aptamers, proteins, or sugars that are naturally present on the membrane of the cell and could offer biomimetic properties to the nanopore. A sugar-oligonucleotide conjugate is notably in development in our group with the work of a PhD student that will defend in 2021. This could offer a fast, versatile, and reversible tool for the detection of virtually any kind of biomolecule target in a solid-state nanopore.

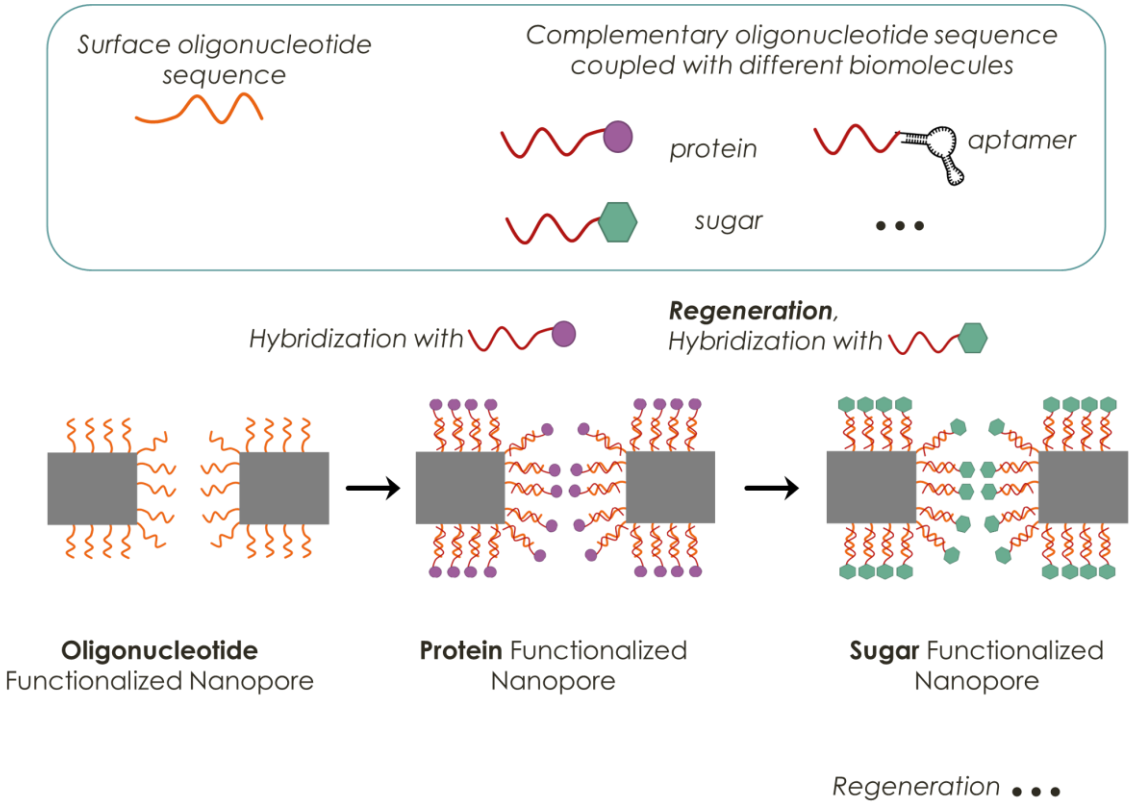

Figure 5.1: DNA-Directed Immobilization perspective with an oligonucleotide-functionalized nanopore. Using complementary sequences coupled with any kind of biomolecule of interest would allow a versatile biosensor.

5.3 References

1. Eisenstein, M. Oxford Nanopore announcement sets sequencing sector abuzz. *Nature Biotechnology* **30**, 295–296 (2012).
2. Plesa, C., Kowalczyk, S. W., Zinsmeester, R., Grosberg, A. Y., Rabin, Y. & Dekker, C. Fast Translocation of Proteins through Solid State Nanopores. *Nano Lett.* **13**, 658–663 (2013).
3. Varongchayakul, N., Song, J., Meller, A. & W. Grinstaff, M. Single-molecule protein sensing in a nanopore: a tutorial. *Chemical Society Reviews* **47**, 8512–8524 (2018).
4. Balme, S., Coulon, P. E., Lepoitevin, M., Charlot, B., Yandrapalli, N., Favard, C., Muriaux, D., Bechelany, M. & Janot, J.-M. Influence of Adsorption on Proteins and Amyloid Detection by Silicon Nitride Nanopore. *Langmuir* **32**, 8916–8925 (2016).
5. Larkin, J., Henley, R. Y., Muthukumar, M., Rosenstein, J. K. & Wanunu, M. High-Bandwidth Protein Analysis Using Solid-State Nanopores. *Biophys J* **106**, 696–704 (2014).
6. Ding, S., Gao, C. & Gu, L.-Q. Capturing Single Molecules of Immunoglobulin and Ricin with an Aptamer-Encoded Glass Nanopore. *Anal. Chem.* **81**, 6649–6655 (2009).
7. Cai, S.-L., Cao, S.-H., Zheng, Y.-B., Zhao, S., Yang, J.-L. & Li, Y.-Q. Surface charge modulated aptasensor in a single glass conical nanopore. *Biosensors and Bioelectronics* **71**, 37–43 (2015).
8. Das, N., Ray, R., Ray, S. & Roychaudhuri, C. Intelligent Quantification of Picomolar Protein Concentration in Serum by Functionalized Nanopores. *IEEE Sensors Journal* **18**, 10183–10191 (2018).
9. Storm, A. J., Chen, J. H., Ling, X. S., Zandbergen, H. W. & Dekker, C. Fabrication of solid-state nanopores with single-nanometre precision. *Nature Materials* **2**, 537–540 (2003).
10. Raillon, C., Granjon, P., Graf, M., J. Steinbock, L. & Radenovic, A. Fast and automatic processing of multi-level events in nanopore translocation experiments. *Nanoscale* **4**, 4916–4924 (2012).
11. Smeets, R. M. M., Keyser, U. F., Dekker, N. H. & Dekker, C. Noise in solid-state nanopores. *PNAS* **105**, 417–421 (2008).

12. Tabard-Cossa, V., Trivedi, D., Wiggin, M., Jetha, N. N. & Marziali, A. Noise analysis and reduction in solid-state nanopores. *Nanotechnology* **18**, 305505 (2007).

13. Chau, C. C., Radford, S. E., Hewitt, E. W. & Actis, P. Macromolecular Crowding Enhances the Detection of DNA and Proteins by a Solid-State Nanopore. *Nano Lett.* **20**, 5553–5561 (2020).

14. Bouchet, A., Descamps, E., Mailley, P., Livache, T., Chatelain, F. & Haguet, V. Contactless Electrofunctionalization of a Single Pore. *Small* **5**, 2297–2303 (2009).

15. Bouchet-Spinelli, A., Descamps, A., Liu, J., Ismail, A., Pham, P., Chatelain, F., Leïchlé, T., Leroy, L., Marche, P. N., Raillon, C., Roget, A., Roupioz, Y., Sojic, N., Buhot, A., Haguet, V., Livache, T. & Mailley, P. Polarization Induced Electro-Functionalization of Pore Walls: A Contactless Technology. *Biosensors* **9**, 121 (2019).

16. Ismail, A., Voci, S., Pham, P., Leroy, L., Maziz, A., Descamps, L., Kuhn, A., Mailley, P., Livache, T., Buhot, A., Leichlé, T., Bouchet-Spinelli, A. & Sojic, N. Enhanced Bipolar Electrochemistry at Solid-State Micropores: Demonstration by Wireless Electrochemiluminescence Imaging. *Anal. Chem.* **91**, 8900–8907 (2019).

17. Meyer, R., Giselbrecht, S., Rapp, B. E., Hirtz, M. & Niemeyer, C. M. Advances in DNA-directed immobilization. *Current Opinion in Chemical Biology* **18**, 8–15 (2014).

Appendix

5.4 I – Experimental Material

In Table i are listed the different oligonucleotides sequences used for this work. Thr1 is intended to be grafted onto silicon nitride surface and thr1c is used for the fluorescent revelation of surface functionalization. Thr2 is a sequence used as a negative control.

Name	Sequence (5'→3')	Supplier
Thr1	TTT-TTT-TTT-TGG-TTG-GTG-TGG-TTG-G	Eurogentec, Belgium
Thr1c	TTT-TTT-TTT-TCC-AAC-CAC-ACC-AAC-C	
Thr2	TTT-TTT-TTT-TAG-TCC-GTG-GTA-GGG-CAG-GTT-GGG-GTG-ACT	

Table i: List of oligonucleotides used in this work.

In Table ii are listed the different biomolecules used for translocation experiments through nanopores.

Analyte	Size (PDB)	Typical concentrations	Supplier
α-thrombin	36700 Da – Ø 5 nm (1D3T)	1 – 100 nM	Cryopep, France
ɣ-thrombin	34300 Da – Ø 5 nm (2HNT)	1 – 100 nM	Thermo Fisher Scientific, USA
Prothrombin	72 kDa – 9 x 5 nm (6BJR)	1 – 100 nM	Cryopep, France
λDNA	48502 bp, 31.5 x 10^6 Da	3 ng/µL (= 93 nM)	Thermo Fisher Scientific, USA

Table ii: List of analytes for nanopore experiments.

5.5 II – Chemical compounds and solutions

All chemicals, gases and solvents used for this work are listed in Table iii.

Chemicals	**Supplier**
(3-aminopropyl)triethoxysilane (APTES)	Sigma Aldrich, USA
SAPE Streptavidin Associated Phycoerythrin	Invitrogen, USA
Trizma Hydochloride (Tris-HCl)	Sigma Aldrich, USA
Magnesium Chloride ($MgCl_2$)	Sigma Aldrich, USA
Sodium Chloride (NaCl)	Sigma Aldrich, USA
Potassium Chloride (KCl)	Prolabo, France
Tris/EDTA (10 mM/1mM)	Thermo Fisher, USA
Phosphate-Buffered Saline (PBS)	Sigma Aldrich, USA
Tween20	Sigma Aldrich, USA
Sodium hypochlorite (Bleach, NaClO)	Teepol Shell Chemicals, United Kingdom
Sulfuric acid (H_2SO_4)	Sigma Aldrich, USA
Hydrogen peroxide (H_2O_2)	Sigma Aldrich, USA
Toluene	Sigma Aldrich, USA
Ethanol Absolute	VWR, USA
Ethanol 96°	Carlo Erba Reagents, France

Table iii: List of main chemicals used in this thesis.

All solutions and buffers listed in Table iv are prepared using purified water (MilliQ, Elga LabWater Veolia, United Kingdom) and filtered through 0.22 µm filters (Filters from Millipore, France and vacuum generator CVC3000 from Vacuubrand, Germany). Compounds are weighted on a balance AUW220D (Shimadzu, Japan) and pH is measured using a BasiC 20 pH-meter (CRISON Instruments, Spain). When necessary, the conductivity of the solution was measured with a Radiometer CDM210 (Radiometer Analytical, France).

Solution	**Composition, Conductivity**
Buffer for translocation of λ-DNA	KCl 1 M, Tris-HCl 1 mM, EDTA 0.1 mM, pH 8 – **9.78 S/m**
Buffer for translocation of proteins **pH 7.4**	Tris-HCl 20 mM, $MgCl_2$ 1mM, NaCl 120 mM, KCl 10 mM, pH 7.4 - **0.953 S/m**
Buffer for translocation of proteins **pH 5**	Tris-HCl 20 mM, $MgCl_2$ 1mM, NaCl 120 mM, KCl 10 mM, pH 5 – **1.411 S/m**
Storing Buffer	Tween20 at 0.15 % v/v
Hybridization Buffer	PBS 100 mM, NaCl 537 mM, KCl 2.7 mM, Tween 0.05 %
Rinsing Buffer	PBS 10 mM, NaCl 537 mM, KCl 2.7 mM, Tween 0.05 %
Piranha Solution *	H_2SO_4 70 %, H_2O_2 30 % *** /!\ dangerous solution /!**

Table iv: List of buffers and solutions used in this thesis.

5.6 III – General Material

In Table v are listed the main equipment used in this thesis.

Machine	**Company, Country**
MilliQ Water purification	Elga LabWater Veolia, United Kingdom
Vacuum generator CVC3000	Vacuubrand, Germany
pH-meter BasiC 20	CRISON Instruments, Spain
Balance AUW220D	Shimadzu, Japan
Conductometer CDM210	Radiometer Analytical, France
Vacuum concentrator Speedvac	Savant Thermo Fischer, USA
Incubator Thermostat plus MTP	Eppendorf, Germany
Spectrophotometer NanoDrop 2000C	Thermo Fischer, USA
Plasma Generator Femto	Diener Electronic, Germany
Amplifier Axopatch 200B	Molecular Devices, USA
A/D Converter NI USB 6361	National Instrument, USA
Oscilloscope Handyscope HS5	TiePie, Netherlands
Microscope DM2500	Leica, Germany
Camera DFC425	Leica, Germany
Microscope BX60	Olympus, Japan
Camera/Controller Chilled CCD C5985	Hamamatsu, Japan
Laser engraving TAU TECH	Cielle, Italy
Laser writer µPG 101	Heidelberg Instruments, Germany
Metal Evaporator MEB550	Plassys, France
Electron Beam Lithography 6300FS	JEOL, Japan
Reactive Ion Etching PLASMALAB100	Oxford, United Kingdom
SEM Ultra 55	Zeiss, Germany
TEM Tecnai Osiris	FEI, USA

Table v: List of equipment used in this work.

In Table vi are listed the main consumables and materials used

Material	**Company, Country**
0.22 µm Filters	Millipore, France
Ag/AgCl Electrodes 0.25 mm diameter	VWR, USA
Ester Noise insulation foam AV40G	Panasorb, Germany
Rebond noise insulation foam Verbund200	Panasorb, Germany
Illustra Nap-5 colums Sephadex G-25	General Electrics Healthcare, USA
Glass slides	VWR, USA
Glass coverslips Menzel Gläser	Thermo Fischer, USA
Glass 5 mL tubes	Superlco, Germany
50 mL Falcon tubes	Corning, USA
2 mL Safe-Lock tubes	Eppendorf, Germany
0.2 mL Safe-Lock tubes	Eppendorf, Germany
Pipette tips epT.I.P.S Reloads	Eppendorf, Germany

Table vi: List of the main materials used in this thesis work.

5.7 IV – List of Softwares

Software	*Use in this work*	*Company/ organization, Country*
KLayout	*Fabrication*: Wafer designs	*none*
CLTerminal	*Fabrication*: Tau Tech Laser design and control	Cielle, Italy
SmartSEM	*Microscopy*: Control of SEM ZEISS ULTRA 55	Zeiss, Germany
Fiji/ImageJ	*Microscopy*: Picture analysis	National Institutes of Health, USA
Anaconda *Python*	*Experimental*: Control of TiePie Oscilloscope for nanopore I-V curves	*none*
DAQExpress	*Experimental*: Data acquisition	National Instrument, USA
Swiss-PdbViewer *4.1.0*	Measuring proteins from their PDB sequence	Swiss Institute of Bioinformatics, Swiss
Protein Dipole Moments Server	Measuring protein dipoles from their PDB sequence	Dept. Structural Biology Weizmann Institute, Israel
MATLAB *R2019a*	*Data Analysis*: "Open Nanopore" and diverse functions	MathWorks, USA
Origin	*Data Analysis*: fitting histogram curves	OriginLab, USA
Open Nanopore *Matlab code*	*Data Analysis*: Nanopore single-events detection and fitting	École Polytechnique Fédérale de Lausanne - A. Radenovic group, Swiss

5.8 V – Nanopore Chip Cleanroom Fabrication: Wafer Designs

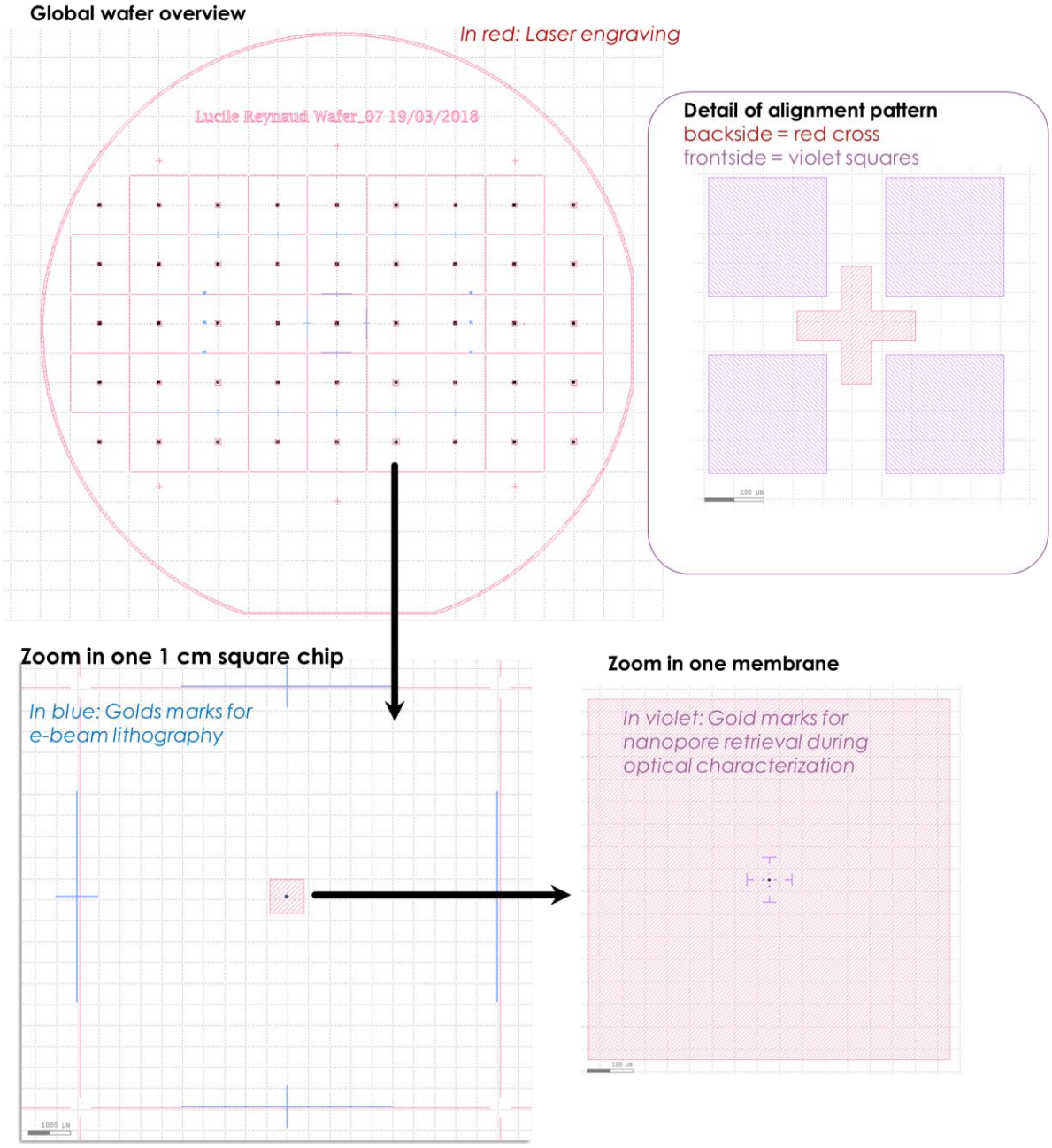

Abbreviations

A/D	Analog-to-Digital converter
ADP	Adenosine diphosphate
AeL	Aerolysin
ALD	Atomic Layer Deposition
ATP	adenosine triphosphate
BSA	bovine serum albumin
CEA	carcinoembryonic antigen
CLEF	ContactLess ElectroFunctionalization
ClyA	Cytolysin A
CVD	Chemical Vapor Deposition
DNA	DeoxyriboNucleic Acid
EDTA	Ethylenediaminetetraacetic acid
EHT	Electron High Tension
FIB	Focused Ion Beam
HIV	Human Immunodeficiency Virus
ICR	Ionic Current Rectification
IPA	Isopropyl alcohol / Isopropanol
I-V	Current-voltage (conductance characterization curve)
K_d	dissociation constant
LBL	Layer-by-layer
LOC	Lab-on-a-chip
LPCVD	Low-Pressure Chemical Vapour Deposition
LSPR	Nanoplasmonic sensing with localized surface plasmon resonance
MIBK	methyl isobutyl ketone
MspA	Mycobacterium smegmatis porin A
NCp7	Nucleocapsid protein 7
NHS	N-HydroxySuccinimide
OmpG	Outer membrane protein G
OTA	Ochratoxin A
PBS	phosphate buffered saline

PCR Polymerase Chain Reaction

PDB Protein Data Bank

PDGF platelet-derived growth factor

PDMS Polydimethylsiloxane

PET polyetheylene terephthalate

PFNC PlateForme NanoCaractérisation

pI Isoelectric point

PLL Poly-L-Lysin

PSD Power Spectral Density

PTA Platefore Technologie Amont

PTFE PolyTetraFluoroEthylene - Teflon

RF Radio Frequency

RIE Reactive Ion Etching

RNA Ribonucleic acid

SAMs Sels-Assembled Monolayers

SAPE Streptavidin-Associated Phycoerythrin

SDS Sodium Dodecyl Sulfate

SELEX Systematic Evolution of Ligands by EXponential Enrichment

SEM Scanning Electrion Microscope

SERS Surface-enhanced Raman spectroscopy

SM-EC Single molecule electrochemical assays

SNR Signal-to-Noise Ratio

TEM Transmission Electron Microscope

UV Ultra-Violet

VEGF Vascular endothelial growth factor

Chemicals

Ag Silver

AgCl Silver chloride

CF_4 tetrafluroromethane

EtOH Ethanol

F Fluorine

HfO_2 hafnium oxide

Hg Mercury

KCl Potassium chloride

KOH Potassium hydroxide

Pb Lead

SF_6 Sulfur hexafluoride gas

Si Silicium

Si_3N_4 - SiN_x Silicon Nitride

SiO2 Silicon dioxide

Units

bp Base pair

Da – kDa Dalton – kilodalton

mV millivolt

nA nanoampere

pA picoampere

Ppb part per billion

sccm standard cubic centimeters per minute

Abstracts

English Abstract

The specific detection of proteins is a major challenge in many biotechnological fields such as biomedical diagnostics or fundamental understanding complex protein interactions. Solid-state nanopores are microfabricated nanoscale apertures in thin dielectric membranes that have raised attention as label-free single-molecule biosensors with high sensitivity. A voltage is applied across the membrane, which drives biomolecules through the nanopore. When the analyte crosses the nanopore, it causes a current blockage for a certain time that provides a specific electrical signature for each molecule of interest. During this thesis, a cleanroom process flow has been developed for the fabrication of nanopore chips as well as the drilling of 15 nm diameter nanopore in a 20 nm thick silicon nitride membrane using a Transmission Electron Microscope. The experimental bench for nanopore sensing has been built up and tested. α-thrombin, ɣ-thrombin (5 nm diameter globular proteins) and prothrombin (5 nm x 9 nm oblate spheroid) are three closely-related proteins involved in blood coagulation cascade. They have been sensed using a bare nanopore down to 1 nM concentration, and prothrombin could be discriminated thanks to its bigger size. In order to discriminate α-thrombin from ɣ-thrombin, which have similar sizes, the nanopore's surface has been chemically functionalized with aptamers. Aptamers are short single stranded DNA sequences selected for their affinity towards a specific biomolecule. We used an aptamer specifically recognizing α-thrombin. We demonstrated that the nanopore functionalization was successful thanks to a measured diameter reduction of the nanopore. Moreover, α-thrombin and ɣ-thrombin present different electrostatic interactions with the functionalization surface of the nanopore, hence a different dwell-time signature in the pore and could be discriminated. Aptamer-functionalized nanopores provide promising and versatile biosensing performances.

Abstract Français

La détection spécifique de protéines est un enjeu majeur dans de nombreux domaines biotechnologiques tels que le diagnostic biomédical ou la compréhension fondamentale des mécanismes d'interaction entre protéines. Les nanopores solides sont des ouvertures de taille nanométriques micro-fabriqués dans des membranes diélectriques fines. Ils sont prometteurs en tant que biocapteurs sensibles pour la détection sans marquages de molécules uniques. Une tension est appliquée de part et d'autre de la membrane, ce qui entraine les biomolécules au travers du pore. Lorsque l'une d'entre elles traverse le nanopore, elle génère un blocage de courant pendant un certain temps, ce qui offre une signature spécifique pour chaque biomolécule d'intérêt. Durant ces travaux de thèse, un procédé en salle blanche a été développé afin de fabriquer des puces avec nanopore. Une autre technique a été d'utiliser un microscope à transmission électronique pour percer des nanopores de 15 nm de diamètre dans des membranes de nitrure de silicium de 20 nm d'épaisseur. Un banc expérimental pour la détection par nanopore a été construit et testé. α-thrombine, ɣ-thrombine (protéines globulaires de 5 nm de diamètre) et prothrombine (sphéroïde de dimensions 5 nm x 9 nm) sont trois protéines de structures proches impliquées dans la coagulation sanguine. Elles ont été détectées avec un nanopore à une concentration de 1 nM. De plus, prothrombine a été discriminée de α-thrombine et ɣ-thrombine grâce à sa plus grande taille. A cause de leur taille similaire et donc de la même signature de blocage de courant qu'elles génèrent, α-thrombine et ɣ-thrombine n'ont pas été discriminée dans ce pore. La surface du nanopore a donc été fonctionnalisée avec des aptamères. Les aptamères sont de courtes séquences d'ADN simple brin capables de se lier avec une grande affinité à des biomolécules. Nous avons choisi un aptamère reconnaissant spécifiquement α-thrombine. La fonctionnalisation a été prouvée grâce à une réduction mesurée du diamètre du nanopore. α-thrombine et ɣ-thrombine ont des interactions électrostatiques différentes l'une et l'autre avec les aptamères en surface. Nous avons donc pu observer des temps de passage différents dans le nanopore fonctionnalisé entre ces deux protéines et avons pu les discriminer. Les nanopores fonctionnalisés avec aptamères offrent donc des performances prometteuses et polyvalentes en matière de bio-détection.